UNIVERSITÉ DE STRASBOURG

École Doctorale de Physique et Chimie-Physique (ED 182)

Institut de Physique et Chimie des Matériaux de Strasbourg (UMR 7504)

THÈSE présentée par :

Guillaume Krieger

Soutenance prévue le : **14 décembre 2022**

pour obtenir le grade de : **Docteur de l'université de Strasbourg**

Discipline/ Spécialité : Science des Matériaux

Structural and orbital engineering in nickelate thin films: on the road of superconductivity

THÈSE dirigée par :

Mme Nathalie Viart	Professeure, IPCMS - Université de Strasbourg
M Daniele Preziosi	Chargé de recherche – IPCMS, Strasbourg

RAPPORTEURS :

Mme Marta Gibert	Professeure, TU Wien
Mme Agnès Barthélémy	Professeure, Paris-Saclay

AUTRES MEMBRES DU JURY :

M Jens Kreisel	Professeur, Université du Luxembourg
M Silviu Colis	Professeur, IPCMS – Université de Strasbourg

Contents

List of abbreviations

AFM Atomic Force Microscopy

AMR Anisotropic magnetoresistance

IP-AMR In-plane Anisotropic magnetoresistance

OOP-AMR Out-of-plane Anisotropic magnetoresistance

BL Buffer layer

CT Charge-transfer

EELS Electron energy loss spectroscopy

FeFED Ferroelectric field-effect devices

H Magnetic field

J Hund’s coupling energy

LAO LaAlO$_3$

LH Lower Hubbard band

LMO LaMnO$_3$

LSAT (La,Sr)(Al,Ta)O$_3$

MIT Metal-to-insulator transition

MH Mott-Hubbard

NSNO$_2$(x) Nd$_{1-x}$Sr$_x$NiO$_2$

NSNO$_3$(x) Nd$_{1-x}$Sr$_x$NiO$_3$

P Polarization

pc pseudocubic

PZT PbZr$_{0.2}$Ti$_{0.8}$O$_3$

RHEED Reflection of high energy electron diffraction

rms root mean square

RSM Reciprocal space mapping

REXS Resonant elastic X-ray scattering

RIXS Resonant Inelastic X-ray scattering

STEM Scanning transmission electron microscopy

STO SrTiO$_3$

TM Transition metal

TMO Transition metal oxides

$T_{\text{Néel}}$ Néel transition temperature

U Coulomb repulsion

u.c. unit cell

UH Upper Hubbard band

XAS X-ray absorption spectroscopy

XLD X-ray linear dichroism

XMCD X-ray magnetic circular dichroism

XRD X-ray diffraction

XRR X-ray reflectivity

Δ charge transfer energy

Δ' effective charge transfer energy

I. Introduction

The massive investment in quantum technologies that is ongoing in France[1] speaks in favour of the big potential that the exotic properties exhibited *in primis* by transition metal oxides can be of practical interest for the foreseen quantum computing devices. In particular, the different functional properties, such as high-temperature superconductivity, colossal magnetoresistance, multiferroïcity, metal-to-insulator transition and topology make transition metal oxides promising candidates for the development of novel electronic architectures that consume less energy. The choice of a particular doping level or strain state can be done in such a way that the system is largely tunable to external stimuli being located at the verge line of two different states. Therefore, the very rich phase diagrams of transition metal oxides allow to endow the properly engineered devices with a control over the desired functional properties. Recent progress in materials synthesis, allowing an improved quality of the material in thin film form, have made it possible to exploit interface-induced phenomena and reduced dimensionality to manipulate the electronic states in transition metal oxides-based heterostructures. This makes it possible to think of going beyond the actual Si-based technology [1].

More than developing new materials with interesting properties, the complete understanding of the mechanisms underneath the aforementioned exotic properties is probably an even bigger dream for the scientific community. The term "strongly correlated", with which one usually refers to transition metal oxides, where a large electron-electron interaction is at play, is mainly at the base of the complexity of the properties displayed by transition metal oxides and that makes their study exciting. For instance, the standard classification of the transport properties such as metallic, semiconductor or insulator is not any longer valid when related to transition metal oxides and new concepts need to be used, such as bad-metal or Fermi liquid behaviour. Beyond classifications, unravelling the microscopic mechanisms controlling the exotic properties of several transition metal oxides still remains the holy grail in solid state physics, and the understanding of high-temperature superconductivity is the best example. The discovery, in 1986 [2], of a superconducting state in the copper oxide perovskite $La_{2-x}Ba_xCuO_4$ at temperatures exceeding those observed in all previously known superconductors, was one of the major events in solid state physics. It soon became clear that the Bardeen-Cooper-Schrieffer (BCS) theory [3] could not explain alone the relatively high critical temperatures typical of copper-based oxides, and researchers are still working to get a full understanding of the mechanisms driving the superconductivity in cuprates. It was suggested in 1999 that mimicking the $3d^9$ electronic configuration of Cu^{2+} ions and their planar coordination in a Ni-based compound could provide a way to push further the understanding of unconventional superconductivity. The recent success in synthesizing the long-pursued Ni^{1+}-based infinite-layer phase has, from one side, re-established the role of the theoreticians, and, from the other side, opened new issues about material synthesis and stabilization [4].

In this thesis, I will start by giving a general introduction about the perovskite transition metal oxides, and then, focus on the perovskite family which is of particular interest here: the rare-earth nickelates, in both bulk and thin film forms, with a main focus on the metal-to-insulator transition for which they have been largely studied. Next, I will introduce the infinite-layer nickelate phase, which, since the first report of superconductivity in August 2019, has started attracting a massive interest from the

---

[1] *https://www.gouvernement.fr/actualite/18-m-eu-en-faveur-des-technologies-quantiques*

condensed matter community. Its initially proposed two-step synthesis process is very challenging and so far, only a handful of works could reproduce it in an independent way. Here in Strasbourg I have been able to optimize the growth of the (Nd,Sr)NiO_3 perovskite phase and the parameters for a reproducible topotactic reduction at different Sr-contents and with the presence/absence of an $SrTiO_3$ capping layer.

I have used a pulsed laser deposition (PLD) technique to grow all the thin films presented in this thesis. This elaboration technique, alongside with the soft-chemistry reduction process, will be described in Chapter III. Therein, I will also outline the techniques used to characterize the samples from structural, morphological and transport points of view. The last part of the Chapter will be dedicated to the description of the different types of synchrotron measurements performed during this thesis.

The optimisation process that I have undertaken for the perovskite $Nd_{1-x}Sr_xNiO_3$ thin films is presented in the first part of Chapter IV. I show that resistivity and X-ray diffraction measurements can be used as proxy to evaluate the quality of my Sr-doped perovskite thin films. A no-toggling ablation process has proved its effectiveness in improving the Nd/Ni cation stoichiometry, especially for the Sr-doped thin films. The second part of the Chapter is devoted to the reduction of the optimized perovskite phase into the infinite-layer phase. The reduction conditions are highly impacted by the amount of Sr and the presence/absence of a $SrTiO_3$ capping-layer, which translated in very different reduction conditions for all the different grown samples.

Resonant inelastic X-ray scattering (RIXS) measurements performed at the ID32 beamline of the ESRF synchrotron in Grenoble allowed to scope the low-energy excitations of the infinite-layer nickelate thin films and will be presented in Chapter V. As a result of an international collaboration we found an interesting dichotomy between charge and magnetic excitations driven substantially by the absence or presence of the $SrTiO_3$ capping-layer. We have also studied how these excitations vary as a function of the Sr-doping. Moreover, thanks to polarization-resolved spectra, which are only possible at the ID32 beamline, we could go deeper into the study of the (presumed) magnetic excitations also in the uncapped samples. In the final part of this Chapter I will introduce my preliminary magnetotransport measurements, which exhibiting differences between capped and uncapped thin films, echo the RIXS results.

In Chapter VI, I will focus again on the perovskite phase and present the studies I performed on $NdNiO_3/PbZr_{0.2}Ti_{0.8}O_3$ (PZT) heterostructures. The idea was to observe the influence of a ferroelectric-field effect on the $NdNiO_3$ metal-to-insulator and paramagnetic-antiferromagnetic transition temperatures. I have soon realized that from the growth point of view the stabilization of the ideal Ni^{3+} valence state in nickelate/ferroelectric heterostructures can be very challenging, due to a rather uncontrollable degree of oxygen vacancies as deduced from structural and transport characterizations. While transport measurements have been performed at the IPCMS (with a Dynacool set-up from Quantum Design), the magnetic order transition has been studied at the I10 beamline of the Diamond synchrotron in Oxfordshire, England. Those measurements allowed evidencing an influence of the PZT polarization, increasing with increasing PZT thickness, on the transition observed in $NdNiO_3$.

A general conclusion will close this manuscript, along with the perspectives and scheduled upcoming experiments.

II. Introduction to the nickelates: from the bulk perovskite phase to the infinite-layer thin films

Rare-earth nickelates are currently the object of an intense and worldwide research effort, largely motivated by the recent finding of superconductivity in infinite layer nickelate thin films. In this introductory part, I will first present the precursors of these compounds, i.e. the rare-earth perovskite nickelates, giving the particularities they owe to their perovskite structure, and presenting their main characteristics in both bulk and thin film forms. I will then present the reduction process through which infinite layer nickelate thin films can be obtained from their perovskite precursors, and finally I will give a review of the current understanding of this synthesis process.

Overviews of the physics of the perovskite nickelates in bulk and/or thin film forms have been explored and detailed in several reviews [5–7] to which the following section will mainly refer to. Despite being a recent subject, reviews exploring the current understanding of the infinite-layer nickelates have already been published [8,9], and have also been a precious source of information for this Chapter.

1. Transition metal perovskites

1. The perovskite structure

Perovskite is the name given to the $CaTiO_3$ mineral, discovered by Gustav Rose in 1839 and named after the Russian mineralogist Lev Perovski (1792-1856). The perovskite structure describes compounds of general formula ABO_3, in which the A and B cations are of different sizes, with the smaller B cations hosted within corner-sharing oxygen octahedra and the bigger A cations at the centre of a cube formed by these octahedra **[Fig. II-1(a)]**. Almost any alkali metal, alkali earth metal or rare earth lanthanide can occupy the A-site. Usually the B-site is occupied by a transition metal, making up the transition metal oxide (TMO) perovskite series [10]. The stability of the structure requires that the tolerance factor t [11], relating the ionic radii of the A and B cations and oxygen anions, respectively R_A, R_B, R_O, through $t = \frac{R_A+R_O}{\sqrt{2}(R_B+R_O)}$, to be close to one. Deviation from this ideal value leads to distortions or rotations (tilts) of the oxygen octahedra resulting in a lowering of the unit cell symmetry. The rotations of the BO_6 octahedra are described via three angles, which are defined with respect to the crystallographic directions of the cubic system ([100], [010] and [001]), and named Glazer angles [12]. The distortions of the ideal cubic structure could be described by a displacement of the bigger A cation, alongside with tilts and rotations of the BO_6 octahedra. An example of $a^-a^-c^+$ octahedra tilts characterizing the metallic *Pbnm* orthorhombic crystal structure of bulk $NdNiO_3$ are shown in **Fig. II-1(b).** The B-O-B bond angle may be used to quantify the degree of distortion in perovskite compounds, as it scales proportionally with the tolerance factor t [13]. Independently of their exact crystal structure, oxide materials are often described in a pseudocubic (pc) notation which is commonly the case for all perovskites. The pc-lattice parameters are generally compared to estimate structural similarities. In particular, the pc lattice parameter is used to calculate the in-plane lattice mismatch between the substrate and the oxide thin film, which is an extremely important quantity to consider to allow a high-quality growth of the material itself.

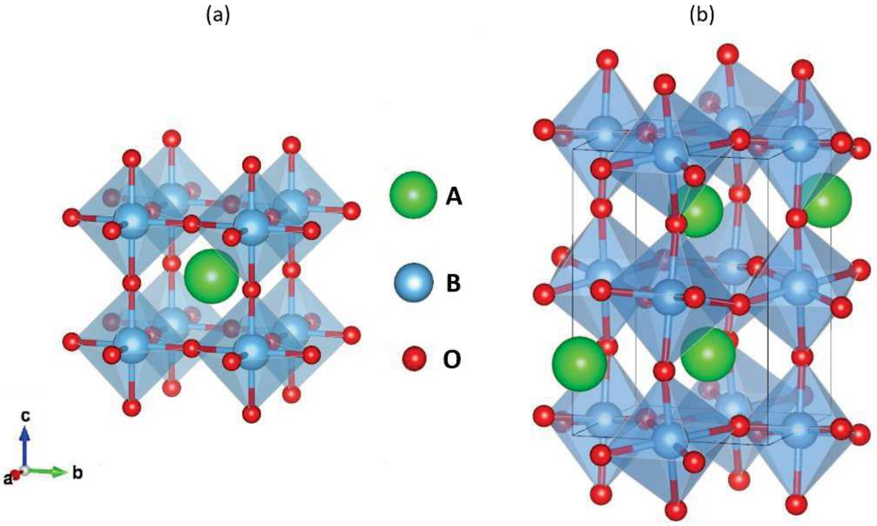

Figure II-1 (a) ABO_3 undistorted perovskite cubic structure, and (b) Pbnm(62) orthorhombic structure corresponding to the crystal structure of bulk $NdNiO_3$ in its metallic phase.

2. Electronic structure of transition metal perovskites

The physics of 3d transition metal oxides (TMO) of perovskite structure is mainly driven by the d-orbitals of the *B* transition metal ions which are represented in **Fig. II-2(a)**. Up to ten electrons can be hosted by these five orbitals. The electrostatic interactions between the B cation and the six surrounding oxygens anions produce a crystal field which lifts the degeneracy of the *d* orbitals. The result is schematized in **Fig. II-2(a)**, where the orbitals pointing towards the oxygen, of e_g symmetry, are lifted to a higher energy compared to those which are pointing in-between the oxygens, the t_{2g} ones. The crystal-field splitting energy between the t_{2g} and e_g orbitals is denoted 10Dq as shown in **Fig. II-2(a)**. Transition metals (TM) often have various stable oxidation states. Since the energy of the oxygen 2p orbitals is usually close to the energy of the *d* orbitals of the TM, electrons transfer between oxygen and TM orbitals are energetically permitted, as well as the transfer of electrons between the different TM orbitals through the oxygen ones [10]. Usually, the valence of the TM is nominally determined by the valence of the A-cation in the perovskite structure.

The lifting of degeneracy produced by the crystal field is synonym of a preferential occupation of some of the orbitals, and in the case of an octahedral crystal field, it translates into a preferential occupation of the t_{2g} states over the e_g ones. Applying Hund's rule of maximum multiplicity, the different orbitals must be filled with electrons of equivalent spin before the same orbital is filled with a pair of electrons. This might lead to an occupation of the e_g states before the t_{2g} ones are fully filled, even though they are lower in energy. This will happen if the crystal field energy is lower than the Hund's coupling energy J [14]. This proximity in energy of the different interactions ruling the physics of the TMO is the basis of the interesting features of these materials, hence, their designation as strongly correlated oxide materials.

As already mentioned, the d-orbitals are highly directional, with, in the BO_6 octahedra, the e_g orbitals pointing towards the oxygen 2p orbitals and the t_{2g} ones point in-between, as schematically shown in **Fig. II-2(b)**. One can observe on this sketch that the oxygen 2p orbitals can hybridize with the d ones of the TM, and that this hybridization is going to be stronger for the e_g than for the t_{2g} because of the specific localized geometry of the orbitals. This overlap between the orbitals is closely related to the bandwidth W of the valence band of the material [15]. Indeed, the stronger the hybridization, the larger the bandwidth, *i.e.* the energy range between the highest and lowest allowed levels within the band. The O-2p TM-3d hybridization being highly directional will be largely sensitive to structural distortions, hence, resulting in a modified bandwidth of the material as schematically shown in **Fig. II-2(c).** Here the <B-O-B> angle (θ) is related to the bandwidth through a $\cos^2(\theta)$ function [16].

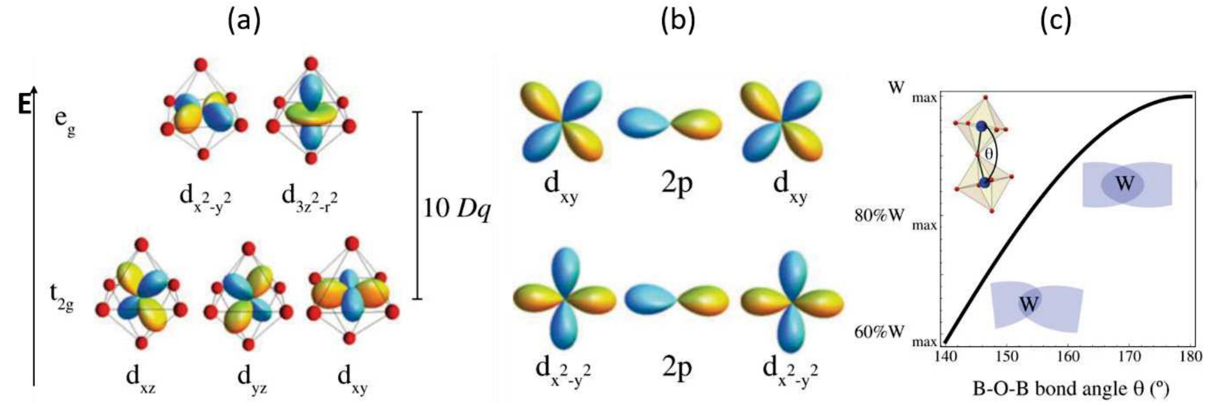

Figure II-2(a) 3d orbitals within the oxygen (red spheres) octahedra with crystal-field (10Dq) in action and generating the e_g and $t2_g$ groups, (b) Comparison of the hybridization possibilities between the TM 3d t_{2g} (top) or e_g (bottom) orbitals and the O 2p orbitals, (c) Variation of the bandwidth W of the valence band as a function of the B-O-B angle through the modification of the orbital overlap. (Taken from [17]*)*

The highly directional 3d-orbitals are spatially confined and the electrons of those orbitals are highly localized, therefore the Coulomb repulsion U becomes an important parameter to consider if one wants to study the physics of such systems. The interplay between the d-orbitals, the Hund's coupling and the Coulomb repulsion is at the origin of the metal-to-insulator transition (MIT) in some perovskite TMO. The study of the electronic interactions in TMO has been the focus of much effort based on the pioneering work of Mott and Hubbard, and the famous Hubbard model [18]. This model describes the movements of the electrons in a periodic lattice, with a single electronic band formed by a single level on each site. The transfer of an electron from one site to another, *i.e.* hopping from site i to site j, brings the system with a j site having two electrons and a i site being empty. It has been pointed out by Mott that the occupancy of the j site with two electrons needs a certain energy to overcome the

Coulomb repulsion U between the electrons. If the kinetic energy of the system, *i.e.* the hopping t of an electron from the i site to the j site is of comparable energy with the coulomb repulsion U, a MIT can occur as a function of U. When U increases (or t decreases, for example, by decreasing the temperature), the single band model splits into two distinct bands, the lower Hubbard (LH) and the upper Hubbard (UH) bands as sketched in **Fig. II-3(a)** for a Mott-Hubbard insulator [19].

In the case of TM, the band structure cannot be described only with the d-d excitations, since the previously mentioned hybridization between the TM and the O mediates hopping process between electrons from the O-2p towards the TM-3d orbitals and vice-versa. This electron transfer is the lowest energy charge excitation, which leaves a hole in the oxygen band, denoted L (ligand hole) with a supplementary electron in the d-orbitals of the TM, and is represented as:

$$d^n \longrightarrow d^{n+1}L$$

The amount of energy required to transfer this electron from the oxygen ligand to the TM orbital is called the charge transfer (CT) energy Δ. It can be assigned to the difference in energy between the oxygen p band and the UH band as shown in **Fig. II-3(b)**. Materials described within this picture are called charge-transfer insulators. The main difference between Mott-Hubbard and Charge-transfer insulators is the interaction controlling the MIT. In particular, for the Mott-Hubbard, it is shown in **Fig. II-3(a)** that the Coulomb repulsion U dictates the gap opening such as $d_i^n + d_j^n \to d_i^{n-1} + d_j^{n+1}$ when the electron from i site hops to the j site, as previously mentioned. While for the CT insulators the bandgap is dictated by Δ, described by the $d^n \rightarrow d^{n+1}L$ process.

Zaanen, Sawatzky and Allen, in their ZSA model [20], predicted that for $U>\Delta$ a CT insulating gap is opened while for $U<\Delta$ it will be a Mott-Hubbard-like gap. With a sufficiently small U, the system becomes metallic because of the overlap of the bottom of the UH and top of the LH bands. With the same idea, one can expect that for a small Δ, the top of the oxygen p-band will overlap with the bottom of the UH band, which defines the zero of the *effective* charge transfer Δ', and that this system will also become metallic in the ZSA scheme. But it has been argued that a negative effective charge transfer $\Delta'<0$ will maintain an insulating state, depending on the value of U and the kinetic energy necessary to perform the hopping from the O-2p to the TM-d orbitals. That is because in a negative charge-transfer, the t_{pd} and U value are bigger than in charge-transfer insulators, as here Δ is considered to be really small. The strong p-d hybridization and Coulomb repulsion results in the formation of a non-zero bandgap [21]. This mechanism is similar to the one in the molecular orbital theory with the formation of splitted bonding and antibonding levels [6]. This behaviour has also been referred to as a negative charge transfer insulator [22], but one has to be careful to differentiate the charge transfer Δ and the *effective* charge transfer Δ' as highlighted in the different schemes presented in **Fig. II-3**. A consequence of the negative *effective* CT energy **[Fig. II-3(c)]** is that the ground state has a dominant contribution from the $d^{n+1}L$ state, while the Mott-Hubbard and CT insulator states present a dominant contribution of the d^n states. The insulating gap process is therefore described by:

$$(d^{n+1}L)_i + (d^{n+1}L)_j \rightarrow (d^{n+1})_i + (d^{n+1}L^2)_j$$

meaning that the insulating gap has a p-p character as highlighted with the orange orbitals in the **Fig. II-3(c)**.

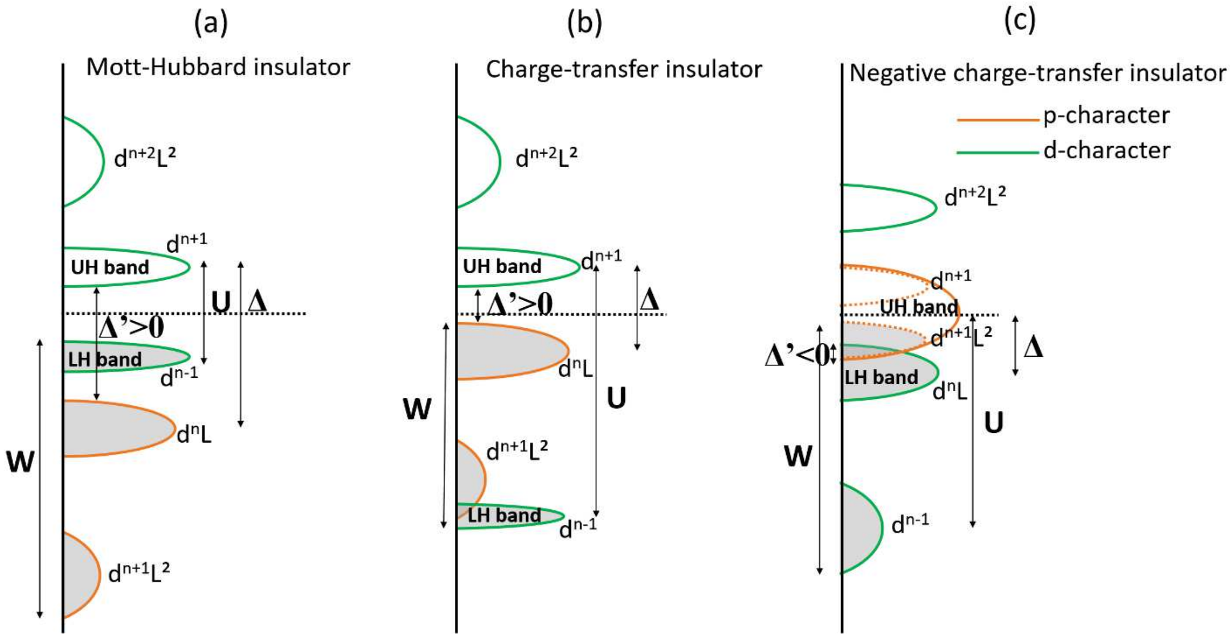

Figure II-3 Schematic band structure of (a) a Mott-Hubbard insulator, (b) a charge transfer insulator and (c) a negative effective charge transfer insulator. Green bands represent the d-character of the density of states while the orange ones have p-character. W is the valence bandwidth, U the on-site Coulomb repulsion, Δ the charge transfer and Δ' the effective charge-transfer. (Adapted from [6,7,17]*)*

There is a strong correlation between charge, spin, orbital and lattice degrees of freedom, with energy scales of the order of the eV, hence the name of strongly correlated electrons material for the TM perovskites. This competition between the different degrees of freedom gives rise to a high number of exciting phenomena, such as magnetism, colossal magnetoresistance [23], ferroelectricity [24], orbital ordering [25], metal-to-insulator transition [19] or high temperature superconductivity [26]. Numerous TM perovskite compounds possess a rich phase diagram, exhibiting some of these phenomena, depending on external parameters such as temperature or pressure. A high number of exotic phenomena naturally leads to a wide range of applications including batteries, memristors, bolometers, water-splitters, resistive switches and smart windows; the possibilities of commercial applications are abundant [7,17].

2. Bulk nickelate perovskites

1. A rich phase diagram

Perovskite rare-earth nickelates ($RNiO_3$, R being a rare-earth) synthesized for the first time by Demazeau *et al.* [27] in 1971 are a family of TM perovskites with a very rich physics, notably due to the possibility to vary the rare-earth element. The review from Medarde in 1997 [5] explains how rich the phase diagram of this family of compounds is. It also highlights that those materials regained interest with the discovery of high-temperature superconductivity and giant magnetoresistance. In the next parts of the Chapter, lots of parallel with cuprates will be done as lots of the presented works had the initial objective to uncover a superconductive state in perovskite rare-earth nickelates.

The structural and physical bulk properties of this family of compounds is summarized in the phase diagram displayed in **Fig. II-4**, where phase transitions are strongly connected to the Ni-O-Ni bond angle, in turn linked to the choice of the rare-earth. This family of compounds has been intensively studied for its sharp MIT (except for R = La) which takes place while decreasing the temperature. It can firstly be noted that this MIT temperature (T_{MIT}) increases with the decreasing size of the rare-earth cation radii, hence with a smaller Ni-O-Ni bond angle. It is to be noted that the reduction of the Ni-O-Ni is due to the decrease of the tolerance factor as previously described and highlighted by Medarde et al. in their review [5].

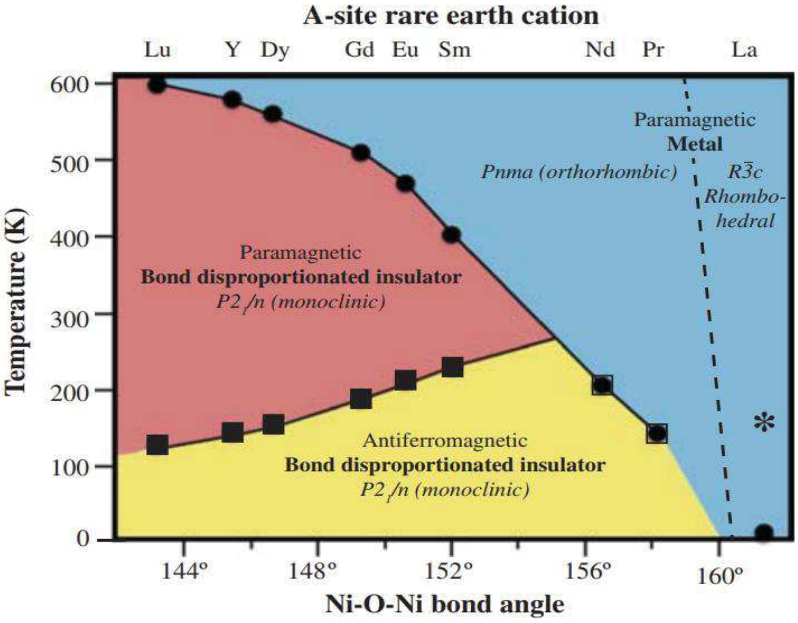

Figure II-4 Bulk phase diagram of perovskite $RNiO_3$ (with R = rare-earth) as a function of the Ni-O-Ni angle. Circles indicate the metal-to-insulator transition, while squares indicate the Néel transition. (Adapted from [17]*)*

At first, the crystal structure of the $RNiO_3$ family (except R = La) was thought to be orthorhombic with a *Pbnm* space group for both the metallic and insulating states. For $LaNiO_3$, a rhombohedral structure is identified with the R-3c space group. However, a combination of neutron and synchrotron diffraction data by Alonso *et al.* [28,29] provided the evidence of the modification of the crystal symmetry, concomitant with the MIT, with a transition from the orthorhombic *Pbnm* space group in the metallic state to the monoclinic $P2_1/n$ one found for the insulating state. Those experiments reported the presence of two alternating NiO_6 octahedra with expanded and contracted Ni-O bonds as displayed in the inset of **Fig. II-6**. This has been described as a breathing distortion mode with alternating Ni-sites in a three-dimensional checkboard pattern. Beyond the structural transition and MIT, a magnetic ordering transition has been put in evidence by Garcia-Munoz *et al.* in 1992 [30] with neutron diffraction technique on $NdNiO_3$ and $PrNiO_3$ powder samples. Those measurements highlighted the presence of a spin density wave along the k = (½, 0, ½) propagation vector in the orthorhombic structure, equivalent of the k = (¼, ¼, ¼) in pseudocubic notation. Further measurements performed on other rare-earth nickelates put in evidence that, in bulk, $T_{Néel} = T_{MIT}$ for R = Ni and Pr, while $T_{Néel} < T_{MIT}$ for the others rare-earth (except La) [31–33]. This is also summarized in the phase diagram reported in **Fig. II-4**.

2. A complex ground-state studied by spectroscopy measurements

The electronic configuration of the $RNiO_3$ compounds is imposed by the trivalent character of the rare-earth which requires that the nickel also be in its trivalent state. In that case, the Ni^{3+} cation nominal shows a $3d^7$ electronic configuration in its ground state after losing two electrons from the 4s orbitals, and one from the 3d orbitals. However, several studies [34–37] have shown that the ground state show a large covalent character due a strong Ni-3d O-2p hybridization: one electron is given by the O to the Ni, resulting in a hole for the O (as already explained above). This charge transfer is leading to a $3d^8L$ electronic configuration for the Ni cation, with L being a hole in the O-2p orbitals. But it is important to note that the charge-transfer energy Δ in $RNiO_3$ is small, making easier the transfer of electrons from the O-2p towards the Ni-3d orbitals. This leads to a Ni cation having two electrons instead of one in its e_g orbitals with a d^8L configuration. So far, the ground state of the nickelate might be described with a mixed configuration $\alpha 3d^7 + \beta 3d^8L$ [5,38,39]. Within this picture, a favourable Jahn-Teller distortion would be expected, to lift the degeneracy of the e_g orbitals [37]. However, no orbital ordering has been found experimentally [40]. On the other side, spectroscopy measurements highlighted the predominance of the $3d^8L$ configuration in the ground-state properties of the $RNiO_3$ compounds, which is consistent with a charge transfer energy Δ being small and even with the *effective* charge transfer Δ' being negative [34,39] as schematized previously in **Fig. II-3(c)**. In a negative charge transfer process the hopping from O-2p towards the Ni-3d states is called self-doping, which is a term frequently used to describe the Ni-O hybridization in nickelates.

This Ni-O hybridization is notably determined by soft X-ray absorption spectroscopy (XAS) measurements at the O-K edge. Indeed, the pre-peak usually found around 528 eV is a qualitative observation of the Ni-O hybridization, and its intensity is directly related to the strength of the hybridization [41]. In the case of the perovskite nickelate, the presence of a strong pre-peak then of a strong hybridization degree, is the synonym of a small amount of defects in the structure [36], hence, can be used as a proxy for the quality of the grown material.

Additionally, careful attention has been dedicated in simulating the Ni L-edge XAS of different nickelates, with the aim to describe their ground-state, which, as already shown before, is characterized by two different Ni sites. Most of the models usually used to simulate a XAS spectrum of TMO define the valence of the cation, and then adjust the different parameters of the systems such as the 10Dq, CT energy, U, etc. to have a proper correspondence with the experimental spectrum shape. However, only one type of cation is defined in most cases, which could be a problem here as we have two different Ni sites. In that sense, an approach made in 2016 by Green *et al.* [42] presented a double cluster model to describe the local electronic properties of the two different Ni sites. The double cluster model considers the two different NiO_6 octahedra, with short and long Ni-O bonds, representing each sublattice of the breathing distortion mode as schematized in **Fig. II-5(e)**. This model permits the incorporation of both charge and bond disproportionation, negative charge transfer energy, and especially, the orbital degeneracy and Coulomb interaction, necessary to simulate core levels. Firstly, the $3d^8L^2$ Ni site attracts the O ligands closer, leading to a shorter Ni-O bond, and so to compressed NiO_6 octahedra, while the $3d^8L^0$ has the opposite effect with expanded NiO_6 octahedra. Also, each Ni site interacts with the ligand (*i.e.* the oxygen) of the other Ni site. This double cluster model is in accordance with the negative charge transfer theory, and most importantly, provides a validation of the bond disproportionation. Moreover, it can be used as a powerful tool for the analysis of nickelates heterostructures, and we will notably rely on this model in the Chapter dedicated to the study of the PZT/NNO//STO heterostructures. **Fig. II-5(a)** shows that the electron occupation on each Ni site is very robust against the amplitude of the breathing distortion. The electron occupation of the t_{2g} orbitals is constant throughout the distortion, and the e_g only show a slightly higher occupation for the expanded site, *i.e.* for the $3d^8L^0$. On the contrary, the oxygen orbitals are very different depending on the considered Ni site, as shown in **Fig. II-5(b)**. This model agrees with the aforementioned image where the ligand holes of the oxygen are shifted towards the compressed Ni octahedra, that is, with the $3d^8L^2$ electronic structure. This leads to a reduction of the spin of the Ni in the compressed octahedra, because the two electrons provided by the ligand holes are coupled in an antiferromagnetic configuration in the Ni 3d orbitals. This results in a low spin state approaching S = 0 for the small Ni octahedra as shown in **Fig. II-5(c)**. While for the expanded Ni octahedra, the ligand holes are more distant. As a consequence, the electrons from the Ni site are not coupled with the ones from the ligand holes. This explains why a spin state of S = 1 is observed for the expanded octahedra, as expected for a Ni $3d^8$ high-spin state. Following this model, it is possible to simulate the XAS spectra as a function of the breathing distortion at the Ni L_3-edge of $RNiO_3$ [**Fig. II-5(d)**]. The characteristic two peaks at the Ni L_3-edge correspond to the short and long Ni-O bonds for the peaks at higher and lower energy, respectively. As the breathing distortion increases, the separation in energy of those two peaks also increases together with a relative variation of the peak amplitude ratio which gives an indication of the relative contribution of the compressed/extended Ni octahedra to the overall XAS signal.

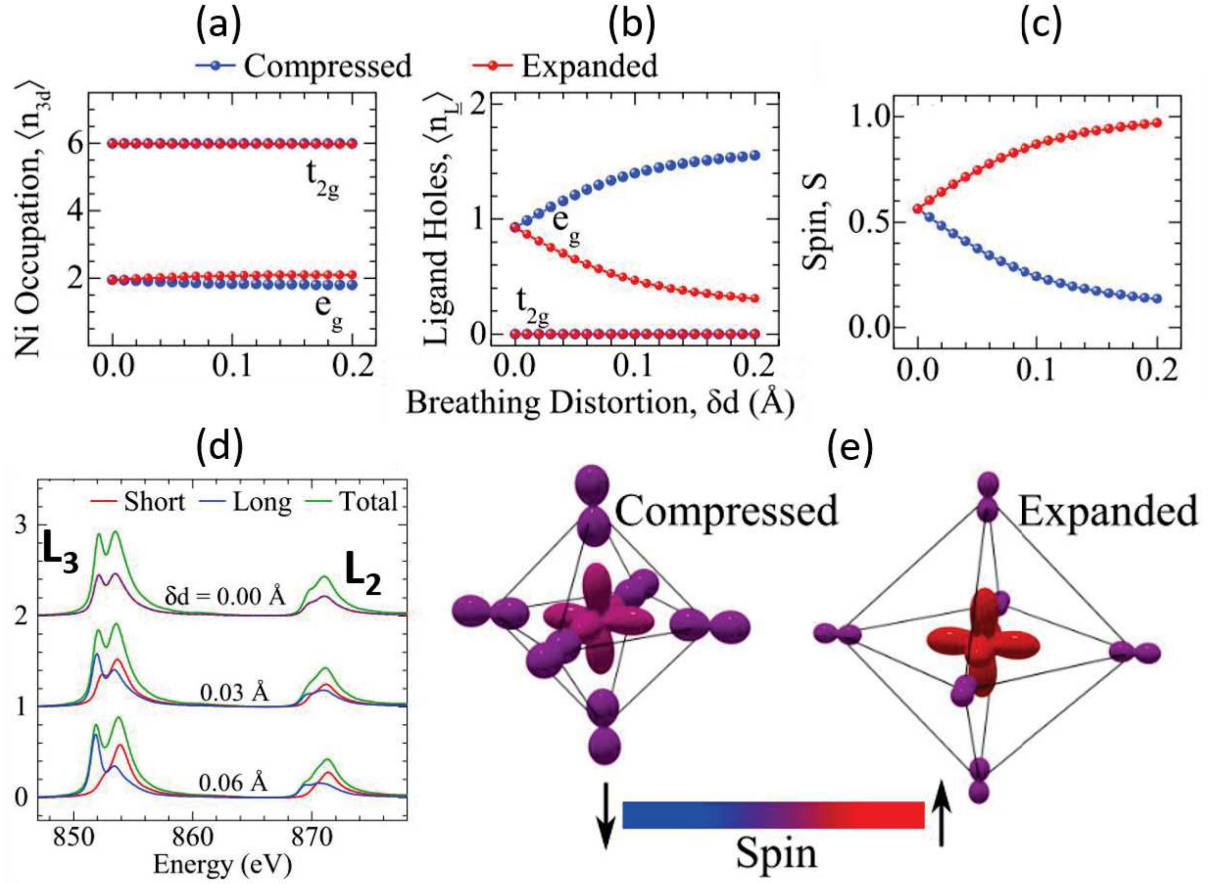

Figure II-5 (a)–(c) $RNiO_3$ ground-state characteristics according to the double-cluster model, with (a) Distribution of Ni 3d electrons over the t_{2g} and e_g orbitals, (b) Distribution of ligand holes, (c) Spins for the compressed and extended octahedra, and (d) XAS spectra for different magnitudes of the breathing distortion. The spectra of the two inequivalent sites are shown, along with their sum. (e) Visualization of the calculated hole density matrices on compressed (left) and expanded (right) octahedra in the distorted phase (ligand hole densities are scaled by a factor of 2 for clarity). (All taken from [42]*)*

3. The metal-to-insulator transition

The sharp MIT is the feature that has attracted the attention of the scientific community on the perovskite rare-earth nickelates, and whose nature has been considerably studied in the past years. The T_{MIT} is related to the degree of orthorhombic distortion, which drives away the Ni-O-Ni bond angle from the perfect 180° angle. It decreases the overlap of the d and p orbitals, increasing the difficulty of an electron from the oxygen to hop towards the Ni-3d orbital. As a consequence, there is a decreasing of the bandwidth W as shown in **Fig. II-2(c)** while decreasing the Ni-O-Ni bond angle, which makes the T_{MIT} increases from 0 K for $LaNiO_3$ (being always metallic), to more than 600 K for $LuNiO_3$ [43] which with the smaller R cation radii the largest distortion and, hence, the higher T_{MIT}. As a result, the MIT in nickelates is an excellent example of a bandwidth controlled transition [19].

The recent understanding of the nickelate ground state supports the picture of an electronic structure close to $3d^8L$ for all the Ni atoms in the metallic state, and that the transition occurring when decreasing the temperature gives rise to a bond disproportionation with a splitting of a unique Ni site in the metallic state, to two different ones in the insulating state [37,44,45]:

$$d^8L + d^8L \rightarrow d^8L^0 + d^8L^2$$

For comparison in first charge-disproportionation models [28,40,46], an alternation between Ni $3d^6$ and $3d^8$ cations was used to described the insulating ground state of the $RNiO_3$ compound. **Fig. II-6** presents the temperature evolution of the resistivity of a 10 nm thick $NdNiO_3$ thin film grown onto STO exhibiting a rather sharp MIT taking place over several order of magnitude. The insets represent the electronic structure of Ni in the metallic state, with only d^8L sites, and in the insulating state, with the alternating d^8L^2 and d^8L^0 sites. The smallest NiO_6 octahedra accommodate the d^8L^2, while the biggest ones accommodate the d^8L^0.

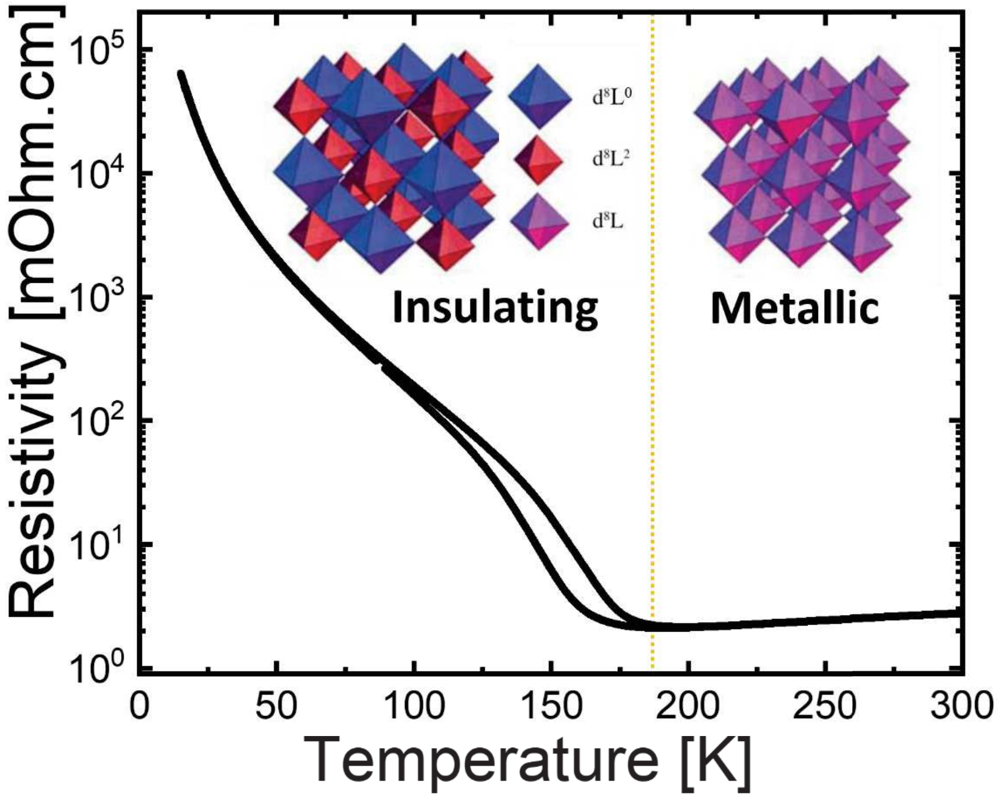

Figure II-6 (a) Temperature dependence of a resistivity measurement acquired for a 10 nm thick $NdNiO_3$ film grown onto $SrTiO_3$ substrate. The insets show a scheme of the breathing distortions taking place from the metallic towards the insulating state (Adapted from [17]*). The dashed orange line represents the T_{MIT} obtained from the zero crossing of the –d(ln(ρ))/dT quantity.*

4. The magnetic structure and Néel transition

In the same way as the ground-state of the nickelates is the subject of ongoing discussions in the scientific community, also their antiferromagnetic ordering is, mainly because of its nature (collinear or non-collinear). Generally, in TM perovskites, the antiferromagnetic order is formed by dominant nearest-neighbours superexchange, resulting in a doubling of the pseudocubic unit cell [47]. However, in nickelate perovskites, the antiferromagnetic ordering has been observed to be of four pseudo cubic unit cells along the [111] direction [30,40,48–51]. It is therefore along the propagation vector $q_0 = [¼\ ¼\ ¼]_{pc}$, which correspond to the $[½\ 0\ ½]_{orth}$ propagation vector. The nature of the antiferromagnetic order remains unresolved, and 2 different spin arrangements that could not be discerned yet are proposed: the collinear (↑↑↓↓) and the non-collinear (↑→↓←) [51]. The magnetic transition can be concomitant or not with the MIT, depending on the rare-earth. Here again, R = La is a special case since, in the bulk phase diagram, it yields the only nickelate which is always paramagnetic. For $NdNiO_3$ and $PrNiO_3$, the Néel transition from a paramagnetic state to an antiferromagnetic (AF) one at lower temperature is concomitant with both the structural transition and MIT. But when the atomic radius of the rare earth decreases further, this concomitance vanishes as previously shown on **Fig.II- 4**. Smaller Ni-O-Ni angles, *i.e.* bigger distortions, decrease the Néel temperature ($T_{Néel}$) of the $RNiO_3$, but increase the MIT temperature. As aforementioned, the breathing distortion mode in the insulating case leads to two different Ni sites with different electronic configurations ($3d^8L^2$ and $3d^8L^0$), both with different charge densities and high-spin and low-spin configurations (S = 1 and S = 0). This give rise in a highly ordered [111] direction in the pseudocubic notation, with each plane along this [111] direction corresponding to one type of Ni sites. An example with non-collinear spin arrangements is shown in **Fig. II-7** with four (↑→↓←) Ni planes along the [111] direction.

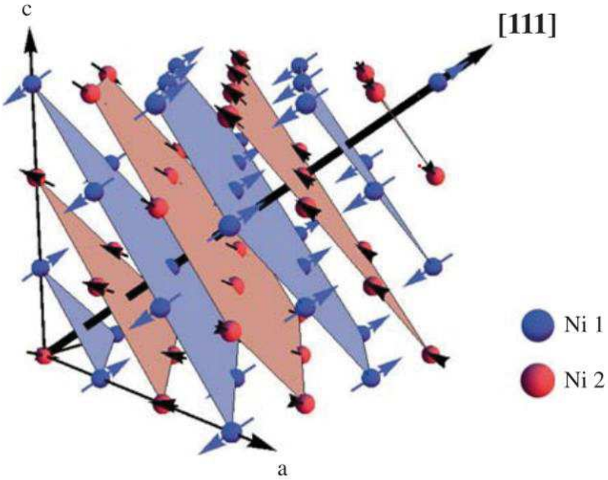

Figure II-7 A possible magnetic structure of $RNiO_3$ with two inequivalent Ni electronic configurations represented in blue and red, with the (111) planes represented in the same colours. (Adapted from [17]*)*

The sharp metal-to-insulator and magnetic transitions are cornerstones of the study of rare earth nickelates. They have been particularly studied and tuned through different stimuli such as hydrostatic pressure [52], light [53], hole/electron doping [54], isotope substitution [55] together with heterostructuring and strain engineering in thin films which will be the main focus of the next section.

3. Perovskite nickelates thin films

1. Interest to grow thin films

The growth of perovskite nickelates as thin films allows the possibility to use new parameters to tune their properties, for example lattice mismatch by choosing a particular substrate. The different single crystals usually used as substrates for the growth experiments are chosen to have a desired lattice mismatch or a particular crystallographic orientation. Three substrates have been used in this work, such as $SrTiO_3$ (STO), $LaAlO_3$ (LAO) and $(LaAlO_3)_{0.3}(Sr_2TaAlO_6)_{0.7}$ (LSAT), all $(001)_{pc}$ oriented. Their pseudocubic lattice parameters are given in **Fig. II-8(a),** alongside with those of some of the materials grown in this thesis. The in-plane biaxial strain ε_{xx} imposed by the substrate on the in-plane lattice parameter of the nickelate thin film can be compressive or tensile, and defined as:

$$\varepsilon_{xx} = \frac{a_{sub} - a_{bulk}}{a_{sub}},$$

where a_{sub} is the pseudocubic lattice parameter of the substrate, and a_{bulk} is the pseudocubic parameter of the bulk form of the grown material. With a positive Poisson's ratio (generally 0.3 for nickelate [56]), the consequence of the in-plane strain will be the extension of the out-of-plane parameter in the case of a compressive strain or a contraction of the out-of-plane parameter in the case of a tensile strain. The BO_6 octahedra can either adopt a Jahn-Teller distortion with an elongation of the c-axis stabilizing the out-of-plane orbitals, and a compression of the c-axis stabilizing the in-plane orbitals like in manganites and shown in **Fig. II-8(b)** [13]. They can also adopt a lower symmetry rotation pattern which might lead to a more distorted B-O-B angles, like might be the preferential path for nickelates. The dependence of the Ni-O-Ni angle in $RNiO_3$ as a function of strain, calculated by DFT, is shown in **Fig. II-8(c)**.

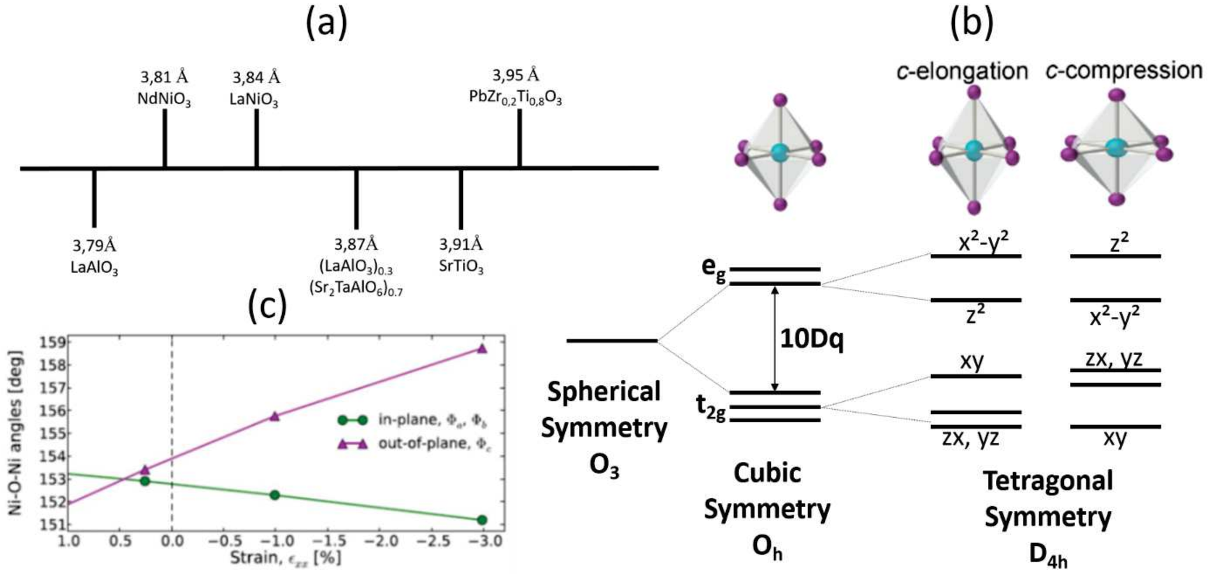

Figure II-8 (a) Pseudocubic in-plane lattice parameters of substrates and materials deposited in this thesis (b) Crystal field splitting effect on the fivefold degenerate 3d orbitals for cubic (O_h) and tetragonal (D_{4h}) symmetry (Adapted from [57]*) (c) DFT calculations showing the strain dependence of the in-plane (green) and out-of-plane (purple) Ni-O-Ni angle (taken from* [7]*)*

The choice of the substrate of the $RNiO_3$ thin films will have multiple implications on their properties, but first I will introduce some details on the challenge of growing of high-quality epitaxial $RNiO_3$ thin films.

2. Persistent challenge in the nickelate thin film growth

The synthesis of the nickelates in the form of thin films brings supplementary levers to tune the properties of the material, such as the T_{MIT} and $T_{Néel}$ transitions, and can even bring out new properties such as antiferromagnetism in superlattices with two u.c. of $LaNiO_3$ alternated two u.c. of $LaAlO_3$, while bulk LNO is paramagnetic at all temperatures [58]. Despite constant improvement in thin films synthesis throughout the last decades [1], the growth of perovskite nickelate thin films remains challenging, notably when heterostructures or doping come in the picture. We should keep in mind that the synthesis of $RNiO_3$ single-crystals is also a challenging experimental task, probably even more challenging than thin films, although the last years have witnessed some improvements [59].

The challenge mostly resides in the valence value of the Ni cations in the perovskite structure. It should indeed be 3+ to maintain a charge neutrality, considering that the rare-earth is 3+ and the oxygen 2-, while the most stable valence of the Ni cation is 2+. In nickelates thin films, when the Ni oxidation state is not properly optimized results in the appearance of $RE_{n+1}Ni_nO_{3n+1}$ spurious phases, called Ruddlesden-Popper (RP) phases (n is a finite number) [60]. Rare-earth nickelates are considered as the n = ∞ member of this RP family. The RP phases are constituted by n layers of rare-earth perovskite structure $RNiO_3$ separated by a layer of R involved in a rock salt structure as shown in **Fig. II-9.** This structure is very stable since it lowers the valence of the Ni cations. To prevent its formation in thin films, the growth conditions must be optimized to favour the formation of Ni^{3+}, which is mainly done by the oxygen partial pressure in the deposition chamber. By considering Pulsed laser deposition technique (see next Chapter) the laser fluence and the surface state of the ablated target area must also be finely tuned to prevent any Ni off-stoichiometry that could lead to an excess of rare-earth, and thus to a higher proportion of RP phase [61]. Overcoming those obstacles is challenging and time-demanding, but mandatory to be able to obtain pristine perovskite nickelates thin films.

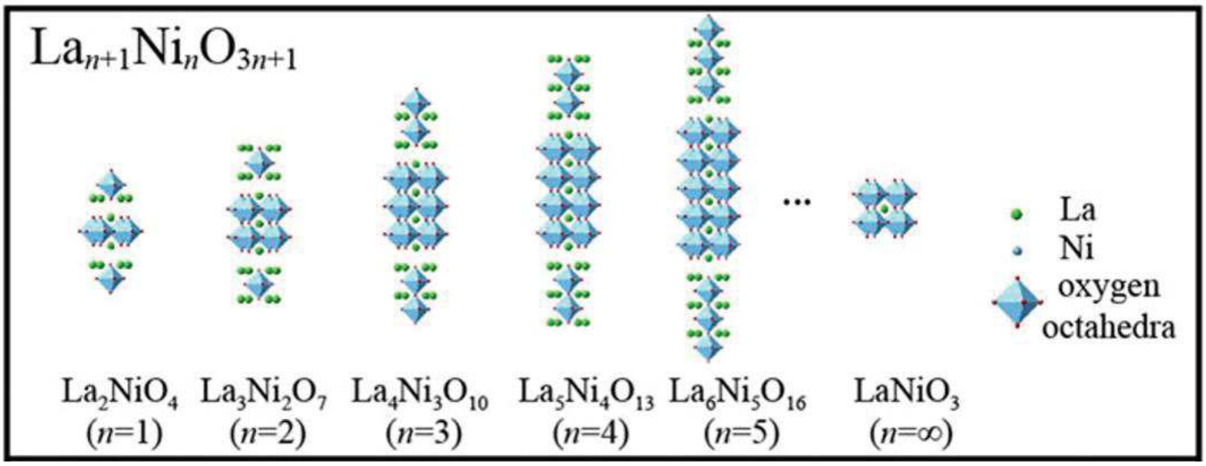

Figure II-9 Crystal structures of Ruddlesden-Popper $RE_{n+1}Ni_nO_{3n+1}$ phases for R = La (Adapted from [60]*).*

It might be good to remember that most of the studies performed on $RNiO_3$ thin films had as main goal the search of a superconducting state, and one of the main approach has been a combination of interfacial orbital engineering and charge transfer mechanisms in nickelate-based heterostructures. As a result, in the following sections, the influence of the substrate' strain and crystallographic orientations combined to interfacial effects on the preferential orbital occupation will be mainly addressed. Those efforts have been successful in tuning both the MIT and Néel transition temperatures, and failing in unveiling the superconducting state. The effects of the presence of oxygen vacancies on the MIT will also be detailed as they are one of the main challenges in the optimization of our thin films as will be more clear in the dedicated Chapters.

3. Strain engineering and interfacial effects: the search of superconductivity

We already mentioned that the research in TMO has been amplified by the discovery of high-temperature superconductivity in copper oxides materials. The efforts to obtain superconductivity in perovskite nickelates has been a productive research field in the last two decades prompted by the seminal theoretical work of Anisimov *et al.* [62] where it was delineated the possibility that nickelates could be potential candidate to mimic the cuprates properties. In their work, they describe the necessity to have NiO_2 planes where the challenging Ni^{1+} ions could have a planar coordination with spin S= ½. In that sense, the orbital ordering of the e_g orbitals to stabilize the x^2-y^2 orbitals in $RNiO_3$ thin films has been a promising approach, favouring the possibility of a spin one-half state for the electron residing in the x^2-y^2 orbital [63], therefore, leading to a cuprate-like Fermi-surface with less than half-filled $3d_{x^2-y^2}$ orbitals to mimic the hole-doping properties of cuprates to stabilize the superconducting state [64]. In this section I will present the experimental efforts undertaken to synthesize $RNiO_3$-based heterostructures to pursue a superconducting state which, unfortunately has not yet been uncovered, but demonstrate the possibility to tune the already interesting properties of nickelates.

The influence of the in-plane biaxial strain of the substrate on the nickelate thin film orbital occupation is not so straightforward. For example, ultrathin films of $LaNiO_3$ show an asymmetric response with the lattice mismatch [65,66], with a tensile strain inducing no preferential orbital occupation while a compressive strain does. An interplay of strain and confinement of the $3dz^2$ orbital in the z direction, inducing octahedral rotation, distortion and altered covalency has been said to be the reason of this asymmetry. A quantification of the orbital occupation can be achieved from linear dichroism of soft X-ray spectroscopies in order to get further insight on the role of the different parameters on the orbital occupation as shown by Benckiser *et al.* [67].

The effects imposed on the film by the substrate depends also on the particular crystalline orientation. This parameter is therefore another lever used to tune the properties of nickelate thin films. As an example, $NdNiO_3$ thin films grown onto $NdGaO_3$ single-crystal as substrates with a $(111)_{pc}$ orientation resulted in a huge increases of the T_{MIT}, when compared to the growth onto the $(001)_{pc}$ ones, and also induces separated T_{MIT} and $T_{Néel}$ temperatures while they are the same for bulk, because of the specific tilt pattern imposed to the NiO_6 octahedra [46]. With this $(111)_{pc}$ orientation, but on $LaAlO_3$ (LAO) substrate, superlattices of (2 u.c.)LNO/(4 u.c.)LAO have shown an antiferro-orbital order in the ground state, not attainable in bulk or along the $(001)_{pc}$ direction, and so proving the potential of geometrical engineering to obtain exotic properties [68]. Another work on $LAO(111)_{pc}$ substrates has also demonstrated the emergence of a ferroelectric state in $NdNiO_3$ thin films [69]. In this case the LAO octahedral tilt pattern is said to counteract the one in $NdNiO_3$, leading to a stabilization of peculiar polar displacements of the Nd cation.

Interfacial effects combined to possible charge transfer between different transition metal oxides are a vast field of research. For example, heterostructures combining nickelates and titanates have shown that the charge transfer from Ti to Ni can be tuned by the size of the rare-earth [70]. Another work on $LaTiO_3/LaNiO_3/LaAlO_3$ tricomponent superlattices shows a preferential occupation of the Ni-$3d_{z^2}$ orbitals enhanced up to 50% [71]. In the same approach, superlattices composed of (4 u.c.) $LaNiO_3$ and (4 u.c.) of insulating $GaScO_3$ revealed an orbital polarization of 25% of the Ni-e_g electrons [72]. Heterostructures of $LaNiO_3/LaMnO_3$ have also been synthesised and have shown that Ni accepts an electron from Mn, which leads to the preferential Ni^{2+} cation [73,74] and gives rise to a ferromagnetic order below 85 K while bulk $LaNiO_3$ is paramagnetic at all temperatures. The aforementioned orbital engineering based on symmetry breaking and exchange bias [75] can create new electronic systems that exhibit novel properties.

Field-effects, and more specifically ferroelectric field-effects have also been used in nickelate/ferroelectric heterostructures to induce modification of the nickelate properties through the accumulation or depletion of charges at the interface between the two layers [76,77]. Chen *et al.* studied the $PbZr_{0.2}Ti_{0.8}O_3/Sm_{0.5}Nd_{0.5}NiO_3/La_{0.67}Sr_{0.33}MnO_3$ heterostructure and evidenced an interplay between the charge screening at the $PbZr_{0.2}Ti_{0.8}O_3/Sm_{0.5}Nd_{0.5}NiO_3$ interface and the charge transfer at the $Sm_{0.5}Nd_{0.5}NiO_3/La_{0.67}Sr_{0.33}MnO_3$ interface. This resulted in a resistive switching behaviour, exhibiting a difference of two orders of magnitude between the two polarizations state with a charge transfer of 0.1 electron from the Mn towards the Ni cations. Those experimental achievements are promising for the development of oxide-based high-performance electronic devices as ferroelectric field-effect-based transistors. A part of my research work during this thesis focused on such an approach with the study of $NdNiO_3/PbZr_{0.2}Ti_{0.8}O_3$ heterostructures with the main goal to control the nickelate functional properties upon reversing the $PbZr_{0.2}Ti_{0.8}O_3$ ferroelectric polarization.

4. The control of the properties through oxygen vacancies

I wish to introduce in this section the importance of the oxygen vacancies on the growth of nickelates thin films, and how they can influence the properties of this material. In particular, Oxygen vacancies will be addressed in the Chapter concerning the thin films optimisation, where I have first tried to minimize their presence during the growth of my perovskite phase, and then intentionally performed a subsequent reduction that selectively take out the apical oxygens of the perovskite thin films. In the Chapter focusing on the $NdNiO_3/PbZr_{0.2}Ti_{0.8}O_3$ heterostructures, I will present how challenging it is to grow a high-quality interface between these two layers, *i.e.* without oxygen vacancies in the nickelate layer. For all these reasons, I wish to present here a literature review on how the presence of oxygen vacancies in the nickelate thin films can be evidenced, and what their impact can be on the properties of the materials.

a. Evidencing oxygen vacancies

The determination of the presence of oxygen vacancies, their quantification and direct mapping remain a real challenge [78]. The presence of oxygen vacancies in TM oxides usually leads to an expansion of the lattice, that is, if the film is epitaxially strained to the substrate, to an expansion of the out-of-plane lattice parameter [79,80]. This results, on X-ray diffractograms acquired in the θ-2θ mode, in a shift of the thin film peaks towards lower angles [81,82]. The vacancies can be observed by transmission electron microscopy, but this observation is still very challenging, despite progresses in resolution in this domain since two decades [83,84].

b. Strain-induced oxygen vacancies

Evidencing the presence of oxygen vacancies is one thing, but the real goal is to control them, in order to modify the material' properties. The strain, as already mentioned, has a strong influence on the properties of the thin films. It may even play a role on the control of the oxygen vacancies [78]. The oxygen vacancies can then be seen as a side effect. Large tensile strain on $NdNiO_3$ and $SmNiO_3$ thin films have been predicted to increase the amount of oxygen vacancies by DFT calculations, and this was experimentally confirmed with the increase of the out-of-plane lattice parameter [85]. The increase of the tensile strain was also shown to induce a reduction of the Ni cation valence through XAS measurements, and to lead to an increase in the T_{MIT} [81,86]. The authors also claimed that an increase of the oxygen vacancies amount leads to an increase of the room temperature resistivity by up to 6 orders of magnitude.

c. Atmosphere-induced oxygen vacancies

Oxygen vacancies can be induced by a vacuum annealing process, which is another mechanism to control their concentration [87]. They can also be 'tuned' during the growth of the thin films by adjusting the oxygen atmosphere in the deposition chamber. This has been the case for a study on $LaNiO_3$ (LNO) thin films which evidences that the charge carriers density can be governed by disorder-related effects in oxygen-deficient LNO thin films [82]. It results that the transport properties of oxygen-deficient LNO samples can present a resistive behaviour below a certain temperature, while the optimally-oxygenated one are metallic until 2 K. Another way to induce oxygen vacancies in perovskites thin films, which was done in the case of $SmNiO_3$ and $NdNiO_3$, is through Mg traps which can be reversed depending on the oxygen atmosphere [88]. This study demonstrates that the presence of oxygen vacancies leads to carriers localization, because of the reduction of the valence of the Ni cations from Ni^{3+} to Ni^{2+}. The Coulomb repulsion and crystal field splitting of the 3d orbitals then indeed lead to a carriers localization and opening of the bandgap, as the authors schematized in **Fig. II-10**.

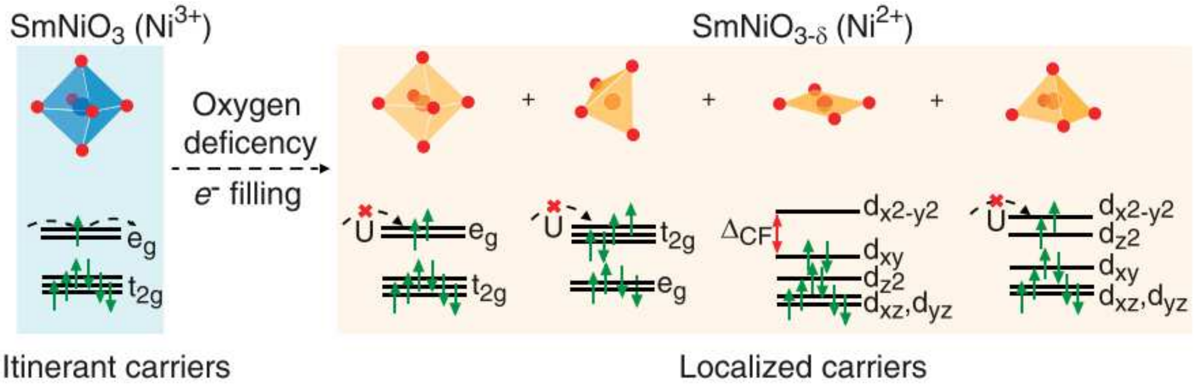

Figure II-10 Oxygen vacancies in $SmNiO_3$: effect of the Coulomb repulsion and crystal field splitting, resulting in a localization of the carriers. (Taken from [88]*)*

With the localization of the carriers and the opening of the bandgap, an increase of the resistivity at room temperature by nearly 7 orders of magnitude has been observed. The authors claim that this behaviour is reversible through the application of electric pulses, and show the potential of nickelate thin films for resistive switching devices. The dynamics of the creation/annihilation of these vacancies can be monitored through XRD, XAS, transport measurements and TEM. For example, in $La_{0.7}Sr_{0.3}MnO_3$, and $SrFeO_3$ it has been demonstrated that the creation of oxygen vacancies can be reversible, using a reductive or oxidative annealing process to, respectively, remove or put back oxygen in the lattice [89,90]. On $SrCoO_{2.5}$, the oxygen vacancies were moved with an electric field and studied by STEM technique, evidencing some preferential occupation of the oxygen vacancies for positions where previous oxygen vacancies belonged before moving because of the electric field [84]. Such a control of the oxygen vacancies to tune the resistivity of a $NdNiO_3$ thin film has been the subject of a study performed in collaboration with the Unité Mixte de Physique CNRS/Thales in Paris [91]. In this work, junctions with amorphous MoSi alloy on top of NNO have been fabricated, and shows large tunnel electroresistance and memristive behaviour. Those effects have been explained by oxygen migration mechanism at the interface, driven by reversible redox reaction between NNO and MoSi layers. We notably highlight different regime where the resistance states can be switchable or not as a function of the temperature, *i.e.* if the material is in its metallic or insulating state. Also, the high-conductance (ON) state of the junction is metastable and relaxes toward the low-conductance (OFF) ground-state over a temperature dependent time-scale. We suggest that the difference of relaxation behaviour may enable synaptic-like (non-volatile states) or neuron-like (relaxing states) functionalities depending on the temperature.

To summarize, literature has shown that the presence of oxygen vacancies increases the c-axis lattice parameter, and are more important in nickelate thin films with tensile strain than compressive one. The higher the number of vacancies, the higher the resistivity of the material, of several orders of magnitude. These structural and transport properties will guide us during the entire optimisation process of the nickelates thin films.

4. Infinite-layer nickelates

1. History and challenges of the synthesis of infinite-layer nickelates

The first experimental report about the synthesis of infinite-layer nickelate phase goes back to 1983 [92] where Crespin *et al.* reduced bulk $LaNiO_3$ into $LaNiO_2$. This reaction is called topotactic reduction, which according to the IUPAC [93] definition account for "*a transition in which the crystal lattice of the product phase shows one or more crystallographically equivalent orientational-relationships to the crystal lattice of the parent phase*". In the case of the infinite-layer phase synthesis, the topotactic reaction refers to the fact that there is a de-intercalation of species (oxygen here), from the host structure resulting in a structural modification via bonds breaking. Concretely, it can be said that a topotactic reaction is a soft-chemistry process in which atoms make small displacements. It does not need much energy to be performed and easily occurs in the solid state. In our case, the reaction modifies the oxidation state of the Ni cations with the number of oxygen coordination reduced from six to four, that is, going from NiO_6 octahedra to a NiO_4 square-planar structure as schematically shown in **Fig. II-11**, where it can be seen that the topotactic reduction maintains similarities in the structures of the initial and final states. In their seminal paper, Crespin *et al.* performed this reaction in a circulation loop with a well-known volume of H_2 gas. The degree of reduction of the sample was measured through the H_2 consumption in the loop, and checked at the end of the experiment by measuring the volume of water produced during the reduction process. At the time of this experiment, the stability of the products and their structural characterization were the centres of interest of the performed investigations. Later on, some works focused on the reduction itself and other ways to perform the topotactic reduction emerged with the use of NaH [94,95], TiH_2, activated carbon [96], or CaH_2 powder [96,97] on both bulk and thin films of nickelates. It is interesting to note that all the aforementioned hydrides can be used to successfully reduce the perovskite into the infinite-layer phase, while the activated carbon fails. Our own experiments and other studies in bulk [94,98,99] and in thin films [100,101] evidenced the importance of a contact between the thin film (or $RNiO_3$ powder), and the hydride powder to obtain the reaction or, perhaps to increase the reactivity. Therefore, it can be concluded that the topotactic process can be considered as both gas-solid and solid-solid reaction, but experiments have proven that the solid-solid reaction is more efficient, since the time of reaction can decrease from days/weeks (gas-solid reaction) to few hours (solid-solid reaction). Also, the lower temperature range necessary for the topotactic reaction to happen when using hydrides powder has to be ascribed to their highly reducing power, with a reduction potential of the H_2/H^- couple estimated at -2.25 V [102].

Interestingly, Hayward *et al.* [94] considering the solid-solid reaction as the main process for the reduction of $LaNiO_3$ in $LaNiO_2$ with NaH powder proposed the following mechanism:

$$NaH(s) + LaNiO_3(s) \rightarrow NaOH(s) + LaNiO_2(s).$$

However, the microscopic mechanism controlling such a reduction is still not fully understood. As a results, we can found a relatively abundant literature concerning the topotactic reduction of oxides with a very wide range of used conditions. Moreover, the incorporation of H^- anion in the structure has also been mentioned as an obstacle to obtain a pristine infinite-layer phase [103]. Its hypothetical effect on the physical properties of the infinite-layer are unknown, and until now, only one study claimed the synthesis of $NdNiO_xH_y$ when performing the reduction process in drastic conditions, *i.e.* higher temperature and reduction time, when compared to the usual conditions found in the literature [104]. Since the effects of H^--incorporation are not known, they should deserve a dedicated study, but this is beyond the scope of the work presented in this thesis considering the difficulty to put in evidence the presence/absence of H in thin films.

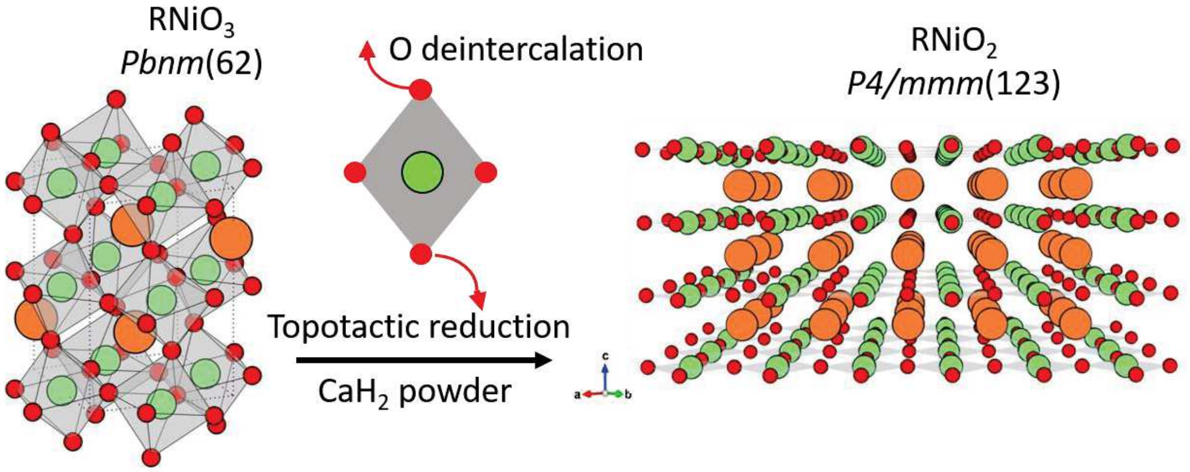

Figure II-11 Schematic representation of the topotactic reduction from the perovskite phase to the infinite-layer phase. The Ni cations are represented in green, the rare-earth element in orange, and the oxygen in red.

2. Superconducting issues

The evidence of superconductivity in Sr-doped infinite-layer nickelates [105] obtained from the topotactic reduction of a perovskite phase has been a tremendous catalyst to the exploration of this reaction with the main goal to reproduce this result. However, only a few groups [106–108] managed to reach a superconducting state in infinite-layer nickelates, which still remains a big challenge for the rest of the community. Our own efforts to reproduce those results will be presented in Chapter IV.

Here, I will present a quasi-exhaustive overview of the last three years' experimental studies on infinite-layer nickelates, with the determination of their phase diagram as a function of the nature of the rare-earth, doping, or choice of the substrate, just to mention some of the most important parameters.

When a new superconducting material is discovered, one of the first attempts is to define its superconducting dome, most of the time as a function of the doping, as lots of materials get their superconducting properties modified through doping. Several doping levels are then studied for this material in order to define the range where the sample is superconducting, and this is probably the most efficient method to look for the optimal doping associated to the highest T_C. In the case of infinite-layer nickelates, this has first been performed as a function of the Sr-doping level in $Nd_{1-x}Sr_xNiO_2$ thin films deposited on STO substrates [106,109]. The superconducting state was firstly evidenced only with the Nd rare earth, but in the upcoming months and years, superconductivity was also discovered with Pr [110] and La [111]. A change of the dopant [112] (Ca instead of Sr), and substrate [113] (LSAT instead of STO) it has also been proved successful in obtaining a superconducting state. The obtained superconducting domes are shown in **Fig. II-12**.

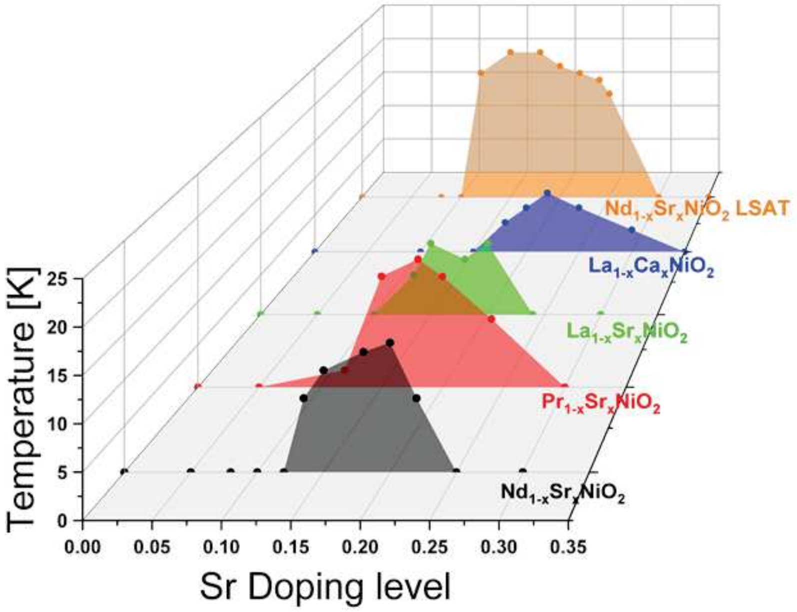

Figure II-12 Reported superconducting domes of different infinite-layer nickelates as a function of the Sr doping-level grown onto STO, apart for the orange dome indicating samples grown onto LSAT [106,110,112–114].

On STO substrates, the range of the superconducting dome as a function of the doping is similar for the different rare-earth cations, but $Pr_{1-x}Sr_xNiO_2$ seems to have the highest T_C. The use of Ca as a dopant instead of Sr seems to require a higher concentration of dopant, but at the same time, preserve a superconductive state at a higher doping. The use of LSAT substrates instead of STO led to an increase of the T_C value [113,114]. The increased T_C for LSAT grown sample has been correlated to the hybridization between the Ni 3d and O 2p orbitals and also the highest quality of the samples that present less defects when optimally grow and reduced on LSAT substrates. Ren et al. [114] performed XAS experiments at the O K-edge on $Pr_{0.8}Sr_{0.2}NiO_2$ thin film grown onto LSAT evidenced a signature of this hybridization from the pre-peak intensity. This pre-peak is not present for superconducting samples grown on STO, while being present for samples grown on LSAT, which possess a higher T_C. They therefore suggest that the charge-transfer might play a role in the pairing mechanism. However, it is important to remember that the quality of the samples itself might be able to explain the different T_C. The fact that the lattice mismatch of the perovskite phase with LSAT is smaller than with STO leads to a higher quality growth of the precursor perovskite phase, which is probably one of the most important prerequisites to obtain a high-quality infinite-layer phase [101]. Here, I would like to highlight that even if the LSAT substrate allows an increase of the T_C of the infinite-layer nickelates, the pre-edge of the O K-edge observed for $Pr_{0.8}Sr_{0.2}NiO_2$ grown on LSAT (and not when grown on STO) might in fact be a fingerprint of a non-optimized infinite-layer on LSAT, and not necessarily the fingerprint of a charge-transfer between Ni and O that could be implied in the pairing mechanism. With this assumption, we could consider that the reminiscent pre-peak might be due to the presence of non-reduced perovskite phase in the sample. However, the mysterious role of the charge-transfer will be more specifically discussed in the upcoming sections. It is important to note that the quality of the several samples synthesized and studied so far in literature can be very different as the optimisation process is still ongoing, and basically a reproducible root is still missing.

3. Superconductivity, beyond the $RNiO_2$ thin films form

Since a superconducting state had been found in infinite-layer nickelate thin films, studies were also performed on bulk, both in poly- and single-crystalline forms. Polycrystalline bulk infinite-layer nickelates doped with Sr, $Nd_{0.8}Sr_{0.2}NiO_2$, were found to be insulating [115,116]. This might be an indicator of the importance of the role of the strain in thin films. However, those studies insist on the difficulty to obtain a pure perovskite phase when the doping level increases. Indeed, the issues observed for the synthesis of Sr-doped perovskite thin films being mainly related to the oxidation degree of Ni, which is 3+x with x = Sr, appears even more challenging for the bulk. It has been suggested that a Ni deficiency in the infinite-layer phase might be a reason for the absence of superconductivity [115]. Especially that in bulk, the reduction of the perovskite phase, which already is hard to obtain as a single-phase when doped with Sr as previously stated, might lead to the production of metallic Ni because of its higher stability than the Ni^{1+}-based samples [116]. Also, differently from the thin films, all the bulk infinite-layer nickelate samples show an insulating resistivity at all doping levels. Further studies on polycrystalline samples are however mandatory to understand the physics of the compounds, and notably give an insight on the role of the epitaxial strain of the thin films. It is clear that further improvements of the sample quality are extremely necessary provide useful information on this material’s family.

Regarding single-crystals, $La_{1-x}Ca_xNiO_3$ has been reduced by Puphal *et al.* through the topotactic reaction [117]. The synthesis of the perovskite phase is performed at very high-pressure and temperature, and the reduction time is of a few weeks, compared to a few hours usually used for thin films. Indeed, they have observed that after 1 day, most of the crystals transformed into the intermediate phase $La_{1-x}Ca_xNiO_{2.5}$, but needed approximately two weeks, depending on the crystal size, shape, and Ca substitution, to be fully reduced to the infinite-layer phase. The authors managed to synthesize the perovskite phase up to x = 0.16, but performed the reduction only with x = 0.08. For this Ca-doping level, the reduced material displayed a metallic resistivity behaviour until 60 K, and then becoming insulating at lower temperatures. Therefore, it is not yet possible to be fully conclusive about the superconductivity in single-crystals. The reported transport properties, similar to what observed for thin films at equivalent doping, is however very promising, and it will be interesting to observe the results for infinite-layer phase single-crystals with higher doping levels.

All the different studies presented until now mainly focused on the reduction of a $RNiO_3$ perovskite phase into the infinite-layer $RNiO_2$ phase, but a work from G. A. Pan *et al.* [118] has also demonstrated a superconducting state in an undoped quintuple-layer square-planer infinite-layer $Nd_6Ni_5O_{12}$ obtained from the reduction of the Ruddlesden-Popper phase $Nd_6Ni_5O_{16}$ as shown in **Figs. II-13(a)-(b)**. The authors suggest that it was possible because, for this quintuple-layer structure, a band filling of $d^{8.8}$ was obtained on the Ni sites, similar to the one in $Nd_{0.8}Sr_{0.2}NiO_2$, showing that dimensionality is another tuning tool within this new field of superconducting infinite-layer nickelates. The dimensionality, also called order, is represented by the number of layers (n) of the nickelate lattice. With this (n), the oxidation degree of Ni can be evaluated, considering valences of +3 for Nd and -2 for O. So, for the RP phase, the Ni valence can be defined as Ni$_{RP}$ = $3-\frac{1}{n}$, while for the reduced phase, as Ni$_{red}$ = $\frac{n+1}{n}$. The results are summarized for various n in **Fig. II-13(c)**, in which a $d^{8.8}$ band filling is indeed observed for the n = 5 (quintuple) reduced nickelates.

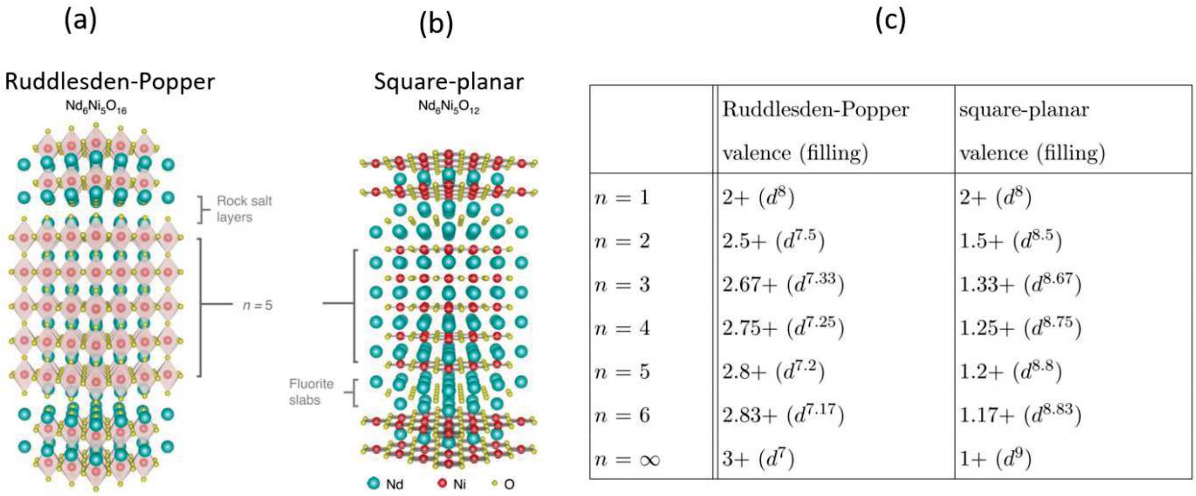

	Ruddlesden-Popper valence (filling)	square-planar valence (filling)
$n=1$	2+ (d^8)	2+ (d^8)
$n=2$	2.5+ ($d^{7.5}$)	1.5+ ($d^{8.5}$)
$n=3$	2.67+ ($d^{7.33}$)	1.33+ ($d^{8.67}$)
$n=4$	2.75+ ($d^{7.25}$)	1.25+ ($d^{8.75}$)
$n=5$	2.8+ ($d^{7.2}$)	1.2+ ($d^{8.8}$)
$n=6$	2.83+ ($d^{7.17}$)	1.17+ ($d^{8.83}$)
$n=\infty$	3+ (d^7)	1+ (d^9)

Figure II-13 (a) Crystal structure of the quintuple-layer Ruddlesden-Popper phase $Nd_6Ni_5O_{16}$ and (b) of its reduced phase, the square-planar layer $Nd_6Ni_5O_{12}$, (c) Values of the electronic filling of the Ni d orbitals for different layered structures.

It is also possible to increase the critical temperature T$_C$ of the superconductor by applying an external stimulus. For example, pressure has been used to increase T$_C$ in $Pr_{0.82}Sr_{0.18}NiO_2$ from 17 K at ambient pressure conditions to 31 K under 12.1 GPa [119]. The authors attributed this enhancement to the lattice contraction, and to the more important hybridization between Ni-3d orbitals and Pr-5d orbitals due to the applied pressure. Here I want to note that we do observe an opposite correlation between the Ni-Nd hybridization and the rise of the superconductivity in our own measurements, as we observed a decrease of this hybridization when increasing the doping. However, we will speak about this in details in the Chapter V.

4. Low-energy excitations in the infinite-layer nickelates

The discovery of a new family of superconducting materials is always a big event, as the new studies it prompts unavoidably contribute to further improve the understanding about the theory of superconductivity, which still remains one of the biggest challenge in solid-state physics. In the case of the infinite-layer nickelates, the similarities of their electronic structure with the one of the high-T$_C$ cuprates enhance this thirst of knowledge. As already said, nickelate analogs to cuprates have been an experimental goal for 20 years, for which the main requirements as suggested by Rice *et al.* in 1999 [62] accounted for (1)NiO_2 square planar planes similar to the CuO_2 ones in cuprates, with (2) Ni^{1+} cations, different from the NiO_6 octahedra observed for the perovskite phase with Ni^{3+}. We know that in cuprates, the superconductivity is due to the quais-2D CuO_2 square planes of (x^2-y^2) symmetry at all doping levels, and the Cu-$3d^9$ sites leading to a spin ½ atomic momentum [120]. With those assignments, numerous works have been done on infinite-layer nickelates to study the differences and similarities with cuprates. Electron energy loss spectroscopy (EELS) measurements allowed evidencing the effect of hole doping in the infinite-layer nickelates. It was shown to affect not only the O 2p orbitals but also the Ni 3d and Nd 5d, providing direct evidence of the multiband electronic structure of the infinite-layer nickelates while cuprates are defined as a single-band system [121]. Theoretical works have put forward another key difference, which is that the energy separation between the O 2p and the Ni 3d bands, of about 4 eV, is higher than the one between the O 2p and Cu 3d bands, of only ca. 2 eV [122]. This difference in charge transfer is explained by the fact that for Ni^{1+} cations, the attraction force from the nucleus is smaller than for Cu^{2+}, and so, the energy of the 3d orbitals is higher [8]. This higher energy of the 3d orbitals leads to an overlap with the Nd 5d orbitals, instead of the O 2p orbitals as in the cuprates [122,123]. A qualitative observation of this difference could be made thanks to X-ray absorption spectroscopy (XAS) measurements at the O-K edge, where the aforementioned pre-peak feature usually observed at around 528 eV, and linked to the TM-O hybridization, is not present for the infinite-layer nickelates, while it is present in the layered cuprates [124,125]. Indeed, the disappearance of this feature is related to a decrease in the charge-transfer between the Ni 3d and O 2p orbitals, which is directly linked to the higher difference between their respective energy bands, making impossible the hybridization between the orbitals. In addition to XAS, Resonant inelastic X-ray scattering (RIXS) measurements have also been performed on infinite-layers, and firstly on undoped LaNiO$_2$ and NdNiO$_2$, showing a strong hybridization between the Ni $3d_{x^2-y^2/z^2}$ and the La/Nd 5d orbitals [124]. Further measurements on Sr-doped infinite-layers evidenced that the Ni-Nd hybridization decreases with the Sr doping level [125,126]. It was thus suggested that doping with holes lowers the Fermi level, which decrease the overlapping of the rare earth 5d band with the Ni 3d one. I want to highlight here that a shift of the Fermi level is one suggestion, but it can also be proposed that the Sr-doping removes electrons from the hybridized band, leading to a decrease of the Ni-Nd hybridization without shifting the Fermi level. Another important result obtained from the RIXS measurements is the presence of a magnon in infinite-layer nickelates when they are capped with a STO layer [127] as shown in **Fig. II-14(a)**, while the presence of a charge order without any magnetic excitation is observed when the thin films are not capped as shown in **Fig. II-14(b)** [128].

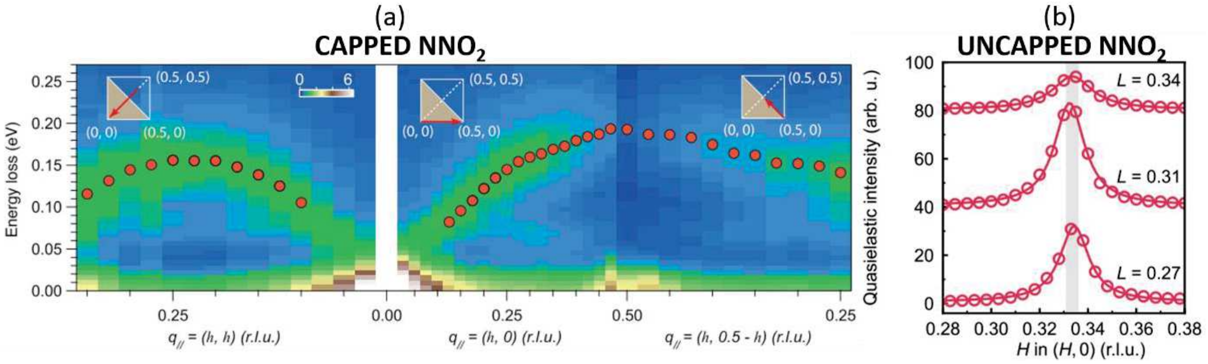

Figure II-14 (a) RIXS intensity maps versus energy loss and projected in-plane momentum transfer along three high-symmetry directions, as indicated with red arrows in the insets. Measurements were taken at 20 K. The red circles indicate peak positions of the magnetic excitation spectra. (Adapted from [127]*) (b) The integrated quasielastic peaks and their Lorentzian fits along (H, 0) direction, each acquired at a different L value (Adapted from* [128]*)*

The importance of the capping-layer on low-energy excitations in the infinite-layer has been one of my subjects of interest [126], as it will be presented in Chapter V. It is important to note that this capping-layer-dependent magnon/charge order dichotomy has only been observed with Nd rare-earth cation so far, and a different behaviour has been observed for La$_{1-x}$Sr$_x$NiO$_2$. In this latter system, the magnon and the charge order occur on the same sample when an STO capping-layer of 5 unit cells is present [129]. The presence of such features is quite important as they are fingerprints of high-T$_C$ cuprates, despite not being fully understood yet. The magnon is probably linked to the pairing mechanism in cuprates [130] and the charge order (CO), also called charge density waves (CDW), is said to be related to the presence of a certain instability akin to a superconducting state ; the two excitations may somehow be in competition in several cases [131]. Regarding, the infinite-layer nickelates, the CO vanishes when the doping increases. Therefore, it seems that it is indeed in competition with the superconductivity, which on the other side appears at increasing doping. The magnon is more rapidly damped with increasing doping than in cuprates, for which the magnon persists in the superconducting dome [132]. The information provided by the study of the low-energy excitations in the infinite-layer nickelates are helping in understanding the physics of this new superconductivity, offering also a playground for enlightening analogies with cuprates.

5. Magnetic order in infinite-layer nickelate

Another important comparison between the two families of nickelates and cuprates concerns the magnetic order. A short-range magnetic order is present in both compounds as already presented before, with a strong superexchange of 100 meV $\leq$ J $\leq$ 150 meV [133,134] in cuprates, while in the infinite-layer nickelates the superexchange is lower, with 50 meV $\leq$ J $\leq$ 100 meV [127,135]. But the long-range order has not yet been reported for infinite-layer nickelates, while being well established in cuprates thanks to the possibility to measure bulk and single-crystal samples [134,136]. Regarding, bulk infinite-layer nickelates although they do not show any sign of superconductivity they do not present any long-range magnetic order down to 1.7 K [95].

Muon-spin rotation has been used to study magnetism in infinite-layer nickelates. The observed magnetism was shown to originate from the NiO_2 sublattices [137]. By increasing the doping, the short-range ordered magnetic correlations evolve to a spin-glass-state behaviour at around 150 K. Such a high transition temperature, when compared to that of cuprates, which is usually below 30 K, indicates a behaviour closer to that of the iron pnictides superconductors, for which magnetic order and superconductivity coexist [138].

Magnetoresistance (MR) and angular magnetoresistance (AMR) have been widely studied in cuprates, and their origin was said to be the previously mentioned long-range AF order [139–141]. Such measurements have been performed on superconducting infinite-layer nickelates to observe the influence of the R cation, such as La, Pr and Nd [142]. Different behaviours have been observed and mainly attributed to the 4f magnetic moment of the rare-earth cation, absent in La, but present for both Pr and Nd although differently active under a magnetic field. Indeed, it has been observed that the upper critical field is influenced by the R cation, being the highest for La , while lowest for Nd, , and intermediate for Pr, consistent with a distinct contribution of the Pr^{3+} 4f moments induced by the magnetic field [142].

6. Theoretical models to support the experiment

a. The hypothetic hydrogen-intercalation easier in undoped parent infinite-layer compound

If the adventure of superconductivity in nickelates started more than twenty years ago with a theoretical prediction [62], its experimental discovery did not put an end to the theoretical studies. On the contrary, putting forward a model capable of reproducing the main properties of this new oxide family is an intense field of research since August 2019. For example, the aforementioned problem of the H-intercalation is a synthesis issue, but a theoretical study has tried to understand the mechanism calculating the probability of synthesizing a defect fluorite structure, such as $NdNiO_xH_y$, and suggesting that it could be obtained by over-reduction of the samples with CaH_2 powder [104]. This structure was shown to be favourable only at low Sr-doping levels by simulations with density functional theory (DFT) and dynamical mean field theory (DMFT) [103], which also suggested that compression can be efficient to eliminate the possible H-intercalation. This intercalation would lead the $3d^9$ electronic structure of Ni, with only one hole in the $3d_{x^2-y^2}$, to become a $3d^8$ state with one hole in the $3d_{x^2-y^2}$ and one in the $3d_{z^2-r^2}$ [143]. In the iron pnictides, the intercalation of hydrogen is playing a huge role [144,145], and since some studies already reviewed before, exhibited analogies with this family of material instead of cuprates. I believe that this possibility should be further considered, also experimentally.

b. The electronic structure of the infinite-layer nickelate and comparison with cuprates

Theoretical models have been widely used to study the electronic structure of the infinite-layer nickelates, for example to categorize the parent compounds (the undoped infinite-layer) of the superconducting nickelates, and compare them with cuprates. The analysis of the band character near the Fermi level with first-principles calculations for $RNiO_2$ shows that the $3d_{x^2-y^2}$ orbital creates a large Fermi surface, which is a common feature with cuprates. Apart from this large Fermi surface, electron pockets exist near the Γ(0,0,0) [122,123] and A(π/a, π/a, π/c) [146,147] points, as shown in **Fig. II-15.** The electron pocket around the Γ point is formed by the hybridization between the R $5d_{3z^2-r^2}$ and Ni 3d [148,149], while the one around the A point is present where a large bonding-antibonding energy splitting of more than 10 eV is observed [150], with the bonding part resulting in the electron pocket. Its presence is possible thanks to the absence of any apical oxygens in the lattice and is formed by the bonding state between the interstitial s-like orbital and the Nd $5d_{xy}$ orbital [146]. As the additional electron pockets are formed by the rare-earth layer, Ni $3d_{x^2-y^2}$ orbital deviates from half-filling already in the parent compound [123]. Ni is not $3d^9$ because of this self-doping, and this is observed for different R in $RNiO_2$ [151,152].This is one of the major differences with cuprates, where usually only the $3d_{x^2-y^2}$ of the Cu crosses the Fermi level [123]. It has also been estimated that this self-doping of the Ni $3d_{x^2-y^2}$ is of the order of 0.1 electron from the charge transfer from Ni bands to Nd bands [153].

Other theoretical works focused on the correlation effects on the electronic structure to try to determine and classify the physics model of nickelates. The coupling between the itinerant R orbitals and the correlated Ni 3d orbitals leading to Kondo physics is supported by some works [147,154]. The importance of the Hund's coupling and the essential multi-orbital nature of the Ni 3d manifold is advanced by others studies [155–157]. Some papers insist, on the contrary, on the fact that the correlation effects mainly originate from the $3d_{x^2-y^2}$ single band [158,159]. The different results obtained in those studies arise from the differences in the calculation conditions used in DFT and DMFT, which can be the interaction strength, the orbital basis, or the double-counting correction, which could be described as the portion of the interaction used in the DFT calculations [160].

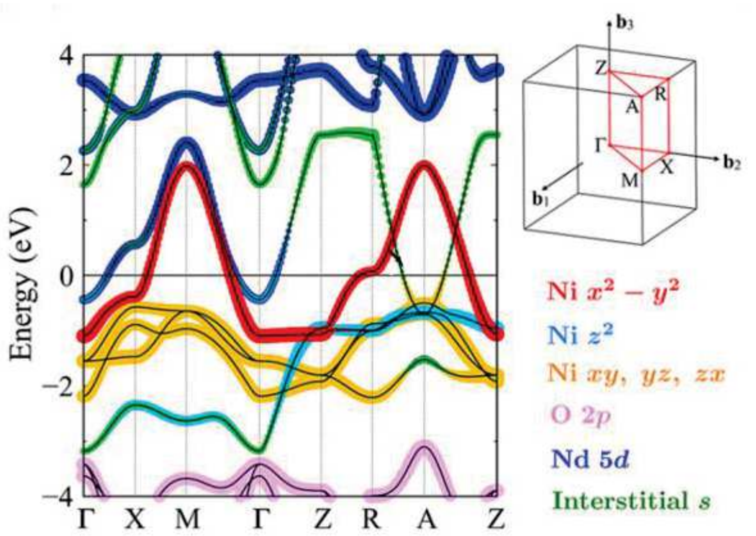

Figure II-15 Electronic structure of $NdNiO_2$ *calculated by DFT (Adapted from* [8]*)*

c. What is essential in the infinite-layer nickelates to observe a superconducting state?

Apart from aiming at the understanding of the electronic structure of the nickelates, those theoretical studies are also used to determine the degree of freedom of the superconductivity. The objective is to determine what is essential in the nickelates to observe superconductivity. In other words, what is the pairing mechanism in the infinite-layer nickelates? It is good to remember that for conventional superconductors, the superconducting behaviour is explained by the BCS theory [3]. In this theory, two electrons are attracted to each other when the energy difference between the electron states involved is lower than the phonon energy. But for unconventional superconductors, such as the cuprates, the BCS theory fails to explain the origin of the superconductivity. In the nickelates, it has also been shown that this electron-phonon coupling cannot lead by itself to the superconducting state, as the estimated T_C with this theory is of the order of 1 K, way lower than the 10 K or above found experimentally [146]. In previously cited papers [90,103–106], it has been shown that the $3d_{x^2-y^2}$ orbital of Ni is of particular importance for the physics of the material, and lots of works attest of a d-wave pairing at the origin of the superconductivity. But other degrees of freedom have been explored to determine if they have an influence on the onset of the superconducting state:

- The role of the 4f orbitals is still under debate, notably with papers suggesting an intra-atomic interaction between the 4f and the 5d orbitals of the R cation affecting the energy of the self-doping band, and so change the size of the electron pockets [161,162]. Hybridization between the 4f orbitals of the R cation and the 3d orbitals of the Ni via the 5d of the R cation is also discussed in some works [152,163], where they claimed that 4f electrons can be at play in the modification of the Fermi surface in different magnetic states. However, evidence of superconductivity in $La_{1-x}Sr_xNiO_2$ [111] is of course reducing the hypothetic influence of the 4f orbitals, as they are not filled for the La cation.
- An increase of the metallic resistivity at low temperatures is observed in the parent compounds of superconducting nickelates. This could be the fingerprint of a Kondo effect, due to the presence of magnetic impurities in the lattice, that might be ascribed to Nd 4f moments.

Theoretical works indeed suggest that the Fermi pockets might not only be a charge reservoir, but might also be at the origin of this resistivity upturn at low temperature [164,165]. Moreover, speculation on a long-range RKKY magnetic interaction mediated by the Nd 5d orbitals in NSNO [127] have been made to underline the importance of those electron pockets. However, experimental work put in evidence that infinite-layer nickelate grown on LSAT does not present a Kondo effect as the resistivity saturates at very low temperature [113].

- For the cuprates, classified as charge-transfer insulators in the Zaanen-Sawatzky-Allen (ZSA) scheme, the O 2p orbitals are the ones which are receiving the holes from doping. This is due to the fact that the charge transfer energy is smaller than the Coulomb interaction for the Cu 3d orbitals, as already mentioned in the previous section. Because of the higher charge transfer energy in infinite-layer nickelates, the hybridization with the O 2p is lower than in cuprates, but not equal to zero [153,166]. This hybridization is responsible for the Zhang-Rice singlet $3d^9L$ in cuprates formed of Cu $3d_{x^2-y^2}$- O $2p_{x,y}$ holes [167–169] which is said to be a degree of freedom of their superconducting state. This is why remembering that this charge-transfer is not zero for nickelates can be of importance here, even if it is weak.
- Even if charge-transfer is not zero, the classification of the infinite-layer nickelates is closer to Mott-Hubbard than to charge-transfer [153,170,171], that is, with a Coulomb repulsion smaller in energy than the charge transfer from the O 2p to the Ni 3d as previously schematized in **Fig II-3**. In this case, the Ni $3d^9$ electronic state is divided into a $3d^9\underline{L}$ and a $3d^8$ states as described in **Fig. II-16**, with a more favourable $3d^8$ electronic state. This leads to another energy scale competition, between the high spin (S=1) and the low spin (S=0) states, with a competition between the crystal field splitting and the Hund's coupling. If the crystal field is the most important, the holes will stay in the $3d_{x^2-y^2}$ orbital, leading to a spin-state of S=0, and so to a single-orbital model. If the Hund's coupling is the highest, a spin-state of S=1 is obtained, described here by a multi-orbital model. And when the Hund's coupling is playing a dominant role, it has been suggested that the pairing might emerge from a spin-freezing scenario due to enhanced local spin fluctuation through the doping [172].

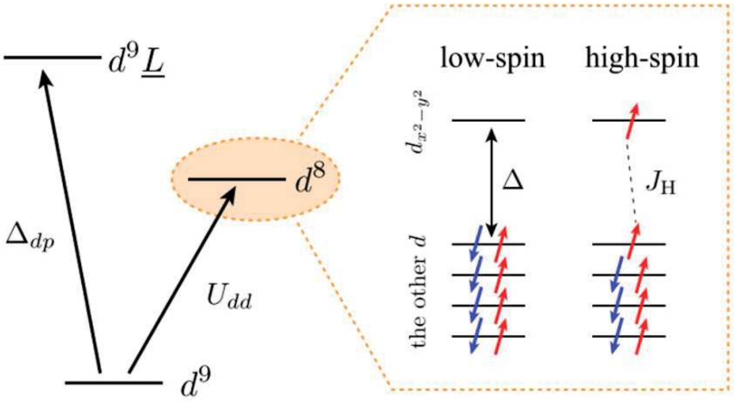

Figure II-16 Electronic schemes of Mott–Hubbard highlighting the difference in energy between charge transfer Δ_{dp} and Coulomb repulsion U_{dd}. A zoom is made on the energy diagram for the hole doping, with a low-spin state (S=0) when the crystal-field energy Δ is dominating, and a high-spin state (S=1) when the Hund's coupling J_H is dominating. (Taken from [8])

- Since so far no superconductivity has been discovered in bulk infinite-layer nickelates [116], the importance of the interface with the substrate must be underlined for thin films. In this case, the difference between a SrO-terminated or TiO_2-terminated STO substrate will modify the electronic structure of the grown film. We assume that STO substrates are mostly TiO_2-

terminated as they are usually treated with HF for this purpose. However, interfacial reconstruction might happen, which can lead to a SrO-terminated substrate [173]. For both surface terminations, the interface seems to flatten the Ni $3d_{z^2}$ band, therein enhancing interface-specific correlation effect [9,173]. Moreover, some studies point out the presence of a lattice reconstruction at the interface between $RNiO_2$ and STO [174], and also claimed the presence of a two-dimensional electron-gas, with a strong occupation of the Ti $3d_{x^2-y^2}$ states [175,176]. The top-surface of the thin film has also been studied and it was confirmed that different terminations will lead to different electronic structures and Fermi surfaces [173]. As a result, the d-wave superconductivity expected in the thin films, transforms to an s-wave at its surface when it is NiO_2 terminated [177].

III. Experimental Methods

1. Elaboration techniques

Here, I will present the experimental techniques that I employed to synthesize the infinite-layer nickelates thin films, from the growth of the perovskite rare-earth nickelate phase to the stabilization of the infinite-layer one. I also will introduce the techniques I used to characterize my samples from structural, morphological and electronic points of view.

1. Thin Films Growth – Pulsed Laser Deposition

The thin films gown in this thesis were prepared by pulsed laser ablation (PLD), which consists in ablating a target with a high energy pulsed laser, thus forming a vapour plume which will deposit the ablated elements onto a heated substrate. The ablation of materials with a laser to obtain thin films was first performed in 1965 by Smith and Turner [178], with the use of a ruby laser [179]. However, in the twenty years that have followed, this deposition technique did not reach a high popularity, until it allowed the growth of high-T_C superconductors $YBa_2Cu_3O_7$ with a higher quality than the other growth techniques [180]. PLD gained its noble letters in the growth of oxides thanks to its stoichiometric transfer of matter from a ceramic target onto the substrate [181]. The small deposition area (a few square centimetres) associated to the technique has certainly been a limit to its transposition to a suitable scale for the industry, limiting its use mostly to research purposes. However, some solutions have been found to counter this disadvantage and PLD can nowadays be considered as a possible source of high-quality oxides thin films for the industry. The Solmates company in Twente, offering the possibility to deposit onto wafers of diameters up to 200 mm, gives an illustration of these solutions.

The material ablation with a laser may be described as follows: the laser is focussed onto a target, and this allows the sublimation of the elements of this target; the interaction between the laser and those elements creates a plasma. The formed plasma plume migrates towards the substrate as shown in **Fig. III-1(b)**, and the sublimated elements then condense on the substrate surface, which results into the growth of the desired material [182]. The frequency of the laser determines the quantity of matter that will reach the substrate per second. This parameter is used to let more or less time for the ionized species to get organized on the substrate and adopt its crystal structure. The geometry in the chamber can also modify the thin film growth. An off-axis deposition can be done by changing the angle between the laser beam and the target and/or the angle between the target and the substrate. The distance between the substrate and the target can also be modified, leading to a decreasing (increasing) growth rate as the ionized species have more (less) distance to travel to encounter the substrate. The lens focus can change the laser imprint on the target and thus modify the fluence, which is the ratio between the laser energy and the laser spot area. The atmosphere in the chamber can be controlled by a dedicated gas valve and a pressure gauge. The quantity of gas in the chamber can be used to tune the kinetic energy of the species, while the nature of the gas can tune, for example, the oxidation degree of the species. As an example, if O_2 is used, it will tend to increase the oxidation degree of the species, on the contrary of an inert gas such as N_2. Some experiments even use O_3 atmosphere to obtain a highly oxidizing atmosphere in the chamber [78].

The deposition chamber of our PLD system is schematically shown in **Fig. III-1(a)**. It is equipped with a KrF excimer laser (COHERENT COMPex Pro 102) with a wavelength of 248 nm. The substrate holder is placed in front of the target carousel which allows up to 5 targets simultaneously in the chamber. The different ceramic targets used in this thesis have a diameter of 25 mm and have been bought from Toshima Manufacturing Co. Depositions are performed in an oxygen atmosphere (P_{O2}). The kinetic energy of the ionized particles colliding with the substrate is determined by the energy of the laser and the oxygen pressure. The single-crystalline substrate is stuck onto the substrate-holder, which is also a heater, with silver paste, and can be heated up to 900°C. Aforementioned parameters (fluence, P_{O2}, heater temperature, …) were modified throughout the thesis in order to obtain the highest-quality thin films, and the optimisation process will be presented in Chapter IV.

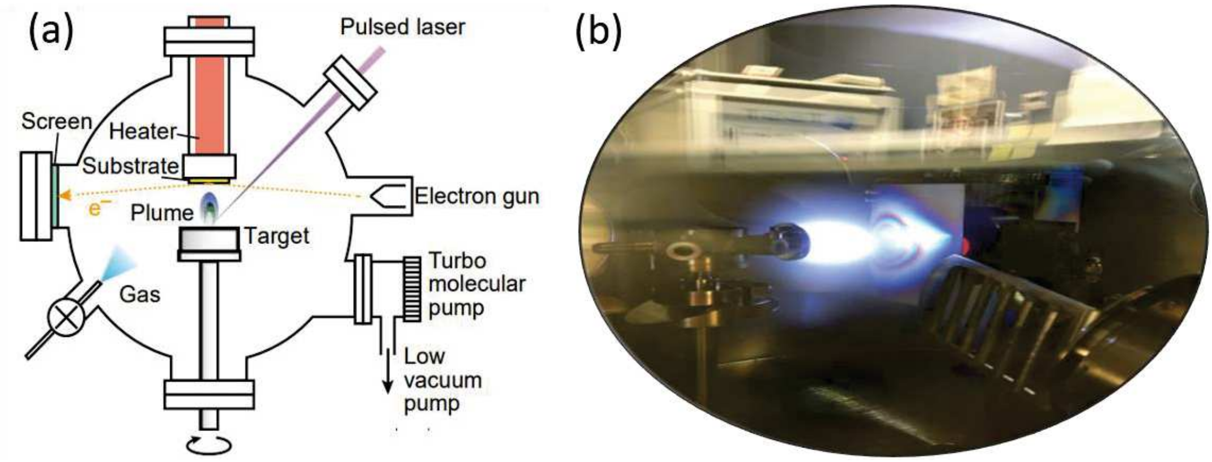

Figure III-1 (a) Scheme of a PLD chamber (Adapted from [182]*) (b) Picture of the ablation of a target inside our PLD chamber*

2. Topotactic reduction of the thin films

In order to obtain infinite-layer nickelate thin films, we resorted to a so-called topotactic reduction, which is a soft-chemistry process. The reaction is performed within a glass tube shown in **Fig. III-2**. The perovskite thin film is introduced with 0.5 g of CaH_2 powder inside the tube (≈50 cm^3) and placed under a static-vacuum (1 mbar). The tube is then heated for durations comprised between 3 and 30 h at a temperature varying between 240°C and 300°C, depending on the Sr-doping level (0, 5 and 20% in our case) and on the presence/absence of a capping-layer. Upon heating, the hydride powder reacts with the thin film material with which it is in contact and reduces the perovskite phase thanks to the highly reducing redox potential of the H-/H2 couple of -2.25 V [102]. Only the apical oxygen are taken away with this reaction [92,183]. The reduced thin films are not stable in air and the infinite-layer-phase starts to deteriorate after about one month if not kept in a desiccator. Alternatively, a better stability is granted for $SrTiO_3$ (STO) capped films, which however still deteriorate, but only after about 6 months in air, from our experience. The optimization of the thin films reduction will be presented in Chapter IV.

Figure III-2 Homemade system to perform the topotactic reduction of the thin films with CaH_2 powder in a static vacuum

2. Thin films characterization

I will introduce here the different techniques used to characterize the structural, morphological and electronic properties of the grown thin films.

1. Reflection High Energy Electron Diffraction

Reflection high energy electron diffraction (RHEED) allows to visualize the reciprocal space of the sample surface. It can be used to characterize the crystalline arrangement of the substrate before the growth, as well as that of the deposited film during its growth (*in situ* monitoring). A coherent electron beam characterized by a voltage of 35 kV is sent to the sample surface with a small incidence angle of 3-4° as shown in **Fig. III-3**. The reflected electron beam is detected on a photoluminescent screen and then monitored by a CCD camera. The diffracted pattern consists in the intersection of the rods of the reciprocal lattice of the sample, perpendicular to its surface, with the Ewald sphere. The coherent length of the electron beam determines the spatial resolution of the RHEED structure analysis; it is usually around 100 nm. Resulting images are shown in **Fig. III-3**. The RHEED pattern of **Fig. III-3(a)** shows spots, representative of a single-crystal $STO(001)_{pc}$ having terrace widths larger than the electron coherence length. When the surface possesses domains with a size smaller than the coherent length of the electron beam, there is an elongation and broadening of the diffracted spots in the RHEED pattern. **Fig. III-3(b)** shows the RHEED pattern of a NNO thin film grown on $STO(001)_{pc}$ substrate, showing intense streaks, which is the signature of a layer-by-layer growth of the thin film and also of a high-crystalline quality. On the contrary, when the surface is so rough that that there is a 3D islands morphology, the electron beam produces a transmission diffraction pattern instead of a reflection one, because it transmits through the 3D islands. Such a behaviour is observed in **Fig. III-3(c)** with the growth of a PZT layer on top of a NNO layer grown on $STO(001)_{pc}$. The presence of the transmission spots clearly indicates the 3D growth of the material in this case. Thanks to the RHEED pattern images, it is possible to obtain real-time insight on the quality of the growth, layer-by-layer or 3D.

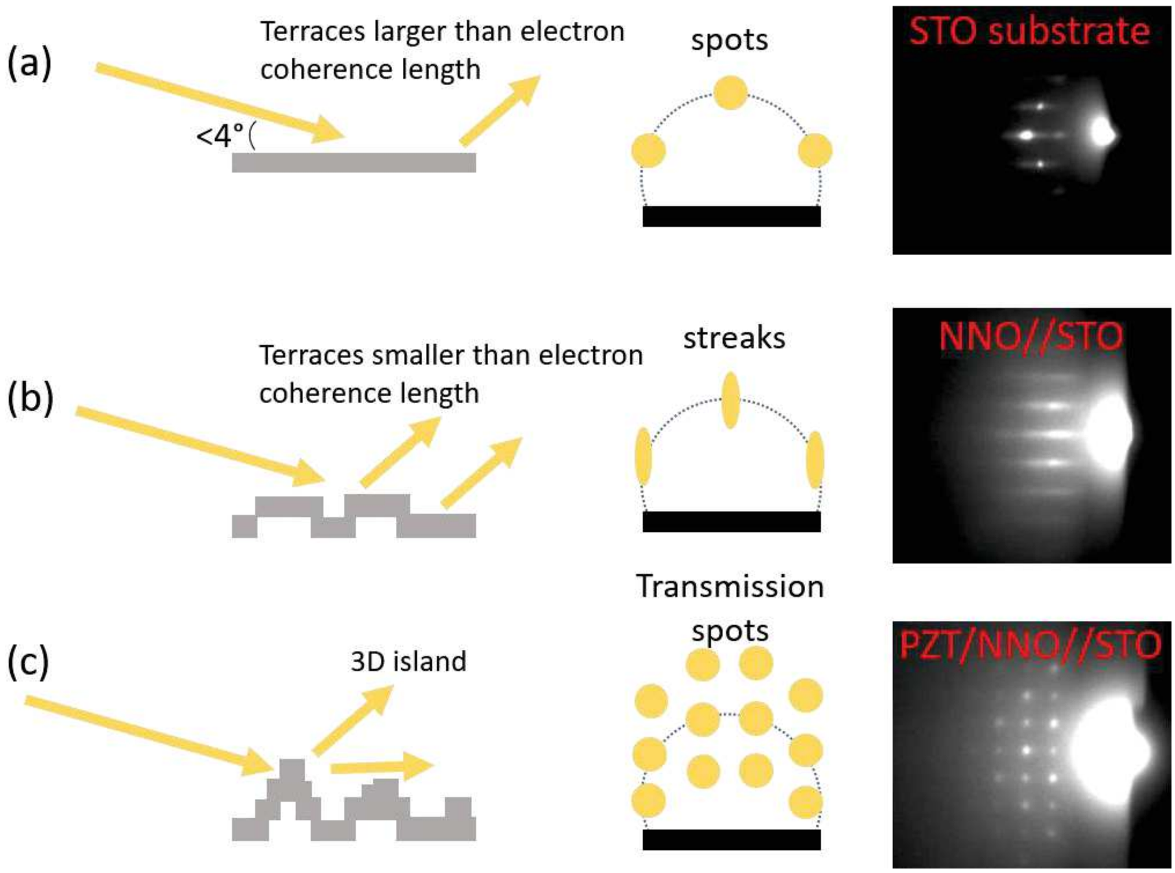

Figure III-3 Schematic and real RHEED patterns for different surface morphologies : for (a) an STO(001)$_{pc}$ single crystal surface with terrace widths that are larger than the electron beam coherence length, (b) an NNO layer grown onto an STO(001)$_{pc}$ substrate and exhibiting a layer-by-layer growth, and (c) a PZT layer grown on top of an NNO thin film grown on STO(001)$_{pc}$ substrate which exhibits a 3D growth. (Adapted from [184]*)*

It is possible to monitor the evolution of the intensity of a diffracted peak to obtain real-time information on the growth rate of the thin film. The result is shown in **Fig. III-4(a)** where each RHEED oscillation stands for the growth of a perovskite single unit-cell layer. Indeed, the intensity of the beam is maximum when the surface is a well-defined monolayer as shown in **Fig. III-4(b)**. In that sense, the decrease of the overall intensity of the RHEED signal is due to a loss of the bidirectional growth through time. The surface roughness is due to a thermodynamic equilibrium between terraces and 3D islands. The RHEED signal stops evolving when this equilibrium state is reached.

In this work, the growth of the thin films has been performed in a high oxygen pressure (0.3 mbar), when considering the usual pressure range for which RHEED is used, even when equipped with a differential pumping, which is our case. A pressure higher than 0.3 mbar will not allow to use RHEED, because the electron beam will start to have difficulties to reach the photoluminescent screen. That’s why the acquisition of nice RHEED pattern images of layer-by-layer growth under those conditions is the proof of a high-quality growth, with even the possibility to observe well-defined RHEED oscillations allowing the determination of the growth rate of the thin films.

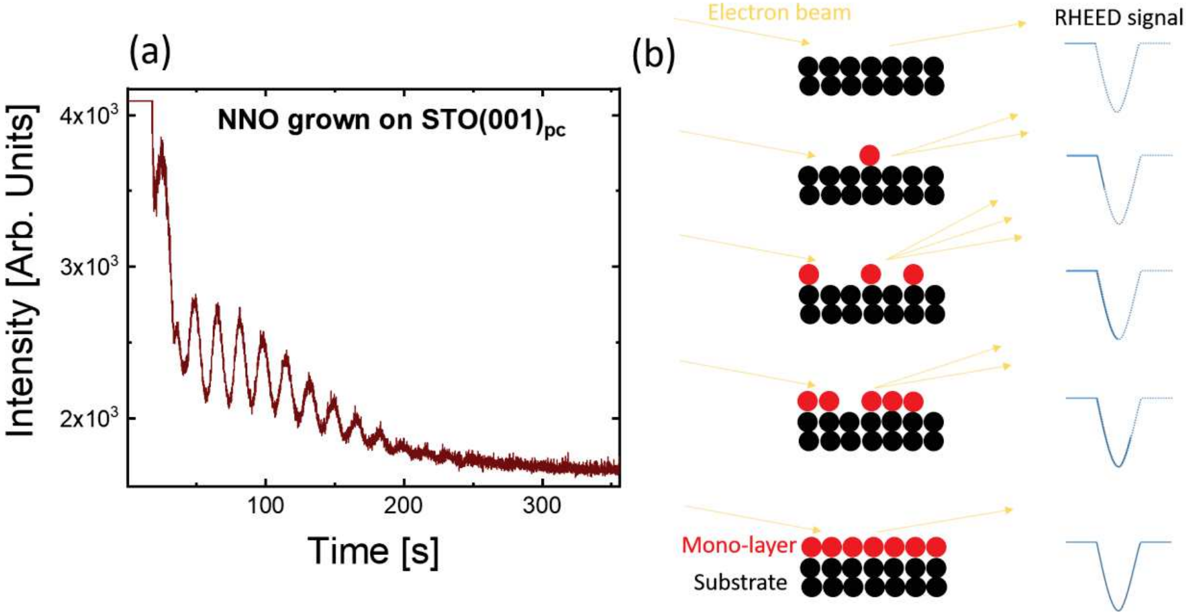

Figure III-4 (a) RHEED oscillations of the specular spot observed during the growth of an NNO thin film under an oxygen pressure of 0.3 mbar, (b) Schematic correspondence between the observed RHEED oscillations and the progress of the mono-layer growth (Adapted from [185]*)*

2. X-ray Diffraction and reflectivity

The crystallographic phase of the thin films and their crystalline quality can be determined through X-ray diffraction (XRD) measurements. In this thesis, the measurements were performed with a Rigaku Smartlab diffractometer equipped with a rotating Cu anode (λ=0.15406 nm). The geometry of the system is shown in **Fig. III-5(a)**. When scans are performed in a θ-2θ mode, only the lattice planes parallel to the sample surface can be observed, when they respect the Bragg diffraction condition: $2d \sin\theta = n\lambda$, with n the diffraction order, λ the wavelength of the X-ray beam, θ half the angle between the incident and diffracted beams as well as the incidence angle of the X-ray beam onto the sample, and d the interplanar distance in the lattice. In our study, only STO (001)$_{pc}$ oriented substrates have been used. Only the (00l) Bragg peaks will therefore be observed for our thin films on θ-2θ scans since they are epitaxially grown on (001)$_{pc}$ oriented substrates. 2D maps of the reciprocal space can be obtained by combining ω-2θ scans acquired for various ω angles, ω being the X-rays incidence angle, around the theoretical position of a diffraction node at a ψ offset angle, as shown in **Fig. III-5(b)**. **Fig. III-6** shows, as an example, a reciprocal space mapping acquired for a $Nd_{0.8}Sr_{0.2}NiO_3$ thin film sample around the 013 reflection of its STO single-crystal substrate. It allows to determine information on the relaxation state of the film. Qx and Qz are the reciprocal space parameters, inversely proportional to the lattice parameters, and defined by:

$$Qx = \frac{4\pi}{\lambda}\sin(\theta)\sin(\Psi)$$

$$Qz = \frac{4\pi}{\lambda}\sin(\theta)\cos(\Psi)$$

The in-plane distances can be determined from the Qx values of the observed peaks. When both the film and substrate peaks have the same Qx, it means that they have identical in-plane parameters, and therefore that the film is fully strained by the substrate.

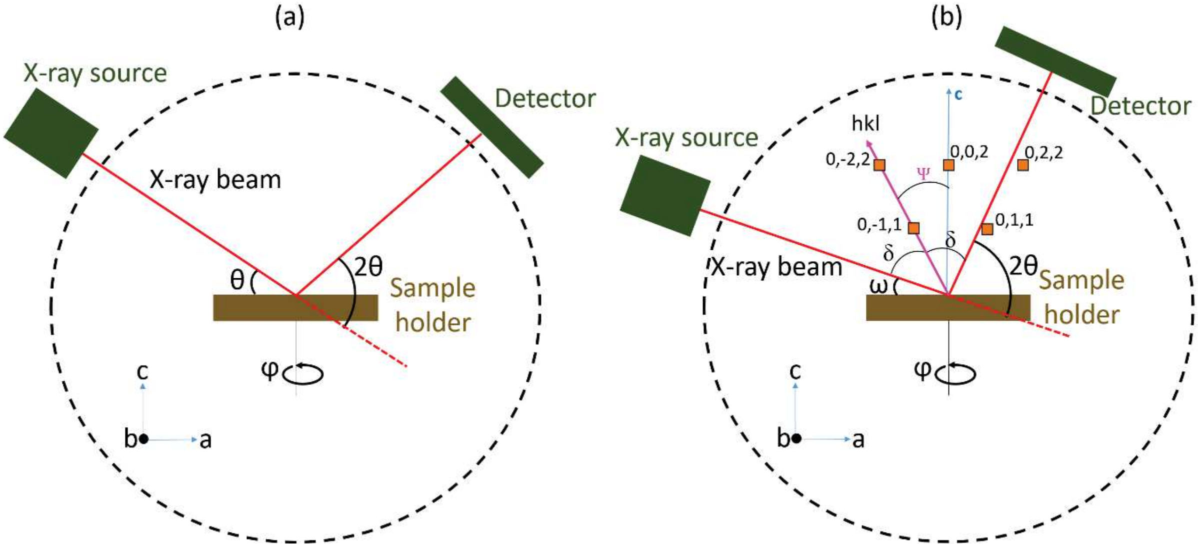

Figure III-5 (a) Scheme of the geometry of our Rigaku diffractometer (a) when a ϑ-2ϑ scan is performed and (b) when a reciprocal space map is performed with ω-2ϑ scans.

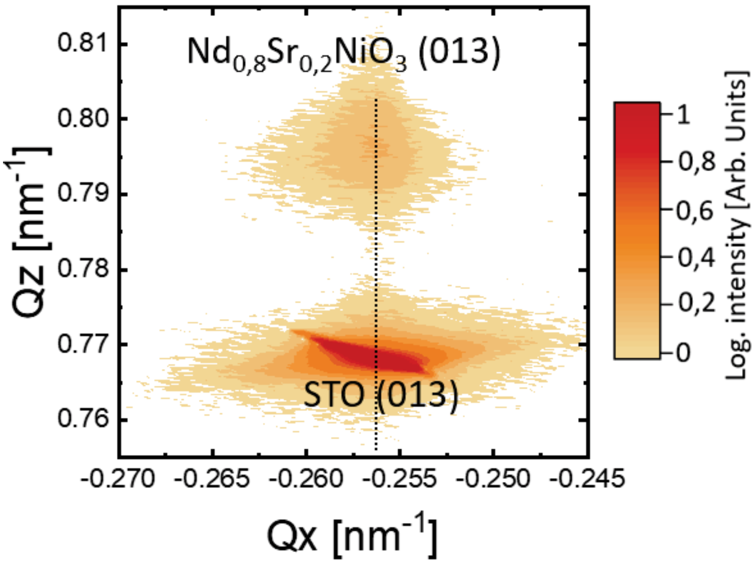

Figure III-6 RSM of a $Nd_{0.8}Sr_{0.2}NiO_3$ thin film around the 013 reflection of its STO substrate, showing that it is fully strained

To obtain information on thickness, density and roughness of a thin film, it is possible to perform X-ray reflectometry measurements, which consist in θ-2θ scans performed at very low angles (2θ < 6°). The reflectivity curves are the product of the interferences observed between the signal at the thin film-atmosphere and thin film-substrate interfaces. Those interferences give rise to oscillations, as shown in **Fig. III-7** for a 10 nm thick $NdNiO_3$ thin film. The oscillations period is dependent on the thickness of the film, the position of the inflexion point, indicating the end of the total reflexion, is related to the density of the film. The oscillation amplitude provides information on the roughness of the thin film. In this thesis, the GlobalFit software provided by Rigaku has been used to fit the reflectivity curves and extract the desired experimental parameters (film thickness, roughness and density).

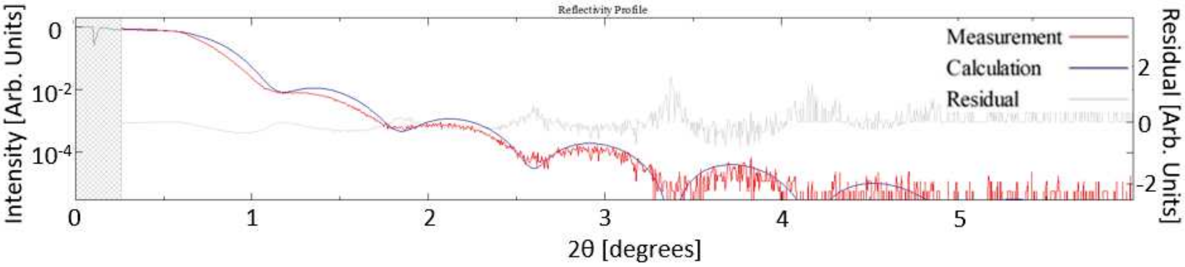

Figure III-7 Reflectivity curve of a NNO thin film (red curve) and the corresponding fit in blue obtained with the GlobalFit software (the values used for the fit are a thickness of 10.3 nm, a roughness of 0.4 nm and a density of 7.5 g/cm^3).

3. Atomic Force Microscopy

In the research field of thin films, the morphology of the surface is usually a good indicator of the quality of the growth. Atomic Force Microscopy (AFM) is a surface sensitive technique in which a microscopic tip mounted on a piezoelectric cantilever is used to sense the surface of the sample [186]. A scheme is given in **Fig. III-8(a)**. Measurements can be performed in contact-mode, where the tip is considered closer to the sample surface (only a few Angstroms) or in tapping-mode (or non-contact mode) with a tip further away from it (a few nm) **[Fig. III-8(b)]**. To obtain information on the surface morphologies of thin films, the tapping-mode is quasi-always used, in order to minimize the risk to damage the tip or the sample surface.

In tapping-mode, the tip is oscillated close to its resonance frequency, and the amplitude and frequency of those oscillations are kept constant. When the tip approaches the surface, the attractive van der Waals forces move the tip away from its initial resonance frequency. This is detected by the internal lock-in amplifier, and a feedback-loop adjusts the position of the tip in order to keep the cantilever in resonance. The topography image is thus produced by analysing the force used to keep the tip in resonance.

It is possible to use interactions other than van der Waals forces, such as, for example, the piezoelectric response of materials, in piezoelectric force microscopy (PFM). In that case, a conductive tip is used in contact-mode and an alternating current is applied to the tip, which leads to a deformation of the sample through the piezoelectric effect. This deformation is detected in the same way as in the aforementioned AFM, and the feedback-loop systems produces the image of the piezoelectric domains and the topography simultaneously.

The AFM system used to perform topography analyses is a XE7 from Park Systems. The system used to perform the PFM measurements is a Dimension Icon from Brucker. The instruments were operated in air and have been isolated from acoustic and vibrational noise through an acoustic enclosure and active damping table, respectively.

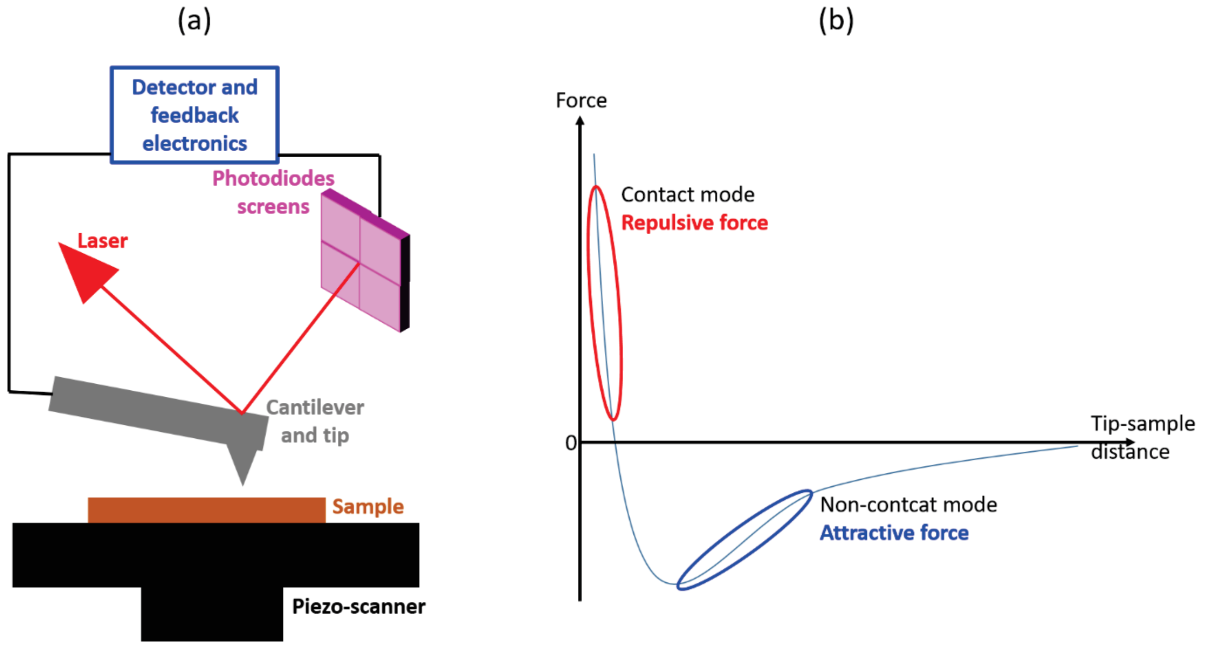

Figure III-8 (a) Basic scheme of the working principle of an atomic force microscope (b) Force versus tip-sample distance graph where contact mode (red) and non-contact mode (blue) working area are circled (Adapted from [57]*).*

4. Scanning Transmission Electron Microscopy

Scanning Transmission Electron Microscopy (STEM) is a powerful technique in solid state physics to probe the structure of thin films with an atomic resolution. In STEM, and this is a difference with conventional TEM **Fig. III-9**, the electron beam is focused as a fine spot (typical spot size of 0.05 – 0.2 nm) which is then scanned over the sample. STEM is compatible with analytical techniques such as annular dark-field imaging (ADF), high-angle annular dark-field (HAADF), spectroscopic mapping by energy dispersive X-ray (EDX) spectroscopy, or electron energy loss spectroscopy (EELS). The combination of annular bright field (ABF) and HAADF has shown the possibility to visualize both oxygen and cation positions in oxides thin film [187]. A highly focussed electron beam is shone through the sample and a detector collects the transmitted beam. The image is formed by the interactions between the electrons of the beam and the local electrostatic potential of the sample. To perform this measurement, the sample must be very thin (a few tens of nm) to allow sufficient transmitted beam. The film samples must thus be thinned, either by manual polishing or by a focused ion beam (FIB), in order to be observable. The FIB uses a Ga-ionized beam to dig in the thin film and take out a part of the sample which will be used for the STEM measurements. The image is observed on a fluorescent screen or a CCD camera and the resolution is close to tens of picometers, a size where atoms are detectable.

In this thesis, the observed lamellae were prepared by a FIB technique by David Troadec at the IEMN in Lille. Some observations were performed at the IPCMS by Corinne Bouillet with a JEOL 2100F, equipped with an EELS spectrometer. Some others were performed by Alexandre Gloter [188] in Laboratoire de Physique des Solides, Paris-Saclay, with whom we have a collaboration. A NION Ultra-STEM200 C_3/C_5-corrected STEM was then used, with HAADF and EELS.

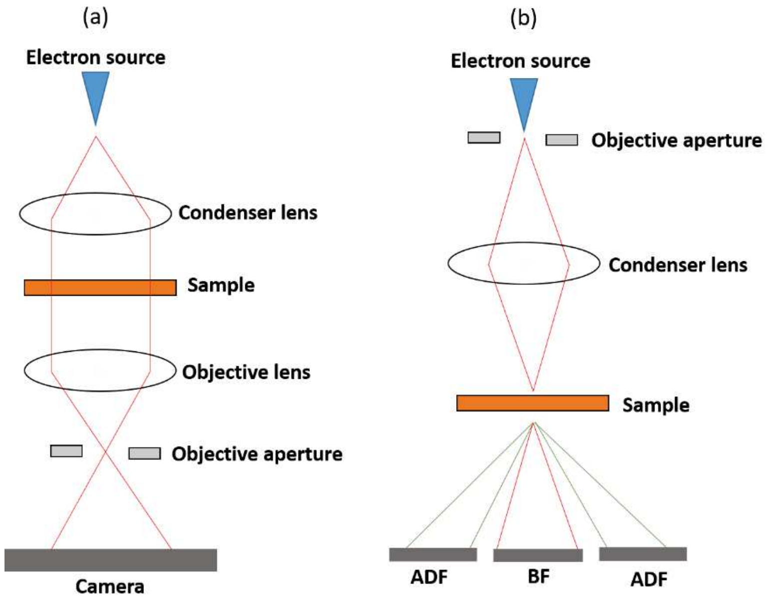

Figure III-9 Scheme of the working principle of a (a)TEM and (b) STEM. ADF = Annular Dark Field, BF = Bright Field. (Adapted from [185]*)*

5. Transport measurements

All transport measurements in this thesis were performed with a Dynacool Physical Properties Measurement System (PPMS) from Quantum Design. Measurements can be performed between 2 K and 400 K, in a magnetic field ranging between -9 and +9 Tesla.

a. Resistivity measurements

Resistivity measurements have been performed in the Van der Pauw geometry with 4-points contacts as shown in **Fig. III-11,** where the current is applied on an edge of the sample, and the voltage drop of the material is measured on the opposite one. This geometry is used to eliminate the contribution for the contact resistance. The resistivity is given in Ohm.cm and allows to compare samples independently of their thickness or lateral sizes. It is calculated by [189]:

$$\rho = \frac{\pi}{\ln(2)}.\mathrm{d}.\mathrm{F}.(\frac{V_{23}}{I_{14}} + \frac{V_{12}}{I_{34}})$$

With d being the sample thickness, V_{23} is defined as V_2 - V_3, I_{14} stands for the current which enters the sample through contact 1 and leaves through contact 4 (as labelled in **Fig. III-11**), and F is the transcendental function. Two measurements are needed in Van der Pauw geometry, for two edges. The F factor is considered to determine the homogeneity of the sample and the quality of the contacts in terms of distance and symmetry [189]. To evaluate the impact of those parameters, the transcendental function is calculated with:

$$\mathrm{F} = 1 - \left[\left(\frac{R_{23}-R_{12}}{R_{23}+R_{12}}\right)^2 . \frac{\ln(2)}{2}\right] - \left[\left(\frac{R_{23}-R_{12}}{R_{23}+R_{12}}\right)^3 . \left(\frac{\ln(2)^2}{4} - \frac{\ln(2)^3}{12}\right)\right],$$

with R_{12} and R_{23} the resistances measured for applied I_{12} and I_{23}, respectively. Typical apply currents were at the order of tens of μA, but the applied current was ranging from 10^{-2}μA to 8mA in the Dynacool system. F=1 indicates a similar resistance for both edges of the sample, hence a perfect homogeneity of the sample, with symmetrical and equally spaced contacts. **Fig. III-10** presents two examples of measurements, for which the level of homogeneity is not the same. The upcoming resistivity measurements, performed on optimized samples, will have a behaviour similar to **Fig. III-10(a)**.

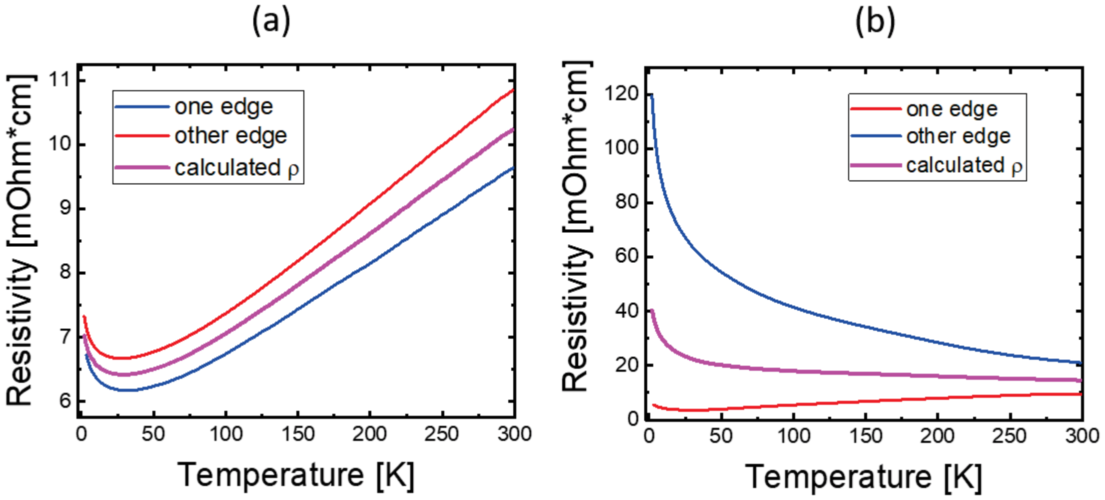

Figure III-10 Resistivity measurements for two $NdNiO_2$ samples. Measurement (a) shows a better homogeneity than the (b) one. The F value was found to be superior to 0.998 for all temperatures for the (a) measurement and was between 0.949 (at 300K) and 0.647 (2K) for the (b) measurements. The resistivity of one edge is obtained by calculating ρ with only R_{12} or R_{23} and using F=1.

The sign of the slope of the resistivity versus temperature function indicates if the material has an insulating behaviour (negative slope) or a metallic behaviour (positive slope). Via resistivity measurements we could study the metal-to-insulator transition (MIT) observed in the perovskite nickelates, and also the superconducting transition in the infinite-layer nickelates.

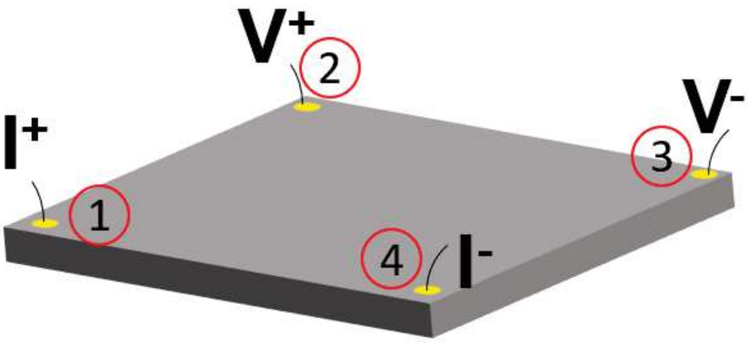

Figure III-11 Scheme of the Van der Pauw geometry used in this thesis for resistivity measurements. Here the current is sent on one edge of the sample, and the voltage sensed on the opposite one.

b. Hall effect measurements

Hall effect measurements allow to determine the concentration of charge carriers, their nature, and their mobility. It can thus provide important insight on the transport properties of strongly correlated materials. Standard Hall effect measurements are performed with a magnetic field applied perpendicularly to the sample surface. In this configuration the charge carriers are deflected by the Lorentz force. This results in the creation of an electric field perpendicular to both the current density and the applied magnetic field, which in turn applies an electric force to the charge carriers. The carriers deflection will stop when the Lorentz and electric forces to which they are subjected perfectly oppose to each other. The Hall voltage experimentally measured allows to determine the strength of the electric field. With the Hall effect measurements geometry shown in **Fig. III-12**, and a square sample, the Hall voltage will be given by [189]:

$$V_H = \frac{R_H B I}{t},$$

where R_H is the Hall coefficient of the material, B is the applied magnetic field, I is the current and t is the thickness of the sample. The Hall coefficient value represents the number of charge carriers, and its sign their nature, described by this formula:

$$R_H = \frac{r}{q(p-n)},$$

with r the Hall scattering factor, q the fundamental electric charge, p and n the positive and negative density of charge carriers in the material, respectively. The Hall scattering factor is usually set to 1 in experimental work [190].

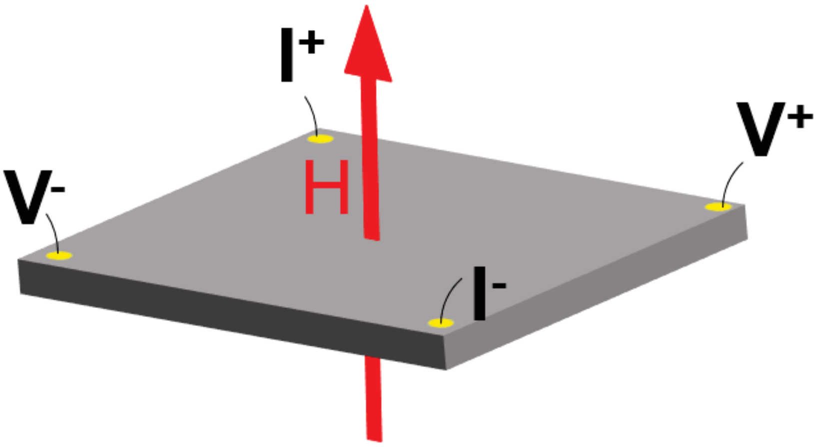

Figure III-12 Scheme of the Van der Pauw geometry used in this thesis for the measurement of the Hall effect. The Hall voltage is measured perpendicularly to the applied current.

c. Magnetoresistance and Angular-Magnetoresistance measurements

Measurements of the resistivity as a function of an applied magnetic field have also been performed in a Van der Pauw geometry with 4-points contact on square samples, as shown in **Fig. III-11**. The value of the magnetoresistance (MR) is given by [140]:

$$MR = \frac{\rho(H)-\rho(0)}{\rho(0)},$$

with $\rho(H)$ the resistivity of the sample for a given magnetic field H, and $\rho(0)$ the resistivity of the sample with no magnetic field applied. This measurement leads to a positive MR in a normal metal, which has a higher resistivity under a magnetic field. For oxides, a negative MR is commonly observed, and has often been attributed to weak localization [191,192].

Angle dependent anisotropic-magnetoresistance (AMR) measurements have been performed with a rotation of the magnetic field in two configurations: in-plane (left) and out-of-plane (right) as described in **Fig. III-13**. The value of the out-of-plane AMR is given by [140]:

$$AMR = \frac{\rho(\theta,T,H)-\rho(0,T,H)}{\rho(0,T,H)},$$

with ρ(θ,T,H) the resistivity of the sample at a given temperature T, under a magnetic field H making an angle θ with the current. A zero value for θ corresponds to the magnetic field *H* being parallel to the current. The in-plane AMR is given by the same formula, but by taking the value of the φ angle instead of the θ one.

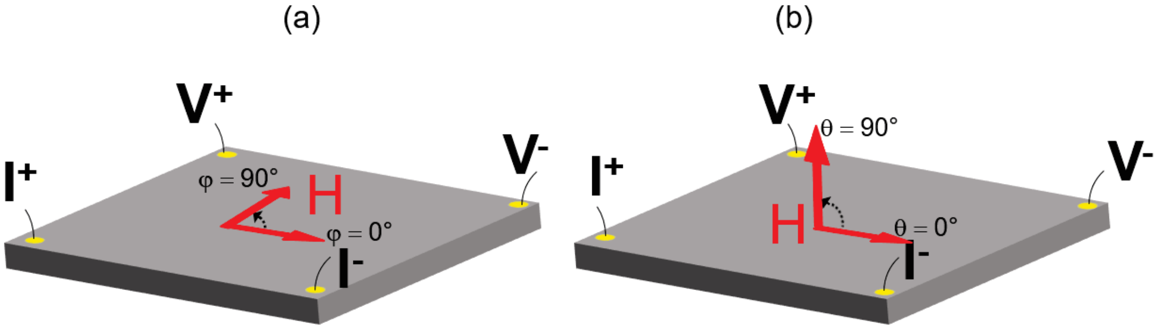

Figure III-13 Transport configuration for (a) in-plane (IP) and (b) out-of-plane (OOP) AMR measurements.

6. Synchrotron radiation-based measurements

a. X-ray Absorption Spectroscopy

X-ray Absorption Spectroscopy (XAS) is an element-sensitive technique providing information on the electronic structure of materials. It necessitates powerful light sources and is usually implemented at synchrotron radiation facilities. X-rays excite the material's core electrons into an empty state above the Fermi level. When a sharp rise of the absorption is observed, it indicates that the X-ray beam has reached an energy equivalent to the binding energy of a core-level electron of one of the elements present in the material. The resulting peak is defined as the absorption edge of the element, and its denomination is K-edge for the excitation of a 1s core-electron, $L_{2,3}$-edge for the excitation of a 2p core-electron and $M_{4,5}$-edge for that of a 3d core-electron. In the case of transition metal oxides, as in this thesis, one mostly focuses on the L-edge. The energy of the absorption edge depends on the environment of the element, and on its electronic structure. The higher the oxidation degree of the cation, the higher the energy of its absorption edge [193]. The XAS technique provides information on the unoccupied states of the investigated element which will be populated after the X-ray absorption. At the $L_{2,3}$-edges of a transition metal, there will be transition of a 2p core-electron into the 3d or 4s empty states: 2p→3d,4s. For the oxygen K-edge, mainly used to study the oxygen absorption in transition metal oxides, the 1s core-electrons will be promoted into p-like empty states: 1s→2p. As aforementioned, the local environment influences a lot the absorption edge. The crystal-field will, for example, have an important incidence on the energy and/or shape of the absorption peak for a transition metal cation [184].

The energy used to study the perovskite rare-earth nickelate elements with XAS ranges from about 520 eV for the oxygen K-edge, to 850 eV for Ni $L_{2,3}$-edges, and 980 eV for the Nd $M_{4,5}$-edges. The data acquisition consists in detecting electrons, for the total electron yield (TEY) mode, or photons, for the fluorescence yield (FY) mode. Those two different measurements rely on two different possibilities for the de-excitation towards the ground state. The TEY mode relies on the emission of an Auger electron [194] and measure via an electrometer the charge current sustained to replace the amount of electron that have left the sample. This process is highly favourable for soft X-rays radiations, with a probability of 99%. In TEY mode the sample has to be properly connected to the ground. In our case we mostly used silver paste. The TEY mode is highly thickness-dependent, since the electrons created deep in the sample will lose too much energy to be able to be extracted [195]. This sample depth limit is a few nanometres. On the contrary, the FY mode is more bulk sensitive, since there, a photodiode measures the photons generated by the creation-annihilation for the core-level state , for which the sampling depth can be up to several hundreds of nanometers [196]. However, the precision in the FY mode in the soft X-rays is not as good as in the TEY one, because the Auger effect is then the main phenomenon. On the other hand, self-absorption effects can occur when an emitted photon is re-absorbed before it can exit the sample. In a sense, the self-absorption effect mitigates the saturation effect by preventing it to be measured; but both self-absorption and saturation effects, are often used interchangeably [197]. In any case, their presence is the cause of a signal non-proportional to the XAS characteristic. It results in a modified shape of the XAS spectra, which is then very complicated to interpret.

b. X-ray linear dichroism

X-ray linear dichroism (XLD) makes use of the XAS elemental-sensitivity with two different linear polarizations of the beam, vertical (LV) or horizontal (LH). The measurement can be performed with various incidence angles θ, from normal to grazing incidence **Fig. III-14**. The polarized light can thus provide information about differently spatially occupied orbitals, usually the out-of-plane or the in-plane ones. In **Fig. III-14** we can observe that when the measurement is performed in grazing incidence, the horizontal polarization (LH) will mostly probe the out-of-plane orbitals. In the case of transition metal perovskites with partially occupied e_g orbitals and grown onto (001) orientated substrates, those orbitals are the $3d_{z^2}$. The vertical polarization (LV) will mainly be sensitive to the in-plane orbitals, i.e. the $3d_{x^2-y^2}$, as shown on **Fig. III-14**. The difference between the signals obtained for the two polarizations results in the XLD spectrum, which can then be related to the relative occupation of the 3d orbitals. This technique has been used a lot for perovskite nickelates to study the modification of their orbital occupation in heterostructures. As aforementioned in Chapter II, the goal of such orbital polarization in nickelates was to achieve a half-filling of the $3d_{x^2-y^2}$ band, in analogy to cuprates [63,71]. In that sense, the XLD spectra can provide a direct measurement of the hole ratio in the e_g orbitals through the following relationship [198,199]:

$$r = \frac{h_{3z^2-r^2}}{h_{x^2-y^2}} = \frac{3I_{LH}}{4I_{LV} - I_{LH}} \, ,$$

with I_{LH} and I_{LV} the intensities of, respectively, the horizontally and vertically polarized light. For a non-degenerate system where the z^2 and x^2-y^2 orbitals are separated in energy and where the z^2 is principally occupied, *r* ranges between 0 and 1. In such a case, it leaves some holes in the x^2-y^2 orbital to mimic the cuprate hole doped $3d_{x^2-y^2}$ electronic structure. When r is close to 0, it means that the atom (Ni our case) has a small degree of unoccupied states in the z^2 orbital. A value of r=1 indicates that the e_g orbitals are fully degenerate. Tuning the orbital occupation eventually failed to reach a superconductive state in nickelate. More than tuning the orbital occupation, it has been demonstrated that a modification of the nickelate structure from the NiO_6 octahedra to the NiO_2 square planar symmetry similar as the CuO_2 in cuprates was mandatory. The experimental evidence from 2019 by Li et al. [105] also highlights the necessity of doping this infinite-layer phase structure. Measuring the orbital occupation of this new structure along with the doping range will undoubtedly provide useful knowledge, especially when it will be compared to isostructural high-T_C cuprates.

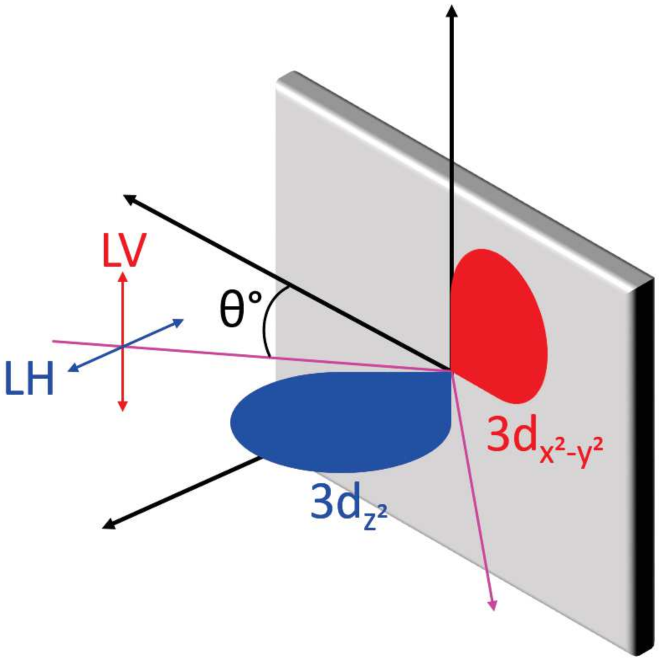

Figure III-14 Geometry of the XLD measurements, with an incidence angle θ. For grazing incidences, the horizontally polarized beam, LH, mainly probes the out-of-plane orbitals, here the $3d_{z^2}$. Whatever the incidence, the vertically polarized beam, LV, probes the in-plane orbitals, here the $3d_{x^2-y^2}$.

c. X-ray magnetic circular dichroism

X-ray magnetic circular dichroism (XMCD) uses the difference of XAS spectra acquired with left (CL) and right (CR) circularly polarized light to obtain magnetic information on the material. The measurement can be performed in normal or grazing incidence, with the same geometry as for the XLD measurements shown in **Fig. III-14**. It is conventionally adopted that CR carries an angular momentum with helicity vector parallel, and CL antiparallel, to the propagation direction. The photon carries an angular momentum which is converted into spins via spin-orbit-coupling. **Fig. III-15** presents schematically the XMCD process, where it is observed that the acquired spin of the 2p band sign depends on the circular polarization of the incident beam. Also, according to the selection rules, spin-up photoelectrons from the 2p states can only be excited into spin-up 3d states, and inversely for spin-down. The 2p core levels have two opposite spin-orbit coupling $^2P_{1/2}$ and $^2P_{3/2}$, hence the spin polarization will also be opposite at the L_3 and L_2, edges, respectively. A difference in spin or orbital momentum in the unoccupied d-states will be demonstrated by an XMCD signal.

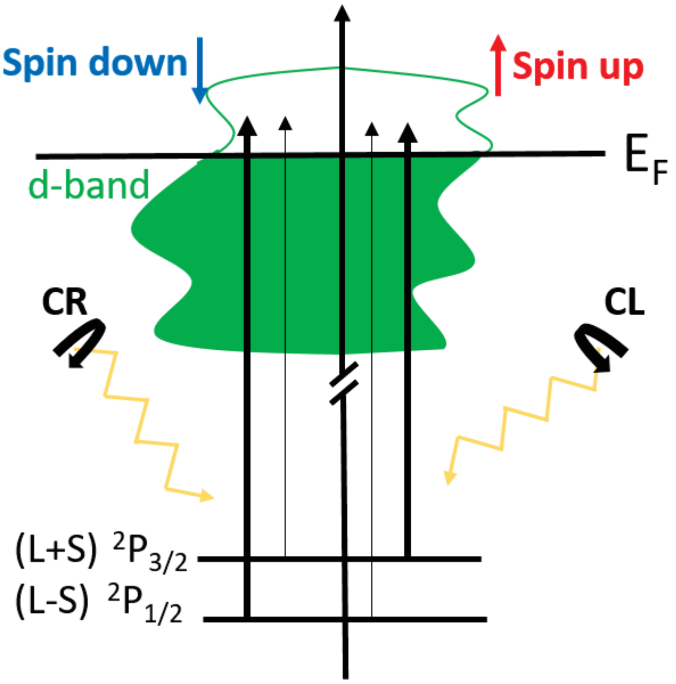

Figure III-15 Scheme of the XMCD principle at $L_{2,3}$-edges. The 3d band is here split into spin-up and spin-down sub-bands according to the Stoner model [200]*. The absorption of CL photons mainly excites spin-up ($^2P_{3/2}$) electrons and on the opposite, the CR mainly excites the spin-down ($^2P_{1/2}$).*

L and S respectively define the spin and angular moments of the core electrons. They allow to denote the electronic configuration of an atom or ion with the spectroscopic term ^{2S+1}L. The degeneracy of an electronic configuration is given by (2L+1).(2S+1) and by taking in count the spin-orbit coupling, the partially lifted degeneracy gives 2J+1 energy levels with $\vec{J}=\vec{L}+\vec{S}$ being the total orbital moment. And the total orbital moment is characterized by $|L-S|\leq J \leq |L+S|$ and so the final term describing the electronic configuration is denoted $^{2S+1}L_J$ with 2S+1 the spin multiplicity and J the orbital moment. In **Fig. III-15**, the 2p state lost an electron as follows: $2p^6d^n \rightarrow 2p^5d^{n+1}$. The core level is therefore described as a $2p^5$ configuration, with L = 1 (hence the letter P), S= ½ and so J= 1/2 and 3/2. The final terms of this electronic configuration are thus $^2P_{1/2}$ and $^2P_{3/2}$.

The XAS spectrum shown in **Fig. III-16(a)** is the sum of the intensities of the CL and CR spectra and **Fig. III-16(b)** represents the XMCD spectrum from which the magnetic spin μ_S and orbital moment μ_L can be estimated using the following sum rules [201]:

$$\mu_S = -\frac{(6p-4q)(10-n)}{r}$$

$$\mu_L = -\frac{4q(10-n)}{3r}$$

with *r* the integral of the sum of the right and left polarizations spectra, *p* and *q* the integrals of the difference between the two polarizations spectra over the L_3 edge, and over the L_3 and L_2 edges, respectively, and *n* the number of electrons in the valence state.

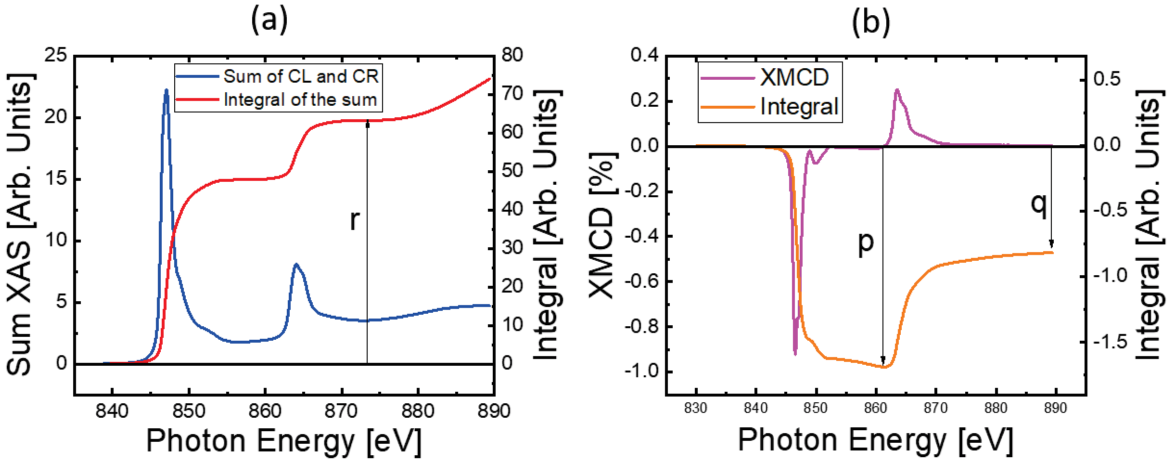

Figure III-16 (a) Sum (XAS) and (b) difference (XMCD) of the right and left polarization spectra at the Ni $L_{2,3}$ edge. The q, p and r features are the values used to calculate the spin and orbital moments with the sum rules.

d. Resonant Elastic X-ray Scattering

X-ray diffraction (XRD) is classically used to determine the structure in solid state materials, i.e. the ordering of the atoms. However, other orderings can be of interest in solid state matter, such as orbital, charge or spin orderings. Those orderings derive mostly from the spatial location of the electrons nearby the Fermi level. When XRD is combined to the previously introduced XAS, a measurement sensitive to valence electrons, it results in the resonant elastic X-ray scattering (REXS) technique. It is commonly used to follow, as a function of temperature, the charge, spin and orbital orderings of materials [131,202]. The resonant process resulting from the use of photon energies close to absorption edges of the elements strongly enhances the scattering cross-section [203]. For example, the cross-section in magnetic scattering can be enhanced by eight orders of magnitude [204]. In REXS measurements, the core electron transferred to the unoccupied states which has a well-defined spin is used as a very sensitive probe. Indeed, in the dipole approximation, the spin does not flip throughout this process, allowing a conservation of the spin which is very sensitive to the atom's magnetic moments since the magnetic moment results from the outer electrons levels [205]. It is when the unoccupied reached state is a 3d, 4f or 5f, for, respectively, transition-metals, lanthanides or actinides, that REXS is the best suited, because those states can be reached by the strong dipole-allowed 2p→3d, 3d→4f, or 4d→5f transitions. Moreover, the characteristic lengths in spin, charge and orbitals orderings is of the order of the nanometre, which is the order of magnitude of the wavelength of the soft X-rays (0.6-6 nm) [131].

In the case of the perovskite nickelates thin films, this technique has been used to determine the Néel transition temperature [206]. Indeed, the available quantity of matter is too small for the other methods usually employed to characterize the magnetic order, such as the neutron diffraction technique. The antiferromagnetic order in perovskite nickelates is oriented along the $[111]_{pc}$ direction of the lattice with a periodicity of four nickel layers [5], that is, characterized by the $[¼\ ¼\ ¼]_{pc}$ vector. The corresponding Bragg peak is strongly resonant at Ni $L_{2,3}$-edges i.e. when the photon energy is around 850 eV. In this thesis, REXS measurements have been performed on the I10 beamline of the Diamond Light Sources in Oxfordshire, England. The beamline and the dedicated measurements will be presented in the dedicated section in Chapter VI.

e. Resonant inelastic X-ray scattering

Resonant inelastic X-ray scattering (RIXS) associates inelastic X-ray scattering with X-ray absorption and emission. This measurement is often described as a photon-in photon-out measurement as shown in **Fig. III-17(a),(b)**, where the energy, momentum and polarization changes of the scattered photon can be measured.

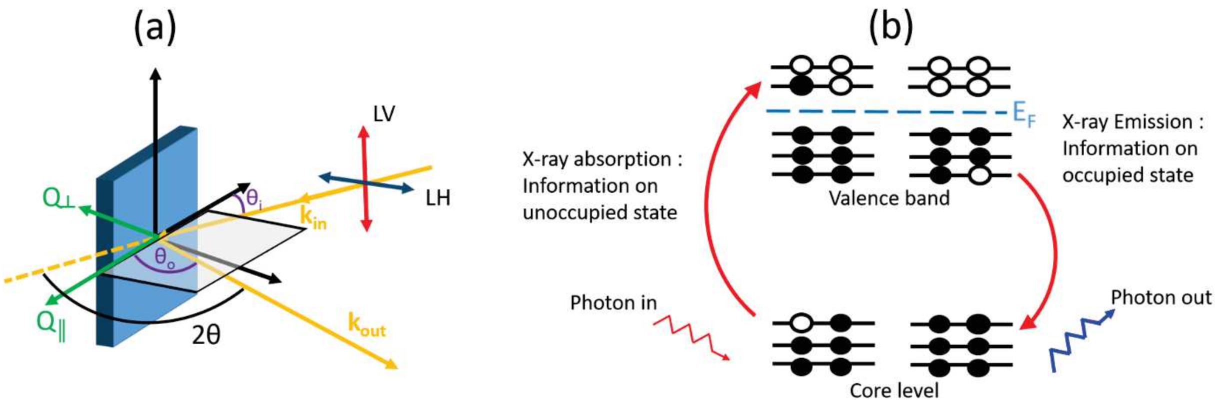

Figure III-17 (a) Geometry of a RIXS measurement (adapted from [207]*) (b) Scheme of the absorption and emission processes in RIXS (adapted from* [208]*), showing the difference in energy between the incident and emitted photons*

This modification between photons -in and -out is due to the transfer of energy, momentum and polarization to intrinsic excitations of the studied material, providing information on the elementary excitations as shown in **Fig. III-18**. The different elementary excitations are defined by a specific range of energy, which, thanks to the recent improvements in RIXS resolution energy, can be discriminated. As an example, our RIXS measurements in Chapter V have been performed with an energy resolution of ≈42 eV, allowing to discriminate a magnon from a phonon. Phonons are the quantized lattice vibration modes of a solid and were only investigated recently at the Cu-L edge thanks to the aforementioned RIXS resolution [209]. This also holds true for the magnetic excitation [210], which are the fingerprint of the short-range magnetic order in a material. The d-d excitations that arise because of the crystal-field splitting of the d levels are well-studied at L and M edges since longer time for different materials such as cuprates [211] or 2DEG [212], for examples. The charge transfer range is dominated by two processes in TMO. The first one is the energy of a charge hopping from a ligand to the metal site, the charge-transfer energy Δ. The second is the Coulomb repulsion U associated to moving one d electron to another metal site. Those two energies have been used to classify materials in the ZSA scheme, with the charge-transfer type for $U>\Delta$ and the Mott-Hubbard type for $U<\Delta$ [20].

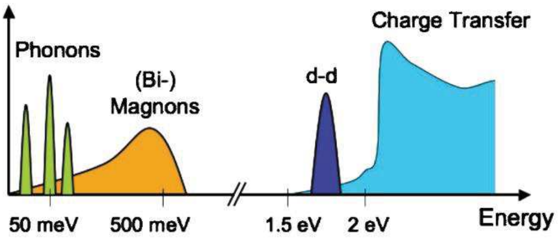

Figure III-18 Different elementary excitations in condensed matter systems and their approximate energy scales in strongly correlated electron materials such as transition-metal oxides. (Taken from [208]*)*

The progress in the RIXS resolution, from around 1.5 eV to <50 meV, have shown the extremely high potential of the method to study the low-energy excitations in TMO. Compared to other techniques used to study elementary excitations, such as neutron and electron spectroscopies, RIXS possesses several advantages. Surely the ones inherent to XAS, such as the element and orbital selectivity, strongly enhancing the inelastic cross-section [208]. This offers a unique way to probe charge, magnetic, and orbital degrees of freedom as observed on selective atomic sites in crystal lattices [208]. The small amount of sample necessary to perform a measurement is certainly another crucial advantage, and it is ideal for thin film studies. This is explained by the relatively strong interaction between photons and matter, when compared to neutron-matter interaction for example. RIXS can also make use of the polarization of the photons, by analysing that of the incident and scattered ones, and then extracting information about the nature and symmetry of the excitation through the use of selection rules [50,213]. A change of polarization of a photon is indeed always related to an angular momentum change. The conservation of the angular momentum significates that any angular momentum lost by the scattered photons is transferred to the elementary excitations in the material. In this work, we have performed polarization-resolved RIXS measurements on the ID32 beamline of the ESRF, Grenoble, France, which in fact is the only beamline to provide the polarization analysis of the scattered photon in a RIXS measurement. Those measurements and the introduction of the polarimeter setup will be presented in the Chapter V.

IV. Thin film optimisation: from the perovskite to the infinite-layer phase

The observation of superconductivity in infinite-layer $Nd_{0.8}Sr_{0.2}NiO_2$ thin films [105] has finally put an end to more than 20-years of sustained experimental efforts devoted at mimicking the hallmarks of cuprates superconductivity. However, so far, the superconducting state in infinite-layer nickelates could be independently reproduced only by few groups [105–108], and despite the great potentialities, this field of research risks to hardly broaden due to evident experimental difficulties. Indeed, from the preparation standpoint the two-step synthesis process [101] is very challenging. The given recipe involves (I) the optimization of the doped perovskite phase, and subsequently, (II) an oxygen de-intercalation process which takes place by fine-tuning the parameters controlling the CaH_2-induced topotactic reduction. In this Chapter, the levers we use to increase the quality of the perovskite and infinite-layer phase will be described for the different doping used in this thesis: 0%, 5% and 20% of Sr doping, with and without a $SrTiO_3$ capping-layer.

1. Growth of Sr-doped perovskite nickelate thin films

1. Substrate preparation

$SrTiO_3$ has a cubic perovskite unit cell with a lattice parameter of 0.3905 nm, and can be considered as a stack of TiO_2 and SrO planes. The one-side polished substrates have been bought in 5x5 mm² size from CODEX-International. When bought, the substrates possess both SrO and TiO_2 chemical terminations. In order to achieve a coherent and epitaxial growth of oxides, it is preferential to possess single-terminated and smooth surfaces. The Kawasaki [214] procedure which allows to obtain a TiO_2-terminated was thus applied to the STO substrates. It consists in a chemically selective etching of the SrO terminations followed by an annealing procedure which results in a step-terraced structure of the surface of the STO substrates. The substrates are ultrasonicated for 5 minutes in 3 consecutive solvents, acetone, ethanol and isopropanol, with a lens paper cleaning step after each solvent. They are then placed in deionized water for 2 minutes before being etched for 18 seconds in a 50 mL aqueous solution containing 1.5 mL of NH_4F (10.6 mol.L^{-1}) and 0.5 mL of HF (20 mol.L^{-1}). The NH_4F solution has been prepared with 39.2g of solid NH_4F for 100mL of H_2O, and the HF solution is the 40%-mass commercial HF solution. The etching is stopped by immersing the substrates into deionized water. The substrates are then dried out with inert N_2 gas. The annealing process is performed at

950°C, in air, for 2 hours. The resulting surface is shown in **Fig. IV-1(a)** with very well defined steps which exhibit, after a flattening process of the AFM images, a single-unit-cell height **Fig. IV-1(b)**.

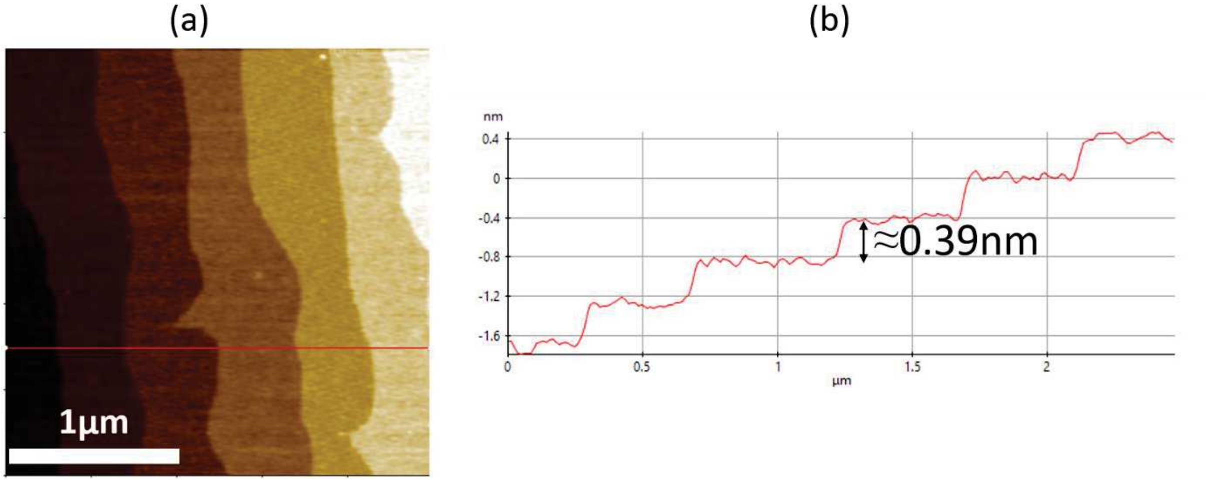

Figure IV-1 (a) 2.5x2.5µm AFM image of a STO(001)$_{pc}$ substrate HF-treated (after flattening of the image) (b) profile line along the red-line of (a), exhibiting one-unit-cell terraces.

2. The challenges of the growth of the Sr-doped nickelate perovskite

We have grown our Sr-doped perovskite nickelates thin films by pulsed laser deposition (PLD) assisted by reflection high-energy electron diffraction (RHEED) to monitor the growth *in situ*. Undoped $NdNiO_3$ [hereafter indicated as $NSNO_3$(0)] thin films were obtained by ablating a $NdNiO_3$ single-phase ceramic target (Toshima Manufacturing Co.), while Sr-doped thin films were obtained by ablating ceramic targets composed of a mixture of NiO and Sr-doped Nd_2NiO_4 phases (Toshima Manufacturing Co.), with two compositions in Sr, $Nd_{0.95}Sr_{0.05}NiO_3$ and $Nd_{0.8}Sr_{0.2}NiO_3$ further indicated as $NSNO_3$(5) and $NSNO_3$(20). $5x10^{-8}$ mbar was the usual base pressure of the PLD chamber prior deposition. All growth experiments were performed under an imposed oxygen partial pressure $P(O_2)$.

Bulk $NSNO_3$(0) exhibits an orthorhombic crystal structure with a lattice parameter of *ca*. 0.381 nm in pseudo-cubic notation. Thus, the large tensile strain experienced onto STO single crystals (a=0.390 nm) when grown as thin film produces a contraction of the out-of-plane lattice parameter (c-axis), whose nominal value is expected to be equal to 0.375 nm ($2\theta \sim 48.5°$), accounting for a Poisson ratio of 0.3 [56]. This c-axis value can be used as a proxy to highlight possible oxygen deficiencies which not only provoke a lattice expansion, as demonstrated in similar PLD-grown $NSNO_3$(0) thin films [215], but also modifies the unstable Ni^{3+} valence landscape, by creating defect-zones where the unitary Nd/Ni stoichiometry level is not conserved. This direct link between c-axis elongation and off-stoichiometry issues may become more complicated to make in the case of Sr-doping for which an elongation of the c-axis is, indeed, expected as a result of the chemical substitution with a cation of a larger ionic radius. As a result, a study of the influence of the oxygen partial pressure combined to the respective transport behaviour is a necessary step to ascertain that a 'pure phase' of Sr-doped perovskite nickelate thin films can be, indeed, stabilized. The out-of-plane cell parameter deduced from the $\theta/2\theta$ peaks, combined to the transport properties gives important information about Nd/Ni off-stoichiometries and/or oxygen vacancies [216]. Garcia *et al.* have already showed that hole-doping bulk $NdNiO_3$ by chemical substitution results in a gradual closing up of the charge-transfer gap. As a result, the usually observed metal-to-insulator transition (MIT) for undoped samples is heavily modified, and at already 5% at. Sr doping the samples exhibit an overall metallic behaviour [54].

3. Influence of the oxygen partial pressure

Here, the optimization of the oxygen partial pressure has been performed on $NSNO_3$(5) sample, which could seem strange as usually this kind of optimization are performed with the undoped parent compound. This is explained by the context of the discovery of the superconductivity in infinite-layer nickelate. When Li et al. [105] paper has been published in August 2019, they showed the superconductivity in $NSNO_2$(20) and its absence in undoped infinite-layer. With this result, we firstly think that a smaller doping would be sufficient to reach the superconductive state, hence the oxygen partial pressure optimization of the $NSNO_3$(5) sample. Of course, the superconducting dome prove that we were wrong in our first expectations.

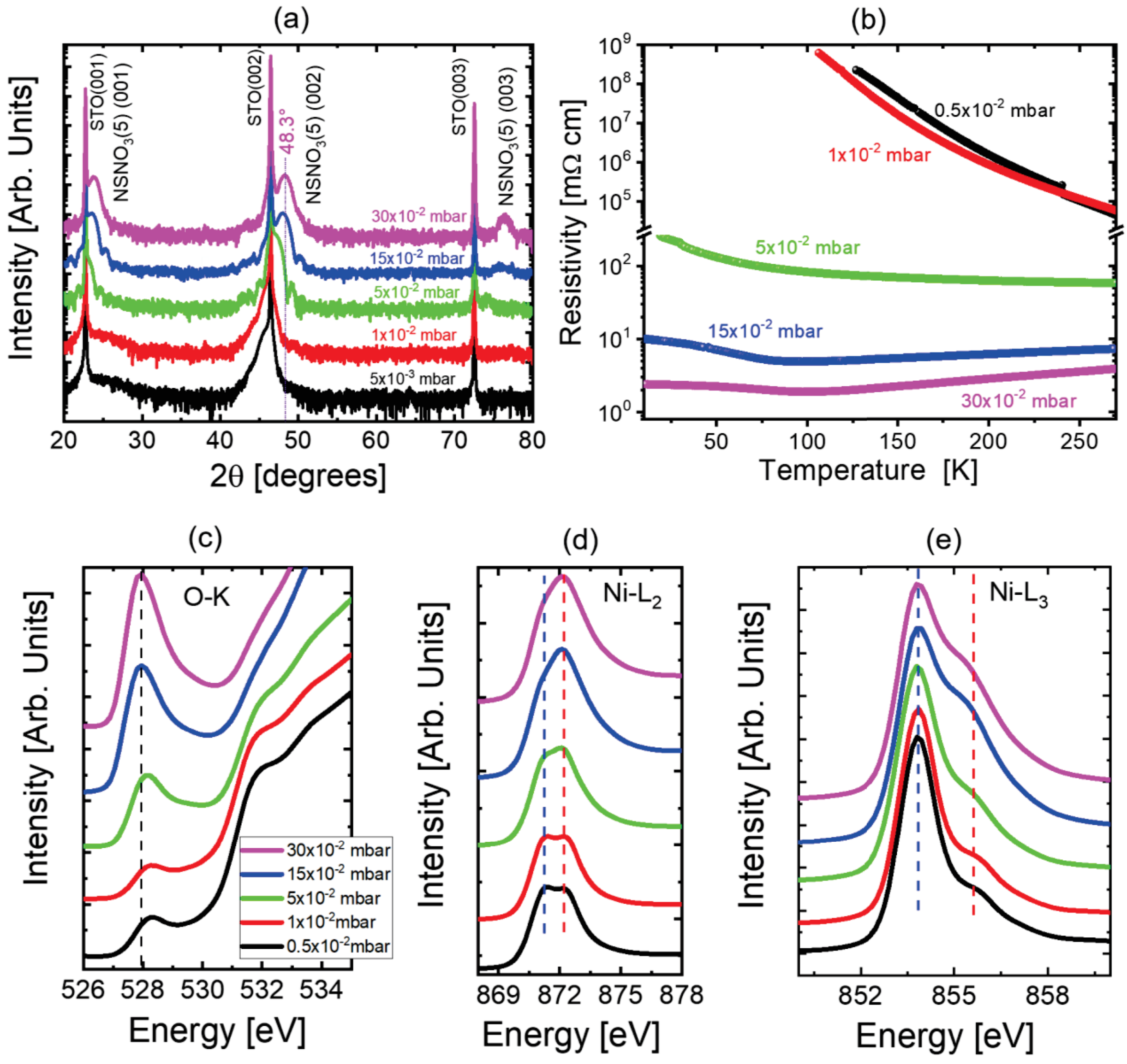

Figure IV-2 Characterization of NSNO$_3$(5) thin films grown at different P(O$_2$) : (a) XRD (b) Resistivity. X-ray absorption of (c) O-K edge pre-peak with the dashed line representing the pre-peak corresponding to the Ni-O hybridization (d) Ni-L$_2$ edge (e) Ni-L$_3$ edge. At the Ni-L edge, the blue (red) dashed line represent the peak which the higher contribution of Ni^{2+} (Ni^{3+})

Fig. IV-2(a) shows XRD patterns of uncapped NSNO$_3$(5) thin films grown at different P(O$_2$) values, with a laser fluence of 3.8 J/cm^2. The number of laser pulses was adjusted to account for the P(O$_2$)-modified growth conditions and to guarantee the same thickness value of ca. 10 nm for each sample. For the lowest value of 5x10^{-3} mbar (black curve), the only visible shoulder on the left of the STO 002 reflection, points at a not properly crystallized sample. Due to the very low oxidizing conditions, this shoulder can be ascribed to Ni^{2+}-based phases, such as NiO and/or Sr-doped Nd$_2$NiO$_{4-\delta}$ [217]. By increasing P(O$_2$) for consecutive growth experiments this peak gradually shifts towards higher 2θ values until it reaches the 48.3° position for 0.3 mbar (magenta curve). At this P(O$_2$) value we can also easily observe a relatively intense NSNO$_3$(5) 003 reflection which, according to our experience, highlights that the perovskite nickelate phase is stabilized. Transport measurements are then necessary to demonstrate that a metallic state could be stabilized as indeed expected for a 5% at. Sr doping. **Fig. IV-2(b)** shows the temperature dependence of the resistivity for the entire uncapped NSNO$_3$(5) sample series. As expected, we observed a very different behaviour for the various P(O$_2$) values. Thin films grown at a very low oxygen partial pressure exhibit a fully insulating behaviour typical of Ni^{2+}-based compounds, such as RP phases [218] or NiO [219]. As $P(O_2)$ reaches values for which a degree of oxidation close to Ni^{3+} is guaranteed, we observe a metallic behaviour at room temperature and an upturn below 100 K, less and less pronounced when keeping increasing the oxygen partial pressure. Usually the upturn in resistivity is explained as the result of charge localization triggered in this particular case by the presence of extended defects within the thin films. At 0.3 mbar the sample is characterized by an overall low resistivity (lower than for all the other pressures), but the small upturn which is still present points at a still non-completely properly optimized growth. Higher oxygen partial pressure has been tried (until 0.5mbar), but did not lead to a shift to the right of the 002 Bragg peak of $NSNO_3(5)$ as observed until now when we increase the pressure. We speculate that in too high $P(O_2)$ conditions, the plasma plume shape is altered in such a way that the elements are not reaching the substrate as they used to. We think of this hypothesis because when we observed the plasma plume during the growth, the latter was extremely packed, i.e. kinetics of the elements and their stoichiometry will forcefully be modified compared to lower pressure. Maybe by changing the target-substrate distance, we could have overcome this issue, but modifying the geometry of the PLD chamber will come with its bunch of optimization of the others parameters. Moreover, the 0.3 mbar that we decided was the high-limit of use for the RHEED to follow correctly the growth. Which was convenient to obtain feedback on our thin films deposition conditions.

The X-ray absorption spectroscopy (XAS) measurements shown in **Fig. IV-2(c)-(e)** have been performed at the Diamond synchrotron at Oxfordshire, England, on the I10 beamline. All spectra were acquired at 300 K in the TEY mode and are shown here after being normalized in area in order to be able to compare their peak intensities. XAS at the O-K edge confirms that the films are closer to the desired perovskite phase for the highest $P(O_2)$. The pre-peak at ≈528 eV in **Fig. IV-2(c)** is indeed the signature of O-2p and Ni-3d orbitals hybridization [36]. The stronger this peak, the higher the quality of the perovskite phase. Its highest intensity is reached for the highest $P(O_2)$ value. XAS at the Ni $L_{2,3}$-edge also indicates that the highest quality for the perovskite phase is reached for the highest $P(O_2)$. Both L_2 and L_3 edges exhibit spectra which are all the closer to Ni^{3+} for higher $P(O_2)$ as shown in **Fig. IV-2(d)-(e)**. Lower $P(O_2)$ lead to spectra more similar to those observed for NiO [202], i.e. with a higher presence of Ni^{2+} cation compare to Ni^{3+} [220]. The blue and red dashed lines respectively represent the peak which have a stronger contribution for Ni^{2+} and Ni^{3+} in the **Fig. IV-2(d)-(e)**, where a higher intensity of the peak at the red dashed line energy is observed for higher $P(O_2)$. We can highlight that the intensity of the blue peak is higher than the red one at the Ni-L_3 edge on **Fig. IV-2(e)**, and Bisogni, V. et al. [34] shows that at 300K, a high-quality $NSNO_3(0)$ sample also has the peak at higher energy slightly smaller in intensity than the one at lower energy, as observed here. However, the difference in energy between both peaks is smaller in their case than ours, which can be explained by a higher proportion of oxygen vacancies in our samples, confirming us that the samples must still be better optimized.

4. Overcoming Ni/Nd off-stoichiometry issues

As mentioned in the literature, off-stoichiometry issues can be mitigated by considering within the growth parameters the combination of the target ablation history and laser fluence [61]. On this basis, we resorted to a performing our laser ablation without scanning the target (no-toggling condition), and increased the fluence value to 4.8 J/cm². This approach gave us the proper leverage over the Nd/Ni stoichiometry within the laser-induced plume. **Fig. IV-3(a)** shows the comparison between two XRD patterns acquired for uncapped $NSNO_3(5)$ samples of same thickness prepared in toggling and no-toggling conditions. With the no-toggling condition and at a higher fluence than the one used for $NSNO_3$(0), we could improve the quality of our Sr-doped thin films as indicated by a stronger intensity of the peaks which are now more separated from the STO ones. In parallel to this we could observe, for samples elaborated in no-toggling conditions, a decrease of the resistivity of the samples and the absence of any upturn as evidenced in the resistance data shown in **Fig. IV-3(b)**. The same results hold also for the improvement of the $NSNO_3$(20) samples as evidenced in **Fig. IV-4(a,b)**.

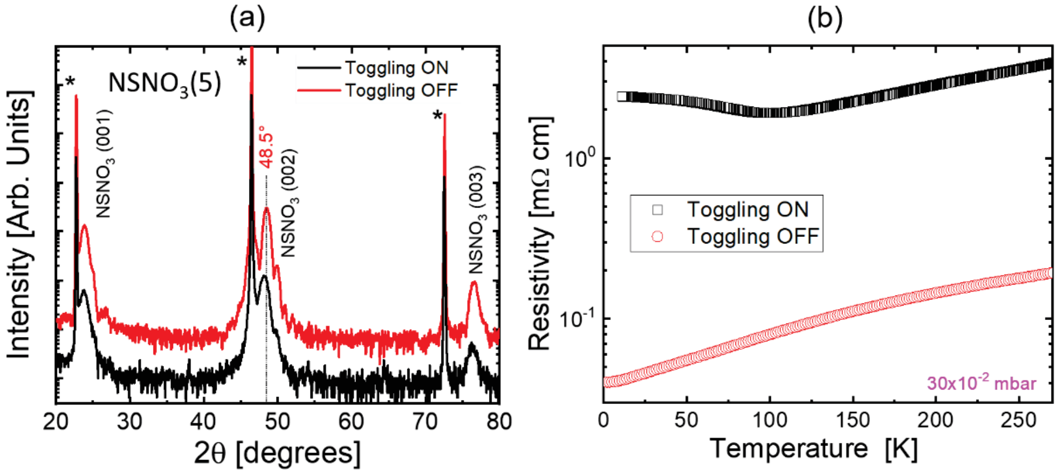

Figure IV-3 (a) XRD and (b) Resistivity measurements of $NSNO_3$(5) sample with toggling ON and OFF

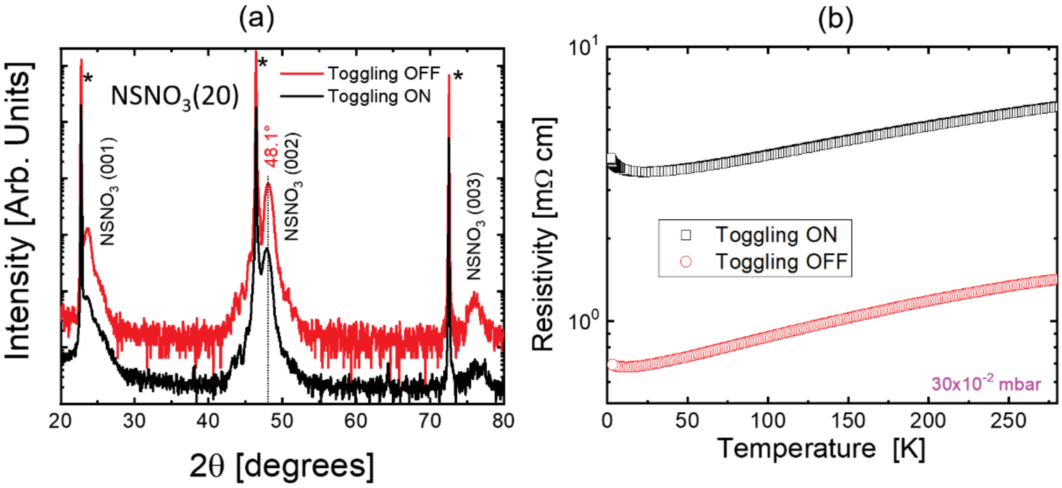

Figure IV-4 (a) XRD and (b) Resistivity measurements of $NSNO_3$(20) sample with toggling ON and OFF

It should be noted that for the $NSNO_3$(20) samples, although the overall resistance decreases when resorting to a no-toggling ablation condition, its value is nevertheless higher than the one measured for optimized $NSNO_3$(5) samples. This is most likely due to a larger presence of extended defects resulting from the increased Sr content. The (002) XRD peak position is found at a lower value (*ca.*

48.1° vs. 48.5°) with respect to the NSNO$_3$(5), due to an increased chemical substitution (lattice expansion).

5. Characterization of the thin films grown with optimal conditions

In this part we will present the structural, morphological and transport characterization of our samples grown with our optimized conditions, which are summarized in *Table1*. It is important to note that we specify the growth conditions of the STO as we have used it as a capping-layer of 3 u.c on our thin films. However, its presence does not affect the structural characterization as it will be shows below, and so the optimization of the thin films is identical, irrespective of the STO capping-layer. We decided to use a capping at first to enhance the quality of our thin films because of its role of as an epitaxial template. And we were surprised to discover that it also changes the elementary-excitations of the infinite-layer phase as it will be presented in the next Chapter. Therefore, we decided to continue to grow both capped and uncapped samples.

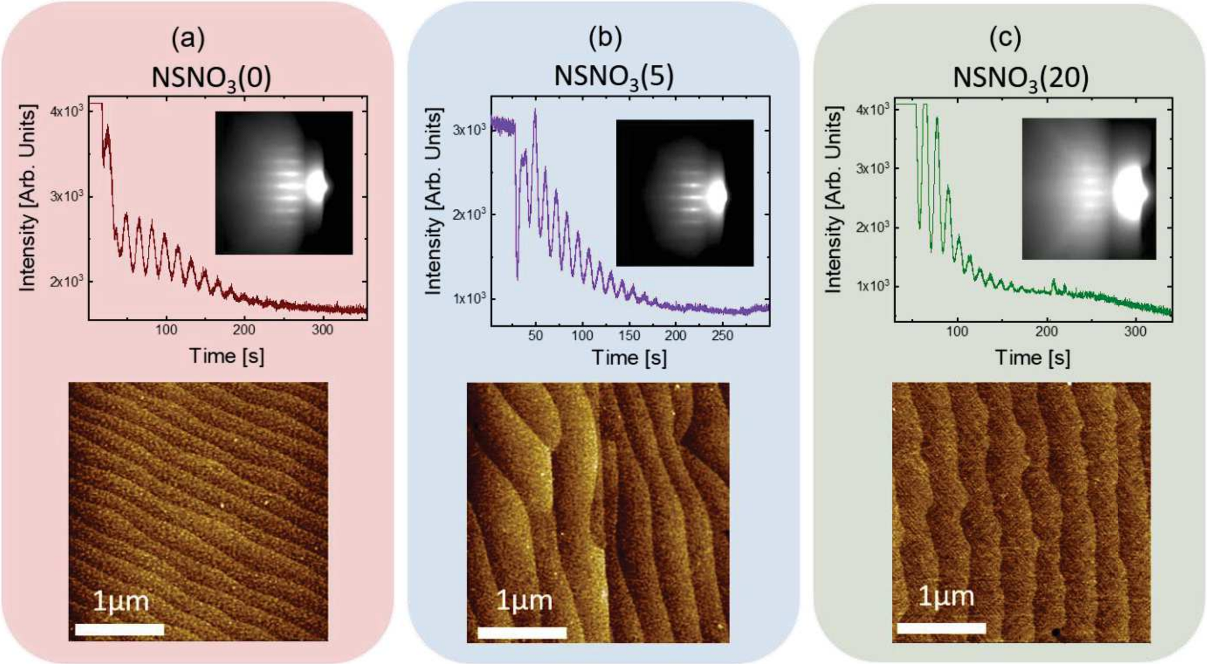

Figure IV-5 (Top part) Temporal evolution of the RHEED intensity during the growth with some initial oscillations, for (a) NSNO$_3$(0), (b) NSNO$_3$(5) and (c) NSNO$_3$(20) samples synthesized with optimized growth parameters. The insets show the final RHEED pattern exhibiting a small 3D modulation over a 2D one. (Bottom part) AFM images showing a perfect step-terraced image mimicking the STO surface profile for (a) NSNO$_3$(0), (b) NSNO$_3$(5) and (c) NSNO$_3$(20) samples. Calculated Root--Mean-Square (RMS) roughness are within the 0.2-0.3 nm range.

Fig. IV-5 summarizes the surface characterizations of our Sr-doped perovskite thin films obtained by monitoring the intensity of the RHEED oscillations and patterns during growth (upper part of **Fig. IV-5**), and by atomic force microscope (AFM) measurements after growth (lower part of **Fig. IV-5**). Very clear oscillations of the RHEED intensity could be observed for all the samples at the beginning of the growth (estimated growth rate ranging between 25-30 pulses/u.c. depending upon the Sr-content), and disappear progressively as the deposition proceeds. It is to note that more oscillations are observed for low-doping in **Fig. IV-5(a)-(b)** compare to higher doping in **Fig. IV-5(c)**. We think that the impossibility to observe the RHEED oscillations until the end of the deposition experiments (overall 700-1000 laser pulses), can be ascribed to the relatively large P(O_2) and small substrate-temperature values necessary to properly stabilize the Ni^{3+x} valence state during the growth. We believe that this particular combination of growth parameters may not be able to set the optimal kinetic energy of the ad-atoms necessary to properly diffuse and fully cover the substrate's terraces, which then experience an incremental increase of their roughness level. This is most likely the cause of the stabilization of detrimental secondary and/or Sr-segregated phases which manifest as a 2D-3D transition on the RHEED patterns. Which explained the lower number of oscillations for $NSNO_3$(20) as spurious phases have a higher growth probability due to the increasing aforementioned synthesis difficulty. According to our experience thicker Sr-doped thin films (>15 nm) exhibit, indeed, a fully 3D RHEED pattern, and the usual metallic behaviour is replaced by an insulating state. This imposes severe limitations to the maximum allowed thickness for this system. On this basis, we have calibrated our deposition time by monitoring the emergence of those 3D-like features on the RHEED patterns. We have observed that they keep a very high 2D character, only slightly modulated in intensity, up to thicknesses equal to *ca.* 10 nm, as it is possible to infer by a close inspection of the insets depicted in the top part of **Fig. 39**. Finally, our Sr-doped perovskite samples of 10 nm in thickness, show atomically flat AFM images with a step-and-terrace morphology typical of a coherent layer-by-layer growth.

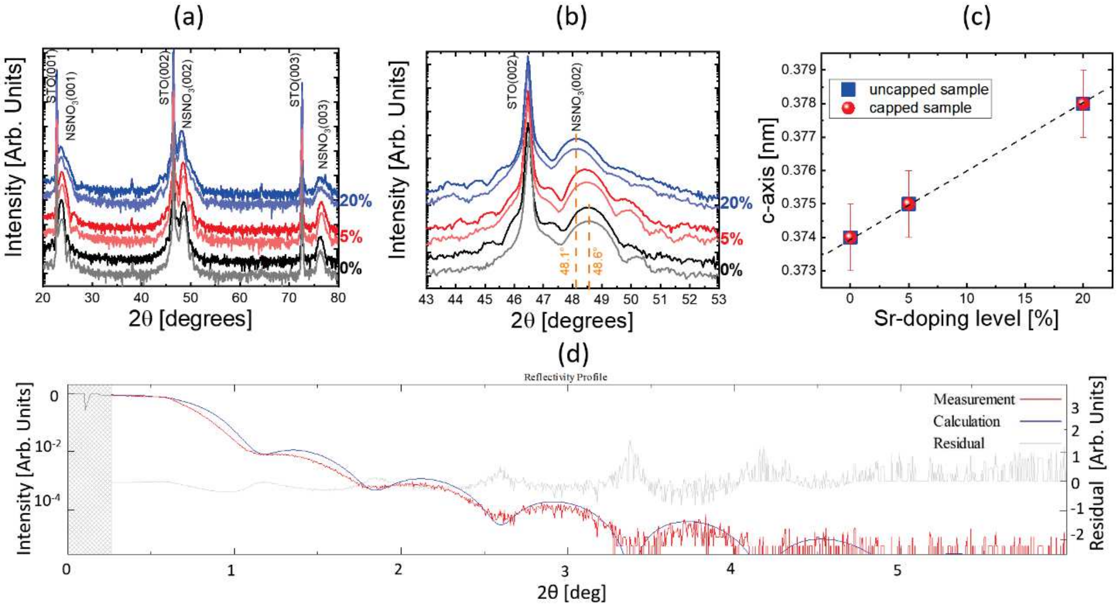

Figure IV-6 (a) XRD for the three different studied Sr-doping levels of the perovskite films, with and without an STO capping layer. Bright colours are for the capped samples, and light colours for the uncapped samples. (b) zoom on the (002) peak of the thin films (c) evolution of the x-axis parameter with the Sr-doping level for capped and uncapped perovskite thin films (d) Reflectivity measurement (red) and fitting (blue) (GlobalFit software) of a 10.8 nm $NSNO_3$(5) thin film.

We present in **Fig. IV-6(a)** the XRD patterns acquired for our $NSNO_3$(x) sample series (x = 0, 5 and 20 %) grown by using the optimized parameters as listed in Table 1, with (bright colours) and without (light colours) an STO capping layer. The three perovskite peaks, (001), (002), and (003), are present with a high-intensity, demonstrating a good crystallinity quality of the perovskite phase. The zoomed area taken around the $NSNO_3$(x) (002) peak position, and presented in **Fig. IV-6(b)**, beyond showing an increase of the out-of-plane lattice parameter as a function of the Sr-doping, demonstrates that the relatively thin capping layer of STO (3 u.c.), does not relevantly affect the XRD patterns from a macroscopic point of view. This information is displayed in **Fig. IV-6(c)** where we can infer that the increase of the Sr-content yields a linear increase of the c-axis parameters with the same values for capped and uncapped samples, within the experimental error. The thickness of the sample, which was calculated from growth rate extracted from the RHEED oscillations in a first time, is confirmed by reflectivity measurements, such as the one presented in **Fig. IV-6(d)**, with a thickness comprised between 10 and 11 nm for all nickelate perovskite thin films. The GlobalFit software from Rigaku has been used to fit the measured data (as described in the experimental techniques Chapter). The crystalline structure (of the substrate and the thin films), the density, the roughness and the thickness are parameters that can be modified to fit to the experimental curves. In our fittings, the density of the film material always had a value close to 8 g/cm^3, in accordance with the density of TMO perovskite, and the roughness has a value similar to the one observed in AFM, i.e. inferior to 0.5 nm for the different thin films.

Target	Thin film	Fluence	Temperature	Oxygen	Ablated area
$NdNiO_3$	$NdNiO_3$	3.8 J/cm²	675 °C	0.3 mbar	5x5 mm²
$Nd_{1.9}Sr_{0.1}NiO_4$+NiO	$Nd_{0.95}Sr_{0.05}NiO_3$	4.8 J/cm²			No scanning
$Nd_{1.6}Sr_{0.4}NiO_4$+NiO	$Nd_{0.8}Sr_{0.2}NiO_3$				
$SrTiO_3$ single crystal	$SrTiO_3$	2.4 J/cm²			3x3 mm²

Table 1: Optimized growth parameters for the perovskite nickelate samples series.

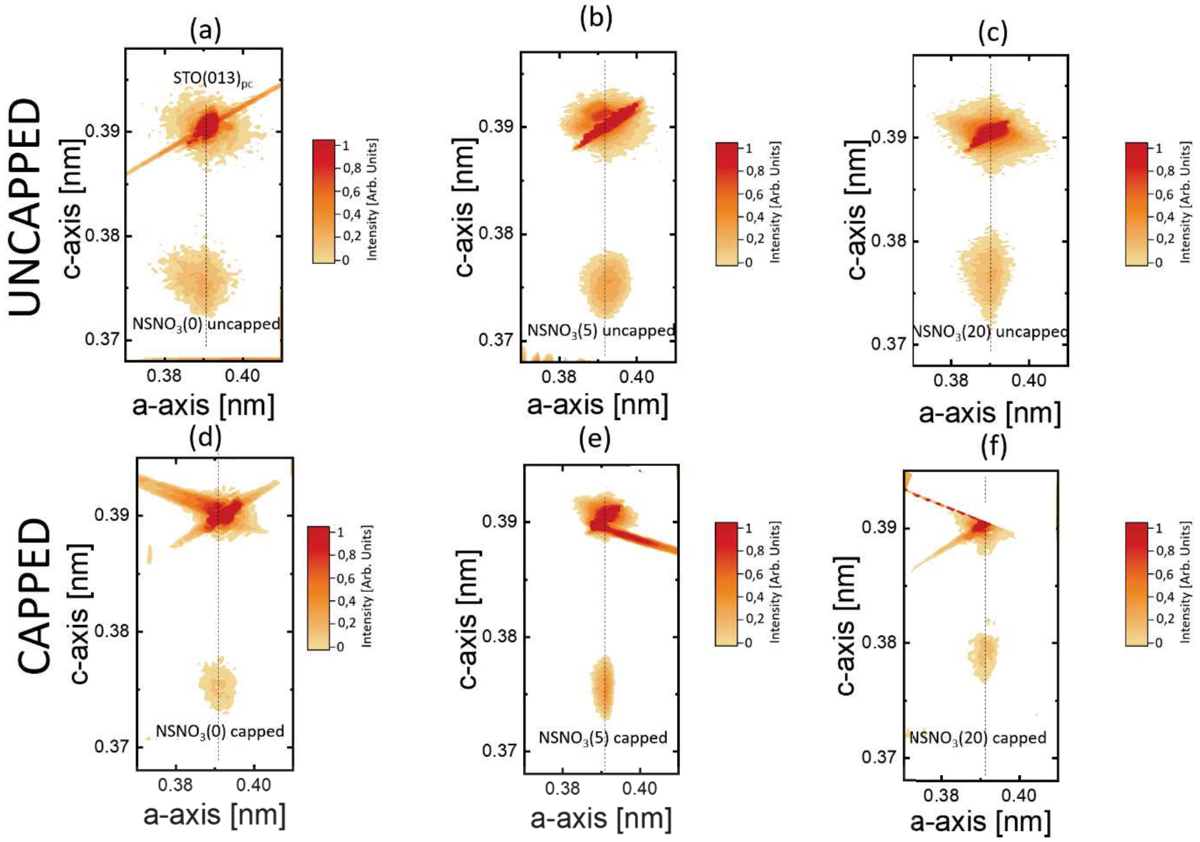

Figure IV-7 RSM of uncapped (top) and capped (bottom) (a,d) $NSNO_3(0)$ (b,e) $NSNO_3(5)$ (c,f) $NSNO_3(20)$ 10 nm thick perovskite thin films. All thin films are strained to the substrate.

The reciprocal space maps shown in **Fig. IV-7** exhibit an in-plane lattice parameter of the different thin films identical to that of the STO substrate. It can be concluded that the perovskite thin films are fully strained, independently of the Sr-doping level and/or the presence/absence of the capping-layer.

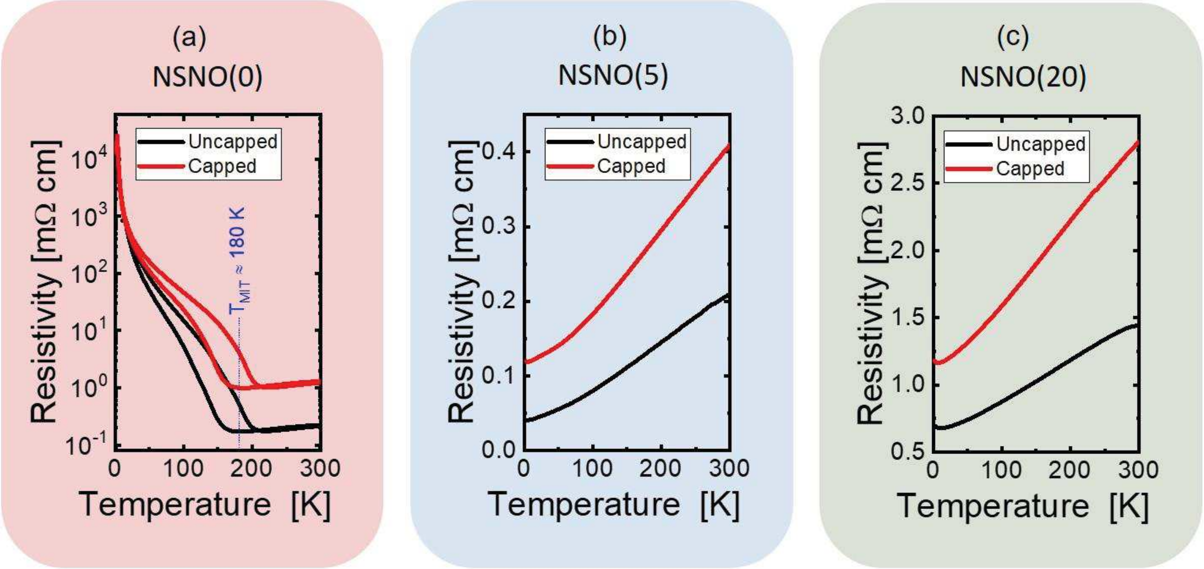

Figure IV-8 Temperature dependence of resistivity for the three different doping levels of perovskite, with and without capping-layer. Bright colours are for the capped samples, light colours for the uncapped.

To conclude this first part dedicated to the growth optimization of our perovskite Sr-doped nickelate thin films we show in **Fig. IV-8** a comparison of the transport properties for the capped and uncapped sample series. The only 3 u.c. thick STO capping layer does not alter the temperature onset of the metal-to-insulator transition (MIT) for our undoped samples which show same values as bulk [5]. Upon Sr-doping the MIT is fully destroyed as already discussed before, and we observe a higher resistivity value for the capped samples. It is worth noticing that $RNiO_3$ (R being a rare-earth element), have been studied since decades for their sharp MIT properties [5]. The rich phase diagram of bulk $RNiO_3$ displays an intimate connection between the Ni-O-Ni bond angles/lengths (controlled by the choice of R), and the temperature at which the MIT is encountered (T_{MIT}). The modulation of the MIT through epitaxial strain and/or electron/hole-doping in thin films has been a productive field of research [221–224]. The oxygen vacancies may also play a decisive role in the measured T_{MIT} values by locally altering the Ni-O-Ni network path. This possibility is largely enhanced in the presence of an oxide capping layer, as it is the case here. Indeed, if not properly optimized, the growth of the STO capping layer can alter the interfacial Ni-O-Ni bond angles/lengths, and, together with a modified Ni valence state, cause important variations of the transport properties.

2. Synthesis of infinite-layer nickelate thin films

In this part, I will present the optimization of the topotactic reduction process for our thin films. As highlighted in the Experimental Techniques Chapter, this reaction is not fully mastered. The experimental parameters, such as temperature, time of reaction and volume, vary from work to work in the literature [101,105,107–111,113,225]. We will indeed show that the optimum topotactic reduction conditions vary a lot with the doping and presence/absence of the capping-layer.

1. The sealing issue

We have performed the topotactic reductions in systems similar to the ones described in the literature to obtain superconductive infinite-layer [101,105]. The reaction is performed under vacuum in a sealed silica tube, which we prepared ourselves. Firstly, the silica tube cylinders are sealed on one side, before incorporating the CaH_2 powder with the thin film. Then, the glass was evacuated thanks to an attached pump, and sealed when under vacuum, as shown on **Fig. IV-9(a)**. However, the sealing process is a delicate step which gave us a hard time. It was very difficult to determine whether the tube was properly sealed or not. Indeed, as shown in **Fig. IV-9(b)**, the extremities of the tube were not well "defined", due to the (mis)use of the blowtorch, it was hence not simple to conclude that there was no leak in the seal. We therefore had the IPCMS workshop produce a tube connected to a membrane valve as shown in **Fig. IV-9(c)** in order to get rid of the sealing issues that we encountered in our first experiments. With this system, vacuum was simply obtained by connecting the valve to a pump. The valve was then closed in order to maintain a static vacuum and proceed to the reduction in the oven. This system does not only solve the sealing issues, but also allows to keep the exact same volume for all the experiments, comforting us in the reproducibility of our thin films reduction. The upcoming optimization of the topotactic reduction conditions has been performed with this homemade system with a quantity of 0.5 g of CaH_2 (Sigma Aldrich) put in direct contact with the 10 nm thick $NSNO_3$(x) thin films. It is to note that I first wrapped the thin films in aluminium foil, but I observed no modification if I didn't wrap them. So I decided not to use aluminium foil anymore once I noticed this.

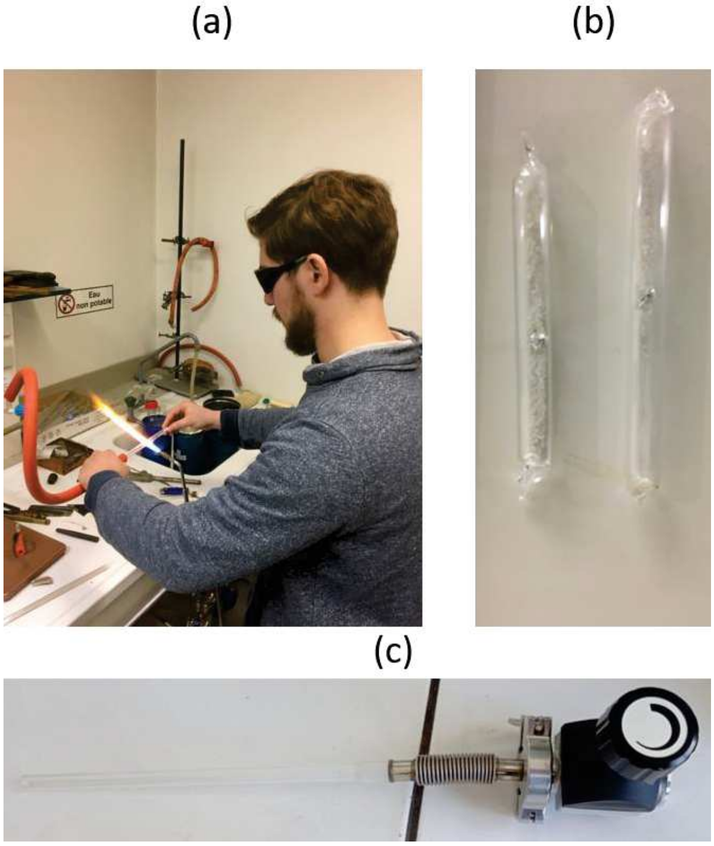

Figure IV-9 (a) picture of the tube being sealed while being pumped (b) sealed glass tube with CaH_2 powder and thin film inside (c) Silica tube attached to a valve in order to maintain a static vacuum for the topotactic reduction

2. Optimisation of the reduction process for uncapped and capped samples

To guarantee a relatively large degree of reproducibility of the reduction process, we have optimized our parameters trying to keep relatively low-temperature and high-reaction-time values in order to allow a slow oxygen de-intercalation process.

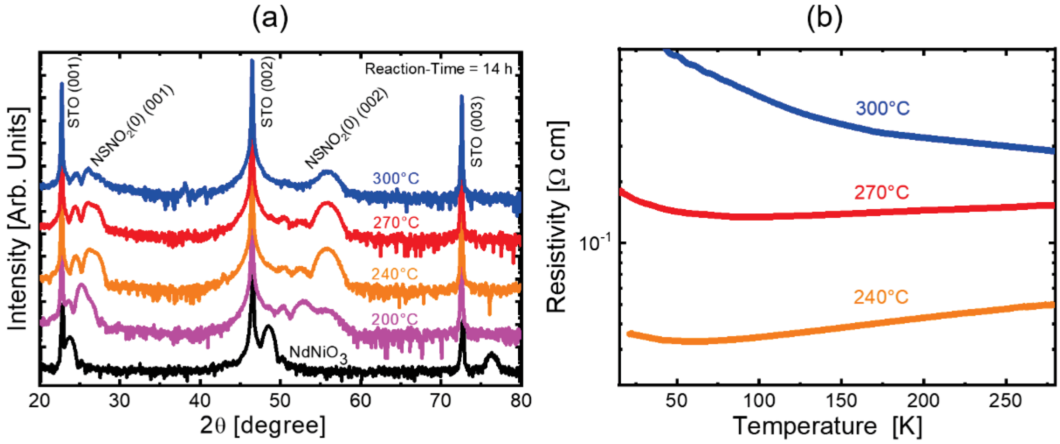

Figure IV-10 (a) XRD of $NSNO_2(0)$ after different topotactic processes with (b) the related different transport properties.

Fig. IV-10(a)-(b) show the temperature study of a series of topotactic reduction processes (14 hours long) undertaken for uncapped $NSNO_3(0)$ samples. At 200 °C the infinite-layer phase is not properly stabilized since the shift of the XRD peaks is only partial. At the higher temperatures of 240 °C and 270 °C the XRD peaks are found at the expected positions [101], and high intensity, which indicates a proper crystallinity of the infinite-layer phase. Further increasing the temperature has no relevant effect on the position of the peaks, but the diminished intensity marks a worsening of the infinite-layer crystallinity, as can be seen for the 300 °C data. This is also confirmed by the overall insulating properties observed for this temperature **[Fig. IV-10(b)]**. On the other side, at 240 °C and 270 °C we observed the expected transport properties for undoped samples, i.e. metallic followed by a small upturn around 70 K. In **Fig. IV-10(b)** we can easily infer that the 240 °C reduction temperature leads to an overall lower resistance for the infinite-layer phase, and therefore, we kept this value for all our $NSNO_3(0)$ reduction experiments. Interestingly, the set of optimized parameters (14 hours and 240°C) gave similar results for $NSNO_3(5)$ thin films, perhaps due to the relatively small difference in Sr-content between the two precursor phases.

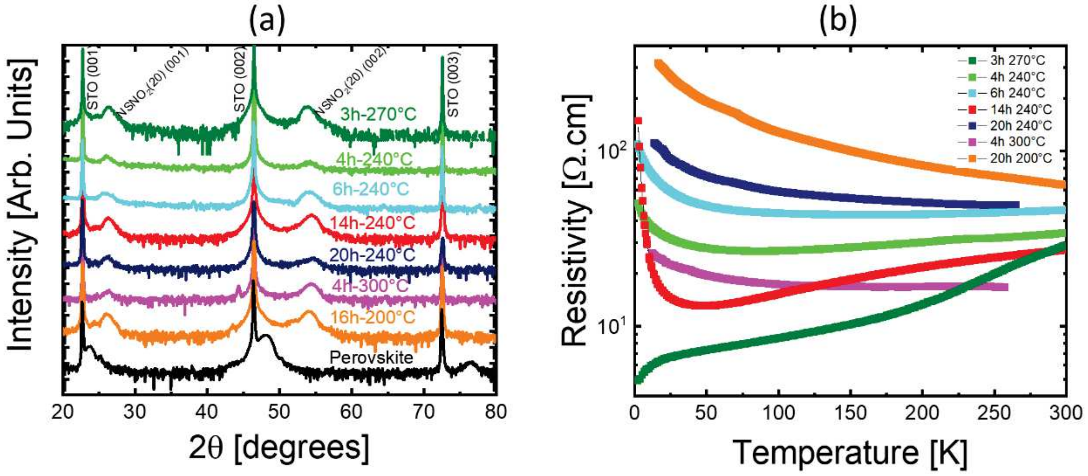

Figure IV-11 (a) XRD of $NSNO_2(20)$ after different topotactic processes with (b) the related transport properties.

However, these parameters (14 hours and 240°C) did not lead to any sign of superconductivity for $NSNO_2(20)$ thin films, which we could observe only after decreasing the reduction time to 3 hours and increasing the temperature to 270°C as shown in **Fig. IV-11(b)**. The reductions performed with different conditions exhibits very different behaviours, from insulating to fully metallic with a superconducting transition. The XRD patterns obtained for the films reduced with the different topotactic processes however all look very similar, with a 002 diffraction peak around 2θ=54°, as can be seen in **Fig. IV-11(a)**. We can speculate that the reduction process for the $NSNO_3(20)$ samples take place more rapidly because of a larger number of extended defects, due to the incorporation of a larger amount of Sr, when compared to the undoped or underdoped samples. Those defects act as a favoured pathway for the oxygen to de-intercalate, and react with the CaH_2 reducing agent. It is clear that one has to keep at the minimum level the presence of those defects to properly reproduce the recently observed zero-resistance state below 10 K in Sr-highly-doped infinite-layer $NdNiO_2$ thin films. Future work has to focus on further improving the quality of the perovskite phase for $NSNO_3(20)$ samples.

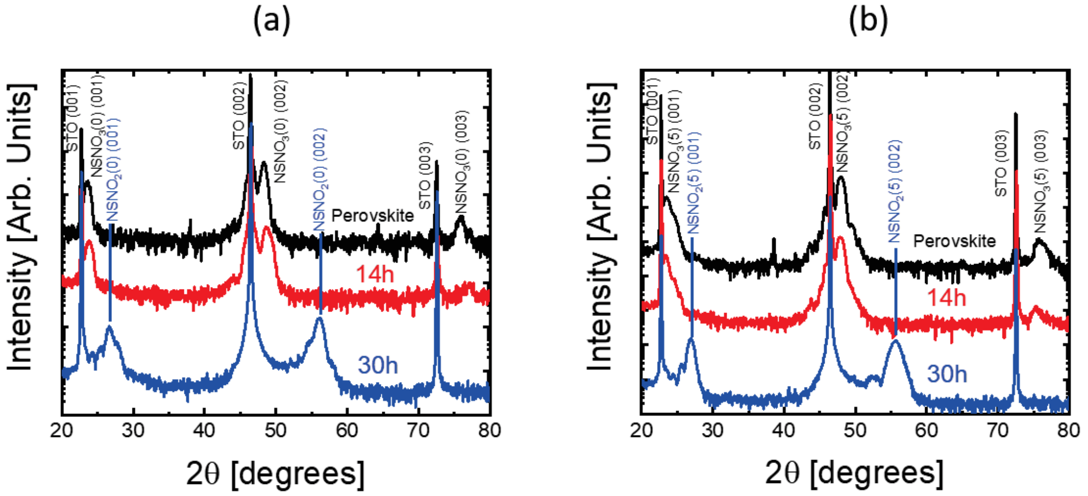

Figure IV-12 Comparison of 14 h vs. 30 h reduction time at 240°C for capped (a) NSNO(0) and (b) NSNO(5) thin films

The reduction conditions need to be re-adapted with the presence of the 3 u.c. STO capping-layer, as shown in Table 2. A reduction time of 30 hours was necessary to observe the expected shift of the XRD peaks with a strong intensity (blue curve) as shown in **Fig. IV-12** for NSNO$_2$(0) and NSNO$_2$(5) samples. If the same process as the one used for the uncapped samples is used, no shift of the diffracted peak is observed (red curve). At this point, we do not know if the fact that the reduction is more time-demanding is due to a slower diffusion of the oxygen through the capping-layer (while being only 3 u.c.), or if the assumption that extended defects create favoured pathways demonstrates that the capped-samples have less defects. This could be explained by the fact that the capping layer acts as an epitaxial template [101]. To observe a signature of the superconducting transition for our capped NSNO$_2$(20) thin films, it was necessary to use a higher reduction temperature of 300°C.

Table 2 Optimized temperatures and duration times for the topotactic reduction as a function of the different Sr-doping levels, and the presence/absence of an STO capping-layer.

Precursor phase	STO Capping-layer	Temperature	Time
$NdNiO_3$ and $Nd_{0.95}Sr_{0.05}NiO_3$	No	240°C	14 h
	Yes	240°C	30 h
$Nd_{0.8}Sr_{0.2}NiO_3$	No	270°C	3h
	Yes	300°C	3h

3. Characterization of the optimized infinite-layers

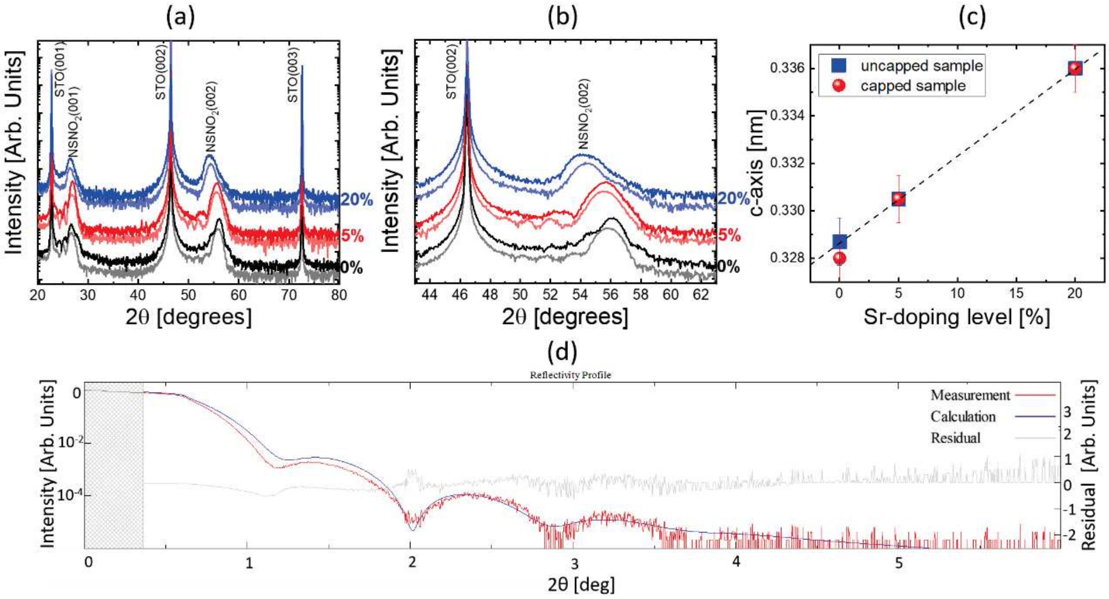

Figure IV-13 (a) XRD for the three different x doping levels of the perovskite samples, with and without capping layer. Bright colours are for the capped samples, and light colours for the uncapped samples. (b) zoom on the (002) peak of the thin films (c) evolution of the c-axis parameter with the Sr-doping level for capped and uncapped infinite-layer thin films (d) Reflectivity measurement (red) and the fitting (blue) (GlobalFit software) of a 9.5 nm thick NSNO$_2$(5) thin film.

Fig. IV-13(a)-b) present the XRD spectra acquired for our NSNO$_2$(x) samples with (bright colours) and without (light colours) an STO capping-layer, and reduced by using the optimized parameters listed in Table 2. As it is possible to infer from **Fig. IV-13(c)** the c-axis parameters are not modified within the experimental error by the presence of the capping-layer, and increase linearly with the Sr doping level. The thickness of the thin films decrease when performing the topotactic reduction, as observed with reflectivity measurements shown in **Fig. IV-13(d)**. By decreasing from 10-11 nm in the perovskite phase to 9-10 nm in the infinite-layer phase, the thin film is approximately 10 % thinner after the reduction. This value is in accordance with the c-axis value, which decreases from 0.337 nm in the perovskite phase to 0.330 nm in the infinite-layer phase, also corresponding to a reduction of 10 % of the thin film thickness.

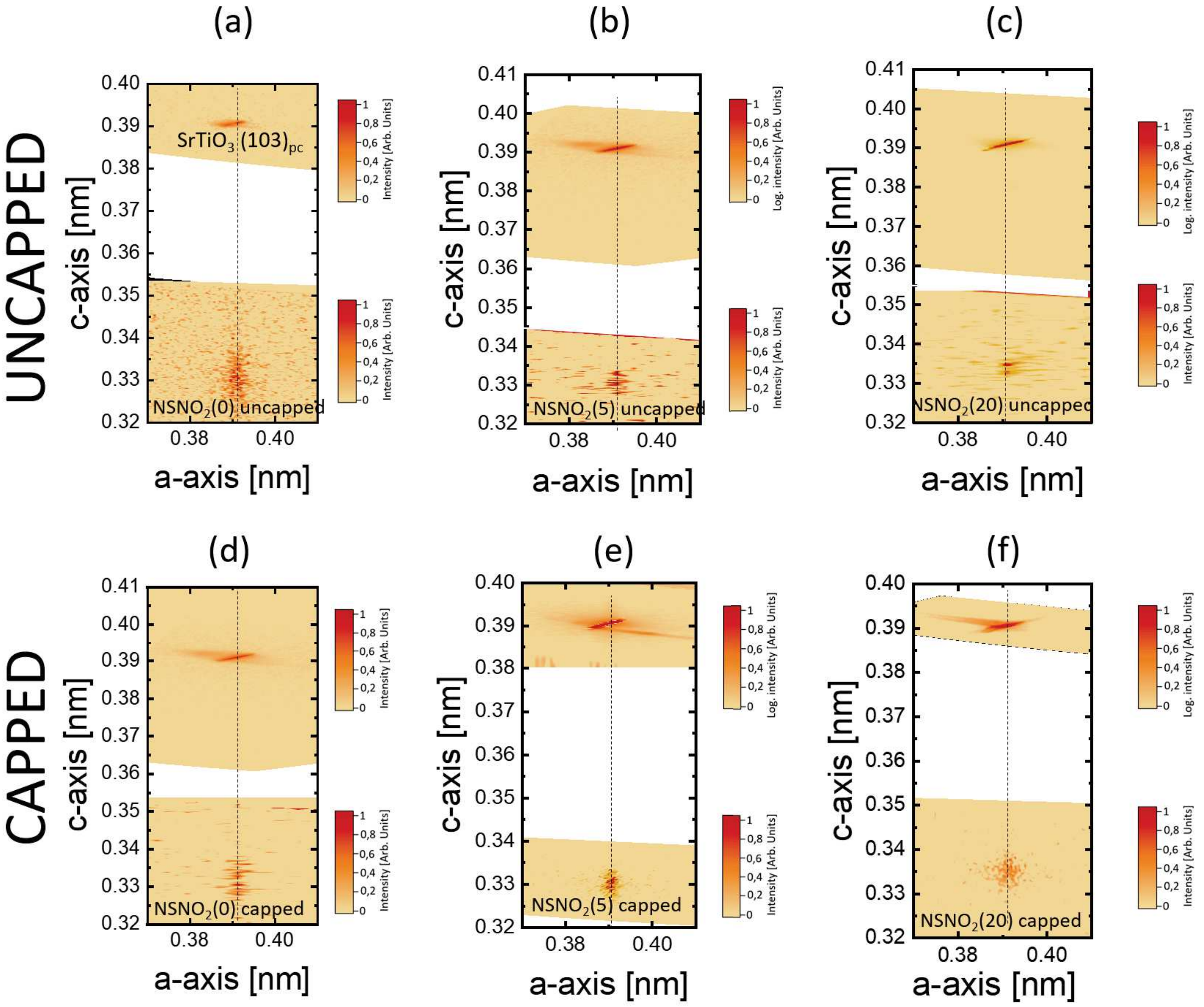

Figure IV-14 RSM of uncapped (a) $NSNO_2(0)$ (b) $NSNO_2(5)$ (c) $NSNO_2(20)$ and capped (d) $NSNO_2(0)$ (e) $NSNO_2(5)$ (f) $NSNO_2(20)$ 10 nm thick infinite-layer thin films. All thin films are fully strained to the substrate.

The $NSNO_2(x)$ samples remain fully strained to the substrate after the reduction as can be seen from the reciprocal space mappings reported in **Fig. IV-14**, independently of the Sr-doping level and the presence/absence of the capping-layer. The RSM confirmed the value of the c-axis extracted from the θ-2θ measurements with similar values and trends with the doping.

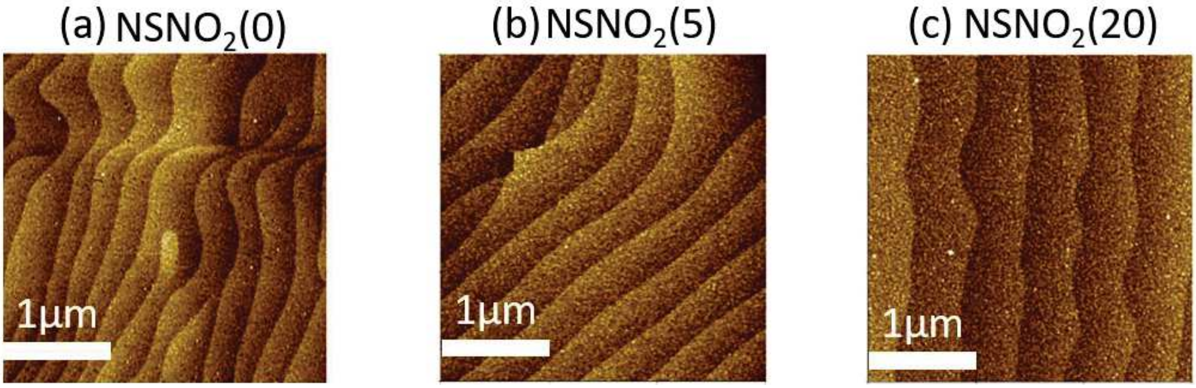

Figure IV-15 3x3 µm² AFM images of capped (a) $NSNO_2(0)$ (b) $NSNO_2(5)$ and (c) $NSNO_2(20)$ thin film, characterized by a 0.3-0.4 nm RSM-roughness value.

It has been reported that topotactic reduction processes damage the surface of the precursor phase, and that a post-reduction vacuum annealing was mandatory to re-observe the step-terraced morphologies [226]. The topotactic reduction presented here, granting relatively small temperatures and long times for the reaction to take place, allowed to preserve the smoothness of the precursors' surface for the morphologies of the infinite-layer phase. **Fig. IV-15** summarizes the AFM study of our reduced NSNO$_2$(x) sample series characterized by a RMS-roughness value ranging in the 0.3-0.4 nm.

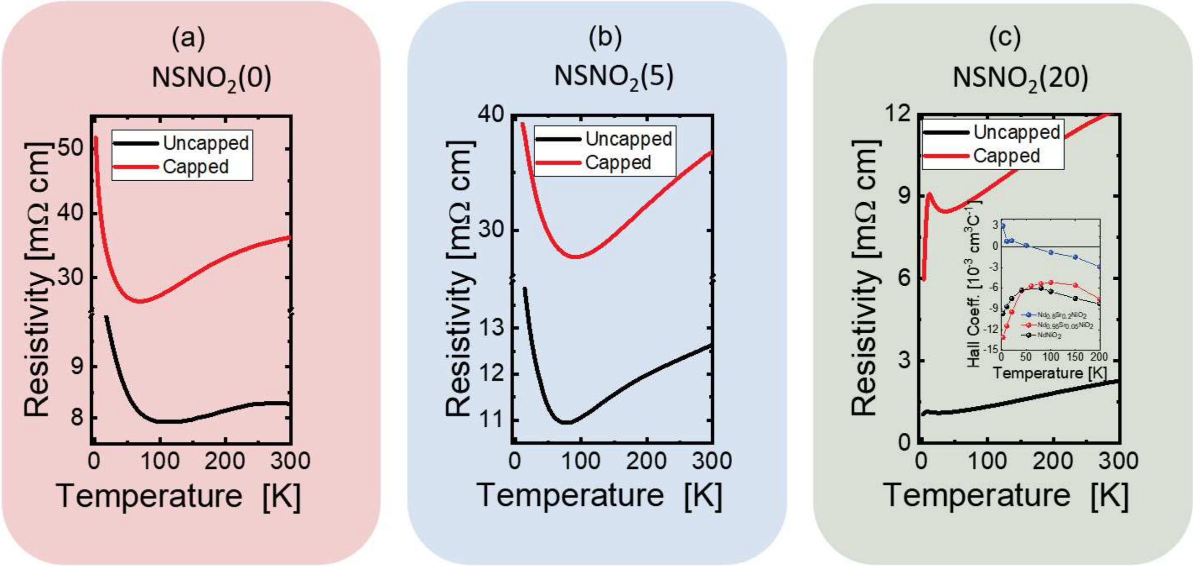

Figure IV-16 Temperature dependent resistivity curves of the infinite-layer samples for the three different doping levels, with and without capping-layer.

Fig. IV-16 shows the temperature dependence of the resistivity curves acquired after reduction for our NSNO$_2$(x) capped and uncapped sample series. The transport properties of NSNO$_2$(0) and NSNO$_2$(5) are representative of those found in the literature [105,106], for both capped and uncapped cases. NSNO$_2$(20) samples are showing a superconducting transition, but do not reach a complete zero-resistance state, as already discussed before. In the inset we also show the Hall coefficient measurements exhibiting the same behaviour as reported in previous works. To be noticed, the sign change of the majority charge carriers around 50 K in the case of the superconducting samples (from electrons to holes) [105,106].

4. Degradation of the infinite-layer in contact with air

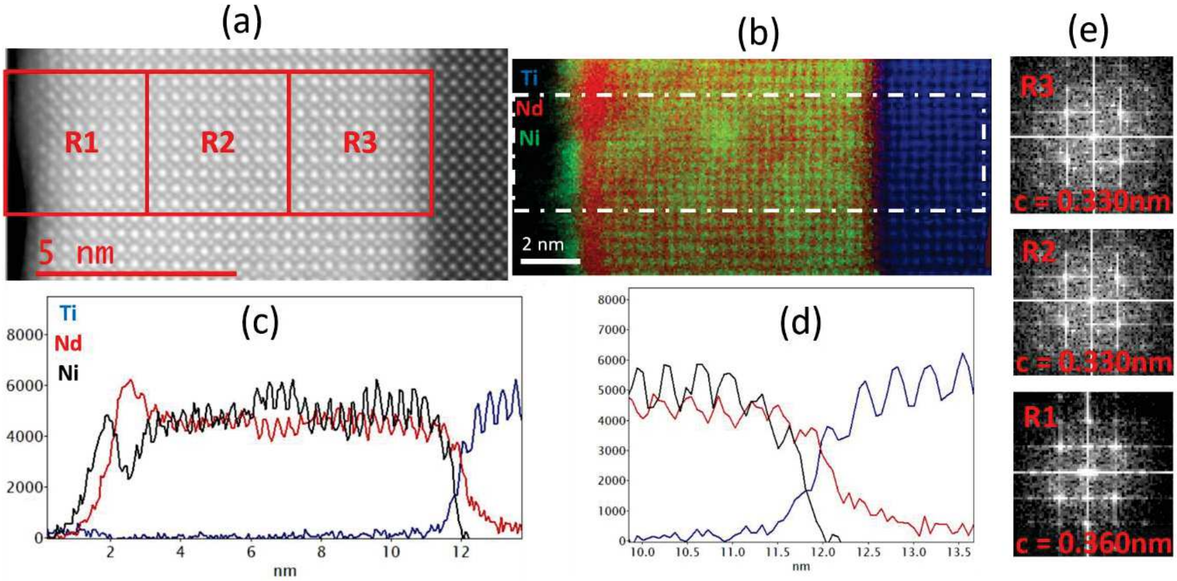

Figure IV-17 (a) STEM image of a 10 nm thick NSNO(0) uncapped thin film, (b) elemental STEM-EELS Nd, Ni, and Ti maps, (c) elemental profiles integrated over 5 nm (over the dash-dotted rectangle of (b)) showing a Ni/Nd ratio close to 1 over the whole thin film, except for the surface and substrate/film interface for which one observes some segregation, (d) close-up on the elemental profiles at the NSNO$_2$(0)/STO interface, in good agreement with the NiO2-Nd-TiO2 interface predicted by DFT calculations [173]*, (e) FFT of the 3 regions indicated by red boxes in (a), exhibiting c-axis parameters of 0.330 nm for R3 and R2, and 0.360 nm for R1.*

To conclude this Chapter, we show in **Fig. IV-17** the STEM and EELS measurement of an uncapped NSNO$_2$(0) sample which has been exposed to air for approximately four months. The atomically resolved HAADF STEM image of **Fig. IV-17(a)** clearly demonstrates the high crystallinity of the NSNO$_2$(0) with a coherent growth on the STO substrate. The fast Fourier transform (FFT) of different regions of the film are shown in **Fig. IV-17(e)**. The c-axis parameter of the centre (R2) and substrate interface (R3) regions is of 0.330 nm, in agreement with the infinite-layer lattice parameter and is getting larger at the surface of the thin film (R1) (0.360 nm). The elemental profiles have been obtained from the Ni-L and Nd-M EELS edges **[Fig. IV-17(c)]**. The elemental quantification from calculated EELS cross sections have low accuracy when comparing edges of different shells. We have first experimentally estimated the Ni-L / Nd-M EELS cross-section ratio on a reference NdNiO$_3$ thin film and applied it to the NSNO$_2$(0), confirming a Ni/Nd ratio close to 1 over the whole thin film. The elemental analysis however indicates a possible degradation of the infinite-layer phase with a peculiar Nd/Ni off-stoichiometry at the surface of the thin film. The elongation of the c-axis parameter alongside the off-stoichiometry might suggest the formation of a spurious phase with the Ni valence varying from 1+ towards higher valences near the surface of the thin film, because of a re-oxidation process. A zoom on the elemental EELS distribution at the film-substrate interface is in **Fig. IV-17(d)**, and clearly demonstrates that the NNO is Nd terminated. The Sr EELS signal was not collected, but the Ti profile position is in agreement with a Ti-terminated STO, rendering a possible NiO$_2$-Nd-TiO$_2$-SrO interface reconstruction, in perfect agreement with DFT calculation [173].

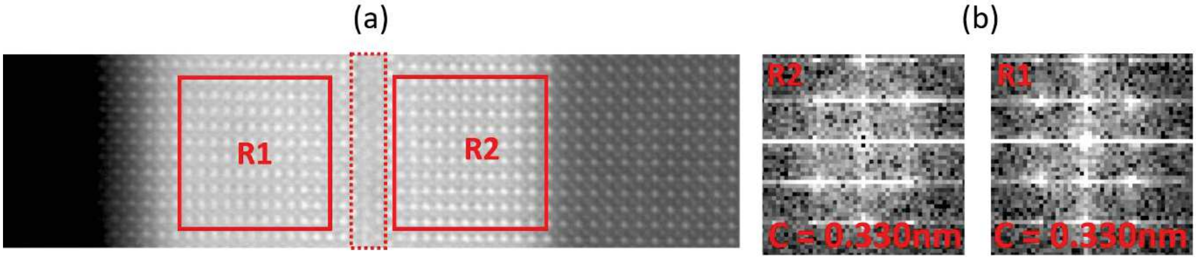

Figure IV-18 (a) STEM image of a 10 nm thick $NSNO_2(0)$ uncapped thin film (b) FFT of the 2 regions indicated by red boxes in (a) exhibiting c-axis parameter of 0.330 nm for both regions.

On the contrary, the capped $NSNO_2(0)$ sample does not exhibit a deterioration of the thin film surface when exposed to air for the same amount of time. Despite the observation of a stacking fault in the middle of the thin film in **Fig. IV-18(a)** (dashed red rectangle), a high crystalline quality similar to the one observed in the uncapped sample is observed here. FFT of regions close to the substrate (R2) and to the surface (R1) on **Fig. IV-18(b)** show similar c-axis parameters of 0.330 nm, also similar to the one observed in the regions close to the substrate in the uncapped sample **Fig. IV-17(e)**. With this result, the assumption that the capping-layer act as a brake on the deterioration of the infinite-layer phase seems relevant.

3. Summary

In this Chapter, we have reported the optimisation of the growth of the $Nd_{1-x}Sr_xNiO_3$ perovskite thin films and their reduction in the $Nd_{1-x}Sr_xNiO_2$ infinite-layer phase. The challenges inherent in the synthesis of the material have been detailed, as well as the levers used to overcome them. The no-toggling method for the growth of the perovskite, used to overcome the Ni/Nd cation off-stoichiometry issues, proved its efficiency. Our optimized topotactic reduction processes tend to have longer reaction times and lower temperatures than what is announced in the literature for undoped and underdoped $NSNO_2(x)$ (x=0, 0.05) STO-capped and uncapped thin films. Our optimized process rendered very smooth and step-terraced surface morphologies which are a necessary and sufficient condition to perform surface-sensitive measurements, such as scanning tunnelling and/or ARPES, which are planned in the near future.

We also observed that the presence of a capping-layer acts as a brake for the deterioration of the infinite-layer phase in contact with air. In the upcoming Chapter, we will show that the capping-layer does not just enhance the crystalline quality of the infinite-layer phase and protect it, but also modifies the physics of the material.

V. Electronic and magneto-transport properties of infinite-layer nickelate thin films

In this Chapter, I will present X-ray absorption (XAS), resonant inelastic X-ray scattering (RIXS) and (magneto)transport experiments undertaken on infinite-layer nickelate thin films prepared at different Sr content with and without a capping layer. As extensively discussed before the search and finally the discovery of superconductivity in infinite-layer nickelates was mainly motivated by the possibility to synthesize a material capable of being at the same time isostructural and isoelectronic to infinite-layer cuprates. Therefore, being capable of reproducing such a challenging synthesis process resulting in the stabilization of the infinite-layer phase could not be considered a task with an end in itself, and relatively quick we could propose a comprehensive study of the charge transfer, d-d and low energy excitations (including magnons and phonons) of Sr-doped $Nd_{1-x}Sr_xNiO_2$ (x=0, 0.05, 0.2) thin films via Ni-L_3 and Nd-M_5 high-resolution RIXS. After a total of three consecutive RIXS experiments we found that the role of the capping layer in the electronic properties including the low-energy excitations is extremely important. In particular Ni-L_3 edge high-energy-resolution RIXS at beamline ID32 disclosed strong charge density correlations in uncapped $NdNiO_2$ thin films and clearly dispersing magnetic excitations for $SrTiO_3$ capped $NdNiO_2$ samples. The uncapped and capped samples also present a different degree of Ni3d-Nd5d hybridization, identifiable in the RIXS map as a well-defined $3d^8R$ feature at around -0.6 eV energy loss, and a modified anisotropy of the Ni3d occupation. In particular, uncapped $NdNiO_2$ shows much larger Ni3d-Nd5d hybridisation, and lower anisotropy with respect to capped samples. We used these results to motivate also very first angle-dependent anisotropic magnetoresistance (AMR) measurements whose main results will be introduced at the end of this Chapter. We found that the capping-layer plays a key role also in controlling the magnitude and the anisotropy of the AMR properties of our samples. We discuss this control in terms of a combined effect between the Nd-Ni hybridization and an intra-atomic exchange coupling between the Nd-4f and Nd-5d states, the latter essentially contributing to the (magneto)transport. Further studies foresee the influence of different capping layer on infinite-layer nickelates with no magnetic rare-earth.

1. The puzzling role of the capping-layer on the RIXS low-energy excitations

1. Motivation for RIXS experiment

RIXS measurements have been widely used to mainly study the elementary excitations characterizing strongly correlated materials [208]. This technique has proved its importance in providing information about the localized character of the electrons wavefunctions of both d or f states, and about the coulomb interaction for materials such as high-T_C cuprates [131] and the colossal magnetoresistance manganites [227]. The recent discovery of the zero-resistance state below 15 K in $Nd_{0.8}Sr_{0.2}NiO_2$ thin films initially synthesized with an STO(001) substrate bring the necessity to explore the electronic configuration of this new superconductor material. The infinite-layer nickelate is isostructural and isoelectronic to high-T_C cuprates where superconductivity is linked to a quasi2D electronic structure with $3dx^2{-}y^2$ symmetry at all doping levels [26], and to the spin ½ of Cu-$3d^9$ sites. Soon after the first report of superconductivity in $Nd_{0.8}Sr_{0.2}NiO_2$ thin films, electron energy-loss spectroscopy [121], x-ray absorption spectroscopy (XAS) and resonant inelastic x-ray scattering (RIXS) experiments on undoped ($LaNiO_2$, $NdNiO_2$) [124] and doped ($Nd_{1-x}Sr_xNiO_2$) samples [125] showed that the O-2p and Ni-3d bands are more separated in energy in the nickelate infinite-layer (~4 eV) than in layered cuprates (~2 eV) [122]. Although still debated [153,170,171], these results would place nickelate parent compounds in the Mott-Hubbard region of the Zaanen–Sawatzky–Allen classification scheme, implying that injecting holes leads towards a Ni-$3d^8$ electronic configuration. This is at odds with cuprates, classified as charge-transfer insulators, where doping holes go to the oxygen sites and form the so called Zhang-Rice singlets [168,169], Cu-$3d^9\underline{L}$. Moreover, in infinite-layer nickelates a contribution of the Nd-5d bands at the Fermi level leads to an important hybridization between Nd-5d and Ni-3d states [122,124], whereas in cuprates the inter-layer cations do not contribute to the electronic states relevant to transport. Besides these differences, the analogy with cuprates was recently strengthened by the observation of magnons in $NdNiO_2$ [127], dispersing similarly to those of cuprates, but on a smaller energy range. Interestingly, magnons were found so far only in nickelates capped with epitaxial STO before the topotactic reduction [126], whereas the capping is not necessary to get superconductivity [106]. An important feature of all cuprates is the charge density instability of hole doped CuO_2 planes [228–230]. It emerges in the form of charge density waves (CDW) in selected regions of the temperature/doping (T/p) phase diagram [131,231–233], and of charge density fluctuations (CDF) over a more extended set of T and p values [234–236]. Therefore, it was natural to ask if similar CDW or CDF could be present in our nickelate samples. Interestingly, after our first report similar RIXS studies corroborated our finding [128,129] about the presence of charge order.

Here, I will present RIXS measurements at the Ni L_3-edge performed to obtain important information about both spin and charge correlations characterizing the NiO_2 planes. I will compare data of $Nd_{1-x}Sr_xNiO_2$ thin films ($NSNO_2(x)$) with three doping levels (x=0.00, 0.05, 0.20), with and without the STO capping layer. As a part of an international collaboration we confirmed the presence of spin-spin correlation by detecting dispersing magnons in capped samples, and we observed a resonant quasi-zero-energy-loss scattering signal peaking at (1/3, 0) [r.l.u.] in uncapped samples. We also found other relevant differences related to the presence of the capping layer in the RIXS and XAS spectra, that I will thoroughly discuss below.

2. Thin film characterizations

Fig. V-1 summarizes XRD and transport characterizations of the first series of uncapped NSNO(x) (with x = 0, 0.05, 0.2) samples in both perovskite and infinite-layer phases (the superconducting sample was obtained from NSU within our collaboration with Prof. A. Ariando) that we measured at ID32. In particular**, Fig. V-1(a),(d),(g)** show X-ray diffraction scans for the NSNO(x) samples. The topotactic reduction led to the expected shift of the (001) diffraction peaks corresponding to the transition from the perovskite towards the infinite-layer structure. The c-axis goes from c = 0.328 nm for the undoped sample to 0.336 nm for the superconducting one (x = 0.2). **Fig. V-1(b),(e),(h)** show the transport properties of the perovskite phase. At x = 0 we recover the usual metal-to-insulator transition (MIT), separating by more than four orders of magnitude the metallic and insulating phases. The relatively high transition temperature of almost 180 K, being not too far from the expected bulk value (200 K [5]), indicates a good optimization of the growth parameters with a low content of oxygen vacancies, as also prompted by the position of the (002) peak in the XRD scan (2θ = 48.5°). Upon Sr doping the MIT is completely destroyed as it is possible to infer from **Fig. V-1(e),(h)** with the temperature dependence of the resistivity characterized by only a small upturn at low temperatures for both x = 0.05 and x = 0.2 Sr doping levels. Regarding the transport properties of the reduced thin films, while the x = 0.05 and x = 0.2 Sr-doped samples show resistivity measurements as a function of the temperature in line with data reported in literature [106] in **Fig. V-1(f),(i)**, with respectively bad-metal and superconducting properties, the undoped parent compound is characterized by a fully insulating character within the measured 50-300 K temperature range in **Fig. V-1(c)**. This is at odd with the report [105] of Li *et al*. where it was shown a bad metal behaviour with a low temperature upturn similar to cuprates just below the critical doping for superconductivity, but reminiscent of the bulk-like behaviour of $NdNiO_2$ as recently reported [124]. However, we could also obtain undoped uncapped infinite-layer samples **[Fig. V-9(c)]**, with bad-metal transport properties. Interestingly, also in this case we could observe similar feature with RIXS measurements that will be introduced later on case. The main difference between the uncapped samples shown in **Figs. V-1(a)** and **V-9(c)** is represented by the set of parameters (temperature/time), used for the topotactic reduction. Namely, 280°C/6h for the insulating samples, and 240°C/14h for the ones exhibiting bad-metal properties. Moreover, our optimized reduction process for the capped samples accounts for 240°C/30h parameters.

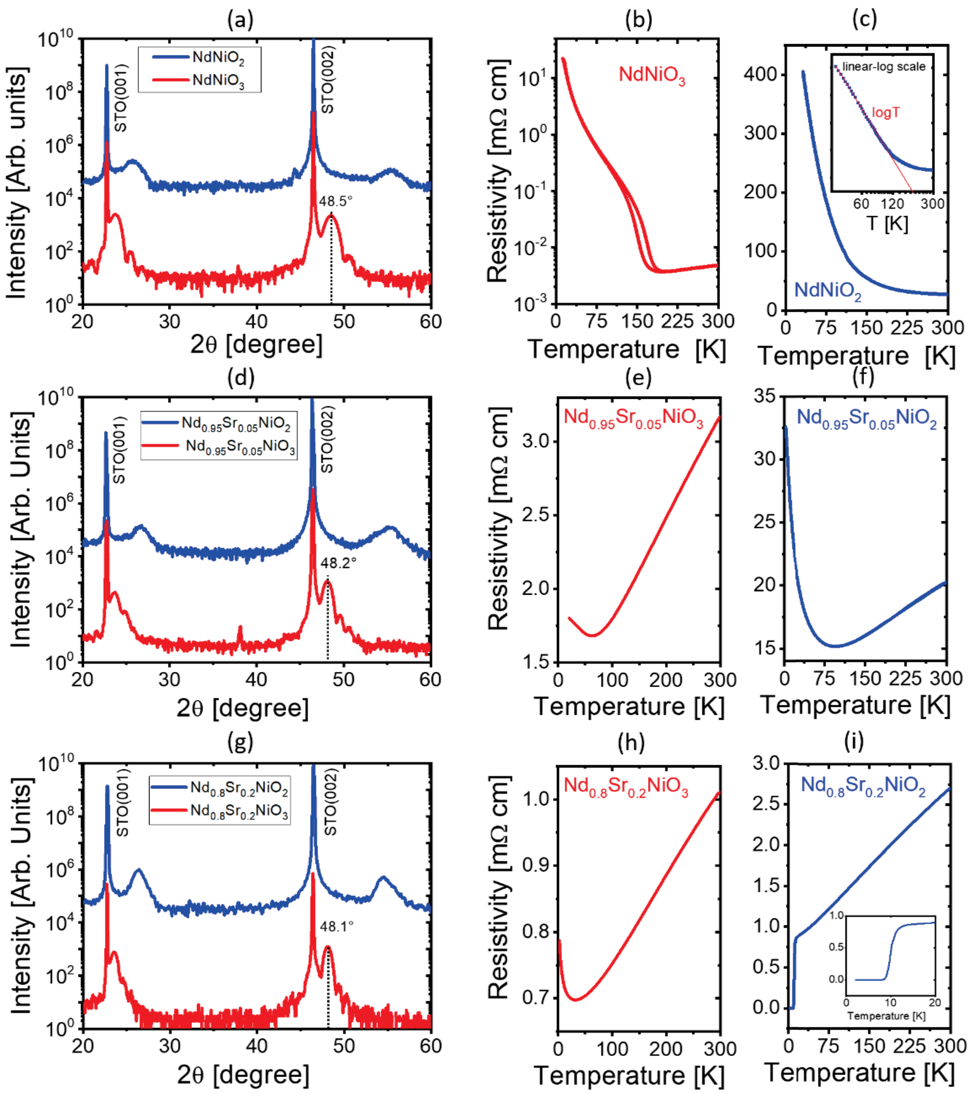

Figure V-1 XRD and resistivity as a function of the temperature for respectively (a-c) NSNO(0) (d-f) NSNO(5) (g-i) NSNO(20)

3. Beamline presentation

The XAS and RIXS measurements were performed at the beam line ID32 of the European Synchrotron – ESRF (Grenoble, France) with the ERIXS spectrometer shown in the **Fig. V-2**. The geometry of the measurement has been already introduced in Chapter III **[Fig III-17(a)]**, and re-proposed here in **Fig. V-3(a),(b)**. The spectrometer is an eleven-meter-long arm that allows to change the scattering angle 2θ from 50° to 150°. In our case, the projection of the transferred momentum q=k'−k in the NiO_2 planes $q_{||}$ was changed by rotating the sample around an axis perpendicular to the scattering plane at fixed scattering angle 2θ = 149.5°, which is the spectrometer position reported in **Fig. V-2**. With the scattering angle fixed, the wavevector q is constant, and it is possible to change $q_{||}$ by rotating the sample. The projection $q_{||}$ can be determined as a function of the incoming wavevector k as follow:

$$q_{||} = -q\cos(\alpha+\theta) = -q\cos\left(\frac{\pi}{2} + \theta - \frac{\sigma}{2}\right) = q\sin\left(\theta-\frac{2\sigma}{2}\right)$$

$$q = 2k\cos(\alpha) = 2k\sin\left(\frac{2\sigma}{2}\right)$$

$$q_{||} = 2k\sin\left(\frac{2\sigma}{2}\right)\sin\left(\theta-\frac{2\sigma}{2}\right)$$

We mainly explored, two high symmetry directions of the Brillouin zone (BZ), namely the (10) (Γ−X) (red arrow in **Fig. V-3(c)**) and the (11) (Γ−M) (green arrow on **Fig. V-3(c)**).

Figure V-2 Picture of the ID32 RIXS beamline setup

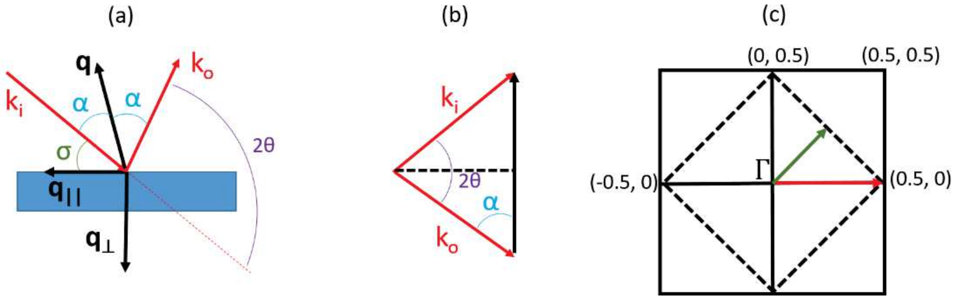

Figure V-3 (a,b) Schematic representation of a RIXS measurement geometry (c) Schematic representation of the first Brillouin zone (the solid line refers to the crystal lattice, dots refer to the magnetic lattice).

Fig. V-4 shows the standard sample holder along with the particular sample mounting geometry. We used Silver paste to glue the samples and also to provide an electric contact with the (grounded) sample holder, necessary to measure XAS in TEY mode.

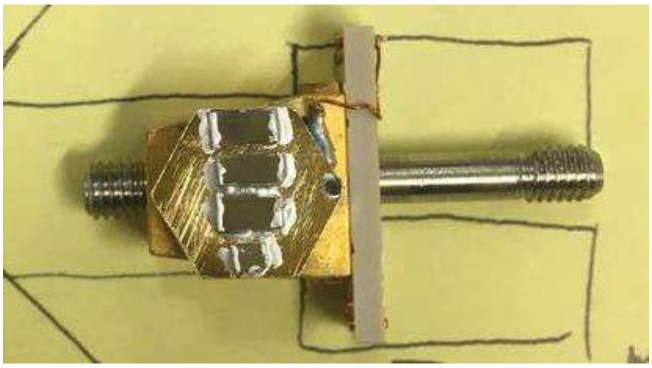

Figure V-4 Picture of a sample holder used for the RIXS beamline

Before presenting our results, I would like to introduce here the formulas I have used to fit the RIXS spectra mainly in the low-energy region [132]. The RIXS spectra in the (-0.1-0.5) eV energy loss range were reproduced by a convolution of Gaussian lineshape for the elastic part (with energy full-width half-maximum (FWHM) equal to the nominal beam-line energy resolution of 43 meV) and an asymmetric Lorentzian for the low-energy (LE) feature. According to the following formula:

$$y = y0 + \frac{b2}{s\sqrt{\frac{\pi}{2}}} * e^{\frac{-2*(x-x0)^2}{s^2}}$$

the Gaussian parameters were y0 for the baseline correction, b2 the elastic amplitude, s the elastic width, and x0 the energy loss factor to correct the elastic peak position, in order to have it at 0 eV. The asymmetric Lorentzian lineshape used for the LE feature is resulting from the difference of two Lorentzian peaks at position ±ωp and same width γ [132]:

$$L(x) = \frac{b1\gamma}{(x - xL)^2 + 4x\gamma^2}$$

with b1 the LE feature amplitude and xL its energy position. Finally, the entire lineshape is described by seven parameters, but only six of them were free to vary in the fit, since, after a first fitting procedure, the energy of the elastic component was set to zero (x0 = 0). The entire procedure for the convolution process operated via Origin is detailed in the appendix A. **Fig. V-5** shows an example of fitting for the RIXS spectrum acquired for an undoped capping-free sample at 20 K and $q_{||}$ = (0.33,0).

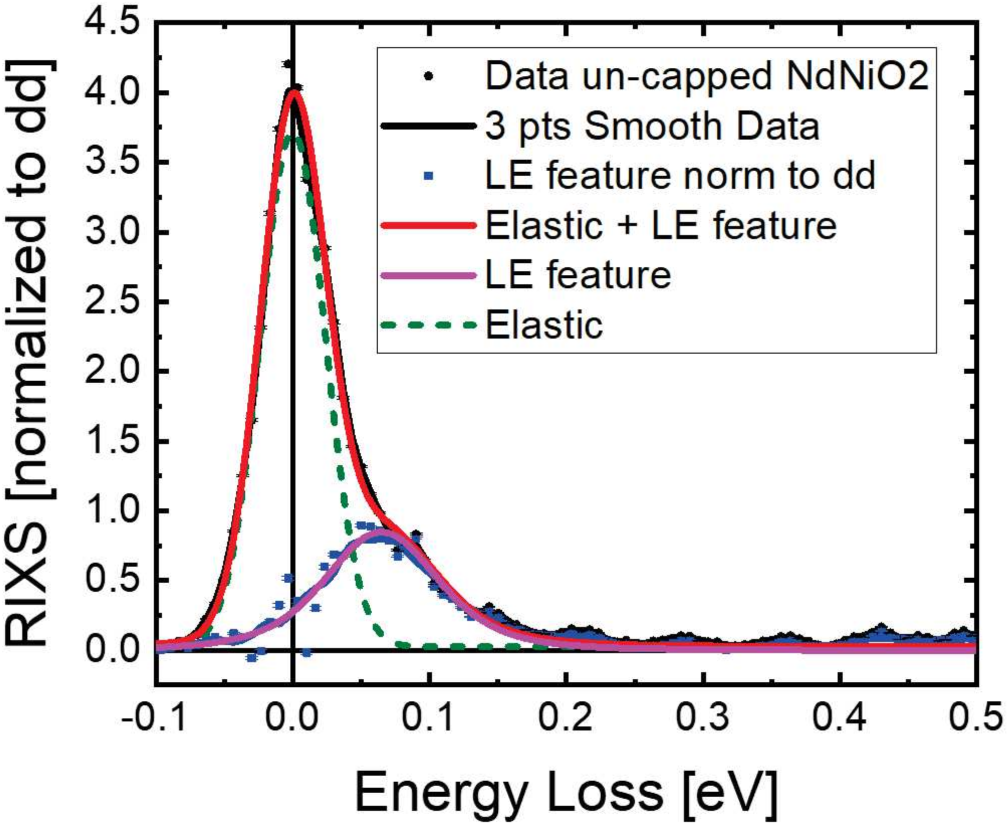

Figure V-5 Example of fitting result for the RIXS spectrum acquired for the undoped sample. q=(0.33,0) T= 20 K.

4. Polarization dependence of the XAS spectra

We measured first the XAS spectra of the different samples in order to, firstly, observe the relative oxidation degree of the Ni cation in the infinite-layer-phase as a function of the Sr-doping and the absence/presence of the capping-layer. Moreover, the RIXS spectra are performed at the resonance of an element which in our case is the Ni. Therefore, the XAS spectra are mandatory in order to obtain the specific resonant energy of the Ni L_3-edge at which we will performed the RIXS measurements. But first of all, the samples have to be properly aligned with respect to the incoming beam, which is done by performing several XAS scans along the x,y,z directions relative to the sample holder in the chamber at both, the nominal resonance of the Ni edge, and further from it. By combining in- and off-resonance scans, a proper alignment can be performed. Specific care has to be devoted to the θ-offset, resulting from the silver paste used to stick the sample, therefore θ-scans are performed to estimate this offset.

Once the alignment is done, we use the incident photon polarization dependence of XAS spectra to devise the orbital character of the electronic states. **Fig. V-6** shows a comparison of the XAS spectra of capped and uncapped $NSNO_2$(x). The spectra were measured at 10° grazing incidence, with linear polarization forming an angle of 0° or 80° to the NiO_2 planes, and labeled for brevity $\parallel NiO_2$ and $\perp NiO_2$, respectively. While for capped samples the main XAS peak is at an energy (∼852.5 eV) corresponding to the nominal Ni^{1+} ground state, in the uncapped samples the maximum of the XAS intensity is at higher energy (∼853 eV), which can be assigned to the nominal Ni^{2+} configuration upon comparison with reference spectra of NiO. In the uncapped samples, the Ni^{1+} feature shows up as a shoulder on the low-energy side of the main peak. It is relatively more prominent in the $\perp NiO_2$ configuration, and its relative weight with respect to the Ni^{2+} peak decreases with doping, as one should expect. The comparison of the XAS spectra in the two geometries tells that the in-plane 3d states are less occupied than out-of-plane ones. Also, the orbital anisotropy is stronger in our capped samples, and comparable to the ones reported in literature [125,127].

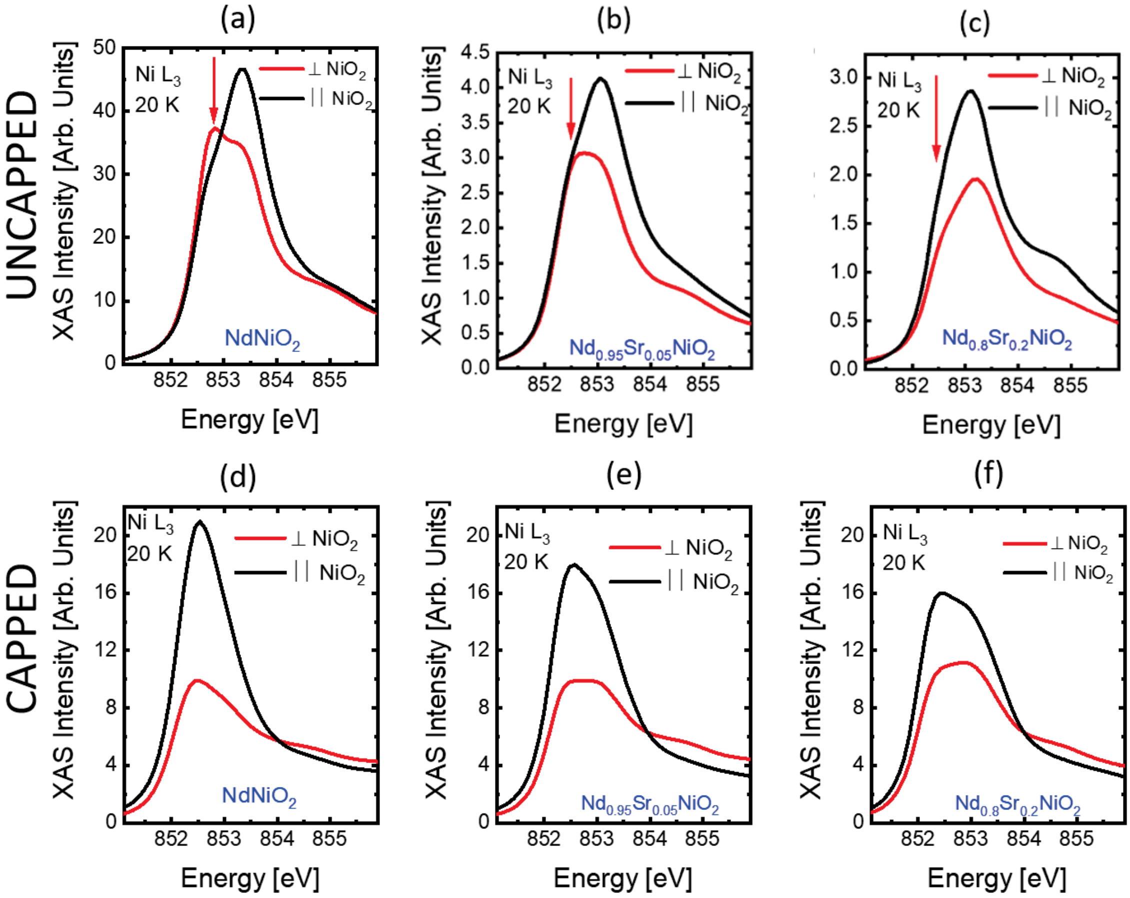

Figure V-6 XAS spectra for the STO-uncapped sample series (top) and capped series (bottom) as a function of the Sr-doping. Spectra were acquired with linear polarization parallel and at 80° to the NiO_2 planes, labelled as $\|NiO_2$ and $\perp NiO_2$, respectively.

5. Charge and spin order dichotomy in $NdNiO_2$ driven by the capping-layer

To obtain information about the low-energy excitation, q-scans were performed along the high symmetry (10), the maps on the right, and (11) directions, the maps on the left, as already introduced in **Fig. V-3(c)**. The momentum-resolved maps shown in **Fig. V-7** have been performed with a q value ranging from 0.22 to 0.45, at an energy of ~852.5 eV corresponding to the main Ni^{1+} XAS resonance **[Fig. V-6]**. The insets of **Fig. V-7(a)** show sketches of uncapped $NSNO_2(0)$ while **Fig. V-7(b)** shows the one from the capped $NSNO_2(0)$ samples. RIXS map of uncapped samples on **Fig. V-7(a)** exhibit a strongly modulated intensity of the quasi-elastic peak, the region around 0 eV energy loss, along the (10) direction. While no modulation is observed along the (11) direction. Such a modulation of the quasi-elastic peak is the signature of localized organization of charge in the material, called charge order (CO). On the contrary, the map of the capped sample in **Fig. V-7(b)** do not show any modulation of the quasi-elastic peak in both directions, (10) and (11). But they both exhibits a low-energy dispersing feature up to $\sim$ 200 meV at the BZ boundary, in agreement with recent results [127]. This specific dispersing feature is the synonym of a magnetic excitation, signature of short-range magnetic order in the infinite-layer phase.

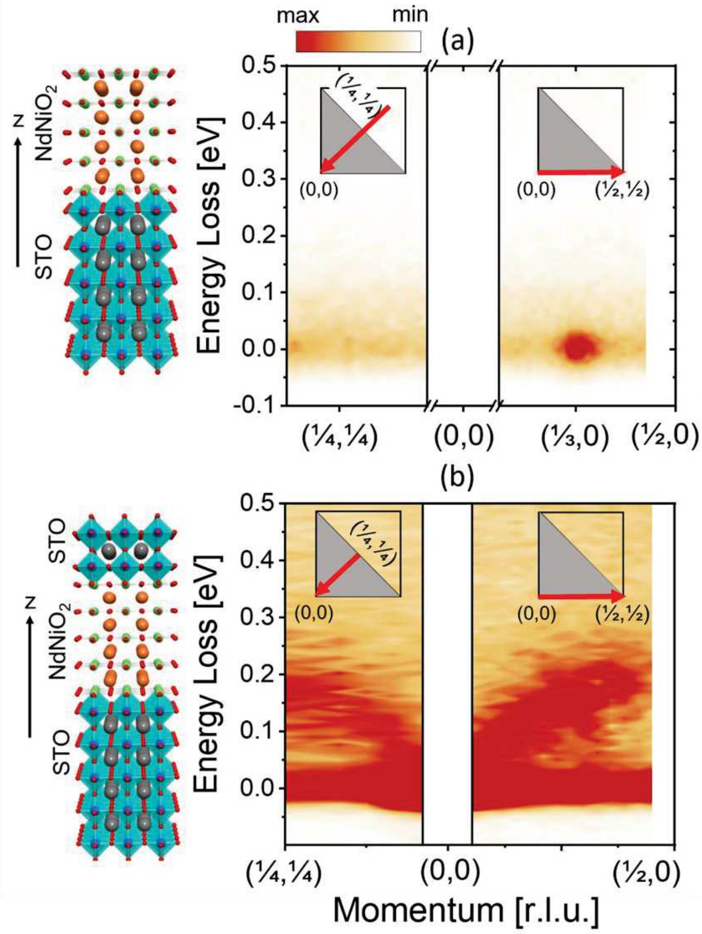

Figure V-7 Summary of the RIXS results for uncapped and STO capped $NSNO_2(0)$ films. (a,b) Energy-loss or in-plane-momentum scattering intensity maps along the high symmetry directions indicated in the insets, excited at incident photon energy $\sim$852.5 eV (Ni^{1+} XAS peak) using π polarization. Lateral panels show sketches of the structure of both (top) uncapped and (bottom) capped samples.

To gain insights on the nature of the resonant quasi-elastic peak, we report in **Fig. V-8(a)** its integrated intensity vs $q_{||}$ along (10), obtained by fitting the RIXS spectra as described before and of which an example is reported in **Fig. V-5**. the observed peak can be fitted by a single Lorentzian centered at H = 0.33 reciprocal lattice units (r.l.u.), with a full width at half maximum (FWHM) of about $\sim$ 0.06 r.l.u., corresponding to a real space periodicity of $\sim$ 3a = 11.7 Å and to a correlation length π·FWHM of $\sim$ 5.3a = 20.7 Å. This feature is strongly resonant, as it disappears when the incident photon energy is detuned by few hundreds meV from the XAS peak as shown in **Fig. V-8(b)**. We can note on this figure that the intensity of the peak is not as strong as the one from **Fig. V-8(a)**, because the modulation intensity of the quasi-elastic peak has been done with samples from **Fig. V-9(b)**, exhibiting a smaller intensity of the quasi-elastic peak. Importantly, no modulation of the quasi-elastic intensity is observed along the (11) direction in both RIXS map **[Fig. V-7(a)]** and as a result of the same procedure for the other direction (10) and which result is shown in orange in Fig. 8a. Also we performed in a relatively smaller q range a series of RIXS measurement as a function of the perpendicular momentum shown in

Fig. V-8(c), where no modulation of the peak is observed from L=0.33 to L=0.25. The absence of modulation of the quasi-elastic peak along the perpendicular momentum suggests a two-dimensional nature of the ordering. Upon doping, the signal quickly weakens by approximately a factor of 3 for x = 0.05 and disappears for x = 0.2. The resonant nature and the peculiar q-dependence suggest close analogies with the charge order of hole doped cuprates [131,231,234]. However, the doping dependence is markedly different, because in cuprates charge ordering is absent below p=0.07 and is maximum at p ~ 0.11–0.13, whereas in nickelates it is maximum at zero doping [131].

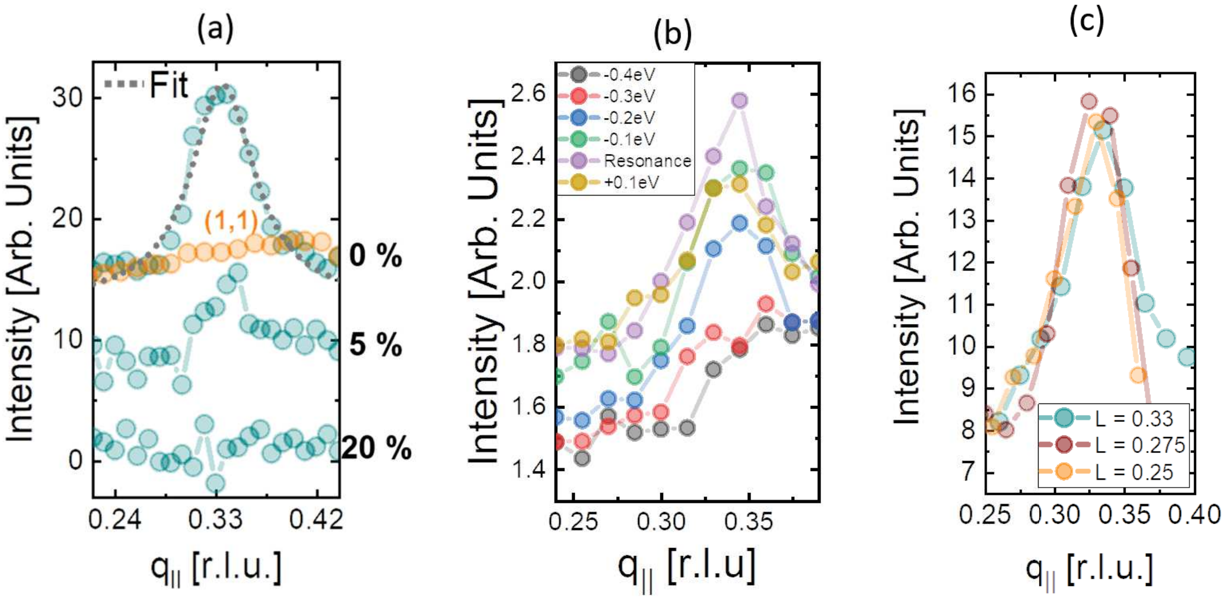

Figure V-8 (a) Quasielastic scattering intensity vs the in-plane transferred momentum along the (10) direction for different doping in uncapped NSNO$_2$(x). Data acquired at 20 K and grazing incidence with π polarization. Corresponding data along the (11) direction (in orange) is presented for comparison as well. (b) Energy dependence of the CDW peak around its resonance energy 852.5 eV for the undoped sample (c) Out-of-plane measurement of the quasi-elastic peak intensity for the undoped sample

Interestingly also NSNO$_2$(0) thin films exhibiting a bad metal character as already presented in Chapter IV gave rise to a similar phenomenology at 20 K, although the measured CO peak along the (10) direction is less intense **[Fig. V-9(b)]**. The CO peak intensity of our NSNO is roughly T independent in the 20–270 K range as shown in **Fig. V-9(a)**, at odds with cuprates except (Bi,Pb)$_{2.12}$Sr$_{1.88}$CuO$_{6+\delta}$ (Bi2201) [237]. The temperature dependence results are not incompatible with a weak evolution of the CO wave vector away from perfectly commensurate, in analogy with the behaviour upon doping observed by Rossi et al. in La$_{1-x}$Sr$_x$NiO$_2$ [129]. Moreover, the CO wave vector q = (~1/3, 0) at low temperature is remarkably reminiscent of the stripe order in trilayer nickelate La$_4$Ni$_3$O$_8$ [238,239]. Especially that in the case of La$_{1-x}$Sr$_x$NiO$_2$ and La$_4$Ni$_3$O$_8$, charge and spin ordering are concomitant in the material, while we observed a dichotomy through the STO capping-layer in NSNO$_2$. We also note that Tam et al. found a strong T dependence of the CO intensity in their NSNO$_2$(0) films [128]. In particular, the normal state is markedly different than in our films, since the high temperature range is dominated by a linear-in-T resistance. On phenomenological grounds, this reminds the scenario occurring in cuprates, where the presence of a narrow quasicritical charge order has been found to be in competition with the strange metal behaviour [233].

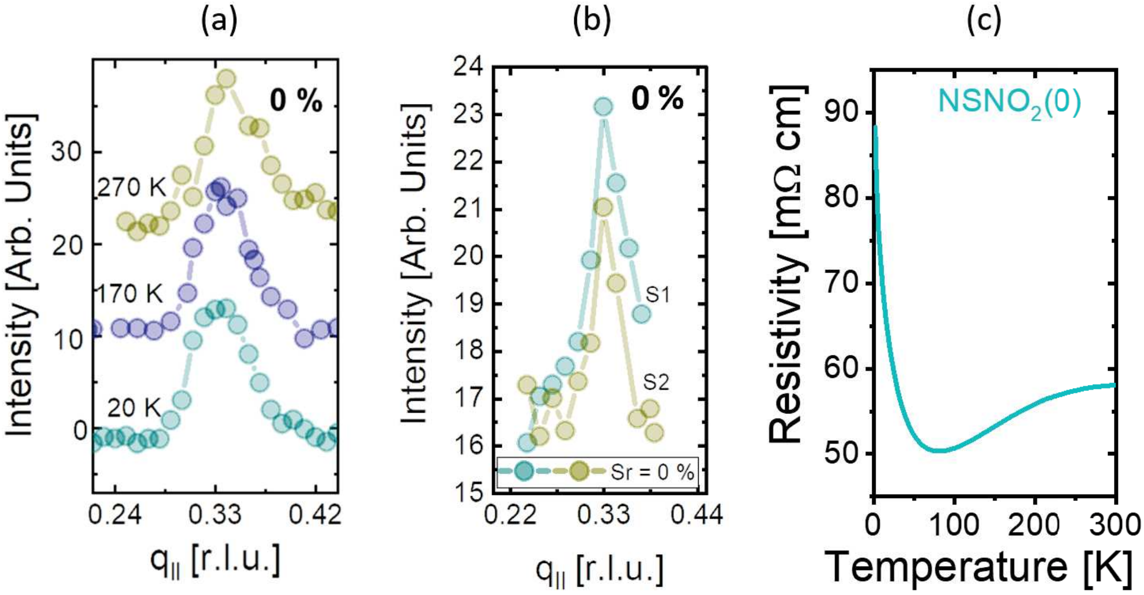

Figure V-9 (a) Temperature dependence of the Quasielastic area along (10) for uncapped NSNO(0) (b) Reproducibility of the CDW peak for two undoped samples showing bad-metal behaviour (c) Resistivity as a function of the temperature with bad-metal behaviour of S1 and S2 samples.

6. From STO to LSAT

It has been shown by two different groups that the use of LSAT as substrate leads to an increase of the T_C onset from 20 K to nearly 40 K [113,114]. This can be explained by an improved crystalline quality of the thin films which is the result of the smaller lattice mismatch between the nickelate perovskite phase when grown onto LSAT single crystals. Therefore, I also tried to grow NSNO$_2$(0) samples onto LSAT and using it also as capping-layer to obtain a first experimental evidence of a possible strain-dependence of the low-energy excitations of the infinite-layer phase. The reduction conditions have been the same as the optimized one presented in Chapter IV, i.e. 30h at 240°C for the LSAT-capped sample in **Fig. V-10(a)** and 14h at 240°C to obtain the uncapped NSNO$_2$(0) in **Fig**. **V-10(c)**. We can observe on both XRD that the NSNO$_2$(0) (002) Braag peak is at 55.5°, in accordance to our optimized samples, but with a lower intensity. However, from our experience, we highlight the importance of an intense (002) Bragg peak to ascertain of a high-quality infinite-layer phase. Nevertheless, we previously shown with NSNO$_2$(0) uncapped samples that even optimized exhibited similar low-excitation features with CO being present for insulating and bad metal samples. Therefore, we decided to measure them and the in-plane momentum scattering intensity maps along the (10) direction are shown in **Fig. V-10(c),(d)**.

On **[Fig. V-10(b)]** it is observed that the choice of LSAT as capping-layer leads to a large decrease of the intensity of the magnon which appears now extremely damped, different from what we observed with an STO capping **[Fig. V-7(b)]**. On the other side, for the uncapped NSNO$_2$(0) grown onto LSAT, we could not observe the presence of both magnetic excitations and CO in **Fig. V-10(d)**. It is to note that the elastic-peak intensity of the LSAT-substrate sample is very intense compare to the LSAT-capped sample as shown in **Fig. V-10(e)**.

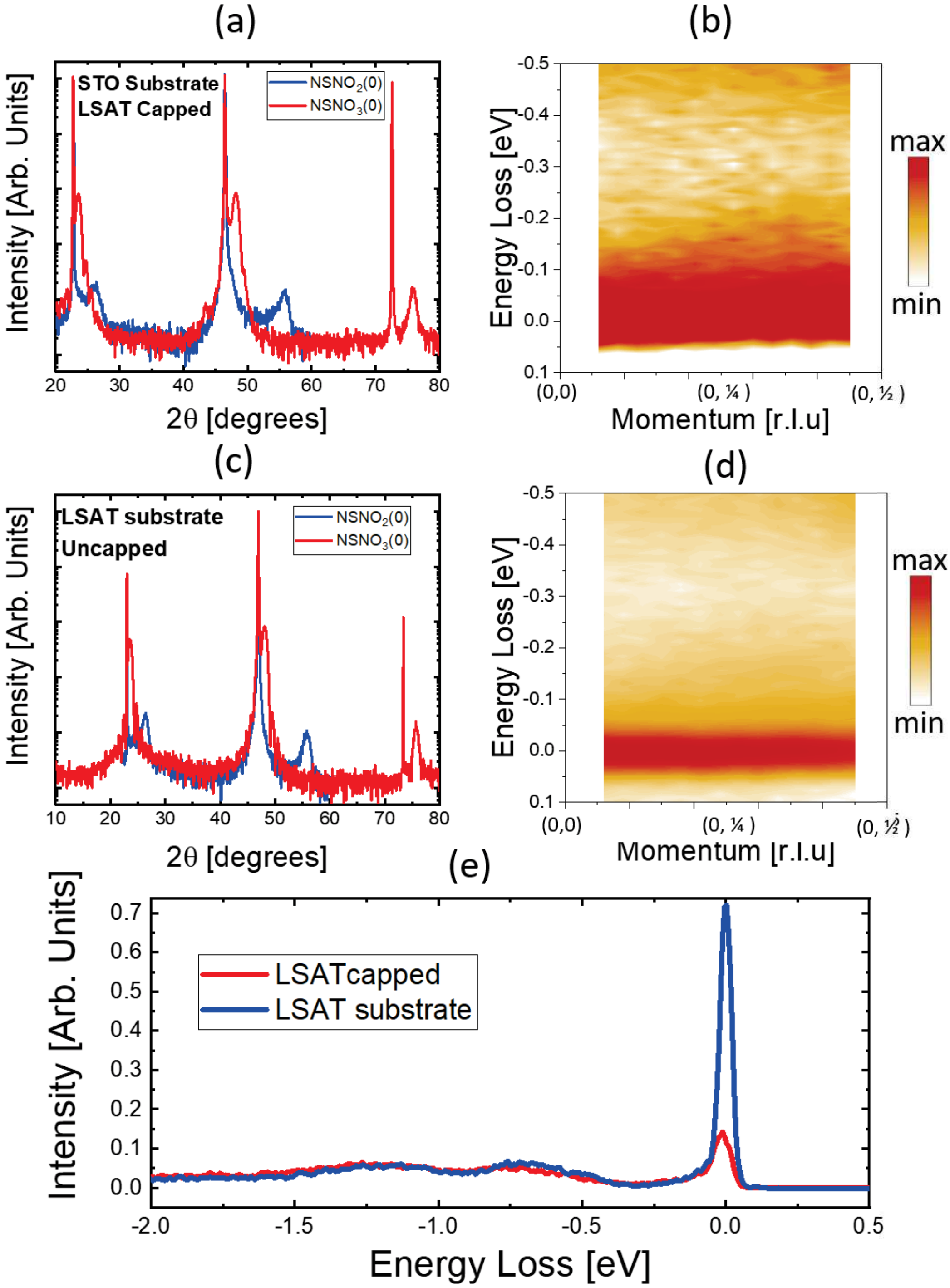

Figure V-10 (a,c) XRD and (b,d) in-plane momentum RIXS map along the (10) direction of NSNO(0) with a LSAT capping-layer grown on STO (top) and a NSNO(0) uncapped grown on LSAT (bottom). (e) RIXS spectra at H=0.45 showing the higher intensity of the elastic peak for LSAT-substrate sample (blue) compare to the LSAT-capped one (red).

7. Ni-Nd hybridization as a function of the Sr doping and the capping-layer

Energy resolved maps have been acquired for NSNO$_2$(0) **[Fig. V-11(a)]** uncapped and **[Fig. V-11(b)]** capped samples in order to observe the low-energy excitations as a function of the absorption energy near the Ni L$_3$-edge. Thanks to those map we have been able to observe a difference in intensity of the excitation around -0.6eV. This feature is commonly associated to the 3d^{8}R final state [124], where an electron is transferred from Ni-3d to Nd-5d, and we observed that is much more intense in uncapped sample. The excitation between -1 and -1.5 eV is the signature of the d-d excitation, which possess an equivalent intensity for both samples. Over -1.5 eV, a more pronounced fluorescence-tail is observed for the capped sample. The STO is known for its strong fluorescence in soft X-ray, therefore the 3 u.c used as capping might explain this more intense feature.

The dashed black line at 852.5 eV represent the resonant of the first peak indicated by red arrows in XAS spectra from **Fig. V-6(a),(b),(c)**, which was the energy used for the momentum-resolved map.

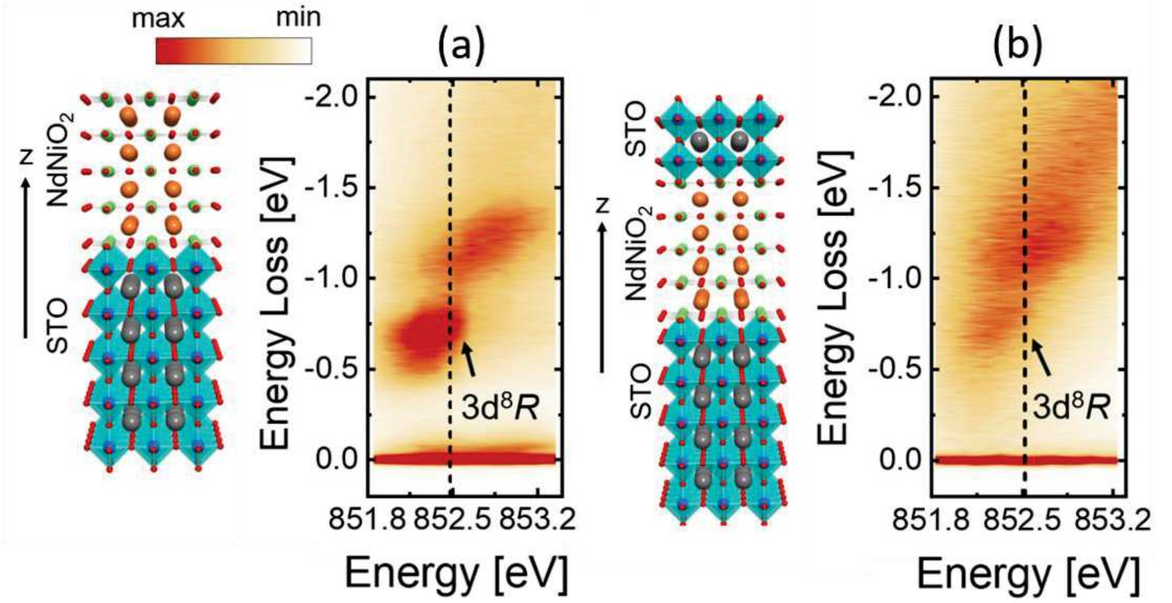

Figure V-11 Energy-loss or excitation-energy maps across the Ni L3 edge at 10° grazing incidence for NSNO$_2$(0) (a) uncapped and (b) capped.

We just observe that the feature related to the Ni-3d and Nd-5d hybridization is more intense when the sample is uncapped. Along the dichotomy between CO and magnons, this is the second striking difference between capped and uncapped NSNO$_2$(0). Hepting et al. [124] already questioned the role of this hybridization in the rise of the superconductivity in infinite-layer nickelate. That's why we also wanted to observe the evolution of this feature at -0.6 eV along the doping for uncapped samples.

In a first time, we observed that the differences in the electronic structure revealed by the XAS spectra in **Fig. V-6** echo in the RIXS maps of **Fig. V-12**. In the uncapped films the 3d^{8}R peak around −0.6 eV energy loss is indeed very strong only in the $\perp$NiO$_2$ geometries and resonates at the Ni^{1+} XAS peak. Moreover, it decreases as a function of the Sr doping similarly to the Ni^{1+} shoulder in the XAS spectra, which suggests a direct correlation between the large Ni-Nd hybridization and the substantial contribution to the ground state of the out-of-plane 3d orbitals. The RIXS spectra at the resonance of the Ni^{1+} peak (852.5 eV) for the different samples are summarized in **Fig. V-12(g)** where the decreasing intensity of the of the -0.6 eV feature is clearly observed, with the capped sample exhibiting a smaller feature than the 20%-doped uncapped infinite-layer nickelate.

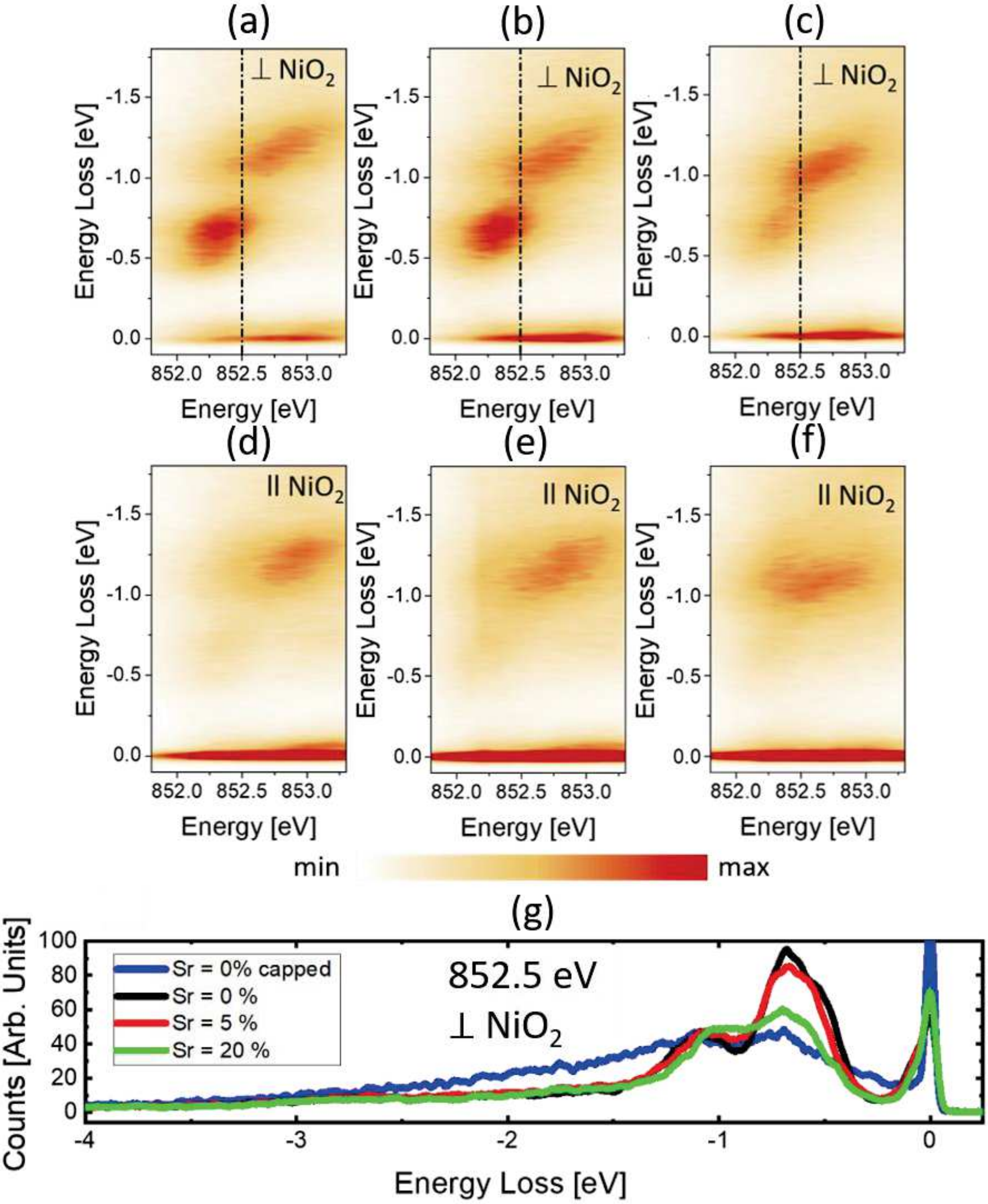

Figure V-12 (a-f) Images of the RIXS energy maps for linearly polarized light 80° to NiO$_2$ (top) and parallel to NiO$_2$ (bottom) as a function of the Sr-doping. (g) RIXS spectra excited at 852.5eV in ⊥NiO$_2$ geometry. It shows that the 3d^{8}R feature at -0.6eV decreases with doping, and also with the presence of the capping with the blue curve for capped NSNO$_2$(0) and the black one for the uncapped.

8. Discussion

The experimental results pose several questions about the relationship between the electronic properties revealed by XAS and RIXS and the quasielastic scattering intensity modulation. In particular, it is unclear whether it should be attributed to a charge density wave phenomenon or to a superstructure in the lattice, and why it is suppressed in capped samples that, on the other hand, show dispersing magnon-excitations. Moreover, switching from a STO substrate to a LSAT one makes disappear the localization of the quasielastic peak intensity in uncapped $NSNO_2(0)$, only leaving an intense elastic peak without clear modulation. While switching from a STO capping-layer to a LSAT makes vanish, or highly damping, the magnetic excitation which characterized the capped $NSNO_2(0)$ samples. However, the upcoming discussion will not take in consideration the preliminary observation we obtained with LSAT substrate or capping, as I did not gather enough measurements to pretend to understand the influence of a modification of the substrate on the electronic structure. Furthermore, I highlight the unoptimal quality of the LSAT samples present in **Fig. V-10**, casting doubt on the few measurements we performed.

From our study on $NSNO_2(x)$ samples grown (capped) on (with) STO, an intriguing correlation emerges between a strong out-of-plane Ni-Nd hybridization and the observation of CO in undoped and slightly Sr-doped infinite-layer nickelate thin films, which is difficult to understand at this stage. According to our data, the resonant character of the CO peak has to do with a spatial charge modulation within the NiO_2 planes. In undoped NSNO(0) this implies an intrinsic hole doping of the planes, which can be explained in terms of an electron transfer from Ni toward Nd states, hence a self- doping of the system; recent density-functional theory calculations [122] estimated that this effect could account for as much as 0.1 holes/Ni in bulk $NdNiO_2$. Interestingly, we also observed the CO peak centred at H=0.33 r.l.u at the Nd M_5 edge in **Fig. V-13**, which, although probing Nd-4f states, indirectly reflects a charge modulation of the Nd-5d states. We note that this sensitivity of rare-earth electrons to charge modulations has been observed before in bilayer cuprates [170], where the local environment of the rare-earth atom is equivalent to infinite-layer compounds. Thus, the picture that emerges is a correlation between the strong Ni-Nd out-of-plane hybridization and CO, which both compete with magnetic excitations and, ultimately, with superconductivity. Thus, the physics of cuprates is effectively re-established in infinite-layer nickelates only if the Nd-5d states are sufficiently far in energy from the Ni-$3dz^2$ states.

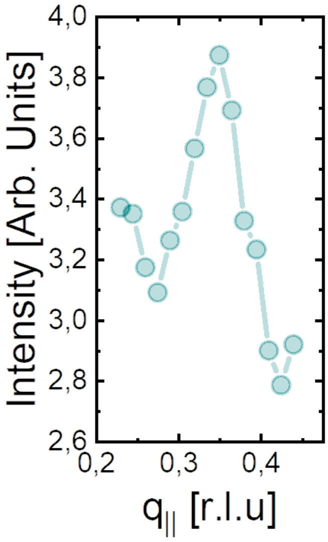

Figure V-13 CO peak at the Nd M5-edge for the undoped sample with an energy of 978.68eV

Our results call for a discussion of the role of the STO capping layer in the very unique electronic properties of $NdNiO_2$. From the structural analysis of the two sample families, we do not find relevant differences in the average distance between the NiO_2 planes. However, differences might be induced by the kinetics of the topotactic reaction, influenced by the presence of the capping layer. In particular, the topotactic deintercalation of oxygen ions might result in the eventual inclusion of hydrogen ions. According to density-functional theory calculations [103], the $NdNiO_2H$ phase, is favourable in $NdNiO_2$, while unfavourable in Sr-doped $NdNiO_2$. The two phases differ substantially in their electronic properties but have mostly identical lattice parameters. In particular, the Nd-5d electron pocket at the Fermi level disappears in the case of the $NdNiO_2H$ phase with a predominant Ni^{2+} valence state, and almost equal occupancy of $3dz^2$ and $3dx^2{-}y^2$ orbitals.

Some of these electronic characteristics are, indeed, observed in uncapped $NSNO_2(x)$. Therefore, while it can be regarded as an unlikely occurrence, we cannot discard the possibility that H atoms get organized as a superstructure, in itself invisible to x-ray diffraction, able to induce a modulation of the electronic structure that results in a CO peak. Neutron diffraction might be the only structural characterization that might scope the presence of H atoms in a lattice, hence the necessity to obtain high quality powder and/or single-crystal infinite-layer, as thin film does not possess enough matter to perform such measurements. We can also speculate that an incorporation of H might increase the c-axis parameter and that high resolution STEM images might be able to detect such a small hypothetic extension of the lattice. Nevertheless, one might speculate that H atoms reduce the occupation anisotropy of Ni-3d states by acting as a bridge to the Nd planes, although calculations predict an overall reduction of the hybridization of Ni-$3dz^2$ and Nd-5d states by interstitial hydrogen. It remains that we observe a positive correlation between the $3d^8R$ RIXS feature and the intensity of the CO peak.

These results suggest that the stability of the superconducting state in nickelates could be effectively extended by reducing the role of the rare-earth electronic states on the NiO_2 planes. In that sense, recent results highlight the increase of the T_C from 20K up to 40K by uniaxial pressure [119] or compressive strain imposed by the substrate [113,114]. We could also think of modulate the occupation of the electron pocket through light-induced excitation that could populate the Nd-5d which would destroy the hybridization with the Ni-3d.

2. Zoom on the magnetic excitation via polarimeter measurements

The aforementioned results have shown the importance of the capping-layer on the electronic structure and elementary excitations characterizing the infinite-layer nickelate thin films presented in this thesis. To uniquely consider the feature around 70 meV energy loss like a phonon as discussed before, we performed polarimeter-based RIXS measurement to ascertain the effective magnetic nature of this excitation. That's why we mainly focus this study on the capped $NSNO_2(x)$ samples with x=0, 0.05 and 0.20, in order to explore the evolution across the doping of the magnetic excitation observed in undoped sample.

1. Motivation for this experiment

In cuprates, undoped parent compounds are defined as Mott insulators, with antiferromagnetic square lattice formed by the spin –½ of the Cu^{2+} ions within the CuO_2 planes [207]. Then, the superconductivity arises when the number of mobile carriers, being electrons or holes, is tuned with chemical substitution or by varying the oxygen content in the charge reservoirs [240]. The close interplay between the antiferromagnetism and the superconductivity is still debated with the antiferromagnetic fluctuations potentially acting as a glue for the pairing mechanism [241]. In particular, despite the loss of the long-range antiferromagnetic order in cuprates across the superconducting dome, it has been observed by RIXS that short-range AF correlations persist in cuprates up to very high doping levels [133,209,242–244]. In that sense, the change of the spectral weight of the magnetic excitation along the hole-doping in infinite-layer nickelate is different from what has been observed in copper oxide-based superconductors compounds [127,133]. The most probable explanation for the infinite-layer nickelate behaviour is a spin dilution due to the incorporation of holes, causing the substitution of spins by holes [127]. We already speculated about the interplay between the Γ-centered electron-pocket, linked to the Ni-Nd hybridization, being in competition with the rise of the superconductivity at first sight. A complete study about the damping of the magnetic excitations via hole-doping and/or the presence/absence of the capping-layer, might provide useful information on the pairing mechanism in the infinite-layer nickelates system. However, the broadening of the spectra upon hole-doping represents an experimental issue for the analysis of the short-range magnetic order, being the highest energy resolution is not sufficient to resolve and unambiguously assign spectral features [207]. However, this limitation can be lifted by measuring the polarization dependence of the low-energy excitation of the RIXS spectra, on the expense of the time of acquisition

Here, the difference of the magnons observed for $NSNO_2$(0)-capped/uncapped and $NSNO_2$(20)-capped infinite-layer nickelate thin films have been explored with polarimeter-assisted RIXS measurements at the Ni L_3-edge. We have been able to confirm also in our samples the presence of a damped magnon upon hole-doping [127], but more importantly, we could univocally associate to the LE-feature observed for undoped and uncapped samples to a damped magnon .

2. Origin of the magnetic excitations in a RIXS process

The magnetic excitation of the short range magnetic order is associated to a sign-spin variation in the d orbitals involved in the superexchange with the neighbouring oxygen [211]. Let's first remember that in the case of the cuprates and also nickelates being both tetragonally coordinated with the oxygen nearest-neighbours, the d orbital degeneracy is lifted by the crystal field. In the $3d^9$ ground state, there is only one hole in the $3d_{x^2-y^2}$ orbital, prevented from selection rules to jump to another d state [211]. As described in the absorption emission scheme in **Fig. V-14**, the hole created in the 2p states by the excited electron, can be filled by any other electron of the d orbitals. If the two electrons involved in the process have an opposite spin, a spin-flop of the of the hole is obtained. This is in principle possible since the strong spin-orbit coupling of the 2p states makes the spin not a good quantum number [242]. This results in the situation in which any electrons can fill the hole of the 2p state, independently of their respective spin. In that sense, if the electron comes from any of the d orbitals, the change of the spin does not affect the excitation, apart if it comes from the $3d_{x^2-y^2}$ orbital. It is due to the superexchange with the neighbouring oxygen where only the $3d_{x^2-y^2}$ orbital is involved, meaning that if there is a change of spin in this orbital, the system energy increases because of the antiferromagnetic coupling constant J. The increase of the system energy creates what is called the magnetic excitation, for which the conservation of the angular momentum require a switch of 90° of the light polarization [132], enabling its measurement via a polarimeter.

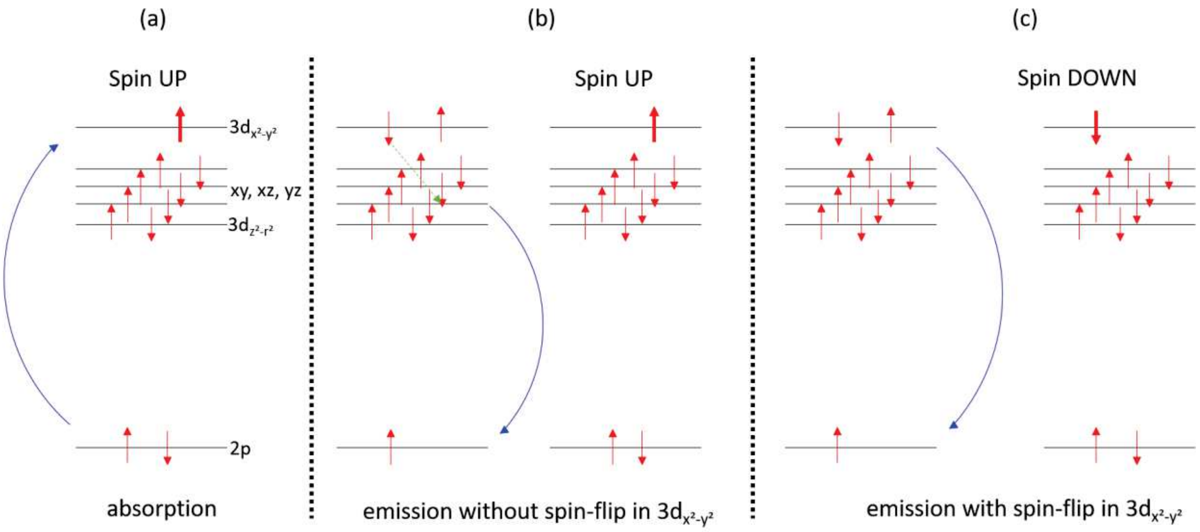

Figure V-14 (a) Excitation of a core-hole electron through x-ray absorption (b) desexcitation of the unstable d-state leading to a photon emission without spin-flip (c) desexcitation of the unstable d-state leading to a photon emission with spin-flip

3. Energy dependence of the magnetic excitation

To assure a proper measurement of the magnetic excitations one has to better define at which photon energy perform the RIXS experiments. Figures 15a shows the evolution of the magnetic excitation around the Ni L_3-edge within a 1.2 eV range. I show in **Fig. V-15(b)** the normalized intensity of the magnetic excitation, obtained by fitting the data as shown previously in **Fig. V-5** and represented by the solid lines in **Fig. V-15(a)**. It is clearly observed that the magnon weight resonates strongly in a narrow energy range, which corresponds to the energy associated with the Ni^{1+} state, therefore one can conclude that the magnon is associated to the NiO_2 infinite-layer planes.

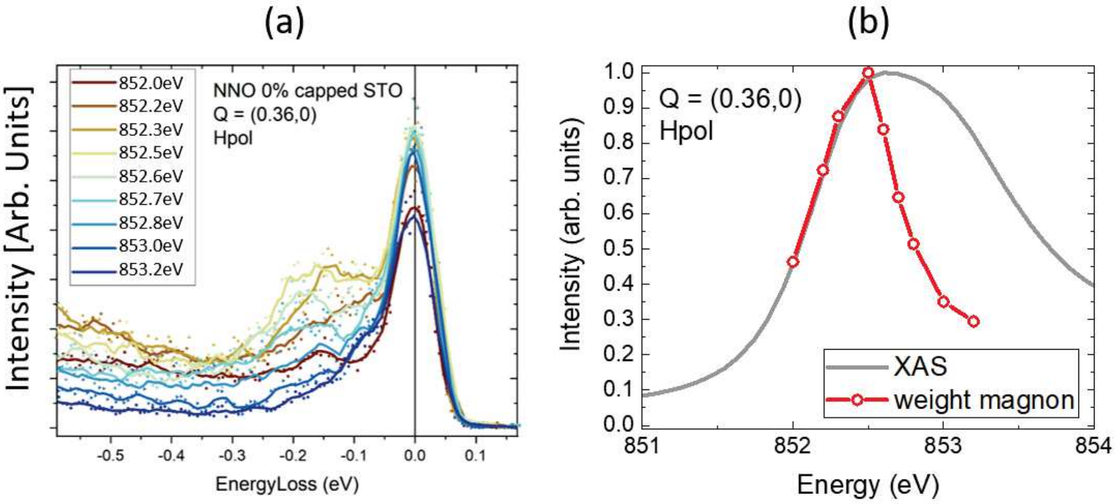

Figure V-15 (a) Energy dependence of the RIXS spectra around the Ni L_3-edge of $NSNO_2(0)$ capped thin film (b) Energy dependence of the weight of the magnon compared to the XAS spectra of the $NSNO_2(0)$ capped thin film.

4. Polarimeter working principle

The ID32 beamline at the ESRF is currently the only facility that provide the use of a polarimeter, which allowing to measure the change of the scattered light polarization can help in determining the magnetic nature of the studied excitation. The polarimeter is based on a W/B_4C multilayer mirror and is located just before the CCD detector as shown in **Fig. V-16**.

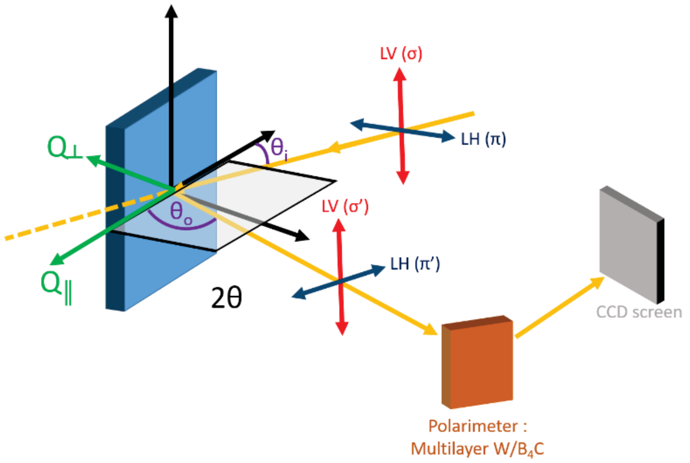

Figure V-16 Scheme of the RIXS measurement geometry while using the polarimeter

It operates by exploiting the different relative reflectivities of the mirrors for both LH (or π) and LV (or σ) light polarizations. In a first time, the total intensity I of the beam is measured, hence without the polarimeter, which is here the sum of both polarization contribution I_σ and I_π. Then, the measurement with the polarimeter has to take into account the different reflectivity for the two polarizations R_π and R_σ, leading to a total intensity of $I_{pol} = R_\pi I_\pi + R_\sigma I_\sigma$. When the reflectivities of both mirrors are known, the contribution of both polarizations can be obtained by solving the two-equations system:

$$\begin{cases} I_{dir}=I_\pi+I_\sigma \\ I_{pol}=R_\pi I_\pi+R_\sigma I_\sigma \end{cases}$$

Which gives

$$\begin{cases} I_\pi=\dfrac{R_\pi . I_{dir} - I_{pol}}{R_\pi - R_\sigma} \\ I_\sigma=\dfrac{R_\sigma . I_{dir} - I_{pol}}{R_\sigma - R_\pi} \end{cases}$$

The working angle of the mirror is ≈20°, leading to a reflectivity for each polarization $R_{\pi'} = 0.09$ and $R_{\sigma'} = 0.16$. This leads to an average efficiency of the device being $R_0 = (R_{\pi'} + R_{\sigma'})/2 = 13\%$. As a result, each spectrum to have an optimal signal-to-noise ratio has been acquired for longer time (five hours) if compared to the RIXS spectra presented in the previous sections (half-hour). In this new configuration shown in **Fig. 16** we obtained the crossed-(πσ’) and parallel-(ππ’) polarization spectra corresponding to the spin-flip (ΔS = 1) and the no-spin-flip (ΔS = 0) final states, respectively. The magnon is assigned to a peak exhibiting a spin-flip behaviour, while phonons and elastic peak are spin-conserving [207]. All measurements were performed at a photon energy of 852.5 eV at which the magnon shows its largest magnitude as put in evidence from the photon-energy dependence measurements at 20 K and shown in **Fig. V-16**.

5. Polarimeter measurements

I have participated to the polarimeter measurements while the related analysis of the spectra has been done by Leonardo Martinelli and Francesco Rosa, PhD student and Master Student, respectively at Politecnico of Milan under the supervision of Prof. Giacomo Ghiringhelli. The polarimeter spectra were acquired at H = 0.36, since it corresponds to the highest intensity value for the magnon, using π (horizontal, LH) and σ (vertical, LV) polarization for the incident beam.

The red-curves of **Fig. V-17(a)** represent the crossed-polarization components of the RIXS spectra, while the blue ones represent the parallel contributions, and finally the black curve is the sum of both crossed and parallel polarization channels. It is observed that the quasi-elastic peak is mainly represented by the parallel contribution, while the magnetic excitation around 0.2 eV occurs principally in the crossed-polarization channel. The damping of the magnon with the doping is represented in **Fig. V-17(b)** where the intensity of the crossed-polarization is plotted together with the asymmetric Lorenztian used to fit the low-energy feature from the total spectra. The intensity of the magnon and its energy dispersion are lower for the NSNO$_2$(20) sample. In **Fig. V-17(c)**, the flipping ratio is defined by : $\frac{\pi\sigma' - \pi\pi'}{\pi\sigma' + \pi\pi'}$, hence a positive ratio when the crossed-contribution is bigger than the parallel, and a negative one in the opposite case. As already mentioned, the elastic peak, and also the phonons, are defined by a higher proportion of parallel-polarization, defined by the negative ratio close to zero energy loss. The presence of the magnetic excitation increases this ratio until it becomes positive around 0.2 eV, where the magnons dispersion is observed.

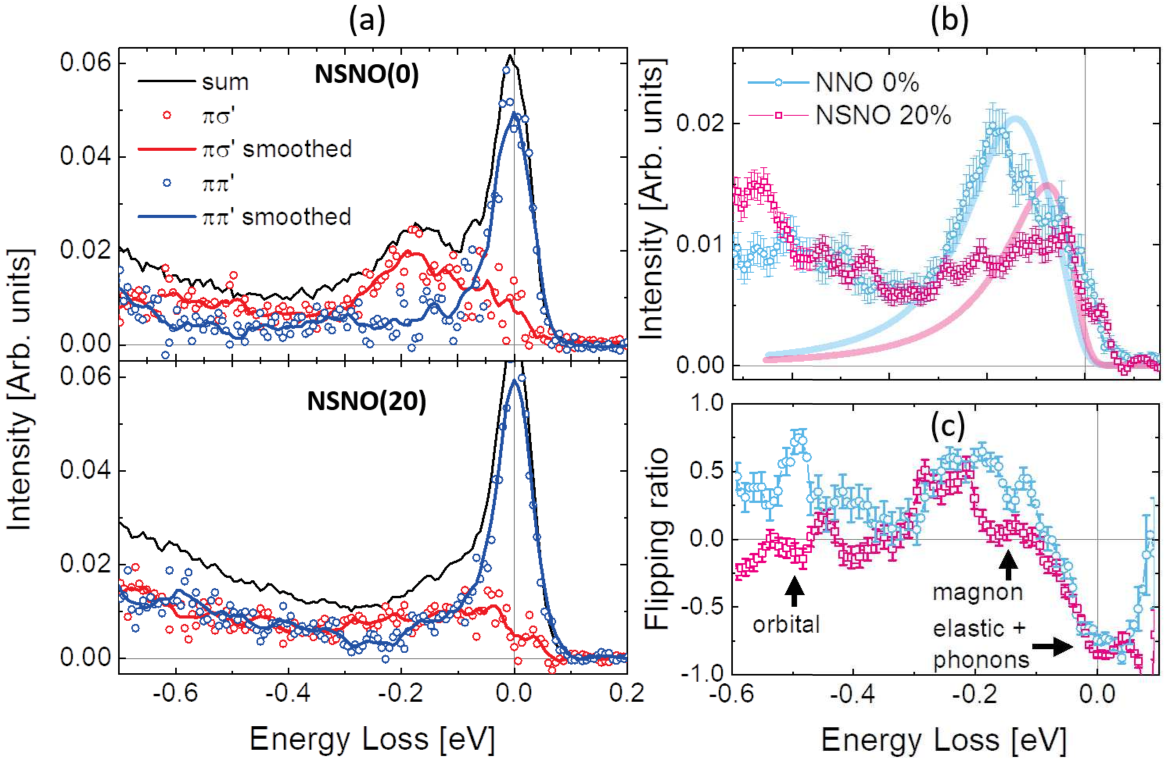

Figure V-17 (a) Polarimeter scan for $NSNO_2$(0) (top) and $NSNO_2$(20) (bottom) (b) Comparison of the spin-flop intensity for $NSNO_2$(0) and $NSNO_2$(20) where the solid lines in the top panel represent the fit with an asymmetric Lorentzian function of the spin-flop intensity, and the scattered-points the experimental data (c) Comparison of the flipping ratio between $NSNO_2$(0) and $NSNO_2$(20)

Since polarized-resolved measurements can unambiguously prove the magnetic nature of a RIXS feature we performed similar measurements also for our uncapped undoped samples. By recalling the main findings about those samples we can summarize that they exhibit a peculiar CO and Nd-Ni hybridization which amplitude is weakened upon Sr-doping. Interestingly, as shown in **Fig. V-18** $NSNO_2$(0)-uncapped samples are characterized by a clear spin-flip signal after the phonon with a non-zero crossed-polarization contribution around 0.2 eV, mimicking the results obtained in the case of STO-capped thin films. Also, inset of **Fig. V-18** shows a higher flipping ratio of the uncapped $NSNO_2$(0) compared to the capped $NSNO_2$(20) below 0.2 eV, hence the magnon seems more damped for the doped sample.

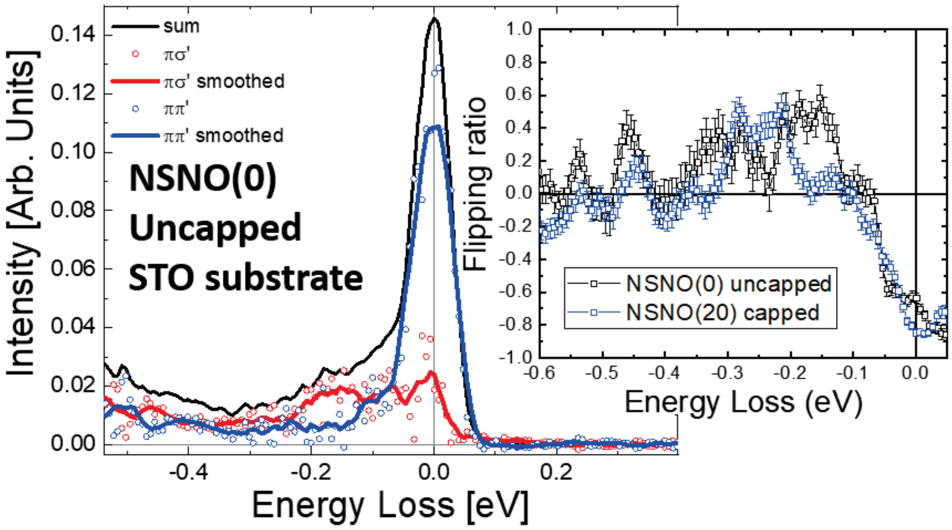

Figure V-18 Polarimeter scan for NSNO(0) uncapped grown on STO substrate. Inset shows the smoothed crossed-polarization πσ' signal for uncapped NSNO$_2$(0) and capped NSNO$_2$(20).

Finally, polarization-resolved RIXS measurements for uncapped NSNO$_2$(0) samples showing a non-zero spin-flip signal of the low-energy excitations, unambiguously demonstrates that they are associated to clear magnetic excitations, although largely damped if compared to the ones observed for capped samples. As already shown before in **Fig. V-12**, our uncapped samples exhibit a large hybridization between Nd 5d and Ni 3d states, and this might be linked to the much more damped property of the magnetic excitations if compared to the capped-NSNO$_2$(0). The magnon is also damped for large doping in capped samples so one first possibility to explain this result is to consider doping effects. The problem here is that we do not really know how many holes we have in the NiO$_2$ planes for both capped and uncapped samples. By looking to the XAS in **Fig. V-6** it seems that the one acquired for the uncapped samples show a large presence of Ni^{2+} which is an intrinsic effect of the Sr-doping. So one may affirm that the more damped nature of the magnon observed for the uncapped and undoped sample reflect only a property linked to an 'effective' doping which is perhaps the result of a larger hybridization with Nd states. Also, one has to consider that the Nd states influencing the charge carrier density at the Fermi level may destroy/limits the magnetic interaction between the spins of the Ni sub-lattice because of a relatively strong Nd-5d Nd-4f intra-atomic exchange coupling [161]. This coupling of an energy estimated around 0.5 eV introducing a spin-disorder of the electron pocket at Γ-point trigger the more damped characteristic of the magnons for the uncapped sample.

Here, we tried to obtain an insight on the role of the magnetic excitations for the superconductivity in infinite-layer nickelate. We have observed that, just like the CO, the magnon seems to be in competition with the superconducting state. While a competition between the CO and the superconductivity has already been observed in cuprates [245], it does not seems to behave similarly between the magnon and the superconductivity state. It even seems to be the opposite, as the presence of the short range magnetic order has been designated as the main candidate to be the driving force of the pairing mechanism [130,241]. The supposed glue role of the magnetic excitation is due to the persistence of their intensity and dispersion across the superconductive dome, with an observation of a damping only for heavily overdoped samples [244,246]. Whereas the magnetic excitation in nickelate in already highly damped inside the superconducting dome, which could suggest a different pairing mechanism as the cuprates.

In that sense, Gao, Q. et al. have already shown that the enhancement of the T_C through LSAT substrate does not scale directly with the bandwidth of the magnons in $PrNiO_2$ infinite-layer nickelate [247]. So apparently, no strong correlations are observed between short range magnetic order and superconductivity in this material at first sight.

3. Modification of the magnetotransport measurements through the capping-layer

1. Motivation for magnetotransport measurements

The RIXS studies presented above have shown the effect on the capping-layer on low-energy excitation of the infinite-layer phase [126], and the damping of the magnetic excitation upon the increase of the Sr-content or the absence of the capping-layer. This could be the first indication on the decisive role played by the electron-pockets due to the Nd-Ni hybridization [127] and maybe providing a valuable direction to study the pairing mechanism itself.

In this context, MR and AMR (defined in experimental methods Chapter) measurements resulting from the intimate interaction between the charge carriers and the spin sub-lattice can offer information about possible differences of the magnetic structure for capped/uncapped infinite-layer nickelate thin films. By monitoring the transport properties under a magnetic field (H), especially in the undoped region of the dome, we expect to observe a signature of the Nd-Ni hybridization which strength is, indeed, modulated by the presence/absence of the STO capping-layer [126]. A comparison with the modulation of the MR and AMR measurements in cuprates and their interpretation will be made along the Chapter. It is worth noting that the interpretations of the different measurements are very different as being highly material dependant. Indeed, data on cuprates are mainly discussed in terms of different mechanisms encompassing the presence of antiferromagnetic long-range order [139–141], spin-orbit coupling [248–250], spin-charge segregation or stripes [251], spin flop transition [252] or antiphase boundaries [253]. Those distinct explanations indicate still a non-reached consensus about the understanding of AMR signals in cuprates, while offering, nevertheless, a potential avenue in uncovering their magnetic nature.

2. The puzzling role of the capping-layer

Magnetoresistance (MR) and anisotropic magnetoresistance measurements (AMR) have been performed on uncapped and STO-capped $NSNO_2(0)$ grown onto STO. It will be shown that the MR as well as the AMR vanish rather quickly upon increasing the temperature, and that the intensity is largely modulated by the presence/absence of the capping layer. Additionally, for the out-of-plane AMR, the overall twofold oscillation symmetry is modified by the appearing of an extra fourfold term at relatively high magnetic fields, this represents the main difference of the anisotropic magnetotransport behaviour that we have found between capped and uncapped infinite-layer nickelate thin films.

• Magnetoresistance measurements

Fig. V-19(a) shows a schematic representation of the MR measurement where the magnetic field varies always in a perpendicular direction to both current direction and sample surface. A relatively large value of the negative MR is observed at 2 K and 9 T, i.e. -7 % **Fig. V-19(b)** which rapidly decreases for higher temperature until reaching almost zero value around 40 K. The MR magnitude is found to be larger for the capped $NSNO_2$(0) samples (full line) if compared to the uncapped ones (dashed lines). By calculating the ratio MR(capped)/MR(uncapped) at 9T one can see that this difference in the magnitude tends towards the unit at higher temperature and at 40 K there is no difference between the MR measured between capped and uncapped samples.

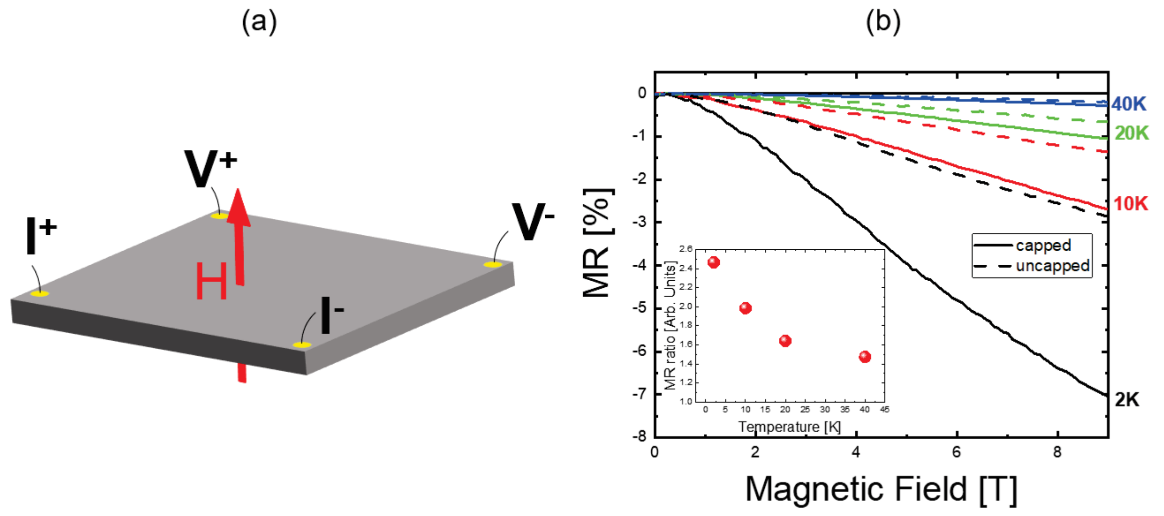

Figure V-19 (a) Schema of the MR measurements. (b) MR from -9 T to 9 T as a function of the temperature for undoped samples. Inset represents the ratio between the MR at 9T for the capped sample divided by the uncapped one, as a function of the temperature.

By a close inspection of the MR curves as a function of the external magnetic field, we can note that up to 9T no spin-flop mechanism is observed which account for a saturation of the MR value above a given threshold magnetic field value. In *e*-doped cuprates [136,252,254], the spin-flop has been ascribed to the presence of a non-collinear antiferromagnetic spin-arrangement in adjacent CuO_2 planes where the spin moment of magnetic ion (i.e. Cu) changes its arrangement in the structure as a function of the direction of the applied magnetic field. On the other side, in the case of hole-doped cuprates [255], it has been in particular associated to the presence of stripe order. However, the magnetotransport measurements and their interpretation are extremely material dependent, and require other types of measurements to fully explain the observed behaviours. As an example, a negative MR behaviour has been observed also for $NdNiO_3$ thin films with similar magnitude and for which the authors claimed it to be due to local disorder [256]. In that sense, if the disorder might have an influence in the perovskite phase, it could still be at play when reduce to the infinite-layer phase.

• Anisotropic magnetoresistance measurements

We performed angular-dependent anisotropic magnetoresistance (AMR) measurements allowing the magnetic field (H) rotation for both in-plane (IP) and out-of-plane (OOP) geometries. **Fig. V-20(a)** sketches the H rotation with respect to the sample surface and the current I. Be referring to those sketches, the AMR amplitude is defined as: $\rho(\varphi/\theta)$-$\rho(0)/\rho(0)$. **Fig. V-20(b)** shows a clear fourfold φ-dependence for the IP-AMR data acquired at 2 K and 9 T for both capped and uncapped $NSNO_2(0)$ samples. This fourfold symmetry is found to characterize both samples series down to 1 T. Below this value we did not observe any significant modulation of the resistance with the φ angle. The IP-AMR magnitude is larger for the capped $NSNO_2(0)$ samples, and we observe in both cases the maximum of the IP-AMR at $\pi/4$, along the Ni-Ni bonds, and the minimum at $\pi/2$ along the Ni-O-Ni bond. As shown in **Fig. V-20(c)** the IP-AMR magnitude decreases as the temperature is increased (fully vanishing above 20 K), and it increases as H is moved to higher values with a rather clear tendency to saturate, for both capped and uncapped samples.

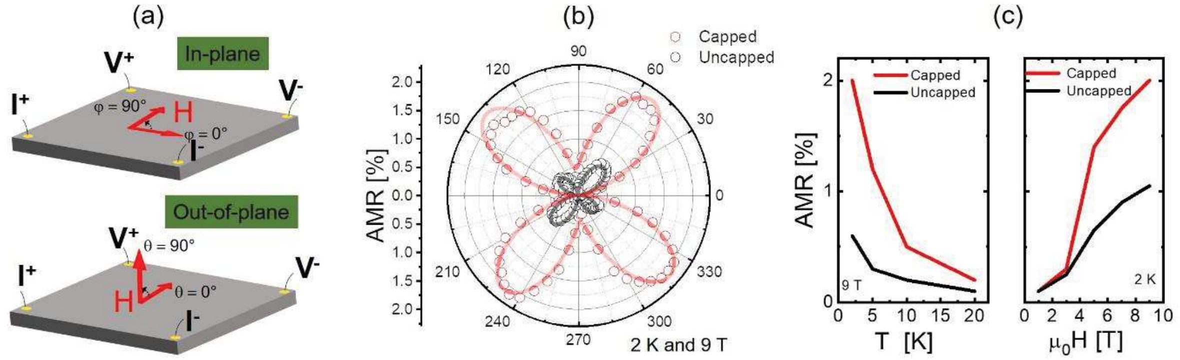

Figure V-20 (a) Transport configuration for in-plane (IP) and out-of-plane (OOP) AMR measurements, (b) Polar plots of in-plane AMR as a function of the φ angle for measurements performed at 2 K under a magnetic field of 9 T for both capped and uncapped NSNO(0)-experimental data as dots and fitting represented with lines, (c) temperature- and field-dependences of AMR for both capped and uncapped NSNO(0).

Fig. V-21(a,b) show the polar plot of the OOP-AMR data acquired at 2 K as a function of H for both capped and uncapped NSNO(0) samples. The OOP-AMR differ from the IP-AMR in the fact that they show an overall twofold symmetry. The magnitude of the signal is still larger for the capped samples, but these samples exhibit a non-monotonous H dependence, with a maximum around 4 T. On the contrary, the uncapped samples show an OOP-AMR intensity constantly increasing as a function of H, with a tendency to saturate at higher field values (upper panel of **Fig. V-21(c)**), like the IP-AMR data.

To gain further insights on our AMR data we decided to decompose them by using the following phenomenological formula, which accounts for both twofold and fourfold components [140]:

$$\rho(\theta/\varphi) = A_2\cdot\sin[2\cdot(\theta/\varphi-p_2)] + A_4\cdot\sin[4\cdot(\theta/\varphi- p_4)] + C,$$

where A_2 and A_4 are the amplitudes of the twofold and fourfold terms, respectively, and p_2 and p_4 their respective phases. C is a constant for a given set of H and temperature values. The θ and φ angles are defined as sketched in **Fig. V-20(a)**. It was possible to satisfactorily fit the IP-AMR data with this formula, as shown in **Fig. V-20(b)** (solid lines). This fitting confirms that the fourfold A_4 component is indeed much more prominent for the capped samples, as expected from our results. It was also possible to perfectly fit the OOP-AMR data acquired at 9 T and 2 K for both capped and uncapped $NSNO_2(0)$ (**[Fig. V-21(d)]**). The overall two-fold symmetry is largely modified by a feature appearing at θ = 0°, 180° especially pronounced for the capped samples. From the fitting procedure, we found that the fourfold oscillation contribution A_4 is larger for the capped samples (as in the case of IP-AMR) and increases with increasing H (lower panel of **Fig. V-21(c)**). The twofold contribution A_2 term, for its part, shows the same H dependence as the overall OOP-AMR for both capped and uncapped samples (upper panel of **Fig. V-21(c)**). The slight dropout observed at 9T evidences the increased relevance of the A_4 contribution for high fields.

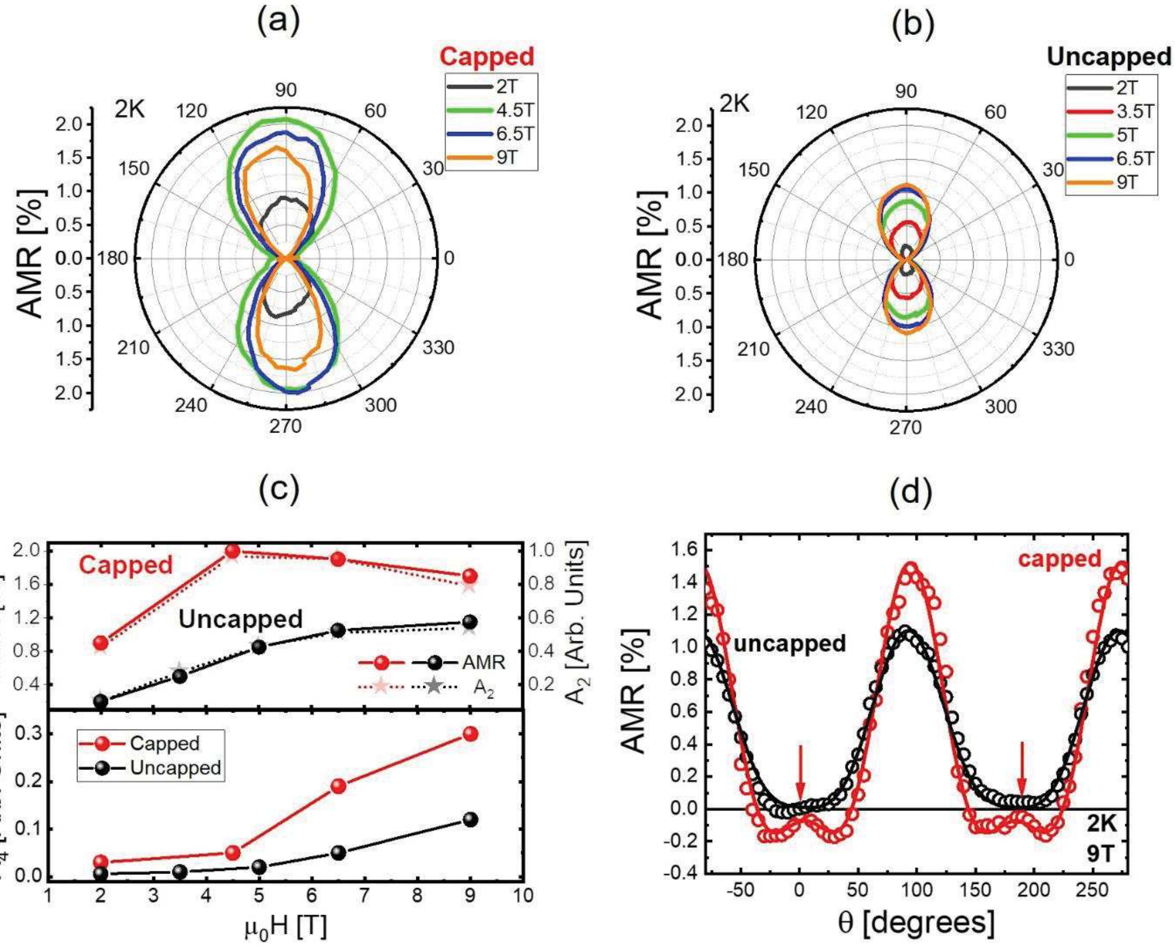

Figure V-21 Polar plots of OOP-AMR for (a) capped and (b) uncapped samples (c) (upper) Comparison of the two-fold contribution A_2 parameter with the overall OOP-AMR as a function of the magnetic field for capped (square) and uncapped (circle) NSNO(0) (lower) magnetic field dependence of the four-fold contribution A_4 parameter for capped and uncapped NSNO (0) (d) Evidence of a four-fold component (red arrows) on the OOP-AMR measured at 2K and 9T.

We previously presented the variety of mechanisms involved in the explanation of the MR and AMR behaviour, notably in cuprates. *De facto*, the AMR phenomenology can become even more intriguing when one has to consider also the 4f magnetic moments of the Nd^{3+} rare-earth sub-lattice, as in the case of NSNO(x) thin films. It has been already reported for (STO-capped) $Nd_{0.8}Sr_{0.2}NiO_2$ thin films that the presence of Nd-4f electrons largely modifies the magnitude of the superconducting upper critical fields, while resulting in AMR signals with complex angular dependences [142]. The observation of our fourfold IP-AMR for H values ranging in the 1-9 T range, can be put in relation with the local Nd^{3+} magnetic moments, which exhibit a planar easy configuration [142]. Indeed, in the case of electron-doped cuprates $Nd_{2-x}Ce_xCuO_4$ the IP-AMR signal showed a fourfold oscillation term [251,252]' [136,254], while for compounds with no 4f states, such as $La_{2-x}Ce_xCuO_4$, the IP-AMR showed only a twofold symmetry term [257]. It is clear that the presence of Kramers doublet Nd^{3+} ions will modify the scattering mechanism of the charge carriers, especially in the very low temperature region and at high magnetic fields. We believe, on the specific case of infinite-layer nickelates, that this is uniquely possible because of an intra-atomic exchange coupling between the Nd-4f and Nd-5d orbitals as put forward theoretically [161]. This exchange coupling, by introducing a spin-disorder broadening of the Γ-centered electron pockets at the Fermi level, influences the scattering mechanism of the charge carriers, together with the Sr-doping level and the unique Nd5d-Ni3d hybridization [158]. The latter is the consequence of a non-zero spectral weight of the Nd-$5dz^2$ bands at the Fermi level which creates electron pockets that self-localize at low temperature, and perhaps, explain the resistivity upturn for undoped and underdoped samples shown in Chapter IV. Those electron pockets are the result of a self-hole doping effect of the NiO_2 planes (up to 0.1 holes [153]), due to the transfer of electrons from the Ni $3d_{x^2-y^2}/3d_{z^2}$ states to the Nd 5d ones [147]. As already showed before, first RIXS measurements in the low energy excitation region rendered spin excitations around 200 meV energy loss for STO-capped samples at different Sr-doping. The observed extra damping of the spin-waves upon increasing the Sr-content, indicates a decisive role played by those electron pockets [127], with (perhaps) consequences on the pairing mechanism itself. As a result, the presence of itinerant Nd-5d electrons marks an extra degree of freedom regarding the magnetic structure of the infinite-layer nickelates if compared to the one of hole-doped cuprates. Our angle-dependent AMR measurements for $NdNiO_2$ samples, suggest that their magnetic properties are also largely altered by the presence/absence of the STO capping-layer. We believe that the intra-atomic exchange coupling between Nd-4f and Nd-5d orbitals combined to the Sr-doping level and the aforementioned Nd-Ni hybridization that, on the other side, it has been clearly shown to be modulated by the presence/absence of a capping layer [126], may concomitantly control the AMR modulation, and therefore explain the magnetic properties of the infinite-layer nickelates as a function of the STO capping-layer. It remains to understand to which extent the Nd-Ni hybridization and/or the intra-atomic coupling between the Nd 5d and 4f states play a role in the intensity modulation of the IP(OOP)-AMR data, and in particular, of the mixed twofold/fourfold symmetry behaviour for the OOP-AMR data in the case of capped samples. Further experiments performed on samples synthesized with different capping layers, Sr-doping levels and rare-earth elements would perhaps contribute to allow a better understanding of those AMR measurements.

3. And the doping?

So far, regarding the magnetotransport properties I have mainly discussed results obtained relatively to undoped samples and focusing on the role played by the capping layer. Here, in this last section although not in a comprehensive way, I will show both MR and AMR measurements for samples of different Sr-content, i.e. $NSNO_2(5)$ and $NSNO_2(20)$.

In particular, **Fig. V-22(a,b)** shows clear fourfold oscillations for the IP AMR also at higher hole-doping levels. The IP AMR of both $NSNO_2(5)$- and $NSNO_2(20)$-capped thin films has an amplitude similar to the one observed for $NSNO_2(0)$ capped thin film at 9T. The temperature dependence of the IP AMR in **Fig. V-22(c)** also shows that it vanishes for both doping over 20K, similar as what has been observed in the undoped sample. However, the main difference is the magnetic field dependence of the AMR. While the $NSNO_2(5)$ sample exhibits a similar behaviour as the $NSNO_2(0)$ with an AMR signal increasing with the magnetic field, the $NSNO_2(20)$ sample shows a maximum of AMR around 4T.

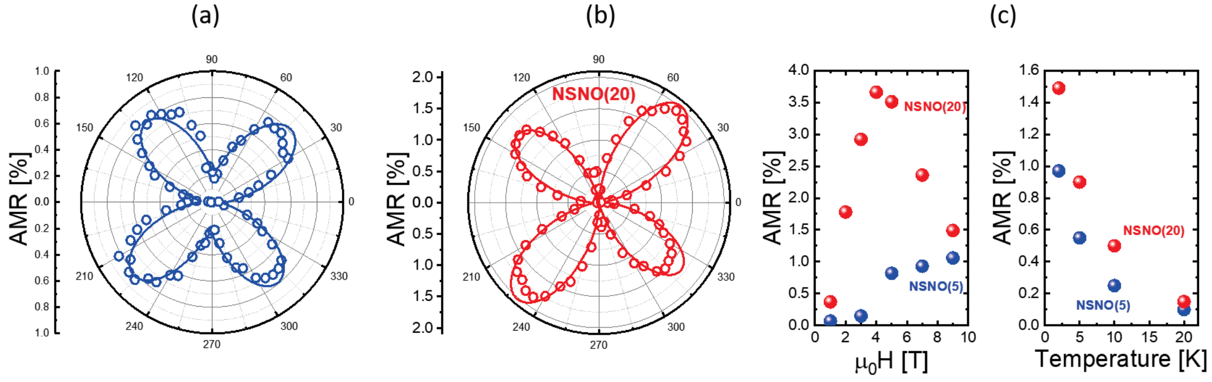

Figure V-22 Polar plots of in-plane AMR as a function of the φ angle for measurements performed at 2 K under a magnetic field of 9 T for (a) NSNO$_2$(5) and (b) NSNO$_2$(20) capped-experimental data as dots and fitting represented with lines, (c) temperature- and field-depend with NSNO$_2$(5) in blue and NSNO$_2$(20) in red.

The NSNO$_2$(5) sample exhibits a negative MR as the undoped one at 2K **[Fig. V-23(a)]**. However, the NSNO$_2$(20) sample shows a strong positive MR, which is the proof of a superconducting behaviour as observed in cuprates because of the suppression of the superconducting fluctuations by a magnetic field [258]. However, the temperature dependence of the MR signal is similar as the one observed for the undoped samples independently of the doping that vanishes over 20K. Moreover, one can observe that the positive magnetoresistance become slightly negative for temperature below 40K **[Fig. V-23b]**, hence, when we are very far for possible superconducting fluctuations.

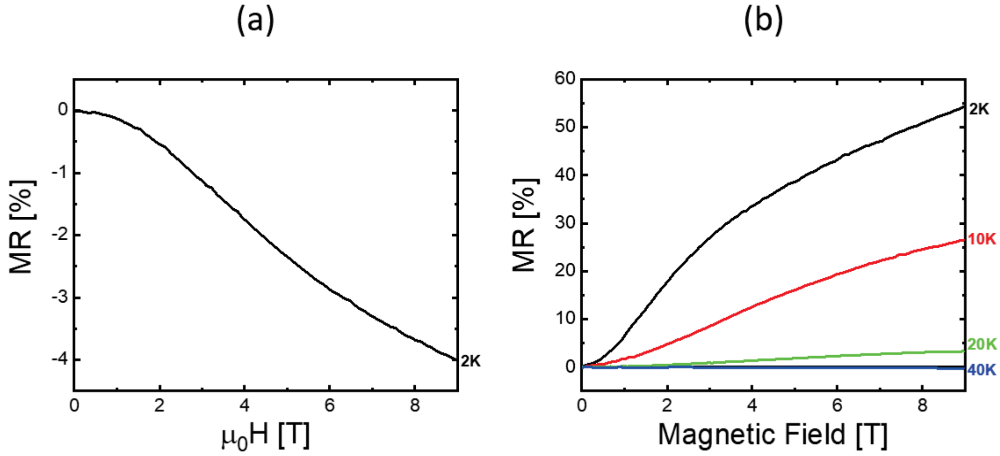

Figure V-23 MR from 0T to 9T as a function of the temperature for (a) NSNO$_2$(5) and (b) NSNO$_2$(20)

While here the fourfold oscillations for IP AMR are robust against the hole-doping, in isostructural cuprates Sr$_{1-x}$La$_x$CuO$_2$, the contribution of the fourfold oscillation is stronger for the most underdoped sample [140]. Jovanovic et al. justify this result by the fact that increasing the doping makes the sample closer to the long-range antiferromagnetic order region in the CuO$_2$ planes, which explained the transition from fourfold (underdoped) to twofold (less underdoped) oscillations. Here, we keep the fourfold oscillation along a long range of doping (up to 20%), that might be explained by a still absence of evidence of a long range antiferromagnetic order in infinite-layer nickelate.

Finally, the magnetic field dependence of the AMR amplitude of the NSNO$_2$(20) in **Fig. V-22(b)** sample might be explained by the critical field of the superconducting state. In that sense, we believed that our sample might have a critical field smaller than the one reported by Wang, B. et al. [142] (around

10 T for a 20%-doped sample) as it does not reach a zero-resistance state, hence having superconductive fluctuations easier to suppress.

4. Summary

In this Chapter, I have uncovered the role played by the STO capping-layer on the physics of infinite-layer nickelate thin films. In term of growth, its presence has been justified to improve the crystalline quality of the thin films. Here, I have shown that its presence modifies the nature of the low-energy excitations region of RIXS spectra, where a CO is found in the absence of the capping which is substituted by the presence of magnons for STO-capped samples. Further measurements performed on the same ID32 beamline by using a polarization-resolved technique allows to scope the damping of the magnetic excitation through the doping and the absence of the capping-layer. Interestingly, we found that the magnon was not fully suppressed by the absence of the capping, but heavily damped out. The evolution of the short-range magnetic order has been proved to be different from the cuprates where the latter possess a more robust magnon through the doping compared to the infinite-layer nickelates.

Moreover, we decided to perform magnetotransport measurements also focusing on the influence of the capping-layer. We overall observed a higher amplitude for both MR and AMR in the case of capped $NSNO_2(0)$ samples if compared to the uncapped ones, and a higher contribution of the fourfold oscillation for the capped $NSNO_2(0)$ when measuring in OOP AMR geometry. The Nd-Ni hybridization and the intra-atomic coupling between Nd 5d and 4f states seems to be at the origin of the measured magnetotransport properties. Also, the observed fourfold oscillation for IP AMR measurements are present for all different studied doping levels, which is different from what usually reported in the case of cuprates. This difference might be explained by a possible absence of long range antiferromagnetic order in infinite-layer nickelate.

Uncovering the physics of the infinite-layer nickelates thin films will need more measurements to be conclusive on the particular role of the capping-layer and the evolution of the electronic structure through the doping. Also, a more exhaustive set of samples will be needed, with different substrate, capping-layer and choice of rare-earth to continue to determine the physics of the infinite-layer nickelates.

VI. Tailoring the electronic properties of perovskite nickelate in ferroelectric-based heterostructures

We will now quit the infinite-layer phase nickelate to come back to the study of the perovskite phase. The focus here is made on $NdNiO_3/PbZr_{0.2}Ti_{0.8}O_3$ (NNO/PZT) heterostructures, with the main goal to study the influence of the PZT ferroelectric polarization (P) on the magnetic and metal-to-insulator phase transitions of the nickelate layer. As thin film form, both temperature and resistance jump of the MIT while being undesirably affected by off-stoichiometry for not properly optimized thin films [216,259], can be statically controlled by opportunely choosing the mismatch and crystallographic orientation of the substrates [46]. In order to obtain a dynamic modulation of the nickelates' functional properties I have worked toward the possibility to tune them in Ferroelectric Field-Effect Devices (FeFED). Therein possible polar distortions combined to electrostatic effects could induce on the adjacently grown $NdNiO_3$ thin film a control over both the MIT and onset of the antiferromagnetic phase via P-reversal. The main idea behind this approach is that tunable polar distortions of the interfacial nickelate unit cells, setting an outstanding tool to alter the Ni-O-Ni bond/angle lengths, could modify the functional properties of the nickelate thin film while granting a path to allow a modulation of the Ni-3de_g orbital hierarchy. The latter possibility has been largely investigated in literature in different nickelate-based heterostructures with the main goal to mimic the cuprate-like quasi-2D layered structure with Ni^{1+} $3d^9$ electronic configuration. On the other side, the growth of nickelate-based FeFEDs is very rare in the literature and, based on my knowledge there exists only a few examples [76,77,260]. **Fig. VI-1** schematically shows the case of a PZT layer used as non-volatile gate grown onto a conductive $LaNiO_3$ thin film. Here, Marshall *et al.* have shown that the P-reversal controlled the conductivity of the channel by mostly modifying the mobility of the accumulated/depleted charge carriers at the only nickelate/ferroelectric interface. Additionally, in manganites-based FeFED [261] it has already been proved that polar distortions have a clear effectiveness in controlling the orbital occupation of the manganite through P-reversal of the ferroelectric layer. The possibility to account for a modification of the bond angles and/or lengths for other nickelate thin films exhibiting a MIT in FeFEDs can be promising in term of orbital engineering.

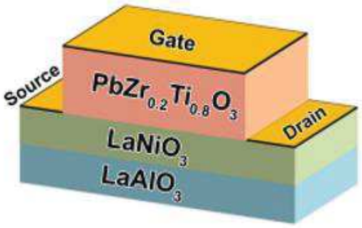

Figure VI-1 A FeFED device, taken from Ref. [[77]*].*

I have studied two different oxide stacks:

1) In the first approach the NNO layer is grown on top of a ferroelectric PZT thin film, of which the polarization direction could be controlled during growth by using a different buffer layer (BL). As a main result the PZT polarization state, *i.e.* upwards or downwards with respect to the BL is found to influence the Néel temperature of the NNO, as evidenced by resonant elastic X-ray scattering (REXS) at the I10 beamline of Diamond Light Source(England). However, both transport and XRD characterizations informed of a worsened quality of the top NNO thin films which might be strictly related to a combination of effects, such as the different temperature synthesis of the two oxides (see Table 1), a not properly optimized PZT layer morphology which translate in a non-optimal starting condition for the NNO growth, and finally, a not optimal oxygen content in the PZT layer which translate in a subsequent NNO layer with a reduced valence state for the Ni ions.

2) In the second approach, the PZT layer is grown on top of an optimized NNO bottom layer. Unfortunately, the PZT ferroelectric polarization could not be macroscopically reversed via Cu top electrodes of 60x60 μm². Therefore, I have studied a PZT(d)/NNO//STO(001) sample series characterized by different thickness value d for the PZT. REXS and transport measurements have demonstrated the modification of, respectively, the Néel and metal-insulator transition temperatures as a function of d.

1. First approach: NNO films grown on top of UP- or DOWN-polarized ferroelectric PZT

1. Motivation

The aim of controlling by static or dynamic approaches the different spin, charge and/or orbital orderings which can take place in transition metal oxides, is at the forefront of the research led in condensed matter. The field effect approach is one of the most promising road which allows a dynamical and reversible alteration of the functional properties by means of external stimuli, offering new pathways for the next generation of oxide-based electronics [192,262]. A control of the electronic properties of perovskite rare-earth nickelates ($RNiO_3$, R being a rare-earth element), has already been obtained through steric effects and/or heterostructuring as introduced in Chapter IV. The Néel transition of this family of compound has been studied by resonant elastic soft X-ray spectroscopy (REXS) along the wave vector $k = (¼, ¼, ¼)_{pc}$, and strain states or different crystal orientations for the growth of $RNiO_3$ thin films have been used as leverage to affect both the Néel transition and the MIT [46,223,263]. In the particular case of $NdNiO_3$ those transitions are concomitant with a structural transition from orthorhombic *Pbnm* (metallic phase) to monoclinic $P2_1/n$ (insulating phase) [5]. When the material is insulating, one observes a so-called bond-disproportionation where alternating NiO_6 octahedra are compressed and expanded in a rock-salt breathing-mode distortion pattern [34,37,42]. This leads to two different Ni sites in the lattice with $3d8L^0$ and $3d8L^2$ electronic configurations for the expanded and compressed sites, respectively. The magnetic properties of the nickelate strongly depend on the Ni-O-Ni bond angle, which governs to what extent the Ni-3d and O-2p orbitals overlap [6].

I have already introduced in Chapter IV, the efforts made by the scientific community in synthesizing nickelate/ferroelectric heterostructures in order to observe the influence of a ferroelectric-field effect on the interfacial charge carrier concentration [76,77,260]. FeFEDs have been mainly engineered with manganite thin films as channel materials [261,264,265]. In particular, a transmission electron microscopy study has demonstrated that beyond the purely electrostatic effects which trigger an accumulation or depletion of charge carriers at the LSMO/BTO interface, structural effects are also at play, emerging via intrinsic polar distortions propagating from the ferroelectric material towards the interfacial unit cells of the LSMO [264]. Indeed, a ferroelectrically-induced polar distortions are susceptible to induce a variation of the TM-O-TM bonding network at the ferroelectric/TMO interface. Additionally, the electric-field generated by the polarization charges [266] has been proved to be a useful tool to achieve a non-volatile and reversible modulation of charge carriers density in manganite thin films [265,267–270] whose functional properties are, indeed, dictated by the doping level [23]. Consequently, due to the very rich and interconnect phase diagram of manganites [23] a dynamical control over the charge carrier density translates into a modification of the magnetic properties. My goal was also to study if in $NdNiO_3$-based FeFEDs it would be possible to induce similar effects on the charge carrier density and magnetic properties via an adjacently grown ferroelectric layer.

In the following I will firstly address the growth of the NNO/PZT heterostructures showing the results obtained by XRD, PFM and transport characterizations. Afterwards, I will present the REXS measurements performed at the I10 beamline, where we could observe the expected modification of the $T_{Néel}$ as a function of the P-direction with respect to the sample surface. I will discuss the challenging aspects of the growth of NNO/PZT/BL//STO heterostructures with high-quality interfaces mostly hindered by the given choice of the oxide stack, and most likely ascribable to morphology, strain and oxygen vacancies effects.

2. The growth of the ferroelectric $PbZr_{0.2}Ti_{0.8}O_3$ layer

PZT, for the composition used in this thesis, $PbZr_{0.2}Ti_{0.8}O_3$, crystallizes in the tetragonal *P4mm* space group, with the following lattice parameters: a=b=0.395 nm and c=0.415 nm. The non-centrosymmetric structure of PZT possesses an off-centering of the central Ti/Zr cations with respect to the oxygen octahedra as shown in **Fig. VI-2**. Jia *et al*. [271] have pointed out that the Zr/Ti cations and the O anions move in the same direction of the tetragonality relatively to the Pb cations. The anions thus show a higher vertical displacement than the cations, which yields the ferroelectric polarization properties of the material. A ceramic target of PZT bought from Pi-Kem Ltd has been used to grow all the PZT thin films in this thesis.

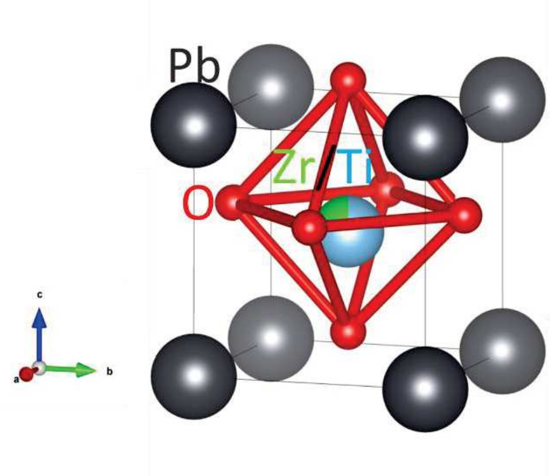

Figure VI-2 Tetragonal perovskite structure of $PbZr_{0.2}Ti_{0.8}O_3$.

The objective was to synthesize two NNO/PZT heterostructures: one with upwards (UP) and one with downwards (DOWN) PZT polarization states. Yu, P. *et al*. [272] have demonstrated the possibility to control the polarization of as-grown ferroelectric layer by the nominal charges of AO and BO_2 layers of the ABO_3 bottom-layer. An example of this mechanism is shown in **Fig. VI-3** where the different termination of the $La_{0.7}Sr_{0.3}MnO_3$ bottom-layer induces different polarization of the $BiFeO_3$ upper-layer. Indeed, the charge of both possible termination of the bottom-layer could be $(MnO_2)^{-0.7}$ and $(La_{0.7}Sr_{0.3}O)^{+0.7}$ which respectively leads to an upwards **[Fig. VI-3(a)]** and downwards **[Fig. VI-3(b)]** polarization state.

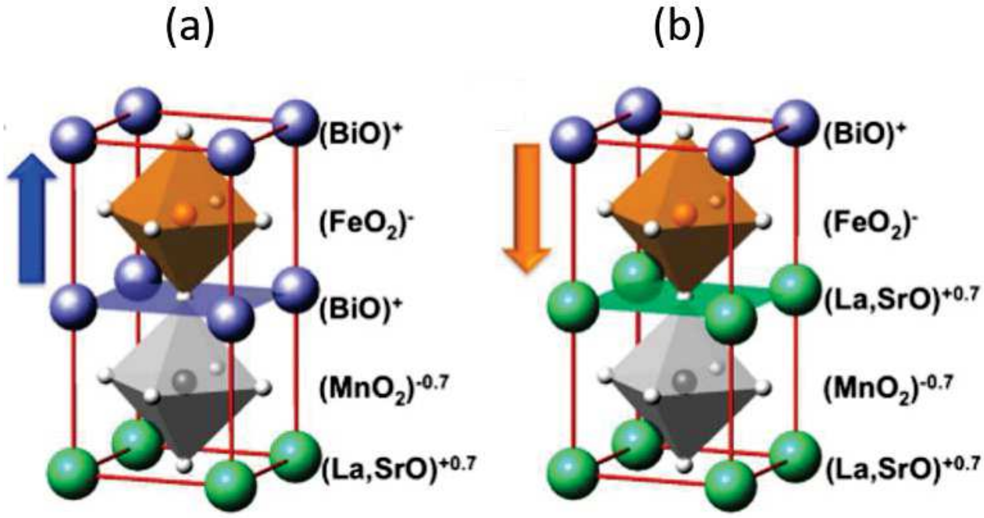

Figure VI-3 Schematic model and experimental design of two possible hetero- interfaces between LSMO and BFO layers. Atomic stacking sequence for LSMO/BFO heterostructures with (a) $La_{0.7}Sr_{0.3}O$*-*MnO_2*-BiO-*FeO_2 *and (b)* MnO_2*-*$La_{0.7}Sr_{0.3}O$*-*FeO_2*-BiO interfaces. (Taken from [[272]])*

I wanted to have here the possibility to tune the as-grown polarization of the ferroelectric material through the influence of the interface with a buffer-layer. Previous growth advancements in the lab have shown that a PZT layer grown onto $LaMnO_3$ (LMO) and NNO as buffer layers with an STO substrate, could shows an UP and DOWN polarization state, respectively. TEM investigations of the PZT/BL interfaces are ongoing to provide further insights for this observation.

3. PZT growth and characterization

5x5 mm² STO substrates (CODEX International) have been used as growth templates. They underwent the Kawasaki procedure [214] as described in Chapter IV to obtain a well-defined step-terraced surface, and to be TiO_2-terminated. To observe the influence of the PZT on the functional properties of the NNO layer, we first needed the guarantee that the as-grown PZT polarization could be controlled by the different BLs. The PZT as-grown polarization state was determined by piezoforce microscopy (PFM) measurements. It is important to say that I have not performed those measurements. **Figs. VI-4(a,b)** show the phase images of the PFM measurements obtained after consecutive writing experiments: the inner square domain with a -5 V for the **Fig. VI-4(a)** and +5 V for the **Fig. VI-4(b)** leading to respectively UP and DOWN polarization states. The outer square domains have been written with opposite voltage values, *i.e.* +5 V for **Fig. VI-4(a)** and -5 V for **Fig. VI-4(b)**, leading to an opposite polarization with respect to the inner domains. The positive and negative voltage values were applied to the PFM tip while keeping the bottom layer to the ground. Then, by performing the PFM on a larger surface area one could also image the as-grown state of the polarization, in order to compare the phase color gradient with the voltage-written domains. We have found that the LMO-buffer sample is characterized by an UP as-grown P-state while the NNO-buffer one by a DOWN as-grown P-state. Both PZT layers have been grown with similar PLD conditions, and the measured thickness is close to 100 nm. The LMO and NNO buffer layers were both 7 nm thick, as determined by previous characterizations.

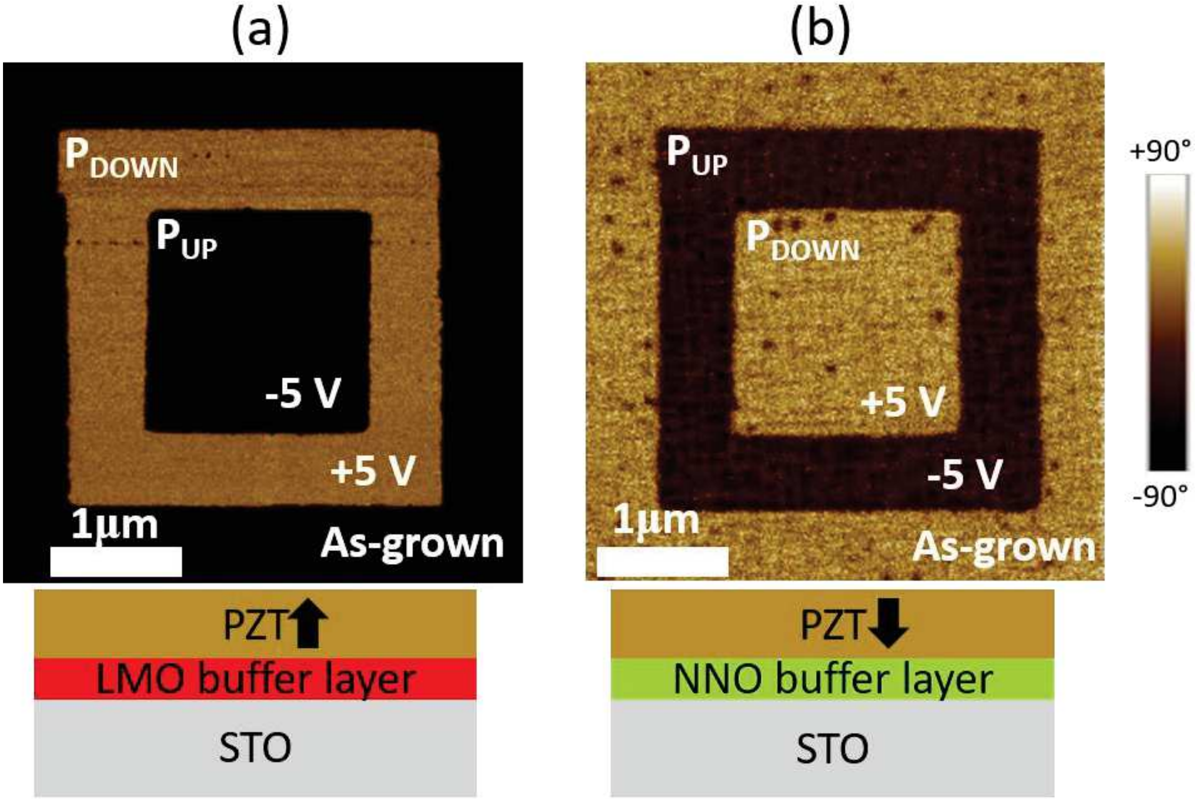

Figure VI-4 PFM phase images of a PZT-layer grown onto (a) LMO and (b) NNO buffer layers. UP domains are written with -5V and DOWN domains with a +5V voltage applied to the PFM tip. Comparison between the PFM-phase values of the as-grown and written domains helped in determining the as-grown polarization states.

Once confirmed the possibility of controlling the as-grown P-states of the PZT layer, a 10 nm thick NNO layer was subsequently grown for both P_{UP} and P_{DOWN} samples. Details of the PLD experiments are presented in Table1. The NNO has been grown in an oxygen partial pressure of 0.15 mbar, lower than the optimized 0.3 mbar. That is explained by the fact that those experiments have been performed before the study of the influence of the oxygen partial pressure on the perovskite nickelate growth presented in Chapter IV. It is also important to note that the cooling-down process, set at 5°C/min, has been stopped at 500°C to perform an oxygen annealing (30 minutes) with an oxygen pressure of 100 mbar. Once the annealing process terminated the cooling process was restarted down to room temperature with this high oxygen partial pressure. To note also the higher NNO growth temperature with respect to the PZT one. This is usually not the case when oxide heterostructures are grown, and usually the same temperature is kept for the entire stack, or at least the subsequent oxides are grown with lower temperature values to reduce possible intermixing effects at the interface. In the particular case of the two chosen oxides, PZT and NNO, this was not possible and we decided to attempt the growth anyway.

Table 2 Growth conditions of NNO/PZT/LMO and NNO/PZT/NNO heterostructures with STO(001)$_{pc}$ *ad substrates.*

Target	Fluence	Temperature	Laser Frequency	O_2 Atmosphere	Cooling
$LaMnO_3$	2.8 J/cm²	700°C	5 Hz	0.1 mbar	5°C/min + annealing at 500°C
$PbZr_{0.2}Ti_{0.8}O_3$		600°C	10 Hz	0.25 mbar	
$NdNiO_3$	3.3 J/cm²	675°C	2 Hz	0.15 mbar	

The growth of the different layers of the heterostructures has been followed *in-situ* by RHEED, for which oscillations could only be observed for the buffer-layers. A higher number of oscillations could be observed for LMO, when compared to NNO [**Fig. VI-5(a)**]. The lattice mismatch with the STO substrate is smaller for LMO(+0.8%) than for NNO(-2.5%), and both buffer-layers exhibited a 2D RHEED pattern at the end of the growth, which is also the case for the PZT layer as shown in **Fig. VI-5(b)** despite starting fully 3D. Finally, also the growth of the upper NNO layer started with a 3D pattern but terminated with a nearly 2D pattern. The showed 3D RHEED is a clear indication that the growth of high-quality PZT/NNO interfaces represents a real challenge, that I had no real time to fully address during my thesis. However, as expected from the qausi-2D RHEED at the end of each growth, the AFM images of both heterostructures show a relatively flat surface with a root-mean square roughness of about 0.5 nm [**Fig. VI-5(c)**].

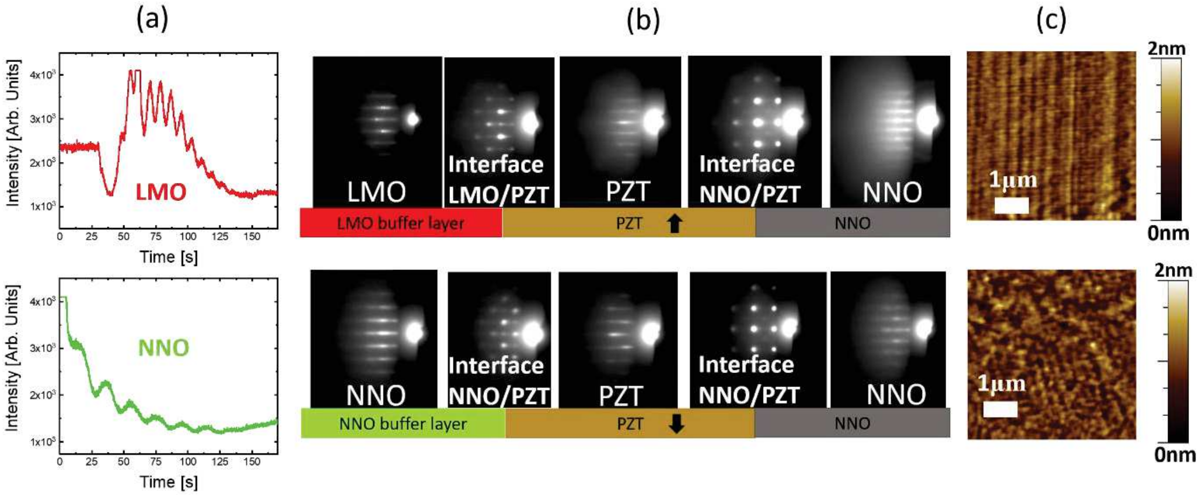

Figure VI-5 (a) RHEED oscillations observed during the growth of LMO buffer-layer (red) and NNO buffer-layer (green) (b) RHEED diffraction patterns for each layer at the end of their growth. The NNO/PZT and PZT/buffer-layer interface pictures shows the RHEED diffraction pattern after the growth of respectively 1 u.c. and 9 u.c (c) 5x5 µm² AFM images of NNO/PZT/LMO (top) and NNO/PZT/NNO (bottom) heterostructures. They exhibit an RMS-roughness of 0.5 nm.

Fig. VI-6(a) shows the XRD patterns of NNO/PZT heterostructures for both buffer layers. The sample with the NNO-buffer layer (green) exhibits a clear NNO (002) Bragg peak at 48.2°, while for the LMO-buffered sample (red), the (002) peak of the NNO is only present as a shoulder of the STO substrate peak, and the 003 NNO peak is not present, which are signatures of not-properly-optimized samples as mentioned in Chapter IV. It is important to note that, from our experience, not seeing clearly the (002) NNO Bragg peak for a 10 nm top-layer NNO means that the nickelate layer possesses a high number of oxygen vacancies, as we already mentioned in Chapter IV in the P(O_2) study, and perhaps pointing at the presence of RP phases with mostly Ni^{2+} valence states. As the (002) NNO peak is observable when the NNO is used as a buffer-layer, this could mean that the buffer NNO has a less concentration of oxygen vacancies and/or defects than the top NNO layers. One has to consider also the fact that the PZT being fully relaxed induces a very large tensile strain, which is indeed detrimental for the correct oxygen content in the NNO layer as I have already explained previously.

The lower quality of the NNO top-layer for both heterostructures, is also confirmed from the resistivity curves shown in **Fig. VI-6(b)** which have been obtained by measuring only the top NNO layers. Both samples exhibited a fully insulating behavior while being nevertheless hysteretic in T. This is expected from our demonstration in Chapter IV that NNO thin films grown in a low-oxygen atmosphere, *i.e.* which have a higher amount of oxygen vacancies, show a resistive behavior below 300 K.

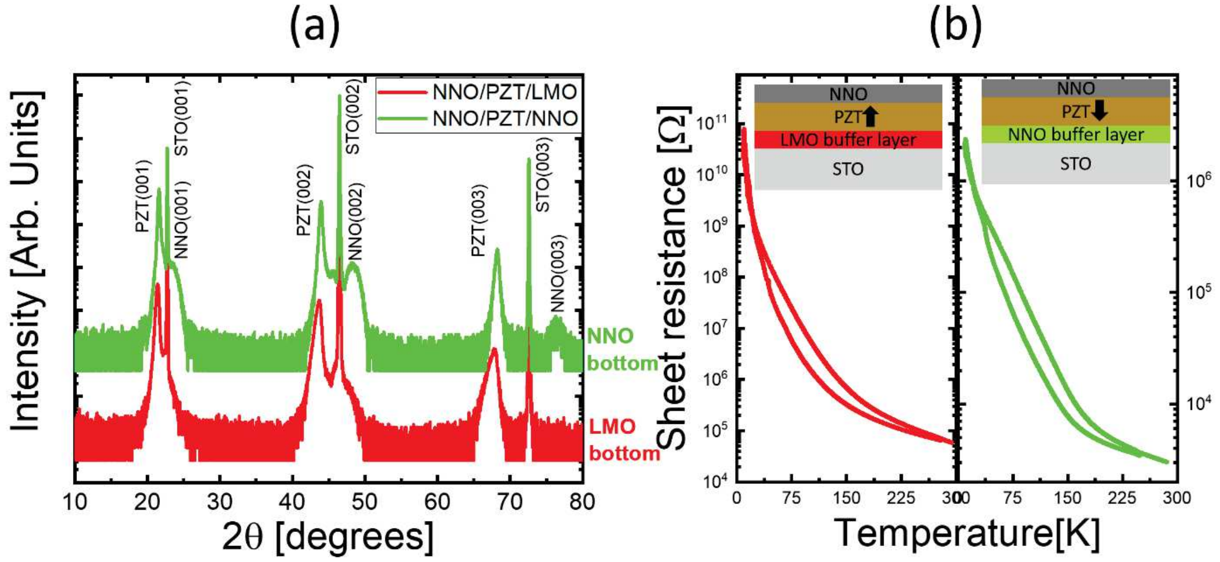

Figure VI-6 (a) XRD patterns of both NNO/PZT/NNO(LMO)//STO heterostructures with related (b) temperature dependence of the resistivity. The insets show the schematic representation of the heterostructures. Here we show the sheet resistance obtained from a two-points contacts measurement, as four points contact in Van der Pauw geometry could not be performed back then.

4. Study the modification of $T_{Néel}$ by resonant elastic X-ray scattering spectroscopy

Resonant elastic X-ray scattering technique is usually used to study the antiferromagnetic transition in $RNiO_3$ thin films, and especially to probe their spin configuration, *i.e.* collinear and/or non-collinear [51]. It has the advantage to be element sensitive with an increased scattering section if compared for example to neutron diffraction. Therefore, with REXS also thin films can be measured, and one can completely disregard the magnetic signal stemming from the substrate which, on the other side, is always present if one resort to SQUID (Superconducting quantum interference devices) measurements.

a. The I10 beamline

XAS and REXS measurements were performed on NNO/PZT heterostructures at the I10 beamline of the Diamond Synchrotron Light Sources in Oxforshire, England, with the help of Paul Steadman, and Raymond Fan. The measurements were performed on the RASOR spectrometer schematized in **Fig. VI-7(a)**. The end-station is equipped with a full polarization analyzer, and a liquid helium cryostat which can reach temperatures as low as 12 K.

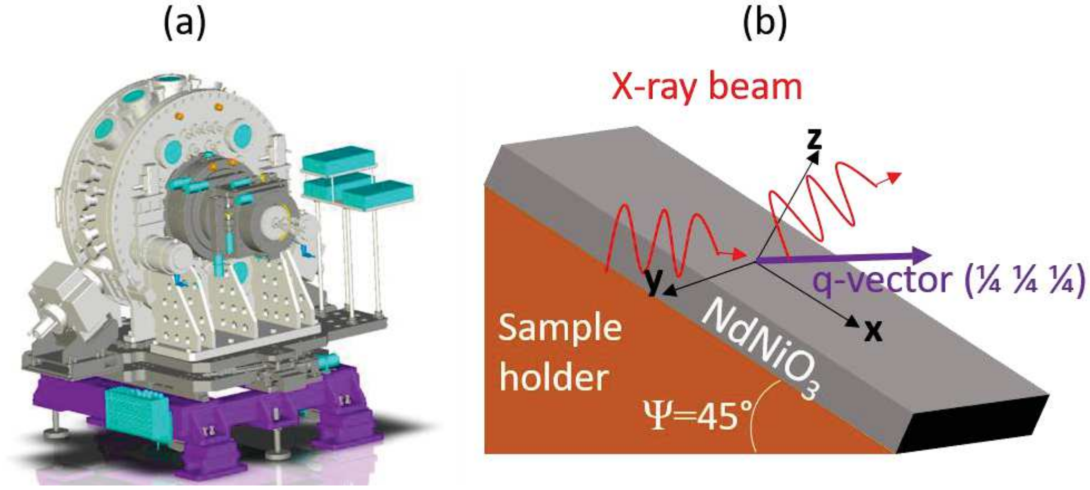

Figure VI-7 (a) Schematic representation of the RASOR end-station (b) Scheme of the thin film on the 55° Cu-wedge allowing to have the [111] and [010] axes in the scattering plane.

Our objective was to determine the NNO $T_{Néel}$ as a function of the P-direction. As previously explained in Chapter II, the antiferromagnetic order has been observed to be of four pseudo cubic (pc) unit cells along the [111] crystallographic direction [40], therefore along the propagation vector $q_0 = [¼,¼,¼]_{pc}$. In order to access the $[111]_{pc}$ direction, the thin films were mounted on a Cu-wedge holder inclined at 45° as shown in **Fig. VI-7(b)** [206]. We could fine tune the ψ value in such a way that the $[111]_{pc}$ crystallographic axis is lying in the scattering plane.

Fig. VI-8(a) shows an image taken with the camera inside the RASOR which is used to position the beam (identified by the main red lines crossing) on the four different samples mounted on the Cu-wedges to facilitate the setting of the samples position. **Fig. VI-8(b)** represents the scheme of the RASOR geometry with the possibility to move the *chi* angle to unavoidably access the propagation vector $q_0 = [¼,¼,¼]_{pc}$.

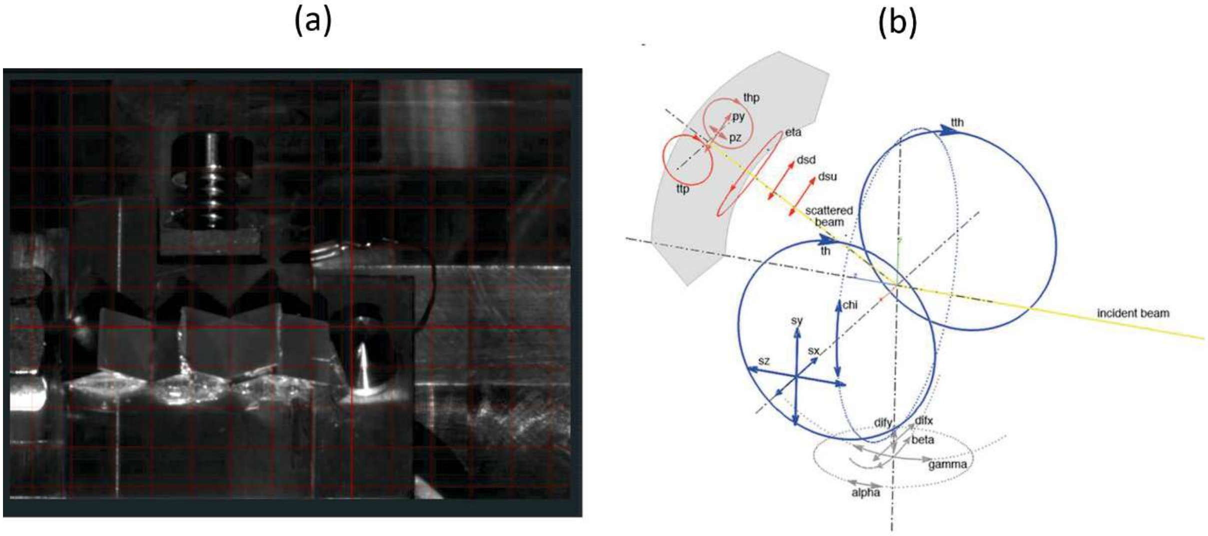

Figure VI-8 (a) Screenshot of the sample holder inside the RASOR spectrometer, (b) along with the schematic reporting its geometry and angle movements.

b. XAS and REXS results

Fig. VI-9(a) shows the isoXAS spectra acquired at the Ni-$L_{3,2}$ edges on both Pol-UP and Pol-DOWN samples at 40 K in TEY mode. The most striking difference is represented by the comparison with the XAS acquired for a bare NNO thin film grown onto STO. The usually observed double feature at the Ni-L_3 edge at low temperature which is a fingerprint of the insulating phase [34,36] is largely modified for our samples, and we observe a very large intensity for a pre-peak that can be attributed to a lower oxidation degree [38] of the Ni, as observed for oxygen-deficient $NdNiO_3$ and NiO, as I have already discussed in the Chapter IV. The presence of the PZT has the effect of broadening the Ni L_2-edge with a clear tendency to form a doublet commonly observed in the case of a higher presence of Ni^{2+} in the material [202]. Also, in the case of Pol-UP (LMO as buffer layer), the two features at Ni L_3-edge are more distinguishable and separated in energy, hence, demonstrating that beyond an overall large amount of Ni^{2+} the P-reversal of the PZT layer affect (somehow), the electronic properties of the $NdNiO_3$ thin films, as I will better explain for the other sample series prepared by following the second approach. Finally, in **Fig. VI-9(b)** we can note that a pre-peak at the O K-edge is present for both samples and is concomitant with the one observed for the bare NNO, although characterized by a smaller intensity. The latter, largely modulated by the P-state as well. This pre-peak is a clear signature of the Ni-3d and O-2p hybridization, and in the case of perovskite nickelates, an intense pre-peak is synonym of a fully-oxygenated $RNiO_3$ samples [36].

In this framework, the LMO-buffered sample (Pol-UP) has a stronger contribution from a more stable Ni^{3+}-based phase if compared to the NNO-buffered sample (Pol DOWN). It could be speculated that between the two different P-states the charge transfer energy is modified, in particular we can claim that in our Pol-DOWN sample exhibits a larger charge transfer energy since a lower intensity for the pre-peak indicates a decrease of covalency.

To conclude this part on the electronic properties of the Pol DOWN/UP samples, it has to be pointed out that behind a clear influence of P-state on the XAS spectra at both Ni-L and O-K edges, a relatively large amount of Ni^{2+}-like phase, such as Ruddlesden-Popper cannot be excluded, which then make a hard task the discrimination between a pure ferroelectric effect and the presence of Ni^{2+}-based defects.

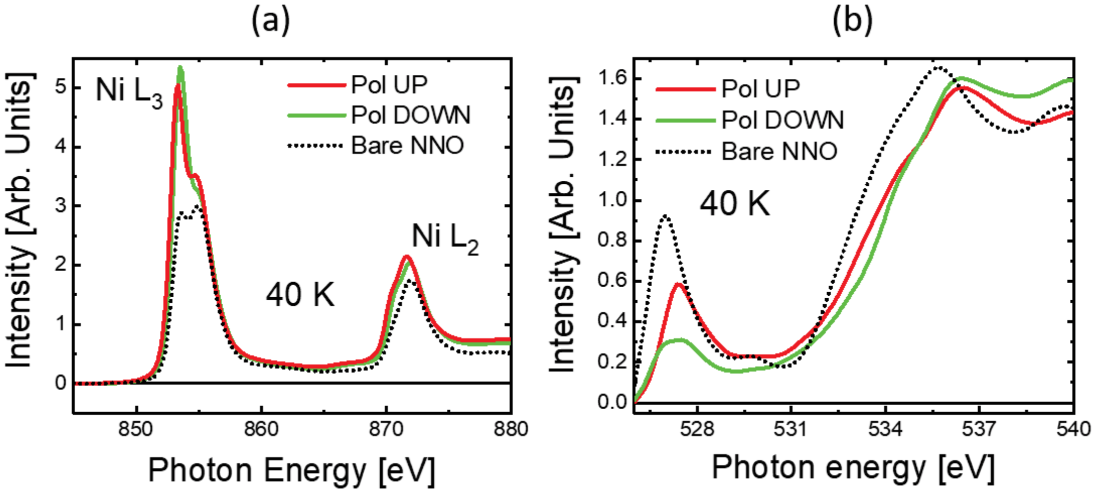

Figure VI-9 XAS of both the LMO-(red) and NNO-(green) heterostructures (a) at the Ni L-edge and (b) at the O K-edge, at 40K.

To study the magnetic ordering of the top NNO layers REXS measurements were performed at the Ni L_3-edge, and by referring to the XAS of **Fig. VI-9(a)** we have chosen the energy value of the first peak (853.5 eV) where indeed also the magnetic scattering diffraction spectrum had its higher intensity as shown in **Fig. VI-10**.

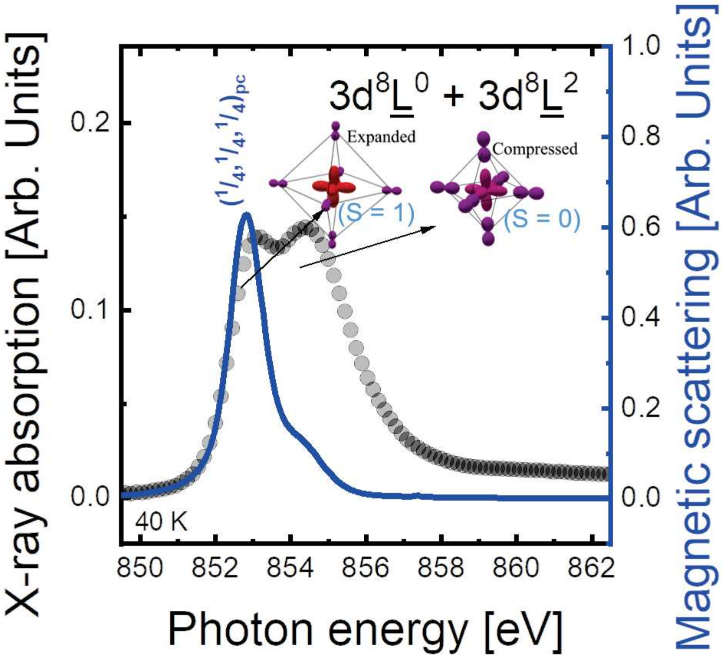

Figure VI-10 XAS of a bare NNO (black curve) at 40K and the corresponding magnetic scattering (blue curve) exhibiting a higher intensity for the first peak associated to the expanded Ni site with S=1.

As already reported in Chapter II the first feature of the Ni L_3-edge XAS peak is associated [42] to a $3d^8L^0$ electronic configuration with S = 1, which indeed explains a higher intensity of the magnetic peak as compared to the second feature of the Ni L_3-edge XAS peak associated to a $3d^8L^2$ electronic configuration with S = 0. The *tth* scan were performed within the 90°-130° range by cooling down the temperature from metallic towards the insulating phase, until 40 K. The magnetic Bragg peaks are shown in **Figs. VI-11(a),(b)**, where we first observe a more intense and sharper peak for the Pol-DOWN (NNO-buffered) sample as compared to the Pol-UP (LMO-buffered) one. However, we consider that this peak is the sum of two peaks, originating from both the top and bottom NNO layers, as demonstrated in **Fig. VI-11(c)**, where the experimental data have been fitted with two Voigt functions. A mix of 40 % Gaussian and 60 % Lorentzian has been used as it provided the smallest standard deviation. The orange curve obtained from the decomposition in **Fig. VI-11(c)** seems very similar to the curve obtained from the LMO-buffered sample. With such similitude, we considered the orange curve to be the contribution of the top-NNO layer, and the blue curve the contribution from the bottom-NNO layer. With this assumption, we could compare the relative evolution of the intensity of all observed peaks as a function of the temperature in **Fig. VI-11(d)**. Here, the $T_{Néel}$ has been chosen when the intensity of the magnetic Bragg diffraction vanishes, better defined by interpolation the discrete number of temperature REXS data [206], and are summarized in Table 2. We observed that the Top-NNO from both samples has indeed a similar intensity of the magnetic Bragg peak as shown with the red and orange curves in **Fig. VI-11(d)**. Interestingly, their $T_{Néel}$ is different, with a 13 K higher transition for the NNO of the Pol-DOWN sample if compared to the NNO of the Pol-UP sample. Also, we observed that the bottom-NNO of the pol-DOWN sample has a higher $T_{Néel}$ of 125K (blue curve in **Fig. VI-11(d)**).

Table 3 $T_{Néel}$ of the different NNO layers from Pol-DOWN and Pol-UP samples

Sample	NNO	$T_{Néel}$
NNO-buffer (**P_{DOWN}**)	**Bottom**-NNO	125 K
	Top-NNO	113 K
LMO-buffer (**P_{UP}**)	**Top**-NNO	100 K

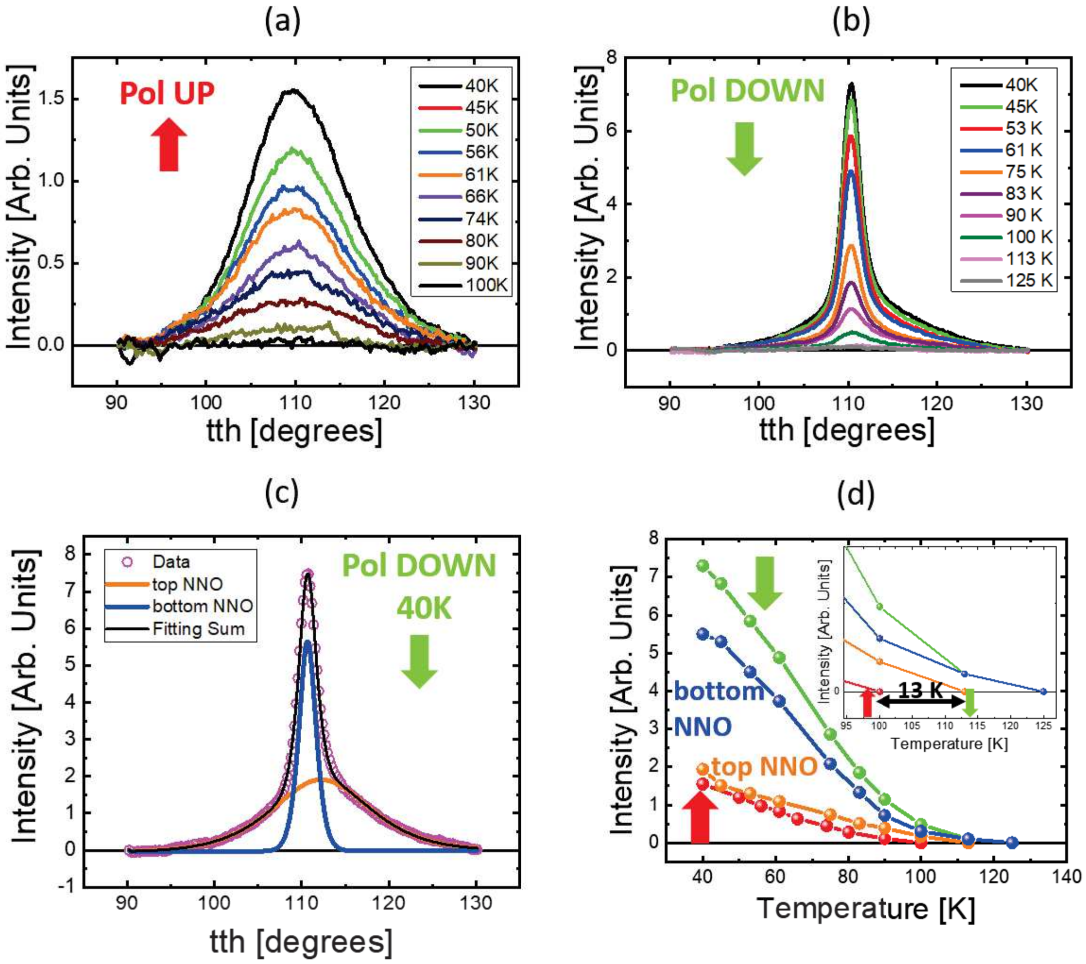

Figure VI-11 Magnetic reflection peaks along the [¼ ¼ ¼] vector for (a) LMO-buffered and (b) NNO-buffered samples (c) Fitting of the NNO-buffered sample magnetic reflection peak at 40 K with two voigts function GL(60), i.e. 40% Gaussian and 60% Lorentzian. (d) Maximum intensities of the magnetic reflection peaks as a function of temperature for LMO-buffered sample (red), NNO buffered-sample (green), and NNO top-and bottom-layers of the NNO-buffered sample (orange and blue, respectively).

We speculate that the difference in $T_{Néel}$ of the NNO top-layer (*i.e.* 13 K), is due to the influence of the two different PZT polarizations, which leads most likely to opposite influence on the Ni-O-Ni bond angle. For the upwards polarization, the polarization charge from the PZT are positive at the interface with the top-layer NNO, hence, approaching the O anions of the nickelate closer to the interface. It would result as a decrease of the Ni-O-Ni bond angle. On the contrary, the downwards polarization has the opposite effect, approaching the Ni/Nd cations closer to the interface with the PZT and pushing the O anions further away. This, clearly, results in a larger Ni-O-Ni bond angle. This modification of the Ni-O-Ni bond angle might be an explanation of the 13 K difference $T_{Néel}$ for both NNO top-layers, with, a smaller Ni-O-Ni bond angle decreasing the $T_{Néel}$, while a larger one increasing the $T_{Néel}$. However, the quality of the samples which is not the highest render difficult to conclude that this difference is due to the accumulation of opposite charge at the interface with PZT, or by slight difference of defects in the sample.

In that sense, we can notably conclude from this study that the quality of the top-layer NNO is not good as the presence of large amount of Ni^{2+} cannot be excluded. But we also observed that the NNO bottom-layer is of higher quality than the top-layer while grown with the same conditions. This growth aspect of the NNO/PZT heterostructures influenced our decision to modify the growth parameters and conditions, as will be presented in the second part of this Chapter.

2. Second approach: Different PZT thickness grown on top of NNO

1. Motivation

The experiments reported in the previous section about the NNO/PZT/BL//STO heterostructures informed that the growth optimization is very challenging, therefore requiring extensive efforts when one wants to grow a very high quality NNO layer on top of other oxides such as PZT. We therefore decided to study a series of PZT(d)/NNO(7 nm)//STO heterostructures, and to vary the PZT thickness value (d = 7, 13 and 30 nm). As already shown before, for high thickness values the as-grown polarization state for the PZT grown onto an NNO layer is downwards with respect to the substrate surface. At lower PZT thickness values the P-state is expected to be different. One has to consider a combination of depolarizing field and strain effects, and the overall PZT polarization state can be varied by using, as a leverage, the thickness-driven strain gradient. In that sense, growing different thicknesses of PZT with NNO as buffer-layer allowed us to have fully strained, partially strained and fully relaxed PZT layers associated to different ferroelectric domain structures for the sample series.

With the same main objective already introduced in the first part of this Chapter, *i.e.* to study the influence of the ferroelectric-field effect on the functional properties of NNO thin films, I will present here REXS measurements for the PZT(d)/NNO(7 nm)//STO heterostructures with d = 6, 13, 30 nm and performed at the I10 beamline of the Diamond Light Sources, using the experimental conditions previously introduced. The polarization domains structure has been characterized by PFM. Measurements of the temperature dependence of the resistivity allowed to determine the MIT temperature of the different samples as a function of the PZT thickness.

2. Growth and characterization of the heterostructures

Table 2 shows the optimized growth conditions for the PZT(d)/NNO(7 nm)//STO heterostructures, and I will refer to them as follows: PZT-6, PZT-13 and PZT-30 for each chosen PZT thickness value of 6, 13 and 30 nm, respectively.

Table 4 Growth conditions of the PZT/NNO//STO heterostructures.

Target	Fluence	Temperature	Laser Frequency	O_2 Atmosphere	Cooling
$PbZr_{0.2}TiO_3$	2.0 J/cm²	600°C	10 Hz	0.3 mbar	5°C/min + annealing at 500°C for 5h
$NdNiO_3$	3.8 J/cm²	675°C	2 Hz		

It is important to note that a higher fluence and a higher P(O_2) have been used for the growth of this second NNO-based samples series, in accordance with the optimized growth conditions presented in Chapter IV, while the PZT has been grown with a lower fluence value [57]. The annealing process under O_2 during the cooling has also been modified, in order to solve the issue of the presence of oxygen vacancies in the heterostructures, clearly evidenced in the first part of this Chapter by XRD, XAS and transport measurements. We therefore decided to extend the annealing time under 100 mbar at 500°C to 5 h before continuing the cooling down at 5°C/min. As evidenced by the RHEED monitoring during growth the obtained patterns and showed in **Fig. VI-12** indicated that the PZT starts growing 3D onto the smooth 2D surface of the 7 nm thick NNO film. However, upon increasing the PZT thickness, the RHEED pattern of the PZT progressively becomes more 2D-like.

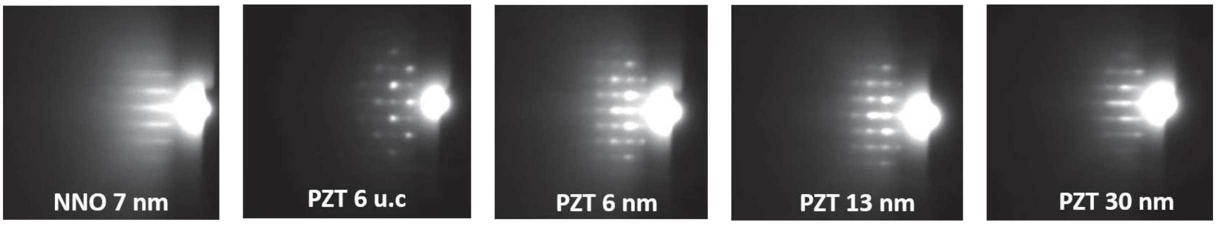

Figure VI-12 RHEED diffraction patterns of (from left to right) a 7 nm thick NNO layer, a 6 u.c PZT layer grown on top of the 7 nm NNO showing a 3D growth, the PZT-6 sample at the end of its growth, still 3D, the PZT-13 sample at the end of its growth which is also still 3D, and the PZT-30 sample which shows a 2D pattern at the end of its growth.

The XRD patterns of the three thin films are shown in **Fig. VI-13(a)**, where now we can nicely observe a relatively high intensity for the (003) NNO peak. Additionally, we highlight the decrease of the out-of-plane parameter of the NNO films when the PZT layer thickness increases, as shown in **Fig. VI-13(b)**. We presented in Chapter IV that a perovskite nickelate of higher quality will have a smaller c-axis parameter, synonym of lower presence of oxygen vacancies, and this value is reported in red in the graph. We can thus infer that the thicker the PZT onto the NNO, the lower the amount of oxygen vacancies in the nickelate films. This was counter-intuitive for us at first, as from the experience feedback we had from the previous part of this Chapter, PZT seemed to take the oxygen from the NNO layer, hence, creating more oxygen vacancies in the underneath NNO thin film. However, the trend of the *c*-axis parameter is against this assumption. It is also important to note that the 0.376 nm value obtained for the PZT-30 sample is higher than the one from the Chapter IV (0.374 nm) for a bare NNO, meaning that oxygen vacancies are nevertheless present in all samples, although with different amounts. The RSM mapping acquired around the asymmetric (013) reflection of the STO, and shown in **Figs. VI-13(c,d,e)** exhibit a NNO fully strained to the STO substrate independently of the PZT thickness. On the other side, the PZT layer is fully strained only for the PZT-6 sample. Upon increasing the PZT thickness values, a partial relaxation of the ferroelectric layer is observed, and it shows an in-plane lattice parameter of 0.395 nm corresponding to its bulk value [273] for the PZT-30 sample with.

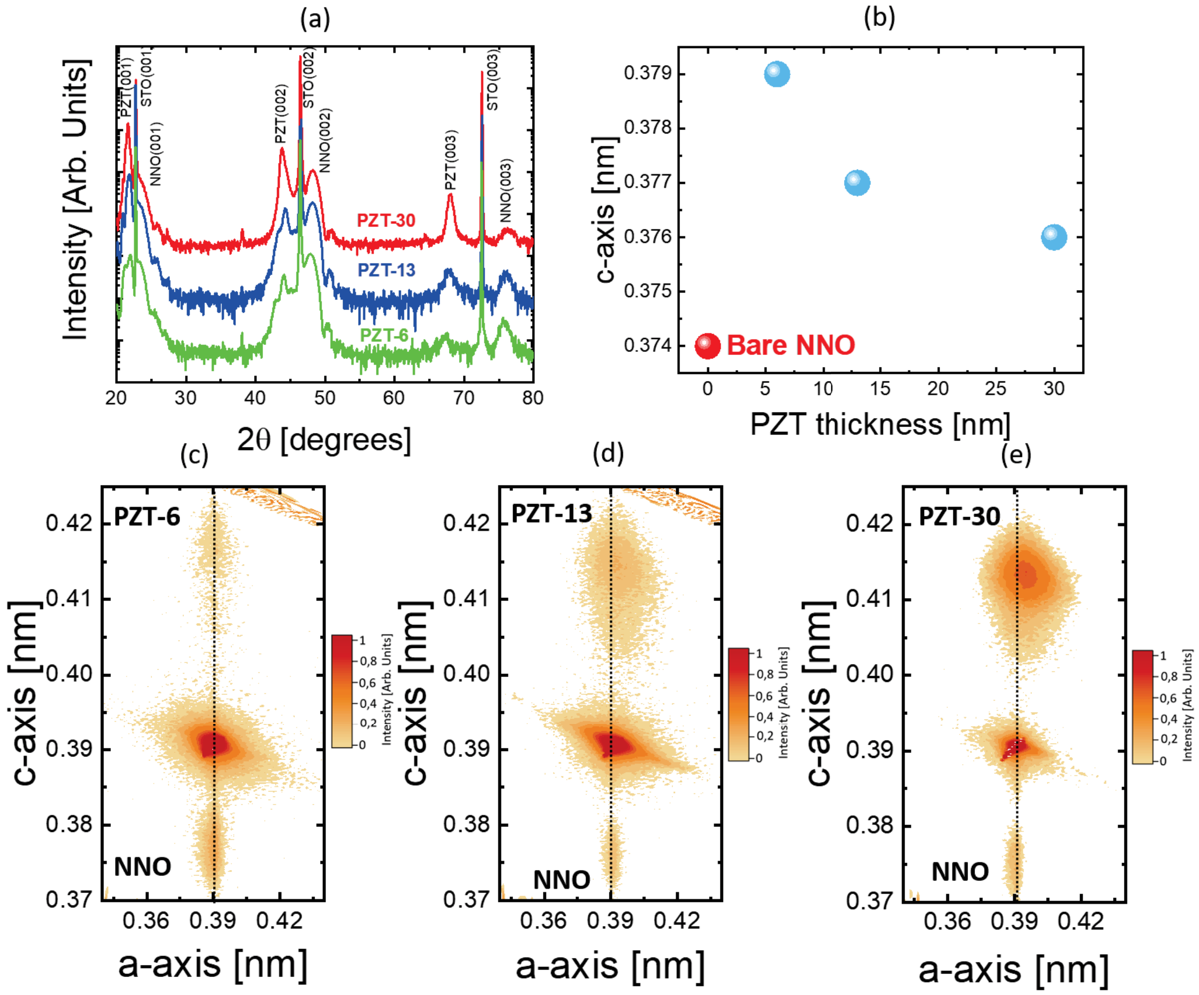

Figure VI-13 (a) XRD patterns of the different NNO/PZT heterostructures, (b) their c-axis parameters, with that of an uncapped NNO in red (optimized sample from the thin film optimisation dedicated Chapter), and (c)-(e) reciprocal space maps around the STO 013 reflections.

The three samples have been characterized by AFM/PFM to observe the as-grown polarization of the different PZT layers [**Fig. VI-14**]. The PZT-6 sample exhibits a multi-domain structure with an equivalent area of UP and DOWN domains in the phase image of the PFM analysis, that, according to the colour map chosen, are represented by black and white region, respectively. The amount of downwards polarized domains increases with the PZT thickness as schematized in the inset at the bottom of **Fig. VI-14**, and the PZT-30 sample shows a full DOWN polarization of the ferroelectric domains. The increase of the proportion of the DOWN as-grown domains with the PZT thickness can be correlated with the relaxation of the PZT layer observed on the RSM.

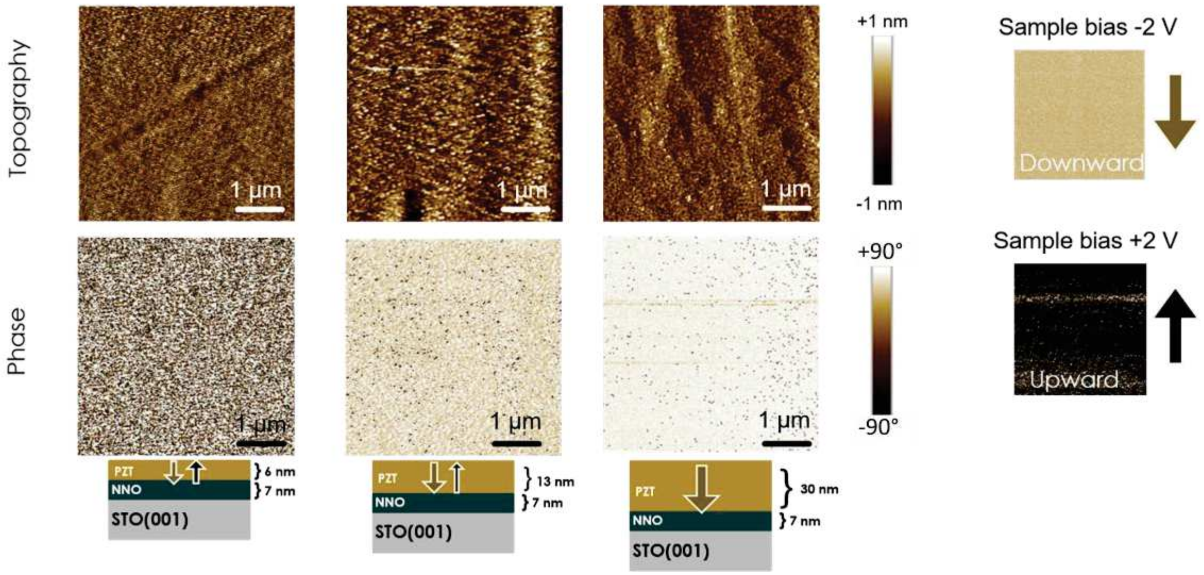

Figure VI-14 Topography and PFM phase images of the PZT/NNO heterostructures with different thicknesses of PZT. Phase analysis images allow the visualization of the polarisation state of the as-grown PZT layer on top of the NNO layer, as a function of the PZT thickness. The polarization is fully reversed with applied biases of -2/+2 V.

Resistivity measurements presented in **Fig. VI-15** show that all the samples exhibit a MIT transition, but at different temperatures depending on the PZT thickness. The smaller the PZT thickness, the higher the temperature of the transition. However, the resistance change of the MIT is very similar for all the investigated HTs, with approximately three orders of magnitude. Also, the room temperature resistivity is, on the overall, similar for all the samples, strengthening the fact that the NNO have the same number of defects independently of the PZT thickness. The MIT temperature has been determined by considering the crossing point of the d(ln(ρ))/dT curve with the $\rho = 0$ axis in the cooling part of the curve (from the metallic towards the insulating state). With this method, we obtained a T_{MIT} of 224 K for PZT-6, 195 K for PZT-13 and 175 K for PZT-30 as summarized in the inset of **Fig. VI-15**. A trend is clearly observed, with a decrease of the T_{MIT} as a function of the PZT thickness. It is also important to remember that the T_{MIT} of an optimized uncapped NNO grown onto STO(001) is around 180 K, as shown in Chapter IV.

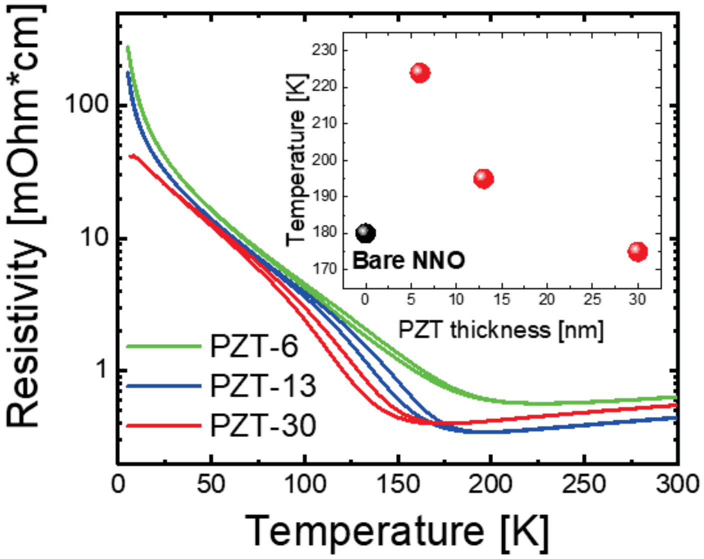

Figure VI-15 (a) Resistivity as a function of the temperature for PZT/NNO heterostructures with different PZT thicknesses. The inset shows the T_{MIT} as a function of the PZT thickness, and the black point is for the MIT of the bare NNO from optimized thin films in Chapter IV.

3. REXS study of the magnetic transition onset temperatures as a function of the PZT polarization

For this new sample series, both XAS and REXS measurements were performed at the I10 beamline of the Diamond Light Sources, Oxfordshire, England. However, unlike the previous measurements, those ones were performed remotely, due to the Covid19 pandemic situation, and both Paul Steadman and Raymond Fan, are deeply acknowledged for their support and especially to have mounted all the samples on the Cu-wedge to assure the tilted scattering geometry necessary to have the $[111]_{pc}$ in the scattering plane.

XAS measurements at the Ni-$L_{3,2}$ edges in FY mode have been performed on the three samples, and **Fig. VI-16(a)** offers a zoom over the Ni-L_3 features (all the XAS were area normalized) acquired at 20 K. We can observe that the thicker the PZT layer, the lower the intensity of the first XAS feature found at *ca*. 853 eV (L-peak), and the higher that of the second one at *ca*. 854.5 eV (S-peak). For a complete comparison, I also show the XAS acquired for a bare NNO, exhibiting features as already reported in literature. The XAS differences are summarized in **Fig. VI-16(b)** where both the L-S energy separation, measured between maximum intensity peaks, and the L/S intensity ratios are plotted. The thicker the PZT, the closer the L-S energy separation and L/S intensity ratios to those of bare NNO. The energy separation between the L and S peaks is used by Green *et al*. to characterize the breathing distortion mode in perovskite rare-earth nickelates [42]. Their model is based on the double cluster model introduced in Chapter II. They evidenced that an enhancement of the breathing distortion increases the gap between L and S peaks and their intensities ratio. I recall here that the L and S peaks are, stemming from the main contributions of the long and short Ni-O bonds, respectively. Following their ascertainment, we can conclude that the PZT-6 sample has a stronger breathing distortion than the one characterizing the PZT-30 sample, which itself has a still larger value than the bare NNO sample.

We have observed with RSM measurements that the thinner PZT-6 is fully strained to the substrate while the thicker ones are less strained. It thus seems that when the PZT is fully strained, it can play a major role on the breathing distortion pattern in the NNO. A role that decreases while the PZT relaxes when increasing its thickness. One must however not forget the role of the oxygen vacancies on the XAS of the NNO as already reported in the first section. We previously stated that the increase of the L-peak intensity at the Ni-L_3 edge was a fingerprint of Ni^{2+}-based defects due to a lack of oxygen in the nickelate lattice. This could be corroborated by the observation of a higher *c*-axis parameter for the samples with the smallest PZT thicknesses [**Fig. VI-13(b)**], which can be related to the presence of a higher number of oxygen vacancies [88,274]. In that sense, we must not forget that the ferroelectric-field effect is not the only parameter at play, as the oxygen vacancies might also influence the breathing-distortion mode.

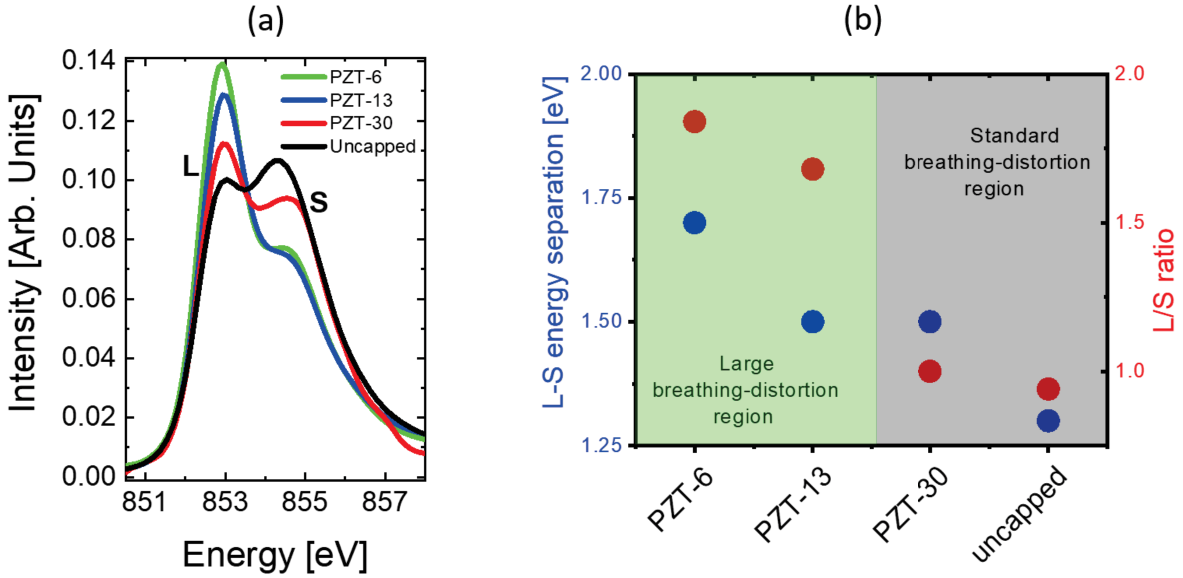

Figure VI-16 (a) XAS spectra of the PZT(d)/NNO heterostructures at the Ni L_3-edge for d = 6, 13 and 30 nm at 20K. (b) Intensity ratio and energy separation between the lowest (L) and highest (S) energy peaks of each XAS spectrum.

REXS measurements were performed along the $[111]_{pc}$ direction for the three samples as a function of the temperature. The $(¼,¼,¼)_{pc}$ magnetic Bragg peak was measured by scanning the *tth* angle from 106° to 114°, and by cooling down the temperature from 220 K to 20 K. The intensities of the magnetic Bragg peaks as a function of the temperature are shown in **Figs. VI-17(a,b,c)** for the three different PZT thicknesses. The evolution of the intensity of the peak for each sample normalized to the maximum is shown in **Fig. VI-17(d)**. The $T_{Néel}$ is determined when the intensity of the magnetic Bragg peak vanishes, and we observed that it decreases for increasing PZT thicknesses. A summary of the T_{MIT} and $T_{Néel}$ is presented in **Fig. VI-17(e)** where the decreases of the two temperatures with increasing PZT thicknesses is clearly observable. The T_{MIT} of the bare NNO sample is similar to the one observed for the PZT-30 sample. It is important to note that both T_{MIT} and $T_{Néel}$ of the PZT-30 sample are nearly concomitant, as observed for bulk NNO [5].

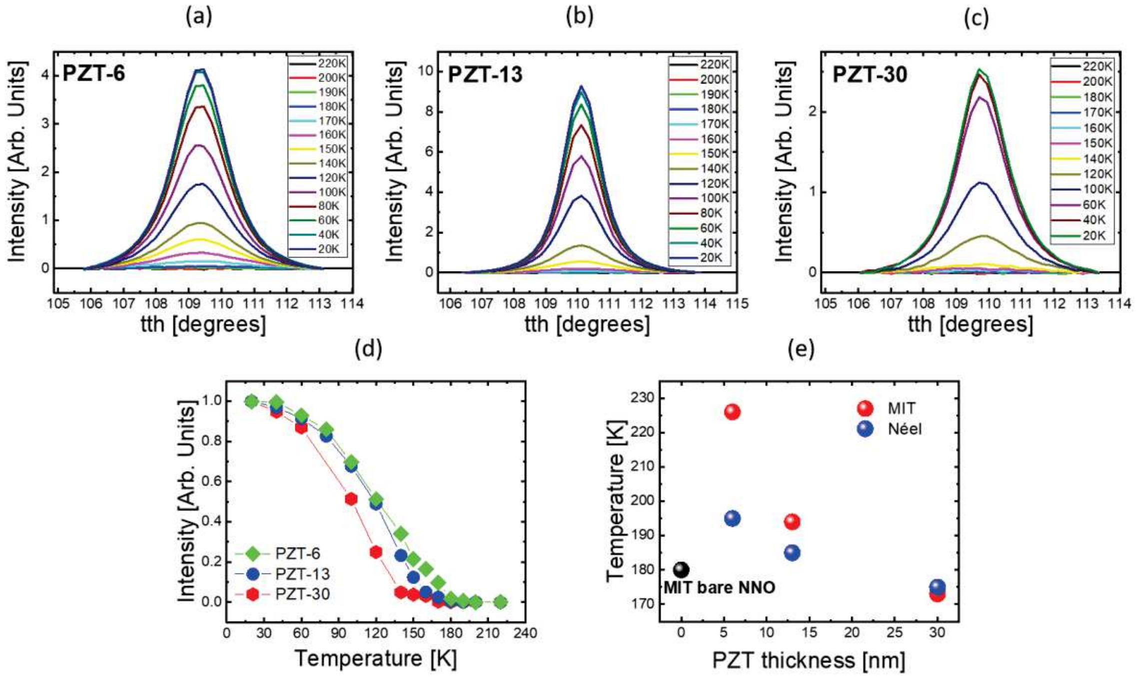

Figure VI-17 (¼,¼,¼)$_{pc}$ Magnetic reflection along the [111] direction for (a) PZT-6 (b) PZT-13 and (c) PZT-30 samples (d) Temperature evolution of the normalized maximum intensity of the magnetic reflection for the three different PZT thicknesses (e) PZT thickness dependence of T_{MIT} (red) and $T_{Néel}$ (blue), T_{MIT} for an optimized uncapped NNO is shown in black, with a temperature close to PZT-30 sample.

4. Discussion

I presented here my work on PZT(d)/NNO(7 nm)//STO heterostructures for which we observed a variation of the NNO MIT and Néel transition temperatures with the PZT thickness. Both T_{MIT} and $T_{Néel}$ decrease with increasing PZT thickness. This decrease of the phase transition temperatures goes along with a decrease of the NNO c-axis parameter. As mentioned previously, the higher c-axis parameters, observed for the samples with the smallest PZT thicknesses, can be related to the presence of oxygen vacancies [88,274], which induce a higher proportion of Ni^{2+} cations in the lattice. Further information on the valence of the Ni cations could be obtained from XAS experiments. The XAS spectrum of the uncapped NNO reference sample exhibits a similar feature to what has been observed in the literature for NNO, with the two peaks, that we labeled as L and S, at nearly equal intensity, and which can be used as a proxy for the high quality of the thin films with a majority of Ni^{3+} cations [220]. The XAS spectra of the PZT/NNO heterostructures are progressively getting similar to that of the uncapped NNO with increasing PZT thicknesses. We can thus consider that we have a higher proportion of Ni^{3+} cations for the PZT-30 samples than for smaller PZT thicknesses, which is in accordance with the *c*-axis parameter evolution. Moreover, by relying on the double cluster model presented by Green *et al.* [42], we observed that the increase of the energy separation between L and S peaks, inversely proportional to the PZT thickness, can be also related to a higher breathing distortion mode, as summarized in **Fig. VI-16**. Based on the L-S energy separation and L/S intensity ratio, we have distinguished two separate regions, one for a large breathing distortion and one for the standard breathing strength. Therefore, we can affirm that the PZT-30 sample has the most 'standard' distortion, as expected for a bulk-like NNO sample. This NNO layer has the smallest c-axis parameter of the entire sample series, and very close to the one characterizing a bare NNO thin film. This result is, as previously said, counter-intuitive since one would have expected that a thicker PZT would induce a higher modulation of the NNO functional properties, accounting for both electrostatic and polar-distortions mechanisms. Those data suggest that the polarization domain structure of the PZT layer plays a crucial role on the breathing distortion properties of the underneath NNO film. A fully strained and multidomain PZT would strongly destabilize it, while it would remain unmodified by a relaxed and monodomain thicker PZT. In **Fig. VI-14** I have shown the phase images of the PFM measurements performed for the entire sample series. The PZT-6 exhibits a multidomain structure for the ferroelectric polarization with an almost equivalent area of UP and DOWN domains. Upon increasing of the PZT thickness the DOWN P-state is progressively strengthened until the PZT-30 sample exhibits a fully DOWN polarization monodomain. Therefore, we should expect that in the case of the PZT-6 sample the two P-states may locally and differently influence the interfacial functional properties of the NNO contrarily to the other two cases where a mostly P-DOWN state is found to alter the underneath NNO in a more uniform way, as schematically represented in **Fig. VI-18**. In the case of PZT-6, the multidomain structure of the overall P-state implies that neighboring Ni-O-Ni bonds are submitted to opposite polar distortions, which could induce very different Ni-O-Ni bond angles on a short length scale. This could be at the origin of the large breathing distortion evidenced by the XAS measurements and the modulation of the T_{MIT} and $T_{Néel}$ .It is clear that behind the 'pure' ferroelectric field effect, which we consider as the combination of electrostatic and polar-distortion effects, one has to consider the unavoidable presence of oxygen vacancies in turn combined to PZT strain-induced distortions, and at this stage it is rather complicated to come up with a unique way to discriminate between all of them.

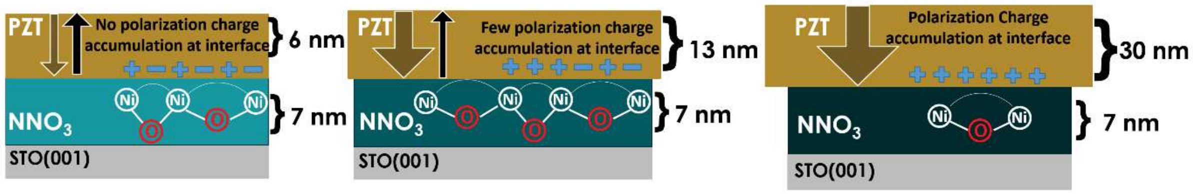

Figure VI-18 Schematic representation of the evolution of the PZT as-grown polarization, interfacial polarization charge, in-plane strain of the PZT and Ni-O-Ni angle as a function of the PZT thickness

If we consider the modulation of the Ni-O-Ni bond angles as the major contribution to the modulation of the onset temperature for both magnetic and transport properties, we can try to see at which position the studied heterostructures sit on the bulk phase diagram of the $RNiO_3$, and re-proposed in **Fig. VI-19**. We would suggest an almost bulk-like value of the Ni-O-Ni angle for the PZT-30 sample which then decreases for the PZT-13 and PZT-6 with a clear separation among the two transition temperatures. STEM-ABF measurements, where we hope to be able to observe the variation of the Ni-O-Ni bond-angles for the entire sample series [83], are ongoing to confirm our hypothesis. Such measurements are scheduled in collaboration with Dr. A. Gloter working at the Laboratoire de Physique des Solides (Université Paris-Saclay). Nevertheless, even if a difference of the Ni-O-Ni bond angle is observed for the different PZT thicknesses, it will be difficult to attribute this to the unique role played by polar distortions as resulting from the ferroelectric field effect, discriminating between the roles played by strain and oxygen vacancies. Therefore, if one wants to investigate the proposed system, and successfully disentangle the different contributions, we believe that a higher quality of the NNO/PZT heterostructures is mandatory. The goal of the growth challenge would be to obtain a structural characterization reflecting the same quality as that of an uncapped NNO thin film. Another growth challenge concerns the growth of a PZT-layer with switchable polarization that would exhibit both remnant and reversible properties, which we were not able to obtain in our case.

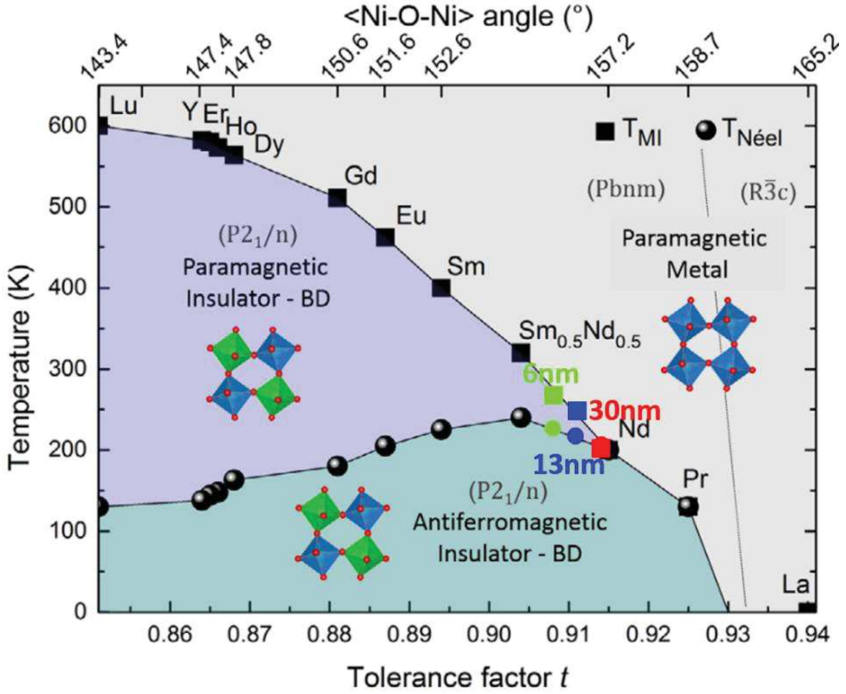

Figure VI-19 Phase diagram of the $RNiO_3$ family exhibiting the structural transition, $T_{Néel}$ and T_{MIT} as a function of the tolerance factor t (bottom x axis) and the Ni–O–Ni angle (top axis). Squares represent the T_{MIT} and circles the $T_{Néel}$. (Taken from Ref. [[7]]). The green, blue and red squares/circles respectively represent the PZT-6, PZT-13 and PZT-30 T_{MIT}/ $T_{Néel}$ of the samples.

3. Summary

We have studied the influence of a ferroelectric PZT layer onto NNO perovskite films through the study of two different kinds of systems. In a first system, consisting in NNO/PZT heterostructures, the polarization state of the PZT layer was fixed by a buffer-layer (either NNO or LMO), and could have an upwards or a downwards orientation of the as-grown ferroelectric polarization. In the second approach, we grew different ferroelectric layer thicknesses on top of the NNO, with a particular polarization structure, from multidomain for the lower PZT thickness (6 nm) to a fully DOWN monodomain for the 30 nm sample. The first system allowed evidencing the ferroelectric effect of PZT on the magnetic order temperature transition of NNO. The difference of polarization can induce a polar distortion in the NNO top-layer that would modify the Ni-O-Ni bond angle which controls the phase transition in the perovskite nickelate as shown in **Fig. VI-19**. Therefore, the difference in Ni-O-Ni bond angle might be at the origin of the 13 K for the $T_{Néel}$ between both PZT polarization configuration. This first part particularly highlights how challenging the synthesis of NNO/PZT heterostructures is. RHEED and XRD characterizations have indeed shown the relatively bad quality of the NNO/PZT interface. It however also evidenced the higher quality of NNO layers when they are grown underneath the PZT.

Thanks to this experience feedback, we decided to synthesize PZT/NNO heterostructures with NNO as the bottom-layer and different thicknesses of the PZT top-layer. For these samples, the quality of the growth conditions of the NNO were the same as the optimized one presented Chapter IV, therefore enhancing the NNO quality when compared to the first experiment. We obtained here a counter-intuitive result: the thicker the PZT top-layer, the closer the structure and electronic properties of the

NNO layer when compared to a bare NNO thin film. The PZT-30 sample has the phase transition temperatures closest to the bare NNO, with a concomitant T_{MIT} and $T_{Néel}$. The PFM measurements highlight the existence of an as-grown multidomain polarization structure for the PZT-6 sample, for which we suggest that UP and DOWN domains lead to opposite polar distortions in the NNO. The opposite local polar distortions induce two different Ni-O-Ni bond angles as schematized in **Fig. VI-18**, and those two different bond angles in the same material are thought to be the consequence of the large observed breathing distortion mode, that we highlighted via XAS measurements. Such large breathing distortions would explain why T_{MIT} and $T_{Néel}$ are further away from the bulk value.

To be more conclusive on the ferroelectric-field effect of the PZT and the hypothetic role played by the polar distortions, high resolution transmission electron microscopy measurements will be performed. The quality of the NNO/PZT interface must also be enhanced to minimize the effect of the oxygen vacancies, and to be able to observe the effect of the ferroelectric-field, alone, on the Ni-O-Ni angle.

VII. Conclusion and perspectives

Perovskite rare-earth nickelates, in both bulk and thin film forms, are of particular interest for both their sharp metal-to-insulator transition (MIT) and their role as promising candidates for high-T_C superconductors mimicking the hallmarks of cuprates. The long experimental and theoretical journey made by the condensed matter community, which has lasted over twenty years, successfully ended in August 2019 with the report of a superconducting state in $Nd_{1-x}Sr_xNiO_2$ infinite-layer nickelate thin films. Since then, lots of efforts have been dedicated to reproduce this result, which still remains a challenge from the synthesis point of view. The experimental and theoretical results published so far on this new superconducting compound, through comparison with those of the largely studied cuprates, offer first useful insights to uncover the physics of these superconducting systems.

The work I have done, and of which I have tried to summarize the main results in this thesis, is mainly focused on this new and hot topic, and my efforts went mostly to the optimisation of the infinite-layer phase synthesis which indeed was the base for all the RIXS characterizations that have followed. Alongside, we also wanted to study the interface effect in perovskite nickelate thin films grown adjacently to a ferroelectric layer in NNO/PZT heterostructures.

I demonstrated our capacity to enhance the quality of nickelate infinite-layer thin films, by first optimizing the growth conditions of the perovskite phase $Nd_{1-x}Sr_xNiO_3$ for three different dopings, x=0, 0.05 and 0.20. I highlight the importance of the oxygen partial pressure in the chamber to reach the desired Ni^{3+} oxidation degree. I also resolved the critical off-stoichiometry issue between the Ni and the Nd cations by performing an ablation of the target without toggling, *i.e.* a single-point ablation. To obtain the infinite-layer phase a two-step synthesis process was necessary. I therefore also had to optimize the reduction conditions, which were different for different Sr dopings and whether an STO capping-layer was present or not. This so-called topotactic reduction is still not properly understood, but our experiences made us speculate that the presence of extended defects in the perovskite structure might act as preferential pathways for the oxygen when performing the reduction. This would explain the shorter in time topotactic process used for the 20%-doped samples. However, those defects, perhaps beyond a given threshold, might also explain the fact that our superconducting samples did not reach a zero-resistance state. As a result of an international collaboration I could perform several RIXS experiment on my samples highlighting the mysterious role of the capping-layer on the low-energy excitations in infinite-layer nickelates. Its presence brings to a strong dispersing magnetic excitation at -0.2 eV of energy loss, while its absence damps the magnon and lets to appear a charge ordering (CO) at $q \approx (1/3, 0)$ r.l.u., robust in temperature for the $NdNiO_2$ parent compound. It was also observed that the CO seems to be in competition with the superconductivity, as it vanishes when the doping increases. Moreover, we had the chance to perform RIXS polarisation-resolved measurements to determine if the observed low-energy excitations were of a magnetic nature or not. As a result, we could discriminate between a phonon and a magnetic excitation. Those RIXS measurements performed with a polarimeter confirmed that even by increasing the doping or in the absence of a capping-layer the magnon is still present but in a damped version. In that sense, we speculate that the damping of the magnon might be linked to the Ni-Nd hybridization which seems stronger for the uncapped and undoped sample since we observe an increase of the -0.6 eV feature spectral weight in our RIXS energy maps. We suggest here that the damping of the magnon might be linked to an ‘effective’ doping which might result from a larger Ni-Nd hybridization. While for cuprates, the damping of the magnetic excitation is observed for highly overdoped samples [244,246], for the infinite-layer nickelates, the magnon is already damped in the superconducting dome, which arouses questions on the pairing mechanism. Indeed, the short-range magnetic order is the main candidate to play the role of the pairing glue in copper oxides-based superconductors. A different mechanism might be in cause in nickelates because of the weaker superexchange interactions, when compared to cuprates, as already suggested by Jiang, M. *et al.* [170].

To continue the investigation, I also measured magnetotransport properties of infinite-layer nickelates, and observed differences between capped and uncapped samples. The collected anisotropy magnetoresistance (AMR) data spoke in favour of a modulation resulting from the Nd-5d Nd-4f intra-atomic coupling and the Ni-Nd hybridisation, the latter largely influenced by the presence/absence of the capping-layer. Out-of-plane AMR, in particular, shows a strong influence of the capping with an intensity modulation of the twofold and fourfold oscillations. In-plane AMR measurements, through the doping, highlight the role of the 4f moment of the Nd cation with robust fourfold oscillations, as already pointed out by Wang, B., Y. *et al*. [142] while comparing the influence of different rare-earths on magnetotransport.

For two decades, experimentalists have largely tried to obtain a superconducting state in nickelate-based heterostructures by orbital-engineering and charge-transfer interface driven phenomena. The here presented study of NNO/PZT heterostructures wanted to follow this road by allowing an orbital polarization with a peculiar Ni-3d e_g orbital filling of the NNO as granted (plausibly) by PZT-induced electrostatic and polar distortion mechanisms. The results firstly highlighted the challenge to obtain high quality NNO/PZT heterostructures characterized by an NNO layer exhibiting bulk-like properties. The structure of the ferroelectric domains in the PZT layer was found to influence the T_{MIT} and $T_{Néel}$ values of the NNO films. I tentatively link this observation to an increase of the Ni-O-Ni angle by referring to the bulk phase diagram of the perovskite rare-earth nickelates [5], in agreement with the modified XAS feature observed at the Ni-L_3 edge. STEM measurements, which are planned with Alexandre Gloter from Laboratoire de physique des Solides, Paris-Saclay, will shed light on this hypothesis. XLD measurements should also be performed on better optimized samples to be conclusive on the expected orbital engineering induced by the ferroelectric field-effect.

Reaching a zero-resistance state for the infinite-layer nickelates thin films is also an ongoing objective. For this, different processes will be tried in the near future, such as an annealing process for the substrate in order to reconstruct the substrate interface, or the use of a target with a higher amount of Ni to eliminate the remanent off-stoichiometry issues, or a fine-tuning of the topotactic process to reduce the possible defects it induces in the thin films. Synthesizing infinite-layer nickelates with different rare-earths is also another prospective, to observe the role of the intra-atomic coupling of the rare earth cation. Modifying the nature of the substrate, and of the capping-layer, is also something I already started, with the first measurement in RIXS shown in Chapter V. Synchrotron beamtimes are already planned for the beginning of 2023 with a week of angle-resolved photoemission spectroscopy (ARPES) at the CASSIOPEE beamline in Soleil, Paris, that will allow to measure the Fermi surface of our thin films exhibiting a very smooth and step-terraced morphologies. We plan to observe the influence of the doping, as well as that of the capping-layer, which with a thickness of only 3 u.c. will not hinder the measurements. Another experiment is scheduled at the ESRF on the ID32 beamline, but for XMCD measurements this time, for which we already have preliminary results as shown in **[Fig1]**. We can observe that our previous XMCD measurements, made on the DEIMOS beamline in Soleil synchrotron, Paris, seems to tend to a non-zero spin moment in the absence of a magnetic field, which is the fingerprint of a magnetic ordering in our thin films. This result is corroborated by the work of Fowlie, J. *et al*. where they highlight the intrinsic magnetism of the infinite layer nickelates through muon spin rotation/relaxation measurements [137]. In order to complete our preliminary measurements, we plan to observe the evolution of the XMCD intensity at low-field, and at different temperatures also for samples with non-magnetic rare-earths, such as La or Pr. Moreover, observing the influence of the capping-layer could also be worth, as its role is still not yet clarified.

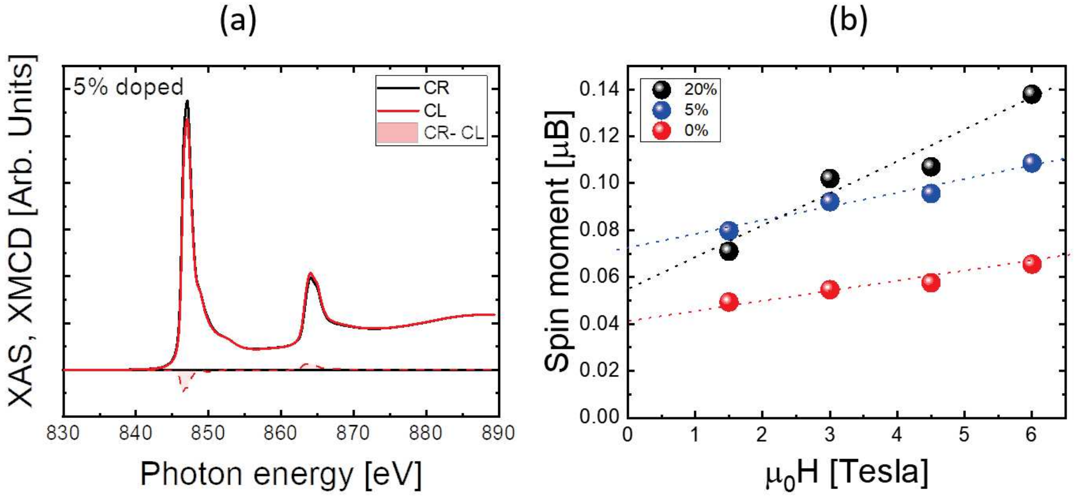

Figure VII-1 (a) XAS and XMCD measurements of a NSNO$_2$(5) sample in grazing incidence (60°) at 20 K in TEY mode (b) Spin moment obtained from XMCD measurements thanks to the sum rules for 0, 5 and 20%-doped infinite-layer nickelates

Finally, I think that the recent synthesis and reduction of infinite-layer single-crystal [117] will provide precious insight on the physics of this new superconductive system. However, the two-step synthesis to obtain the infinite-layer phase in single-crystal form seems even more challenging than in thin films. Until now, the Sr-doping level at the edge of the superconducting dome found in thin films has not been reached yet in single-crystal form [117], leaving many open questions, such as the possible role of the substrate to reach a superconductive state. Moreover, strain and pressure already showed their capacity to enhance the T_C of this system [113,114,119], but it will be interesting to observe how other external stimuli, such as light or electric field-effect, will modify the properties of the infinite-layer phase, even on novel infinite-layer-based heterostructures. I have no doubt that the synthesis difficulties to reach those goals will challenge the scientific community for the next years to come.

Appendix A

OriginLab code of the fitting procedure of the quasi-elastic peak and LE features in RIXS scans:

```
[Fitting Parameters]
Names = x0,xL,tL,s,y0,b1,b2
Initial Values = 0(x0),0.08(xL),0.043(tL),0.043(s),0.02(y0),0.001(b1),0.017(b2)
Lower Bounds = -0.005(I, On),0.05(I, On),0.01(I, On),0.01(I, On),0(X, On),0(X, On),0(X, On)
Upper Bounds = 0.005(I, On),0.2(I, On),0.2(I, On),0.04(I, On),0.03(I, On),--(I, Off),--(I, Off)

[Independent Variables]
x =
[Dependent Variables]
y =
[Formula]
NLFitContext *pCtxt = Project.GetNLFitContext();
 if ( pCtxt )
 {
   // Vector for the output in each iteration.
   static vector vX, vY;

   static int nSize;

   BOOL bIsNewParamValues = pCtxt->IsNewParamValues();

   // If parameters were updated, we will recalculate the convolution result.
   if ( bIsNewParamValues )
   {
```

```
//Sampling Interval
double dx = 0.001;
vX.Data(-0.5, 0.5, dx);
nSize = vX.GetSize();

vector vF, vG, vTerm1, vTerm2, vDenominator, vAddBase;

double Numerator = tL;
vTerm1 = (vX^2 - xL^2)^2;
vTerm2 = 4*tL^2 * vX^2;
vDenominator = vTerm1 + vTerm2;

//Function f(x)
vF =b1*Numerator / vDenominator;

//Function g(x)
vG = 1/(s*sqrt(log(pi/2)))*exp(-2*(vX-xL)^2/s^2);

//Pad zeroes at the end of f and g before convolution
vector vA(2*nSize-1), vB(2*nSize-1);
vA.SetSubVector( vF );
vB.SetSubVector( vG );

//Perform circular convolution
int iRet = fft_fft_convolution(2*nSize-1, vA, vB);

//Truncate the beginning and the end
vY.SetSize(nSize);
vA.GetSubVector( vY, floor(nSize/2), nSize + floor(nSize/2)-1 );

//Baseline
```

```
    vAddBase = y0+b2/(s*sqrt(pi/2))*exp(-2.0*(vX-x0)^2/s^2 );



    //Fitted Y
    vY = dx*vY +  vAddBase;
  }

  //Interpolate y from x for the fitting data on the convolution result.
  ocmath_interpolate( &x, &y, 1, vX, vY, nSize );
}
```

[QuickCheck]

x=0.01

x0=0

xL=0.08

tL=0.043

s=0.043

y0=0.02

b1=0.001

b2=0.017

REFERENCES

[1] J. Heber, *Materials Science: Enter the Oxides*, Nature **459**, 28 (2009).

[2] J. G. Bednorz and K. A. Müller, *Possible High Tc Superconductivity in the Ba-La-Cu-O System*, Zeitschrift Für Phys. B Condens. Matter **64**, 189 (1986).

[3] J. Bardeen, L. N. Cooper, and J. R. Schrieffer, *Theory of Superconductivity*, Phys. Rev. **108**, 1175 (1957).

[4] E. Benckiser, M. Hepting, and B. Keimer, *Neighbours in Charge*, Nat. Mater. **21**, 1102 (2022).

[5] M. L. Medarde, *Structural, Magnetic and Electronic Properties of Perovskites (R = Rare Earth)*, J. Phys. Condens. Matter **9**, 1679 (1997).

[6] S. Middey, J. Chakhalian, P. Mahadevan, J. W. Freeland, A. J. Millis, and D. D. Sarma, *Physics of Ultrathin Films and Heterostructures of Rare-Earth Nickelates*, Annu. Rev. Mater. Res. **46**, 305 (2016).

[7] S. Catalano, M. Gibert, J. Fowlie, J. Iñiguez, J. M. Triscone, and J. Kreisel, *Rare-Earth Nickelates RNiO3: Thin Films and Heterostructures*, Reports Prog. Phys. **81**, (2018).

[8] Y. Nomura and R. Arita, *Superconductivity in Infinite-Layer Nickelates, Key Issues Review.*, Reports Prog. Phys. **85**, 20 (2022).

[9] A. S. Botana, F. Bernardini, and A. Cano, *Nickelate Superconductors: An Ongoing Dialog between Theory and Experiments*, J. Exp. Theor. Phys. **132**, 618 (2021).

[10] D. I. Khomskii, *Transition Metal Compounds* (Cambridge University Press, 2014).

[11] V. M. Goldschmidt, *Die Gesetze Der Krystallochemie*, Naturwissenschaften **14**, 477 (1926).

[12] A. M. Glazer, *Simple Ways of Determining Perovskite Structures*, Acta Crystallogr. Sect. A **31**, 756 (1975).

[13] A. Vailionis, H. Boschker, W. Siemons, E. P. Houwman, D. H. A. Blank, G. Rijnders, and G. Koster, *Misfit Strain Accommodation in Epitaxial ABO3 Perovskites: Lattice Rotations and Lattice Modulations*, Phys. Rev. B - Condens. Matter Mater. Phys. **83**, 6 (2011).

[14] Y. Tokura and N. Nagaosa, *Orbital Physics in Transition-Metal Oxides*, Science (80-.). **288**, 462 (2000).

[15] Y. Okimoto, T. Katsufuji, Y. Okada, T. Arima, and Y. Tokura, *Optical Spectra in (La,Y)TiO3: Variation of Mott-Hubbard Gap Features with Change of Electron Correlation and Band Filling*, Phys. Rev. B **51**, 9581 (1995).

[16] G. A. Sawatzky, W. Geertsma, and C. Haas, *Magnetic Interaction and Covalency Effecs in Mainly Ionic Compounds*, J. Magn. Magn. Mater. **3**, 37 (1976).

[17] J. Fowlie, Electronic and Structural Properties of LaNiO3-Based Heterostructures, University of Geneva, Geneva, Switzerland, 2018.

[18] N. F. Mott, *The Basis of the Electron Theory of Metals, with Special Reference to the Transition Metals*, Proc. Phys. Soc. Sect. A **62**, 416 (1949).

[19] N. F. Mott, *Metal-Insulator Transitions*, Pure Appl. Chem. **52**, 65 (1980).

[20] J. Zaanen, G. A. Sawatzky, and J. W. Allen, *Band Gaps and Electronic Structure of Transition-Metal Compounds*, Phys. Rev. Lett. **55**, 418 (1985).

[21] D. D. Sarma, *Electronic Structure of Transition Metal Compounds: Photoemission Experiments and Model Hamiltonian Calculations*, J. Solid State Chem. **88**, 45 (1990).

[22] T. Mizokawa, H. Namatame, A. Fujimori, K. Akeyama, H. Kondoh, H. Kuroda, and N. Kosugi, *Origin of the Band Gap in the Negative Charge-Transfer-Energy Compound NaCuO2*, Phys. Rev. Lett. **67**, 1638 (1991).

[23] Y. Tokura, *Critical Features of Colossal Magnetoresistive Manganites*, Reports Prog. Phys. **69**, 797 (2006).

[24] S. M. Said, M. F. M. Sabri, and F. Salleh, *Ferroelectrics and Their Applications* (Elsevier Ltd., 2016).

[25] J. B. Goodenough and J. S. Zhou, *Orbital Ordering in Orthorhombic Perovskites*, J. Mater. Chem. **17**, 2394 (2007).

[26] A. M. Oleś, K. Wohlfeld, and G. Khaliullin, *Orbital Symmetry and Orbital Excitations in High-Tc Superconductors*, Condens. Matter **4**, 46 (2019).

[27] G. Demazeau, A. Marbeuf, M. Pouchard, and P. Hagenmuller, *Sur Une Série de Composés Oxygènes Du Nickel Trivalent Derivés de La Perovskite*, J. Solid State Chem. **3**, 582 (1971).

[28] J. A. Alonso, J. L. García-Muñoz, M. T. Fernández-Díaz, M. A. G. Aranda, M. J. Martínez-Lope, and M. T. Casais, *Charge Disproportionation in RNiO3 Perovskites: Simultaneous Metal-Insulator and Structural Transition in YNiO3*, Phys. Rev. Lett. **82**, 3871 (1999).

[29] J. Alonso, M. Martínez-Lope, M. Casais, and J. García-Muñoz, *Room-Temperature Monoclinic Distortion Due to Charge Disproportionation in Perovskites with Small Rare-Earth Cations Y, Er, Tm, Yb, and Lu): A Neutron Diffraction Study*, Phys. Rev. B - Condens. Matter Mater. Phys. **61**, 1756 (2000).

[30] J. L. García-Muñoz, J. Rodríguez-Carvajal, and P. Lacorre, *Sudden Appearance of an Unusual Spin Density Wave at the Metal-Insulator Transition in the Perovskites Rnio3(R = Pr, Nd)*, EPL **20**, 241 (1992).

[31] M. Medarde, M. T. Fernández-Díaz, and P. Lacorre, *Long-Range Charge Order in the Low-Temperature Insulating Phase of PrNiO3*, Phys. Rev. B - Condens. Matter Mater. Phys. **78**, 2 (2008).

[32] P. Lacorre, M. Medarde, M. Zacchigna, M. Grioni, and G. Margaritondo, *Electronic-Structure Evolution through the Metal-Insulator Transition in (Formula Presented)*, Phys. Rev. B - Condens. Matter Mater. Phys. **60**, R8426 (1999).

[33] J. L. García-Muñoz, M. A. G. Aranda, J. A. Alonso, and M. J. Martínez-Lope, *Structure and Charge Order in the Antiferromagnetic Band-Insulating Phase of NdNiO3*, Phys. Rev. B - Condens. Matter Mater. Phys. **79**, 13 (2009).

[34] V. Bisogni, S. Catalano, R. J. Green, M. Gibert, R. Scherwitzl, Y. Huang, V. N. Strocov, P. Zubko, S. Balandeh, J. M. Triscone, G. Sawatzky, and T. Schmitt, *Ground-State Oxygen Holes and the Metal-Insulator Transition in the Negative Charge-Transfer Rare-Earth Nickelates*, Nat. Commun. **7**, 17 (2016).

[35] B. Lau and A. J. Millis, *Theory of the Magnetic and Metal-Insulator Transitions in RNiO3bulk*

and Layered Structures, Phys. Rev. Lett. **110**, 12 (2013).

[36] J. W. Freeland, M. Van Veenendaal, and J. Chakhalian, *Evolution of Electronic Structure across the Rare-Earth RNiO3series*, J. Electron Spectros. Relat. Phenomena **208**, 56 (2016).

[37] T. Mizokawa, D. Khomskii, and G. Sawatzky, *Spin and Charge Ordering in Self-Doped Mott Insulators*, Phys. Rev. B - Condens. Matter Mater. Phys. **61**, 11263 (2000).

[38] M. Medarde, A. Fontaine, and P. Lacorre, *RNi03 Perovskites (R =Pr,Nd): Nickel Valence and the Metal-Insulator Transition Investigated by x-Ray-Absorption Spectroscopy*, **46**, 975 (1992).

[39] T. Mizokawa, A. Fujimori, T. Arima, Y. Tokura, N. Mori, and J. Akimitsu, *Electronic Structure of PrNiO3 Studied by Photoemission and X-Ray-Absorption Spectroscopy: Band Gap and Orbital Ordering*, Phys. Rev. B **52**, 13865 (1995).

[40] V. Scagnoli, U. Staub, A. M. Mulders, M. Janousch, G. I. Meijer, G. Hammerl, J. M. Tonnerre, and N. Stojic, *Role of Magnetic and Orbital Ordering at the Metal-Insulator Transition in NdNiO3*, Phys. Rev. B - Condens. Matter Mater. Phys. **73**, 10 (2006).

[41] M. Alexander, H. Romberg, P. Nücker, P. Adelmann, J. Fink, J. T. Markert, M. B. Maple, S. Uchida, H. Takagi, Y. Tokura, A. C. W. P. James, and D. W. Murphy, *Electronic Structure Studies on the N-Type Doped Superconductors R2-XMxCu04-y (R =Pr, Nd, Sm; M =Ce,Th) and Nd2Cu04-XFx by Electron-Energy-Loss Spectroscopy*, Physycal Rev. B **43**, 333 (1991).

[42] R. J. Green, M. W. Haverkort, and G. A. Sawatzky, *Bond Disproportionation and Dynamical Charge Fluctuations in the Perovskite Rare-Earth Nickelates*, Phys. Rev. B **94**, 19 (2016).

[43] S. R. Barman, A. Chainani, and D. D. Sarma, *Covalency-Driven Unusual Metal-Insulator Transition in Nickelates*, Phys. Rev. B **49**, 8475 (1994).

[44] S. Johnston, A. Mukherjee, I. Elfimov, M. Berciu, and G. A. Sawatzky, *Charge Disproportionation without Charge Transfer in the Rare-Earth-Element Nickelates as a Possible Mechanism for the Metal-Insulator Transition*, Phys. Rev. Lett. **112**, 10 (2014).

[45] H. Park, A. J. Millis, and C. A. Marianetti, *Site-Selective Mott Transition in Rare-Earth-Element Nickelates*, Phys. Rev. Lett. **109**, 15 (2012).

[46] S. Catalano, M. Gibert, V. Bisogni, F. He, R. Sutarto, M. Viret, P. Zubko, R. Scherwitzl, G. A. Sawatzky, T. Schmitt, and J.-M. Triscone, *Tailoring the Electronic Transitions of NdNiO$_3$ Films through (111)$_{Pc}$ Oriented Interfaces*, APL Mater. **3**, 062506 (2015).

[47] M. Hepting, *Ordering Phenomena in Rare-Earth Nickelate Heterostructures*, Vol. 3 (2017).

[48] V. Scagnoli, U. Staub, Y. Bodenthin, M. García-Fernández, A. M. Mulders, G. I. Meijer, and G. Hammerl, *Induced Noncollinear Magnetic Order of Nd3+ in NdNi O3 Observed by Resonant Soft X-Ray Diffraction*, Phys. Rev. B - Condens. Matter Mater. Phys. **77**, 14 (2008).

[49] D. Kumar, K. P. Rajeev, J. A. Alonso, and M. J. Martínez-Lope, *Spin-Canted Magnetism and Decoupling of Charge and Spin Ordering in NdNiO 3*, Phys. Rev. B **88**, 014410 (2013).

[50] Y. Lu, D. Betto, K. Fürsich, H. Suzuki, H. H. Kim, G. Cristiani, G. Logvenov, N. B. Brookes, E. Benckiser, M. W. Haverkort, G. Khaliullin, M. Le Tacon, M. Minola, and B. Keimer, *Site-Selective Probe of Magnetic Excitations in Rare-Earth Nickelates Using Resonant Inelastic X-Ray Scattering*, Phys. Rev. X **8**, 3 (2018).

[51] M. Hepting, R. J. Green, Z. Zhong, M. Bluschke, Y. E. Suyolcu, S. Macke, A. Frano, S. Catalano, M. Gibert, R. Sutarto, F. He, G. Cristiani, G. Logvenov, Y. Wang, P. A. van Aken, P. Hansmann, M. Le Tacon, J. M. Triscone, G. A. Sawatzky, B. Keimer, and E. Benckiser, *Complex Magnetic*

Order in Nickelate Slabs, Nat. Phys. **14**, 1097 (2018).

[52] X. Obradors, L. M. Paulius, M. B. Maple, J. B. Torrance, A. I. Nazzal, J. Fontcuberta, and X. Granados, *Pressure Dependence of the Metal-Insulator Transition in the Charge-Transfer Oxides RNiO3 (R=Pr,Nd,Nd0.7La0.3)*, Phys. Rev. B **47**, 12353 (1993).

[53] A. D. Caviglia, R. Scherwitzl, P. Popovich, W. Hu, H. Bromberger, R. Singla, M. Mitrano, M. C. Hoffmann, S. Kaiser, P. Zubko, S. Gariglio, J. M. Triscone, M. Först, and A. Cavalleri, *Ultrafast Strain Engineering in Complex Oxide Heterostructures*, Phys. Rev. Lett. **108**, (2012).

[54] J. L. García-Muñoz, M. Suaaidi, M. J. Martínez-Lope, and J. A. Alonso, *Influence of Carrier Injection on the Metal-Insulator Transition in Electron- and Hole-Doped R1-XAxNiO3 Perovskites*, Phys. Rev. B **52**, 13563 (1995).

[55] M. Medarde, P. Lacorre, K. Conder, F. Fauth, and A. Furrer, *Giant 16O – 18O Isotope Effect on the Metal-Insulator Transition of RNiO3 Perovskites (R = Rare Earth)*, Phys. Rev. Lett. **80**, 2397 (1998).

[56] X. Li, D. Preziosi, S. Valencia, F. Trier, K. Bouzehouane, T. Cornelissen, L. Lopez-Mir, J. H. Lee, M. Bibes, A. Barthélémy, and A. Gloter, *Direct Mapping of Phase Separation across the Metal–Insulator Transition of NdNiO 3* , Nano Lett. **18**, 2226 (2018).

[57] D. Preziosi, *Studies on the Ferroelectric Field Effect in Perovskite Oxide Heterostructures*, (2014).

[58] A. V. Boris, Y. Matiks, E. Benckiser, A. Frano, P. Popovich, V. Hinkov, P. Wochner, M. Castro-Colin, E. Detemple, V. K. Malik, C. Bernhard, T. Prokscha, A. Suter, Z. Salman, E. Morenzoni, G. Cristiani, H. U. Habermeier, and B. Keimer, *Dimensionality Control of Electronic Phase Transitions in Nickel-Oxide Superlattices*, Science (80-.). **332**, 937 (2011).

[59] J. Zhang, H. Zheng, Y. Ren, and J. F. Mitchell, *High-Pressure Floating-Zone Growth of Perovskite Nickelate LaNiO3 Single Crystals*, Cryst. Growth Des. **17**, 2730 (2017).

[60] Z. Li, W. Guo, T. T. Zhang, J. H. Song, T. Y. Gao, Z. B. Gu, and Y. F. Nie, *Epitaxial Growth and Electronic Structure of Ruddlesden-Popper Nickelates (Lan +1NinO3 n +1, n = 1-5)*, APL Mater. **8**, 091112 (2020).

[61] D. Preziosi, A. Sander, A. Barthélémy, and M. Bibes, *Reproducibility and Off-Stoichiometry Issues in Nickelate Thin Films Grown by Pulsed Laser Deposition*, AIP Adv. **7**, 015210 (2017).

[62] T. M. Rice, A. V. M., and B. D., *Electronic Structure of Possible Nickelate Analogs to the Cuprates*, Phys. Rev. B - Condens. Matter Mater. Phys. **59**, 7901 (1999).

[63] J. Chaloupka and G. Khaliullin, *Orbital Order and Possible Superconductivity in LaNiO3/LaMO3 Superlattices*, Phys. Rev. Lett. **100**, 3 (2008).

[64] P. Hansmann, X. Yang, A. Toschi, G. Khaliullin, O. K. Andersen, and K. Held, *Turning a Nickelate Fermi Surface into a Cupratelike One through Heterostructuring*, Phys. Rev. Lett. **103**, 016401 (2009).

[65] J. Chakhalian, J. M. Rondinelli, J. Liu, B. A. Gray, M. Kareev, E. J. Moon, N. Prasai, J. L. Cohn, M. Varela, I. C. Tung, M. J. Bedzyk, S. G. Altendorf, F. Strigari, B. Dabrowski, L. H. Tjeng, P. J. Ryan, and J. W. Freeland, *Asymmetric Orbital-Lattice Interactions in Ultrathin Correlated Oxide Films*, Phys. Rev. Lett. **107**, 116805(4) (2011).

[66] J. W. Freeland, J. Liu, M. Kareev, B. Gray, J. W. Kim, P. Ryan, R. Pentcheva, and J. Chakhalian, *Orbital Control in Strained Ultra-Thin LaNiO3/LaAlO3 Superlattices*, EPL **96**, 57004 (2011).

[67] E. Benckiser, M. W. Haverkort, S. Brück, E. Goering, S. MacKe, A. Frañ, X. Yang, O. K. Andersen, G. Cristiani, H. U. Habermeier, A. V. Boris, I. Zegkinoglou, P. Wochner, H. J. Kim, V. Hinkov, and B. Keimer, *Orbital Reflectometry of Oxide Heterostructures*, Nat. Mater. **10**, 189 (2011).

[68] O. Janson and K. Held, *Finite-Temperature Phase Diagram of (111) Nickelate Bilayers*, Phys. Rev. B **98**, 11 (2018).

[69] T. H. Kim, D. Puggioni, Y. Yuan, L. Xie, H. Zhou, N. Campbell, P. J. Ryan, Y. Choi, J. W. Kim, J. R. Patzner, S. Ryu, J. P. Podkaminer, J. Irwin, Y. Ma, C. J. Fennie, M. S. Rzchowski, X. Q. Pan, V. Gopalan, J. M. Rondinelli, and C. B. Eom, *Polar Metals by Geometric Design*, Nature **533**, 68 (2016).

[70] M. N. Grisolia, J. Varignon, G. Sanchez-Santolino, A. Arora, S. Valencia, M. Varela, R. Abrudan, E. Weschke, E. Schierle, J. E. Rault, J. P. Rueff, A. Barthélémy, J. Santamaria, and M. Bibes, *Hybridization-Controlled Charge Transfer and Induced Magnetism at Correlated Oxide Interfaces*, Nat. Phys. **12**, 484 (2016).

[71] A. S. Disa, D. P. Kumah, A. Malashevich, H. Chen, D. A. Arena, E. D. Specht, S. Ismail-Beigi, F. J. Walker, and C. H. Ahn, *Orbital Engineering in Symmetry-Breaking Polar Heterostructures*, Phys. Rev. Lett. **114**, 2 (2015).

[72] M. Wu, E. Benckiser, M. W. Haverkort, A. Frano, Y. Lu, U. Nwankwo, S. Brück, P. Audehm, E. Goering, S. Macke, V. Hinkov, P. Wochner, G. Christiani, S. Heinze, G. Logvenov, H.-U. Habermeier, and B. Keimer, *Strain and Composition Dependence of Orbital Polarization in Nickel Oxide Superlattices*, Phys. Rev. B **88**, 125124 (2013).

[73] M. Gibert, P. Zubko, R. Scherwitzl, J. Íñiguez, and J. M. Triscone, *Exchange Bias in LaNiO3-LaMnO3 Superlattices*, Nat. Mater. **11**, 195 (2012).

[74] M. Gibert, M. Viret, A. Torres-Pardo, C. Piamonteze, P. Zubko, N. Jaouen, J. M. Tonnerre, A. Mougin, J. Fowlie, S. Catalano, A. Gloter, O. Stéphan, and J. M. Triscone, *Interfacial Control of Magnetic Properties at LaMnO3/LaNiO3 Interfaces*, Nano Lett. **15**, 7355 (2015).

[75] J. C. Rojas Sánchez, B. Nelson-Cheeseman, M. Granada, E. Arenholz, and L. B. Steren, *Exchange-Bias Effect at La 0.75Sr 0.25MnO 3/LaNiO 3 Interfaces*, Phys. Rev. B - Condens. Matter Mater. Phys. **85**, 2 (2012).

[76] L. Zhang, X. G. Chen, H. J. Gardner, M. A. Koten, J. E. Shield, and X. Hong, *Effect of Strain on Ferroelectric Field Effect in Strongly Correlated Oxide Sm0.5Nd0.5NiO3*, Appl. Phys. Lett. **107**, 152906 (2015).

[77] M. S. J. Marshall, A. Malashevich, A. S. Disa, M. G. Han, H. Chen, Y. Zhu, S. Ismail-Beigi, F. J. Walker, and C. H. Ahn, *Conduction at a Ferroelectric Interface*, Phys. Rev. Appl. **2**, 5 (2014).

[78] A. Herklotz, D. Lee, E. J. Guo, T. L. Meyer, J. R. Petrie, and H. N. Lee, *Strain Coupling of Oxygen Non-Stoichiometry in Perovskite Thin Films*, J. Phys. Condens. Matter **29**, 493001 (2017).

[79] D. Marrocchelli, N. H. Perry, and S. R. Bishop, *Understanding Chemical Expansion in Perovskite-Structured Oxides*, Phys. Chem. Chem. Phys. **17**, 10028 (2015).

[80] H. N. Lee, S. S. Ambrose Seo, W. S. Choi, and C. M. Rouleau, *Growth Control of Oxygen Stoichiometry in Homoepitaxial SrTiO 3 Films by Pulsed Laser Epitaxy in High Vacuum*, Sci. Rep. **6**, 19941 (2016).

[81] S. Heo, C. Oh, J. Son, and H. M. Jang, *Influence of Tensile-Strain-Induced Oxygen Deficiency on Metal-Insulator Transitions in NdNiO3-δ Epitaxial Thin Films*, Sci. Rep. **7**, 4681 (2017).

[82] P. Walke, S. Gupta, Q. R. Li, M. Major, W. Donner, B. Mercey, and U. Lüders, *The Role of*

Oxygen Vacancies on the Weak Localization in LaNiO3-δ Epitaxial Thin Films, J. Phys. Chem. Solids **123**, (2018).

[83] C. L. Jia, M. Lentzen, and K. Urban, *Atomic-Resolution Imaging of Oxygen in Perovskite Ceramics*, Science (80-.). **299**, 870 (2003).

[84] Q. Zhang, X. He, J. Shi, N. Lu, H. Li, Q. Yu, Z. Zhang, L. Q. Chen, B. Morris, Q. Xu, P. Yu, L. Gu, K. Jin, and C. W. Nan, *Atomic-Resolution Imaging of Electrically Induced Oxygen Vacancy Migration and Phase Transformation in SrCoO2.5-σ*, Nat. Commun. **8**, 104 (2017).

[85] T. H. Kim, T. R. Paudel, R. J. Green, K. Song, H. S. Lee, S. Y. Choi, J. Irwin, B. Noesges, L. J. Brillson, M. S. Rzchowski, G. A. Sawatzky, E. Y. Tsymbal, and C. B. Eom, *Strain-Driven Disproportionation at a Correlated Oxide Metal-Insulator Transition*, Phys. Rev. B **101**, 121105 (2020).

[86] L. Wang, K. A. Stoerzinger, L. Chang, X. Yin, Y. Li, C. S. Tang, E. Jia, M. E. Bowden, Z. Yang, A. Abdelsamie, L. You, R. Guo, J. Chen, A. Rusydi, J. Wang, S. A. Chambers, and Y. Du, *Strain Effect on Oxygen Evolution Reaction Activity of Epitaxial NdNiO $_3$ Thin Films*, ACS Appl. Mater. Interfaces **11**, 12941 (2019).

[87] L. Wang, S. Dash, L. Chang, L. You, Y. Feng, X. He, K. Jin, Y. Zhou, H. Guan Ong, P. Ren, S. Wang, L. Chen, and J. Wang, *Oxygen Vacancy Induced Room-Temperature Metal−Insulator Transition in Nickelate Films and Its Potential Application in Photovoltaics*, ACS Appl. Mater. Interfaces **8**, 29 (2016).

[88] M. Kotiuga, Z. Zhang, J. Li, F. Rodolakis, H. Zhou, R. Sutarto, F. He, Q. Wang, Y. Sun, Y. Wang, N. A. Aghamiri, S. B. Hancock, L. P. Rokhinson, D. P. Landau, Y. Abate, J. W. Freeland, R. Comin, S. Ramanathan, and K. M. Rabe, *Carrier Localization in Perovskite Nickelates from Oxygen Vacancies*, Proc. Natl. Acad. Sci. U. S. A. **116**, 21992 (2019).

[89] L. Cao, O. Petracic, P. Zakalek, A. Weber, U. Rücker, J. Schubert, A. Koutsioubas, S. Mattauch, and T. Brückel, *Reversible Control of Physical Properties via an Oxygen-Vacancy-Driven Topotactic Transition in Epitaxial La 0.7 Sr 0.3 MnO 3−δ Thin Films*, Adv. Mater. **31**, 7 (2019).

[90] L. Wang, Z. Yang, M. E. Bowden, and Y. Du, *Brownmillerite Phase Formation and Evolution in Epitaxial Strontium Ferrite Heterostructures*, Appl. Phys. Lett. **114**, 231602 (2019).

[91] V. Humbert, R. El Hage, G. Krieger, G. Sanchez-santolino, A. Sander, S. Collin, J. Trastoy, J. Briatico, J. Santamaria, D. Preziosi, and J. E. Villegas, *An Oxygen Vacancy Memristor Ruled by Electron Correlations*, Adv. Sci. **1**, 2201753 (2022).

[92] M. Crespin, B. Y. P. Levitz, and L. Gatineau, *Reduced Forms of LaNi03 Perovskite*, Local Environ. **79**, 1195 (1983).

[93] M. M. T. J. B. Clarke, J. W. Hastie, L. H. E. Kihlborg, R. Metselaar, *Definitions of Terms Relating to Phase Transitions*, Pure App. Chem **66**, 577 (1994).

[94] M. A. Hayward, M. A. Green, M. J. Rosseinsky, and J. Sloan, *Sodium Hydride as a Powerful Reducing Agent for Topotactic Oxide Deintercalation: Synthesis and Characterization of the Nickel(I) Oxide LaNiO2*, J. Am. Chem. Soc. **121**, 8843 (1999).

[95] M. A. Hayward and M. J. Rosseinsky, *Synthesis of the Infinite Layer Ni(I) Phase NdNiO2+x by Low Temperature Reduction of NdNiO3 with Sodium Hydride*, Solid State Sci. **5**, 839 (2003).

[96] A. Ikeda, T. Manabe, and M. Naito, *Comparison of Reduction Agents in the Synthesis of Infinite-Layer LaNiO2 Films*, Phys. C Supercond. Its Appl. **506**, 83 (2014).

[97] M. Kawai, S. Inoue, M. Mizumaki, N. Kawamura, N. Ichikawa, and Y. Shimakawa, *Reversible*

Changes of Epitaxial Thin Films from Perovskite LaNiO 3 to Infinite-Layer Structure LaNiO2, Appl. Phys. Lett. **94**, 92 (2009).

[98] X. R. Zhou, Z. X. Feng, P. X. Qin, H. Yan, S. Hu, H. X. Guo, X. N. Wang, H. J. Wu, X. Zhang, H. Y. Chen, X. P. Qiu, and Z. Q. Liu, *Absence of Superconductivity in Nd0.8Sr0.2NiOx Thin Films without Chemical Reduction*, Rare Met. **39**, 368 (2020).

[99] Y. Kobayashi, Z. Li, K. Hirai, C. Tassel, F. Loyer, N. Ichikawa, N. Abe, T. Yamamoto, Y. Shimakawa, K. Yoshimura, M. Takano, O. J. Hernandez, and H. Kageyama, *Gas Phase Contributions to Topochemical Hydride Reduction Reactions*, J. Solid State Chem. **207**, 190 (2013).

[100] A. Ikeda, T. Manabe, and M. Naito, *Improved Conductivity of Infinite-Layer LaNiO2 Thin Films by Metal Organic Decomposition*, Phys. C Supercond. Its Appl. **495**, 134 (2013).

[101] K. Lee, B. H. Goodge, D. Li, M. Osada, B. Y. Wang, Y. Cui, L. F. Kourkoutis, and H. Y. Hwang, *Aspects of the Synthesis of Thin Film Superconducting Infinite-Layer Nickelates*, APL Mater. **8**, 41107 (2020).

[102] G. Cotton, F. A.; Wilkinson, *Advanced Inorganic Chemistry*, 5th ed. (1980).

[103] L. Si, W. Xiao, J. Kaufmann, J. M. Tomczak, Y. Lu, Z. Zhong, and K. Held, *Topotactic Hydrogen in Nickelate Superconductors and Akin Infinite-Layer Oxides AB O2*, Phys. Rev. Lett. **124**, 16 (2020).

[104] T. Onozuka, A. Chikamatsu, T. Katayama, T. Fukumura, and T. Hasegawa, *Formation of Defect-Fluorite Structured NdNiO: XHy Epitaxial Thin Films via a Soft Chemical Route from NdNiO3 Precursors*, Dalt. Trans. **45**, 12114 (2016).

[105] D. Li, K. Lee, B. Y. Wang, M. Osada, S. Crossley, H. R. Lee, Y. Cui, Y. Hikita, and H. Y. Hwang, *Superconductivity in an Infinite-Layer Nickelate*, Nature **572**, 624 (2019).

[106] S. Zeng, C. S. Tang, X. Yin, C. Li, M. Li, Z. Huang, J. Hu, W. Liu, G. J. Omar, H. Jani, Z. S. Lim, K. Han, D. Wan, P. Yang, S. J. Pennycook, A. T. S. Wee, and A. Ariando, *Phase Diagram and Superconducting Dome of Infinite-Layer Nd1-XSrxNiO2 Thin Films*, Phys. Rev. Lett. **125**, 14 (2020).

[107] Q. Gao, Y. Zhao, X. J. Zhou, and Z. Zhu, *Preparation of Superconducting Thin Films of Infinite-Layer Nickelate Nd0.8Sr0.2NiO2*, Chinese Phys. Lett. **38**, (2021).

[108] Y. Xiang, Q. Li, Y. Li, H. Yang, Y. Nie, and H. H. Wen, *Physical Properties Revealed by Transport Measurements for Superconducting Nd0.8Sr0.2NiO2Thin Films*, Chinese Phys. Lett. **38**, 047401 (2021).

[109] D. Li, B. Y. Wang, K. Lee, S. P. Harvey, M. Osada, B. H. Goodge, L. F. Kourkoutis, and H. Y. Hwang, *Superconducting Dome in Nd1-XSrxNiO2 Infinite Layer Films*, Phys. Rev. Lett. **125**, 27001 (2020).

[110] M. Osada, B. Y. Wang, K. Lee, D. Li, and H. Y. Hwang, *Phase Diagram of Infinite Layer Praseodymium Nickelate Pr1-XSrxNiO2 Thin Films*, Phys. Rev. Mater. **4**, 12 (2020).

[111] M. Osada, B. Y. Wang, B. H. Goodge, S. P. Harvey, K. Lee, D. Li, L. F. Kourkoutis, and H. Y. Hwang, *Nickelate Superconductivity without Rare-Earth Magnetism: (La,Sr)NiO2*, Adv. Mater. **33**, 45 (2021).

[112] S. Zeng, C. Li, L. Er Chow, Y. Cao, Z. Zhang, C. S. Tang, X. Yin, Z. S. Lim, J. Hu, P. Yang, and A. Ariando, *Superconductivity in Infinite-Layer Nickelate La1-XCaxNiO2 Thin Films*, Sci. Adv. **8**, 9927 (2022).

[113] K. Lee, B. Y. Wang, M. Osada, B. H. Goodge, T. C. Wang, Y. Lee, S. Harvey, W. J. Kim, Y. Yu, C. Murthy, S. Raghu, L. F. Kourkoutis, and H. Y. Hwang, *Character of the "Normal State" of the Nickelate Superconductors*, (2022).

[114] X. Ren, J. Li, W.-C. Chen, Q. Gao, J. J. Sanchez, J. Hales, H. Luo, F. Rodolakis, J. L. Mcchesney, T. Xiang, J. Hu, F.-C. Zhang, R. Comin, Y. Wang, X. J. Zhou, and Z. Zhu, Strain-Induced Enhancement of T c in Infinite-Layer Pr 0.8 Sr 0.2 NiO 2 Films, 2022.

[115] Q. Li, C. He, J. Si, X. Zhu, Y. Zhang, and H.-H. Wen, *Absence of Superconductivity in Bulk Nd1−xSrxNiO2*, Commun. Mater. **1**, 16 (2020).

[116] B. X. Wang, H. Zheng, E. Krivyakina, O. Chmaissem, P. P. Lopes, J. W. Lynn, L. C. Gallington, Y. Ren, S. Rosenkranz, J. F. Mitchell, and D. Phelan, *Synthesis and Characterization of Bulk Nd1-XSrxNi O2 and Nd1-XSrxNi O3*, Phys. Rev. Mater. **4**, 8 (2020).

[117] P. Puphal, Y. M. Wu, K. Fürsich, H. Lee, M. Pakdaman, J. A. N. Bruin, J. Nuss, Y. Eren Suyolcu, P. A. van Aken, B. Keimer, M. Isobe, and M. Hepting, *Topotactic Transformation of Single Crystals: From Perovskite to Infinite-Layer Nickelates*, Sci. Adv. **7**, 8091 (2021).

[118] G. A. Pan, D. Ferenc Segedin, H. LaBollita, Q. Song, E. M. Nica, B. H. Goodge, A. T. Pierce, S. Doyle, S. Novakov, D. Córdova Carrizales, A. T. N'Diaye, P. Shafer, H. Paik, J. T. Heron, J. A. Mason, A. Yacoby, L. F. Kourkoutis, O. Erten, C. M. Brooks, A. S. Botana, and J. A. Mundy, *Superconductivity in a Quintuple-Layer Square-Planar Nickelate*, Nat. Mater. **21**, 160 (2022).

[119] N. N. Wang, M. W. Yang, K. Y. Chen, Z. Yang, H. Zhang, Z. H. Zhu, Y. Uwatoko, X. L. Dong, K. J. Jin, J. P. Sun, and J.-G. Cheng, *Pressure-Induced Monotonic Enhancement of Tc to over 30 K in the Superconducting Pr0.82Sr0.18NiO2 Thin Films*, (2021).

[120] A. M. Oleś, K. Wohlfeld, and G. Khaliullin, *Orbital Symmetry and Orbital Excitations in High-Tc Superconductors*, Condens. Matter **4**, 46 (2019).

[121] B. H. Goodge, D. Li, K. Lee, M. Osada, B. Y. Wang, G. A. Sawatzky, H. Y. Hwang, and L. F. Kourkoutis, *Doping Evolution of the Mott-Hubbard Landscape in Infinite-Layer Nickelates*, Proc. Natl. Acad. Sci. U. S. A. **118**, (2021).

[122] A. S. Botana and M. R. Norman, *Similarities and Differences between LaNiO2 and CaCuO2 and Implications for Superconductivity*, Phys. Rev. X **10**, (2020).

[123] K. W. Lee and W. E. Pickett, *Infinite-Layer LaNiO2: Ni1+ Is Not Cu2+*, Phys. Rev. B - Condens. Matter Mater. Phys. **70**, 1 (2004).

[124] M. Hepting, D. Li, C. J. Jia, H. Lu, E. Paris, Y. Tseng, X. Feng, M. Osada, E. Been, Y. Hikita, Y. D. Chuang, Z. Hussain, K. J. Zhou, A. Nag, M. Garcia-Fernandez, M. Rossi, H. Y. Huang, D. J. Huang, Z. X. Shen, T. Schmitt, H. Y. Hwang, B. Moritz, J. Zaanen, T. P. Devereaux, and W. S. Lee, *Electronic Structure of the Parent Compound of Superconducting Infinite-Layer Nickelates*, Nat. Mater. **19**, 381 (2020).

[125] M. Rossi, H. Lu, A. Nag, D. Li, M. Osada, K. Lee, B. Y. Wang, S. Agrestini, M. Garcia-Fernandez, Y.-D. Chuang, Z. X. Shen, H. Y. Hwang, B. Moritz, K.-J. Zhou, T. P. Devereaux, and W. S. Lee, *Orbital and Spin Character of Doped Carriers in Infinite-Layer Nickelates*, (2020).

[126] G. Krieger, L. Martinelli, S. Zeng, L. E. Chow, K. Kummer, R. Arpaia, M. M. Sala, N. B. Brookes, A. Ariando, N. Viart, M. Salluzzo, G. Ghiringhelli, and D. Preziosi, *Charge and Spin Order Dichotomy in NdNiO2 Driven by SrTiO3 Capping Layer*, Phys. Rev. Lett. **129**, 27002 (2021).

[127] H. Lu, M. Rossi, A. Nag, M. Osada, D. F. Li, K. Lee, B. Y. Wang, M. Garcia-Fernandez, S. Agrestini, Z. X. Shen, E. M. Been, B. Moritz, T. P. Devereaux, J. Zaanen, H. Y. Hwang, K. J. Zhou,

and W. S. Lee, *Magnetic Excitations in Infinite-Layer Nickelates*, Science (80-.). **373**, 213 (2021).

[128] C. C. Tam, J. Choi, X. Ding, S. Agrestini, A. Nag, B. Huang, H. Luo, M. García-Fernández, L. Qiao, and K.-J. Zhou, *Charge Density Waves in Infinite-Layer NdNiO2 Nickelates*, (2021).

[129] M. Rossi, M. Osada, J. Choi, S. Agrestini, D. Jost, Y. Lee, H. Lu, B. Y. Wang, K. Lee, A. Nag, Y.-D. Chuang, C.-T. Kuo, S.-J. Lee, B. Moritz, T. P. Devereaux, Z.-X. Shen, J.-S. Lee, K.-J. Zhou, H. Y. Hwang, and W.-S. Lee, *A Broken Translational Symmetry State in an Infinite-Layer Nickelate*, (2021).

[130] G. Chen and W. A. Goddard, *The Magnon Pairing Mechanism of Superconductivity in Cuprate Ceramics*, Science (80-.). **239**, 899 (1988).

[131] R. Comin and A. Damascelli, *Resonant X-Ray Scattering Studies of Charge Order in Cuprates*, Annu. Rev. Condens. Matter Phys. Is **7**, 369 (2016).

[132] Y. Y. Peng, E. W. Huang, R. Fumagalli, M. Minola, Y. Wang, X. Sun, Y. Ding, K. Kummer, X. J. Zhou, N. B. Brookes, B. Moritz, L. Braicovich, T. P. Devereaux, and G. Ghiringhelli, *Dispersion, Damping, and Intensity of Spin Excitations in the Monolayer (Bi,Pb)2(Sr,La)2CuO6+δ Cuprate Superconductor Family*, Phys. Rev. B **98**, 14 (2018).

[133] M. Le Tacon, G. Ghiringhelli, J. Chaloupka, M. M. Sala, V. Hinkov, M. W. Haverkort, M. Minola, M. Bakr, K. J. Zhou, S. Blanco-Canosa, C. Monney, Y. T. Song, G. L. Sun, C. T. Lin, G. M. De Luca, M. Salluzzo, G. Khaliullin, T. Schmitt, L. Braicovich, and B. Keimer, *Intense Paramagnon Excitations in a Large Family of High-Temperature Superconductors*, Nat. Phys. **7**, 725 (2011).

[134] P. Bourges, H. Casalta, A. S. Ivanov, and D. Petitgrand, *Superexchange Coupling and Spin Susceptibility Spectral Weight in Undoped Monolayer Cuprates*, Phys. Rev. Lett. **79**, 4906 (1997).

[135] J. Q. Lin, P. V. Arribi, G. Fabbris, A. S. Botana, D. Meyers, H. Miao, Y. Shen, D. G. Mazzone, J. Feng, S. G. Chiuzbaian, A. Nag, A. C. Walters, M. Garcia-Fernandez, K.-J. Zhou, J. Pelliciari, I. Jarrige, J. W. Freeland, J. Zhang, J. F. Mitchell, V. Bisogni, X. Liu, M. R. Norman, and M. P. M. Dean, *Strong Superexchange in a d^9 Nickelate Revealed by Resonant Inelastic X-Ray Scattering*, ArXiv (2020).

[136] S. Li, S. D. Wilson, D. Mandrus, B. Zhao, Y. Onose, Y. Tokura, and P. Dai, *Spin-Charge Coupling in Lightly Doped Nd 2-XCe x-CuO 4*, Phys. Rev. B - Condens. Matter Mater. Phys. **71**, 14 (2005).

[137] J. Fowlie, M. Hadjimichael, M. M. Martins, D. Li, M. Osada, B. Y. Wang, K. Lee, Y. Lee, Z. Salman, T. Prokscha, J. M. Triscone, H. Y. Hwang, and A. Suter, *Intrinsic Magnetism in Superconducting Infinite-Layer Nickelates*, Nat. Phys. **18**, 1043 (2022).

[138] G. R. Stewart, *Superconductivity in Iron Compounds*, Rev. Mod. Phys. **83**, 4 (2011).

[139] W. Yu, J. S. Higgins, P. Bach, and R. L. Greene, *Transport Evidence of a Magnetic Quantum Phase Transition in Electron-Doped High-Temperature Superconductors*, Phys. Rev. B - Condens. Matter Mater. Phys. **76**, 2 (2007).

[140] V. P. Jovanović, L. Fruchter, Z. Z. Li, and H. Raffy, *Anisotropy of the In-Plane Angular Magnetoresistance of Electron-Doped Sr1-x Lax CuO2 Thin Films*, Phys. Rev. B - Condens. Matter Mater. Phys. **81**, 13 (2010).

[141] V. P. Jovanović, H. Raffy, Z. Z. Li, G. Reményi, and P. Monceau, *High Magnetic-Field Evolution of the in-Plane Angular Magnetoresistance of Electron-Doped Sr1-XLaxCuO2 in the Normal State*, Phys. Rev. B **103**, 014520 (2021).

[142] B. Y. Wang, T. C. Wang, Y.-T. Hsu, M. Osada, K. Lee, C. Jia, C. Duffy, D. Li, J. Fowlie, M. R. Beasley, T. P. Devereaux, I. R. Fisher, N. E. Hussey, and H. Y. Hwang, *Rare-Earth Control of the Superconducting Upper Critical Field in Infinite-Layer Nickelates*, ArXiv (2022).

[143] K. Held, L. Si, P. Worm, O. Janson, R. Arita, Z. Zhong, J. M. Tomczak, and M. Kitatani, *Phase Diagram of Nickelate Superconductors Calculated by Dynamical Vertex Approximation*, Front. Phys. **9**, 803 (2022).

[144] S. Iimura, S. Matuishi, H. Sato, T. Hanna, Y. Muraba, S. W. Kim, J. E. Kim, M. Takata, and H. Hosono, *Two-Dome Structure in Electron-Doped Iron Arsenide Superconductors*, Nat. Commun. **3**, 943 (2012).

[145] J. Matsumoto, K. Hanzawa, M. Sasase, S. Haindl, T. Katase, H. Hiramatsu, and H. Hosono, *Superconductivity at 48 K of Heavily Hydrogen-Doped SmFeAsO Epitaxial Films Grown by Topotactic Chemical Reaction Using Ca H2*, Phys. Rev. Mater. **3**, 10 (2019).

[146] Y. Nomura, M. Hirayama, T. Tadano, Y. Yoshimoto, K. Nakamura, and R. Arita, *Formation of a Two-Dimensional Single-Component Correlated Electron System and Band Engineering in the Nickelate Superconductor NdNiO 2* , Phys. Rev. B **100**, 20 (2019).

[147] Y. Gu, S. Zhu, X. Wang, J. Hu, and H. Chen, *A Substantial Hybridization between Correlated Ni-d Orbital and Itinerant Electrons in Infinite-Layer Nickelates*, Commun. Phys. **3**, (2020).

[148] H. Sakakibara, H. Usui, K. Suzuki, T. Kotani, H. Aoki, and K. Kuroki, *Model Construction and a Possibility of Cupratelike Pairing in a New D9 Nickelate Superconductor (Nd,Sr)NiO2*, Phys. Rev. Lett. **125**, 77003 (2020).

[149] X. Wu, D. Di Sante, T. Schwemmer, W. Hanke, H. Y. Hwang, S. Raghu, and R. Thomale, *Robust Dx2-Y2-Wave Superconductivity of Infinite-Layer Nickelates*, Phys. Rev. B **101**, 6 (2020).

[150] M. Hirayama, T. Tadano, Y. Nomura, and R. Arita, *Materials Design of Dynamically Stable D9 Layered Nickelates*, Phys. Rev. B **101**, 7 (2020).

[151] E. Been, W. S. Lee, H. Y. Hwang, Y. Cui, J. Zaanen, T. Devereaux, B. Moritz, and C. Jia, *Electronic Structure Trends across the Rare-Earth Series in Superconducting Infinite-Layer Nickelates*, Phys. Rev. X **11**, 011050 (2021).

[152] P. Jiang, L. Si, Z. Liao, and Z. Zhong, *Electronic Structure of Rare-Earth Infinite-Layer RNi O2(R=La,Nd)*, Phys. Rev. B **100**, 20 (2019).

[153] J. Karp, A. S. Botana, M. R. Norman, H. Park, M. Zingl, and A. Millis, *Many-Body Electronic Structure of NdNiO 2 and CaCuO 2*, Phys. Rev. X **10**, (2020).

[154] F. Lechermann, *Doping-Dependent Character and Possible Magnetic Ordering of NdNiO2*, Phys. Rev. Mater. **5**, 4 (2021).

[155] Y. Wang, C. J. Kang, H. Miao, and G. Kotliar, *Hund's Metal Physics: From SrNiO2 to LaNiO2*, Phys. Rev. B **102**, 16 (2020).

[156] F. Lechermann, *Multiorbital Processes Rule the Nd1-XSrxNiO2 Normal State*, Phys. Rev. X **10**, 41002 (2020).

[157] C. J. Kang and G. Kotliar, *Optical Properties of the Infinite-Layer La1-XSrxNiO2 and Hidden Hund's Physics*, Phys. Rev. Lett. **126**, 127401 (2021).

[158] J. Karp, A. Hampel, M. Zingl, A. S. Botana, H. Park, M. R. Norman, and A. J. Millis, *Comparative Many-Body Study of Pr4Ni3 O8 and NdNiO2*, Phys. Rev. B **102**, 24 (2020).

[159] K. Higashi, M. Winder, J. Kuneš, and A. Hariki, *Core-Level X-Ray Spectroscopy of Infinite-Layer*

Nickelate: Study, Phys. Rev. X **11**, 4 (2021).

[160] J. Karp, A. Hampel, and A. J. Millis, *Dependence of DFT+DMFT Results on the Construction of the Correlated Orbitals*, Phys. Rev. B **103**, 19 (2021).

[161] M. Y. Choi, K. W. Lee, and W. E. Pickett, *Role of 4f States in Infinite-Layer NdNiO2*, Phys. Rev. B **101**, 20503 (2020).

[162] S. Bandyopadhyay, P. Adhikary, T. Das, I. Dasgupta, and T. Saha-Dasgupta, *Superconductivity in Infinite-Layer Nickelates: Role of f Orbitals*, Phys. Rev. B **102**, 22 (2020).

[163] R. Zhang, C. Lane, B. Singh, J. Nokelainen, B. Barbiellini, R. S. Markiewicz, A. Bansil, and J. Sun, *Magnetic and F-Electron Effects in LaNiO2 and NdNiO2 Nickelates with Cuprate-like 3dx2−y2 Band*, Commun. Phys. **4**, 1 (2021).

[164] G. M. Zhang, Y. F. Yang, and F. C. Zhang, *Self-Doped Mott Insulator for Parent Compounds of Nickelate Superconductors*, Phys. Rev. B **101**, 1 (2020).

[165] G. A. Sawatzky, *Superconductivity Seen in a Non-Magnetic Nickel Oxide*, Nature **572**, 592 (2019).

[166] Z. J. Lang, R. Jiang, and W. Ku, *Strongly Correlated Doped Hole Carriers in the Superconducting Nickelates: Their Location, Local Many-Body State, and Low-Energy Effective Hamiltonian*, Phys. Rev. B **103**, 18 (2021).

[167] F. C. Zhang and T. M. Rice, *Effective Hamiltonian for the Superconducting Cu Oxides*, Phys. Rev. B **37**, 3759 (1988).

[168] N. B. Brookes, G. Ghiringhelli, O. Tjernberg, L. H. Tjeng, T. Mizokawa, T. W. Li, and A. A. Menovsky, *Detection of Zhang-Rice Singlets Using Spin-Polarized Photoemission*, Phys. Rev. Lett. **87**, 237003 (2001).

[169] E. Pellegrin, N. Nücker, J. Fink, S. L. Molodtsov, A. Gutiérrez, E. Navas, O. Strebel, Z. Hu, M. Domke, G. Kaindl, S. Uchida, Y. Nakamura, J. Markl, M. Klauda, G. Saemann-Ischenko, A. Krol, J. L. Peng, Z. Y. Li, and R. L. Greene, *Orbital Character of States at the Fermi Level in La2-XSrxCuO4 and R2-XCexCuO4 (R=Nd,Sm)*, Phys. Rev. B **47**, 3354 (1993).

[170] M. Jiang, M. Berciu, and G. A. Sawatzky, *Critical Nature of the Ni Spin State in Doped NdNiO2*, Phys. Rev. Lett. **124**, 207004 (2020).

[171] H. Zhang, L. Jin, S. Wang, B. Xi, X. Shi, F. Ye, and J. W. Mei, *Effective Hamiltonian for Nickelate Oxides Nd1-XSrxNiO2*, Phys. Rev. Res. **2**, 013214 (2020).

[172] P. Werner and S. Hoshino, *Nickelate Superconductors: Multiorbital Nature and Spin Freezing*, Phys. Rev. B **101**, 4 (2020).

[173] F. Bernardini and A. Cano, *Stability and Electronic Properties of LaNiO2/SrTiO3 Heterostructures*, JPhys Mater. **3**, 03LT01 (2020).

[174] R. He, P. Jiang, Y. Lu, Y. Song, M. Chen, M. Jin, L. Shui, and Z. Zhong, *Polarity-Induced Electronic and Atomic Reconstruction at NdNiO2/SrTiO3 Interfaces*, Phys. Rev. B **102**, 3 (2020).

[175] B. Geisler and R. Pentcheva, *Fundamental Difference in the Electronic Reconstruction of Infinite-Layer versus Perovskite Neodymium Nickelate Films on SrTiO3 (001)*, Phys. Rev. B **102**, 2 (2020).

[176] Y. Zhang, L. F. Lin, W. Hu, A. Moreo, S. Dong, and E. Dagotto, *Similarities and Differences between Nickelate and Cuprate Films Grown on a SrTiO3 Substrate*, Phys. Rev. B **102**, 195117 (2020).

[177] X. Wu, K. Jiang, D. Di Sante, W. Hanke, A. P. Schnyder, J. Hu, and R. Thomale, *Surface S-Wave Superconductivity for Oxide-Terminated Infinite-Layer Nickelates*, **1** (2020). ArXiv ID : 2008.06009

[178] H. M. Smith and A. F. Turner, *Vacuum Deposited Thin Films Using a Ruby Laser*, Appl. Opt. **4**, 147 (1965).

[179] T. H. Maiman, *Stimulated Optical Radiation in Ruby*, Nature **187**, 493 (1960).

[180] A. Inam, X. D. Wu, T. Venkatesan, S. B. Ogale, C. C. Chang, and D. Dijkkamp, *Pulsed Laser Etching of High Tc Superconducting Films*, Appl. Phys. Lett. **51**, 1112 (1987).

[181] R. Eason, editor , *Pulsed Laser Deposition of Thin Films* (John Wiley & Sons, Inc., Hoboken, NJ, USA, 2006).

[182] D. Oka and T. Fukumura, *Crystal Engineering for Novel Functionalities with Oxide Thin Film Epitaxy*, CrystEngComm **19**, 2144 (2017).

[183] M. Crespin, O. Isnard, F. Dubois, J. Choisnet, and P. Odier, *LaNiO2: Synthesis and Structural Characterization*, J. Solid State Chem. **178**, 1326 (2005).

[184] P. VASCONCELOS, Experimental and Theoretical Study on Fe-Cr-O Thin Films : From Fine Structure to Macroscopic Behavior, Paris-Saclay, 2022.

[185] F. Gellé, *Hétérostructures Épitaxiées Avec Des Propriétés Dépendantes de Spin et de Charges Pour Des Applications En Spintronique*, (2020).

[186] G. Binnig, F. Quate, and C. Gerber, *Atomic Force Microscope*, Vol. 56 (CRC Press, 1986).

[187] R. Aso, D. Kan, Y. Shimakawa, and H. Kurata, *Atomic Level Observation of Octahedral Distortions at the Perovskite Oxide Heterointerface*, Sci. Rep. **3**, 2214 (2013).

[188] A. Gloter, G. Tieri, D. Li, M. Caputo, V. N. Strocov, O. Stéphan, J. M. Triscone, and S. Gariglio, *Role of Point and Line Defects on the Electronic Structure of LaAlO3/SrTiO3 Interfaces*, APL Mater. **8**, (2020).

[189] P. B. . V. H. Conn, *Hall Effect Measurements*, Methods Ecol. Evol. **195**, 1 (2014).

[190] D. C. Look, C. E. Stutz, J. R. Sizelove, and K. R. Evans, *On Hall Scattering Factors for Holes in GaAs*, J. Appl. Phys. **80**, 1913 (1996).

[191] H. Xue, Y. Hong, C. Li, J. Meng, Y. Li, K. Liu, M. Liu, W. Jiang, Z. Zhang, L. He, R. Dou, C. Xiong, and J. Nie, *Large Negative Magnetoresistance Driven by Enhanced Weak Localization and Kondo Effect at the Interface of LaAl O3 and Fe-Doped SrTi O3*, Phys. Rev. B **98**, 8 (2018).

[192] A. D. Caviglia, S. Gariglio, N. Reyren, D. Jaccard, T. Schneider, M. Gabay, S. Thiel, G. Hammerl, J. Mannhart, and J. M. Triscone, *Electric Field Control of the LaAlO3/SrTiO3 Interface Ground State*, Nature **456**, 624 (2008).

[193] M. Kubin, M. Guo, T. Kroll, H. Löchel, E. Källman, M. L. Baker, R. Mitzner, S. Gul, J. Kern, A. Föhlisch, A. Erko, U. Bergmann, V. Yachandra, J. Yano, M. Lundberg, and P. Wernet, *Probing the Oxidation State of Transition Metal Complexes: A Case Study on How Charge and Spin Densities Determine Mn L-Edge X-Ray Absorption Energies*, Chem. Sci. **9**, 6813 (2018).

[194] J. Kanamori and A. Kotani, editors , *Core-Level Spectroscopy in Condensed Systems*, Vol. 81 (Springer Berlin Heidelberg, Berlin, Heidelberg, 1988).

[195] M. Abbate, J. B. Goedkoop, F. M. F. de Groot, M. Grioni, J. C. Fuggle, S. Hofmann, H. Petersen, and M. Sacchi, *Probing Depth of Soft X-ray Absorption Spectroscopy Measured in Total-*

electron-yield Mode, Surf. Interface Anal. **18**, 65 (1992).

[196] M. Kasrai, W. N. Lennard, R. W. Brunner, G. M. Bancroft, J. A. Bardwell, and K. H. Tan, *Sampling Depth of Total Electron and Fluorescence Measurements in Si L- and K-Edge Absorption Spectroscopy*, Appl. Surf. Sci. **99**, 303 (1996).

[197] G. van der Laan and A. I. Figueroa, *X-Ray Magnetic Circular Dichroism - A Versatile Tool to Study Magnetism*, Coord. Chem. Rev. **277**, 95 (2014).

[198] Z. Liao, E. Skoropata, J. W. Freeland, E.-J. Guo, R. Desautels, X. Gao, C. Sohn, A. Rastogi, T. Zac Ward, T. Zou, T. Charlton, M. R. Fitzsimmons, & Ho, and N. Lee, *Large Orbital Polarization in Nickelate-Cuprate Heterostructures by Dimensional Control of Oxygen Coordination*, (n.d.).

[199] G. Van der Laan, *Sum Rules and Fundamental Spectra of Magnetic X-Ray Dichroism in Crystal Field Symmetry*, J. Phys. Soc. Japan **63**, 2393 (1994).

[200] E. C. Stoner and E. P. Wohlfarth, *A Mechanism of Magnetic Hysteresis in Heterogeneous Alloys*, Philos. Trans. R. Soc. London. Ser. A, Math. Phys. Sci. **240**, 599 (1948).

[201] C. T. Chen, Y. U. Idzerda, H. J. Lin, N. V. Smith, G. Meigs, E. Chaban, G. H. Ho, E. Pellegrin, and F. Sette, *Experimental Confirmation of the X-Ray Magnetic Circular Dichroism Sum Rules for Iron and Cobalt*, Phys. Rev. Lett. **75**, 152 (1995).

[202] H. Ishii, Y. Ishiwata, R. Eguchi, Y. Harada, M. Watanabe, A. Chainani, and S. Shin, Resonant Soft X-Ray Emission Spectroscopy of NiO across the Ni L 2,3 Thresholds, 2001.

[203] J. P. Hill and D. F. Mcmorrow, *X-Ray Resonant Exchange Scattering: Polarization Dependence and Correlation Functions*, Acta Crystallogr. Sect. A Found. Crystallogr. **52**, 236 (1996).

[204] J. Fink, E. Schierle, E. Weschke, and J. Geck, *Resonant Elastic Soft X-Ray Scattering*, Rep. Prog. Phys **76**, 56502 (2013).

[205] P. Steadman and R. Fan, *Magnetic Scattering with Polarised Soft X-Rays*, in *Magnetic Materials - Recent Advances and Applications* (IntechOpen, 2022).

[206] S. Catalano, M. Gibert, V. Bisogni, O. E. Peil, F. He, R. Sutarto, M. Viret, P. Zubko, R. Scherwitzl, A. Georges, G. A. Sawatzky, T. Schmitt, and J.-M. Triscone, *Electronic Transitions in Strained SmNiO $_3$ Thin Films*, APL Mater. **2**, 116110 (2014).

[207] R. Fumagalli, L. Braicovich, M. Minola, Y. Y. Peng, K. Kummer, D. Betto, M. Rossi, E. Lefrançois, C. Morawe, M. Salluzzo, H. Suzuki, F. Yakhou, M. Le Tacon, B. Keimer, N. B. Brookes, M. M. Sala, and G. Ghiringhelli, *Polarization-Resolved Cu L3-Edge Resonant Inelastic X-Ray Scattering of Orbital and Spin Excitations in NdBa2Cu3 O7-δ*, Phys. Rev. B **99**, 134517 (2019).

[208] L. J. P. Ament, M. Van Veenendaal, T. P. Devereaux, J. P. Hill, and J. Van Den Brink, *Resonant Inelastic X-Ray Scattering Studies of Elementary Excitations*, Rev. Mod. Phys. **83**, 705 (2011).

[209] L. Braicovich, J. Van Den Brink, V. Bisogni, M. M. Sala, L. J. P. Ament, N. B. Brookes, G. M. De Luca, M. Salluzzo, T. Schmitt, V. N. Strocov, and G. Ghiringhelli, *Magnetic Excitations and Phase Separation in the Underdoped La2-XSrxCuO4 Superconductor Measured by Resonant Inelastic X-Ray Scattering*, Phys. Rev. Lett. **104**, 3 (2010).

[210] L. Braicovich, M. Moretti Sala, L. J. P. Ament, V. Bisogni, M. Minola, G. Balestrino, D. Di Castro, G. M. De Luca, M. Salluzzo, G. Ghiringhelli, and J. Van Den Brink, *Momentum and Polarization Dependence of Single-Magnon Spectral Weight for Cu L3 -Edge Resonant Inelastic x-Ray Scattering from Layered Cuprates*, Phys. Rev. B - Condens. Matter Mater. Phys. **81**, 17 (2010).

[211] M. Moretti Sala, V. Bisogni, C. Aruta, G. Balestrino, H. Berger, N. B. Brookes, G. M. De Luca, D.

Di Castro, M. Grioni, M. Guarise, P. G. Medaglia, F. Miletto Granozio, M. Minola, P. Perna, M. Radovic, M. Salluzzo, T. Schmitt, K. J. Zhou, L. Braicovich, and G. Ghiringhelli, *Energy and Symmetry of Dd Excitations in Undoped Layered Cuprates Measured By Cu L3 Resonant Inelastic X-Ray Scattering*, New J. Phys. **13**, 043026 (2011).

[212] G. Berner, S. Glawion, J. Walde, F. Pfaff, H. Hollmark, L. C. Duda, S. Paetel, C. Richter, J. Mannhart, M. Sing, and R. Claessen, *LaAlO3/SrTiO3 Oxide Heterostructures Studied by Resonant Inelastic x-Ray Scattering*, Phys. Rev. B - Condens. Matter Mater. Phys. **82**, 3 (2010).

[213] J. Schlappa, T. Schmitt, F. Vernay, V. N. Strocov, V. Ilakovac, B. Thielemann, H. M. Rønnow, S. Vanishri, A. Piazzalunga, X. Wang, L. Braicovich, G. Ghiringhelli, C. Marin, J. Mesot, B. Delley, and L. Patthey, *Collective Magnetic Excitations in the Spin Ladder Sr14cu24o41 Measured Using High-Resolution Resonant Inelastic x-Ray Scattering*, Phys. Rev. Lett. **103**, 4 (2009).

[214] M. Kawasaki, K. Takahashi, T. Maeda, R. Tsuchiya, M. Shinohara, O. Ishiyama, T. Yonezawa, M. Yoshimoto, and H. Koinuma, *Atomic Control of the SrTiO3 Crystal Surface*, Science (80-.). **266**, 1540 (1994).

[215] Q. Guo, S. Farokhipoor, C. Magén, F. Rivadulla, and B. Noheda, *Tunable Resistivity Exponents in the Metallic Phase of Epitaxial Nickelates*, (2019).

[216] E. Breckenfeld, Z. Chen, A. R. Damodaran, and L. W. Martin, *Effects of Nonequilibrium Growth, Nonstoichiometry, and Film Orientation on the Metal-to-Insulator Transition in NdNiO3 Thin Films*, ACS Appl. Mater. Interfaces **6**, 22436 (2014).

[217] N. Tsvetkov, Q. Lu, Y. Chen, and B. Yildiz, *Surface Chemistry and Non-Stoichiometry of Nd2NiO4+ Epitaxial Thin Films with Different Orientation and Strain*, ECS Trans. **57**, 1743 (2013).

[218] W. Sun, Y. Li, X. Cai, J. Yang, W. Guo, Z. Gu, Y. Zhu, and Y. Nie, *Electronic and Transport Properties in Ruddlesden-Popper Neodymium Nickelates Ndn+1Nin O3n+1 (N=1-5)*, Phys. Rev. B **104**, 2 (2021).

[219] A. J. Hassan, *Study of Optical and Electrical Properties of Nickel Oxide (NiO) Thin Films Depo-Sited by Using a Spray Pyrolysis Technique*, J. Mod. Phys. **5**, 2184 (2014).

[220] Z. Zhang, D. Schwanz, B. Narayanan, M. Kotiuga, J. A. Dura, M. Cherukara, H. Zhou, J. W. Freeland, J. Li, R. Sutarto, F. He, C. Wu, J. Zhu, Y. Sun, K. Ramadoss, S. S. Nonnenmann, N. Yu, R. Comin, K. M. Rabe, S. K. R. S. Sankaranarayanan, and S. Ramanathan, *Perovskite Nickelates as Electric-Field Sensors in Salt Water*, Nature **553**, 68 (2018).

[221] Q. Guo, S. Farokhipoor, C. Magén, F. Rivadulla, and B. Noheda, *Tunable Resistivity Exponents in the Metallic Phase of Epitaxial Nickelates*, Nat. Commun. **11**, 2949 (2020).

[222] B. Chen, N. Gauquelin, R. J. Green, J. H. Lee, C. Piamonteze, M. Spreitzer, D. Jannis, J. Verbeeck, M. Bibes, M. Huijben, G. Rijnders, and G. Koster, *Spatially Controlled Octahedral Rotations and Metal-Insulator Transitions in Nickelate Superlattices*, Nano Lett. **21**, 1295 (2021).

[223] J. Liu, M. Kargarian, M. Kareev, B. Gray, P. J. Ryan, A. Cruz, N. Tahir, Y. De Chuang, J. Guo, J. M. Rondinelli, J. W. Freeland, G. A. Fiete, and J. Chakhalian, *Heterointerface Engineered Electronic and Magnetic Phases of NdNiO 3 Thin Films*, Nat. Commun. **4**, 2714 (2013).

[224] Z. Liao, N. Gauquelin, R. J. Green, K. Müller-Caspary, I. Lobato, L. Li, S. Van Aert, J. Verbeeck, M. Huijben, M. N. Grisolia, V. Rouco, R. El Hage, J. E. Villegas, A. Mercy, M. Bibes, P. Ghosez, G. A. Sawatzky, G. Rijnders, and G. Koster, *Metal–Insulator-Transition Engineering by Modulation Tilt-Control in Perovskite Nickelates for Room Temperature Optical Switching*, Proc. Natl. Acad.

Sci. U. S. A. **115**, 9515 (2018).

[225] M. Osada, B. Y. Wang, B. H. Goodge, K. Lee, H. Yoon, D. Li, M. Miura, L. F. Kourkoutis, and H. Y. Hwang, *Superconducting Praseodymium Nickelate with Infinite Layer Structure*, 1 (2020).

[226] Q. Gu, Y. Li, S. Wan, H. Li, W. Guo, H. Yang, Q. Li, X. Zhu, X. Pan, Y. Nie, and H. H. Wen, *Single Particle Tunneling Spectrum of Superconducting Nd1-XSrxNiO2 Thin Films*, Nat. Commun. **11**, (2020).

[227] S. Grenier, J. P. Hill, V. Kiryukhin, W. Ku, Y. J. Kim, K. J. Thomas, S. W. Cheong, Y. Tokura, Y. Tomioka, D. Casa, and T. Gog, *D-d Excitations in Manganites Probed by Resonant Inelastic X-Ray Scattering*, Phys. Rev. Lett. **94**, 2 (2005).

[228] V. J. Emery and S. A. Kivelson, *Frustrated Electronic Phase Separation and High-Temperature Superconductors*, Phys. C Supercond. Its Appl. **209**, 597 (1993).

[229] C. Castellani, C. Di Castro, and M. Grilli, *Singular Quasiparticle Scattering in the Proximity of Charge Instabilities*, Phys. Rev. Lett. **75**, 4650 (1995).

[230] C. Castellani, C. Di Castro, and M. Grilli, *Non-Fermi-Liquid Behavior and d-Wave Superconductivity near the Charge-Density-Wave Quantum Critical Point*, Zeitschrift Fur Phys. B-Condensed Matter **103**, 137 (1996).

[231] G. Ghiringhelli, M. Le Tacon, M. Minola, S. Blanco-Canosa, C. Mazzoli, N. B. Brookes, G. M. De Luca, A. Frano, D. G. Hawthorn, F. He, T. Loew, M. Moretti Sala, D. C. Peets, M. Salluzzo, E. Schierle, R. Sutarto, G. A. Sawatzky, E. Weschke, B. Keimer, and L. Braicovich, *Long-Range Incommensurate Charge Fluctuations in (Y,Nd)Ba 2Cu3O6+x*, Science (80-.). **337**, 821 (2012).

[232] A. J. Achkar, R. Sutarto, X. Mao, F. He, A. Frano, S. Blanco-Canosa, M. Le Tacon, G. Ghiringhelli, L. Braicovich, M. Minola, M. Moretti Sala, C. Mazzoli, R. Liang, D. A. Bonn, W. N. Hardy, B. Keimer, G. A. Sawatzky, and D. G. Hawthorn, *Distinct Charge Orders in the Planes and Chains of Ortho-III-Ordered YBa 2Cu 3O 6+δ Superconductors Identified by Resonant Elastic X-Ray Scattering*, Phys. Rev. Lett. **109**, 16 (2012).

[233] E. Wahlberg, R. Arpaia, G. Seibold, M. Rossi, R. Fumagalli, E. Trabaldo, N. B. Brookes, L. Braicovich, S. Caprara, U. Gran, G. Ghiringhelli, T. Bauch, and F. Lombardi, *Restored Strange Metal Phase through Suppression of Charge Density Waves in Underdoped YBa2Cu3O7–D*, Science (80-.). **373**, 1506 (2021).

[234] R. Arpaia, S. Caprara, R. Fumagalli, G. De Vecchi, Y. Y. Peng, E. Andersson, D. Betto, G. M. De Luca, N. B. Brookes, F. Lombardi, M. Salluzzo, L. Braicovich, C. Di Castro, M. Grilli, and G. Ghiringhelli, *Dynamical Charge Density Fluctuations Pervading the Phase Diagram of a Cu-Based High-Tc Superconductor*, Science (80-.). **365**, 906 (2019).

[235] G. Seibold, R. Arpaia, Y. Y. Peng, R. Fumagalli, L. Braicovich, C. Di Castro, M. Grilli, G. C. Ghiringhelli, and S. Caprara, *Strange Metal Behaviour from Charge Density Fluctuations in Cuprates*, Commun. Phys. **4**, 7 (2021).

[236] R. Arpaia and G. Ghiringhelli, *Charge Order at High Temperature in Cuprate Superconductors*, J. Phys. Soc. Japan **90**, (2021).

[237] Y. Y. Peng, R. Fumagalli, Y. Ding, M. Minola, S. Caprara, D. Betto, M. Bluschke, G. M. De Luca, K. Kummer, E. Lefrançois, M. Salluzzo, H. Suzuki, M. Le Tacon, X. J. Zhou, N. B. Brookes, B. Keimer, L. Braicovich, M. Grilli, and G. Ghiringhelli, *Re-Entrant Charge Order in Overdoped (Bi,Pb)2.12Sr1.88CuO6+δ Outside the Pseudogap Regime*, Nat. Mater. **17**, 697 (2018).

[238] J. Zhang, D. M. Pajerowski, A. S. Botana, H. Zheng, L. Harriger, J. Rodriguez-Rivera, J. P. C. Ruff,

N. J. Schreiber, B. Wang, Y. S. Chen, W. C. Chen, M. R. Norman, S. Rosenkranz, J. F. Mitchell, and D. Phelan, *Spin Stripe Order in a Square Planar Trilayer Nickelate*, Phys. Rev. Lett. **122**, 247201 (2019).

[239] J. Zhang, Y. S. Chen, D. Phelan, H. Zheng, M. R. Norman, and J. F. Mitchell, *Stacked Charge Stripes in the Quasi-2D Trilayer Nickelate La4 Ni3 O8*, Proc. Natl. Acad. Sci. U. S. A. **113**, 8945 (2016).

[240] B. Keimer, S. A. Kivelson, M. R. Norman, S. Uchida, and J. Zaanen, *From Quantum Matter to High-Temperature Superconductivity in Copper Oxides*, Nature **518**, 179 (2015).

[241] D. J. Scalapino, *A Common Thread: The Pairing Interaction for Unconventional Superconductors*, Rev. Mod. Phys. **84**, 1383 (2012).

[242] L. Braicovich, L. J. P. Ament, V. Bisogni, F. Forte, C. Aruta, G. Balestrino, N. B. Brookes, G. M. De Luca, P. G. Medaglia, F. M. Granozio, M. Radovic, M. Salluzzo, J. Van Den Brink, and G. Ghiringhelli, *Dispersion of Magnetic Excitations in the Cuprate La2CuO4 and CaCuO2 Compounds Measured Using Resonant X-Ray Scattering*, Phys. Rev. Lett. **102**, 22 (2009).

[243] C. J. Jia, E. A. Nowadnick, K. Wohlfeld, Y. F. Kung, C. C. Chen, S. Johnston, T. Tohyama, B. Moritz, and T. P. Devereaux, *Persistent Spin Excitations in Doped Antiferromagnets Revealed by Resonant Inelastic Light Scattering*, Nat. Commun. **5**, 3314 (2014).

[244] M. P. M. Dean, G. Dellea, R. S. Springell, F. Yakhou-Harris, K. Kummer, N. B. Brookes, X. Liu, Y. J. Sun, J. Strle, T. Schmitt, L. Braicovich, G. Ghiringhelli, I. Božović, and J. P. Hill, *Persistence of Magnetic Excitations in La2-XSr XCuO4 from the Undoped Insulator to the Heavily Overdoped Non-Superconducting Metal*, Nat. Mater. **12**, 1019 (2013).

[245] C. W. Chen, J. Choe, and E. Morosan, *Charge Density Waves in Strongly Correlated Electron Systems*, Reports Prog. Phys. **79**, 084505 (2016).

[246] S. Wakimoto, H. Zhang, K. Yamada, I. Swainson, H. Kim, and R. J. Birgeneau, *Direct Relation between the Low-Energy Spin Excitations and Superconductivity of Overdoped High-Tc Superconductors*, Phys. Rev. Lett. **92**, 28 (2004).

[247] Q. Gao, S. Fan, Q. Wang, J. Li, X. Ren, I. Biało, A. Drewanowski, P. Rothenbühler, J. Choi, Y. Wang, T. Xiang, J. Hu, K.-J. Zhou, V. Bisogni, R. Comin, J. Chang, J. Pelliciari, X. J. Zhou, and Z. Zhu, *Magnetic Excitations in Strained Infinite-Layer Nickelate PrNiO2*, (2022). ArXiv ID: 10.1038/srep02834

[248] R. Ramos, S. K. Arora, and I. V. Shvets, *Anomalous Anisotropic Magnetoresistance in Epitaxial Fe3 O 4 Thin Films on MgO(001)*, Phys. Rev. B - Condens. Matter Mater. Phys. **78**, 21 (2008).

[249] J. O'Donnell, J. N. Eckstein, and M. S. Rzchowski, *Temperature and Magnetic Field Dependent Transport Anisotropies in La0.7Ca0.3MnO3 Films*, Appl. Phys. Lett. **76**, 218 (2000).

[250] J. Li, S. L. Li, W. Wu, S. Li, F. Chu, J. Wang, Y. Zhang, Y. Tian, and D. N. Zheng, *A Phenomenological Approach to the Anisotropic Magnetoresistance and Planar Hall Effect in Tetragonal La 2/3 Ca 1/3 MnO 3 Thin Films*, J. Phys. Condens. Matter **22**, 146006 (2010).

[251] P. Fournier, M.-E. Gosselin, S. Savard, J. Renaud, I. Hetel, P. Richard, and G. Riou, *Fourfold Oscillations and Anomalous Magnetoresistance Irreversibility in the Nonmetallic Regime of Pr 1.85 Ce 0.15 CuO 4*, Phys. Rev. B **69**, 220501 (2004).

[252] A. N. Lavrov, H. J. Kang, Y. Kurita, T. Suzuki, S. Komiya, J. W. Lynn, S. H. Lee, P. Dai, and Y. Ando, *Spin-Flop Transition and the Anisotropic Magnetoresistance of Prc 1.3-XLa0.7CexCuO4: Unexpectedly Strong Spin-Charge Coupling in the Electron-Doped Cuprates*, Phys. Rev. Lett. **92**,

3 (2004).

[253] P. Li, E. Y. Jiang, and H. L. Bai, *Fourfold Symmetric Anisotropic Magnetoresistance Based on Magnetocrystalline Anisotropy and Antiphase Boundaries in Reactive Sputtered Epitaxial Fe3O4 Films*, Appl. Phys. Lett. **96**, 092502 (2010).

[254] T. Wu, C. H. Wang, G. Wu, D. F. Fang, J. L. Luo, G. T. Liu, and X. H. Chen, *Giant Anisotropy of the Magnetoresistance and the "spin Valve" Effect in Antiferromagnetic Nd2-XCexCuO4*, J. Phys. Condens. Matter **20**, 8 (2008).

[255] Y. Ando, A. N. Lavrov, and S. Komiya, *Anisotropic Magnetoresistance in Lightly Doped [Formula Presented]: Impact of Antiphase Domain Boundaries on the Electron Transport*, Phys. Rev. Lett. **90**, 4 (2003).

[256] A. Stupakov, O. Pacherova, T. Kocourek, M. Jelinek, A. Dejneka, and M. Tyunina, *Negative Magnetoresistance in Epitaxial Films of Neodymium Nickelate*, Phys. Rev. B **99**, 8 (2019).

[257] K. Jin, X. H. Zhang, P. Bach, and R. L. Greene, *Evidence for Antiferromagnetic Order in La2-x Cex CuO4 from Angular Magnetoresistance Measurements*, Phys. Rev. B - Condens. Matter Mater. Phys. **80**, 012501 (2009).

[258] V. Jovanovic, Z. Z. Li, F. Bouquet, L. Fruchter, and H. Raffy, *Magnetoresistance and Hall Effect in E-Doped Superconducting SrLaCuO Thin Films*, J. Phys. Conf. Ser. **150**, (2009).

[259] D. Preziosi, A. Sander, A. Barthélémy, and M. Bibes, *Reproducibility and Off-Stoichiometry Issues in Nickelate Thin Films Grown by Pulsed Laser Deposition*, AIP Adv. **7**, 015210 (2017).

[260] X. Chen, X. Zhang, M. A. Koten, H. Chen, Z. Xiao, L. Zhang, J. E. Shield, P. A. Dowben, and X. Hong, *Interfacial Charge Engineering in Ferroelectric-Controlled Mott Transistors*, Adv. Mater. **29**, 31 (2017).

[261] D. Preziosi, M. Alexe, D. Hesse, and M. Salluzzo, *Electric-Field Control of the Orbital Occupancy and Magnetic Moment of a Transition-Metal Oxide*, Phys. Rev. Lett. **115**, 157401 (2015).

[262] R. Scherwitzl, P. Zubko, C. Lichtensteiger, and J. M. Triscone, *Electric-Field Tuning of the Metal-Insulator Transition in Ultrathin Films of LaNiO3*, Appl. Phys. Lett. **95**, 222114 (2009).

[263] A. M. Alsaqqa, S. Singh, S. Middey, M. Kareev, J. Chakhalian, and G. Sambandamurthy, *Phase Coexistence and Dynamical Behavior in NdNiO3 Ultrathin Films*, Phys. Rev. B **95**, 12 (2017).

[264] H. Chen, Q. Qiao, M. S. J. Marshall, A. B. Georgescu, A. Gulec, P. J. Phillips, R. F. Klie, F. J. Walker, C. H. Ahn, and S. Ismail-Beigi, *Reversible Modulation of Orbital Occupations via an Interface-Induced Polar State in Metallic Manganites*, Nano Lett. **14**, 4965 (2014).

[265] D. Preziosi, I. Fina, E. Pippel, D. Hesse, X. Marti, F. Bern, M. Ziese, and M. Alexe, *Tailoring the Interfacial Magnetic Anisotropy in Multiferroic Field-Effect Devices*, Phys. Rev. B - Condens. Matter Mater. Phys. **90**, (2014).

[266] M. Imada, A. Fujimori, and Y. Tokura, *Metal-Insulator Transition*, Rev. Morder Phys. **70**, 1039 (1998).

[267] D. H. Erwin, T. Great, P. Crisis, K. Kubo, Y. Isozaki, M. Matsuo, S. Mathews, R. Ramesh, T. Venkatesan, and J. Benedetto, *Ferroelectric Field Effect Transistor Based on Epitaxial Perovskite Heterostructures*, **276**, 238 (1997).

[268] X. Hong, J. B. Yau, J. D. Hoffman, C. H. Ahn, Y. Bason, and L. Klein, *Effect of Electric Field Doping on the Anisotropic Magnetoresistance in Doped Manganites*, Phys. Rev. B - Condens. Matter Mater. Phys. **74**, 17 (2006).

[269] C. A. F. Vaz, J. Hoffman, C. H. Ahn, and R. Ramesh, *Magnetoelectric Coupling Effects in Multiferroic Complex Oxide Composite Structures*, Adv. Mater. **22**, 2900 (2010).

[270] H. Yamada, M. Marinova, P. Altuntas, A. Crassous, L. Bégon-Lours, S. Fusil, E. Jacquet, V. Garcia, K. Bouzehouane, A. Gloter, J. E. Villegas, A. Barthélémy, and M. Bibes, *Ferroelectric Control of a Mott Insulator*, Sci. Rep. **3**, 2834 (2013).

[271] C. L. Jia, S. B. Mi, K. Urban, I. Vrejoiu, M. Alexe, and D. Hesse, *Atomic-Scale Study of Electric Dipoles near Charged and Uncharged Domain Walls in Ferroelectric Films*, Nat. Mater. **7**, 57 (2008).

[272] P. Yu, W. Luo, D. Yi, J. X. Zhang, M. D. Rossell, C. H. Yang, L. You, G. Singh-Bhalla, S. Y. Yang, Q. He, Q. M. Ramasse, R. Erni, L. W. Martin, Y. H. Chu, S. T. Pantelides, S. J. Pennycook, and R. Ramesh, *Interface Control of Bulk Ferroelectric Polarization*, Proc. Natl. Acad. Sci. U. S. A. **109**, 9710 (2012).

[273] D. G. Schlom, L.-Q. Chen, C.-B. Eom, K. M. Rabe, S. K. Streiffer, and J.-M. Triscone, *Strain Tuning of Ferroelectric Thin Films*, Annu. Rev. Mater. Res. **37**, 589 (2007).

[274] J. Li, R. J. Green, Z. Zhang, R. Sutarto, J. T. Sadowski, Z. Zhu, G. Zhang, D. Zhou, Y. Sun, F. He, S. Ramanathan, and R. Comin, *Sudden Collapse of Magnetic Order in Oxygen-Deficient Nickelate Films*, Phys. Rev. Lett. **126**, 187602 (2021).

École doctorale
Physique, chimie-physique
ED 182
Université de Strasbourg

Guillaume Krieger

Structural and orbital engineering in nickelate thin films: on the road of superconductivity

Résumé

L’objectif de ma thèse est de synthétiser les couches minces infinies de nickelates $Nd_{1-x}Sr_xNiO_2$, afin d’étudier leurs propriétés supraconductrices.

Pour cela, la synthèse des couches minces de 10nm a été optimisé tout au long de mon travail par un processus en deux étapes : la croissance de la phase pérovskite par ablation laser pulsée, puis une réduction de chimie douce dite topotactique, afin d’obtenir la phase de couches infinies. Une transition supraconductrice à 11K a été obtenu pour les couches dopée à hauteur de 20% en Sr, comme reporté dans la littérature. Ces couches minces à différents dopages ont notamment été mesurées par spectroscopie d’absorption des rayons X, permettant d’étudier la structure électronique des matériaux, à la résonance spécifique d’un élément. Une série de mesures de résonance inélastique des rayons X à l’ESRF de Grenoble a permis de mettre en avant la présence d’ordre de charge et d’excitation magnétique dans ces matériaux, en fonction de la présence d’une couche protectrice. En effet, les intensités de ces excitations de basse énergie sont en effet modulées par le dopage en Sr, comme cela a pu être observé dans els cuprates, mais aussi par la présence d’une couche protectrice de 3 mailles élémentaires, au-dessus de la couche infinie de nickelate. De plus, des heterostructures $NdNiO_3/PbZrTiO_3$ ont été synthétisées afin d’observer l’effet de champ ferroélectrique sur les températures de transition de phase du NNO, afin d’apporter un levier supplémentaire à la modulation de ces propriétés.

Mots-clefs : nickelates, supraconductivité, couches minces, absorption des rayons X, croissance

Résumé en anglais

The objective of my thesis is to synthesize infinite-layer nickelate $Nd_{1-x}Sr_xNiO_2$ thin films to study their superconductive properties.

The optimization of the 10nm thin films have been the keystone of my work, through a two-step process: the growth of the perovskite phase with pulsed laser deposition, and the reduction in infinite-layer phase through the topotactic reaction. A superconductive transition has been obtained around 11K as observed in literature for 20% Sr-doped thin films. Different doping levels have been measured by soft X-ray absorption in order to study the electronic structure of the material at the resonance of specific elements. A series of resonant inelastic X-ray spectroscopies beamtimes at the ESRF put in evidence the presence of charge order and magnetic excitation as a function of the presence of a capping-layer. Indeed, the intensity of those low-energy excitations were modulated by the Sr doping-level as it could have been observed in cuprates, but also by the presence of a 3-unit cell capping-layer on top of the infinite-layer nickelate. Moreover, $NdNiO_3/PbZrTiO_3$ heterostructures have been synthesized to observe the ferroelectric-field effect on the phase transition temperature.

Key words: nickelates, superconductivity, thin films, X-ray absorption, growth

Résumé en français : Ingénierie structurale et orbitalaire dans les couches minces de nickelates : vers la supraconductivité

1. Introduction

La découverte de nouveaux matériaux afin d'augmenter la puissance et la durabilité des dispositifs existants, ou de permettre de nouvelles applications, est un des fers de lance de la recherche scientifique en microélectronique. Les oxydes de métaux de transition dits « corrélés », car présentant des interactions fortes entre électrons, sont très étudiés dans ce domaine, notamment en raison de leur riche diagramme de phases. Connaître l'origine de ces transitions de phase, et ainsi l'état de base des matériaux a notamment été une grande question qui stimule encore la recherche en science des matériaux corrélés. Dans ce sens, le modèle de Mott-Hubbard (MH)[1] a notamment permit de schématiser les mouvements électrons au sein d'une maille, avec une seule bande électronique formée par un unique niveau d'énergie sur chaque site. Le transfert d'un électron d'un site à l'autre, *i.e.* sautant d'un site i à un site j, amène le système avec un site j possédant deux électrons et un site i qui est vide. Il a été montré grâce au modèle de Mott-Hubbard qu'il fallait une énergie supérieure à la répulsion de Coulomb U pour posséder deux électrons sur le site j. Si l'énergie cinétique du système, *i.e.* l'énergie nécessaire pour faire sauter un électron du site i au site j, est du même ordre de grandeur que la répulsion de Coulomb, alors le matériau peut présenter une transition métal-isolant (MIT) en fonction de U. Cela amène le modèle a une bande à se diviser en deux bandes distinctes, la Hubbard basse (LH) et la Hubbard haute (UH) comme montré dans la **Fig. 1(a)** pour un isolant de Mott-Hubbard. Dans le cas des oxydes métaux de transitions, la structure de bande ne peut être décrite uniquement avec les électrons des orbitales d, car une hybridation avec les orbitales p des oxygènes est possible. Cela s'explique par la direction des orbitales d, qui selon la structure cristallographique, peuvent pointer vers les orbitales p des oxygènes. Ainsi, des électrons des orbitales O-2p peuvent sauter vers les orbitales 3d des métaux de transition et vice-versa. Le transfert d'un électron depuis une orbitale O-2p laisse un trou dans cette-dernière, noté L, avec un électron supplémentaire dans les orbitales d du métal de transition tel que : $d^n \rightarrow d^{n+1}L$. L'énergie requise pour réaliser ce transfert de charge (CT) est notée Δ et peut être assignée à la différence d'énergie à la différence d'énergie entre les bandes p de l'oxygène et la UH band comme montré sur la **Fig. 1(b)**. Zaanen, Sawatzky and Allen, dans leur modèle ZSA[2], ont prédit que pour $U>\Delta$, un comportement avec un intervalle de transfert de charge est observé, alors que pour $U<\Delta$, ce sera un intervalle dit de Mott-Hubbard. Puis lorsque U devient suffisamment petit, le système devient métallique à cause de la superposition de LH et UH. Avec la même idée, on peut penser que pour un Δ suffisamment petit, le dessus du niveau d'énergie de la bande de l'oxygène va se superposer avec UH, et donc aussi mener à un système métallique. Cela définirait le zéro du transfert de charge effectif Δ'. Mais il a été débattu qu'un transfert de charge effectif négatif tel que $\Delta'<0$ maintiendrait un état isolant du système. Cela a été expliqué par une forte hybridation des orbitales p-d ainsi qu'une forte répulsion de Coulomb, qui, lorsque ces deux valeurs sont élevées dans un système, maintiennent un intervalle d'énergie et donc un comportement isolant comme montré dans la **Fig. 1(c)**. Cet intervalle d'énergie est décrit par : $(d^{n+1}L)_i + (d^{n+1}L)_j \rightarrow (d^{n+1})_i + (d^{n+1}L^2)_j$.

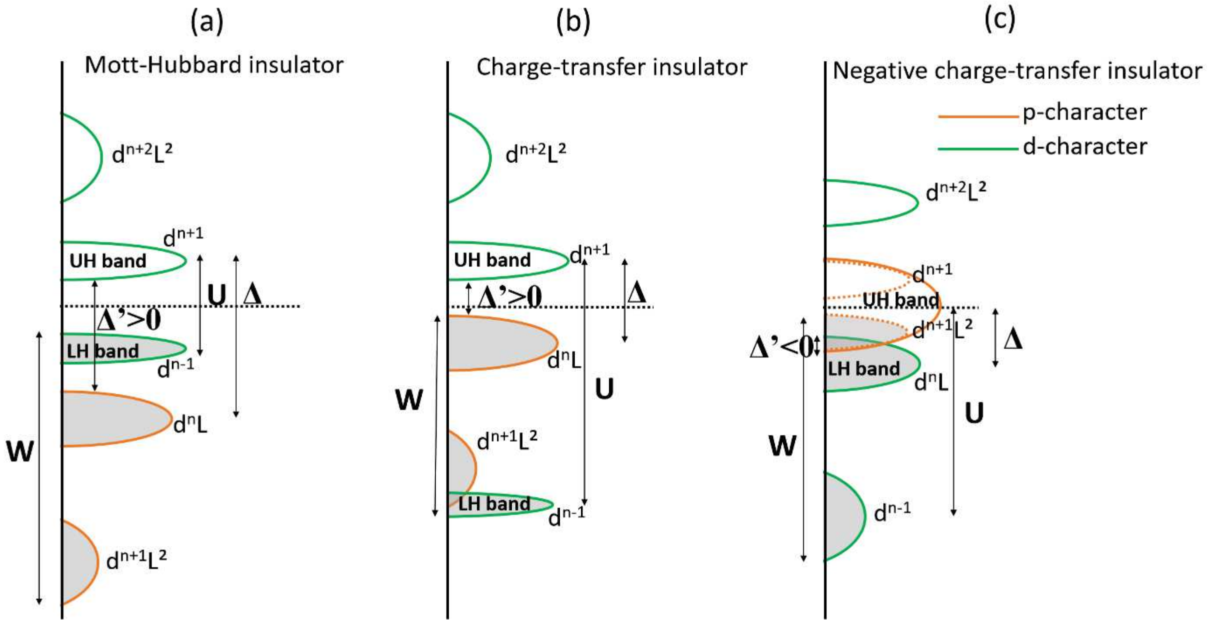

Figure 1 Structure de bande schématique de (a) un isolant de Mott-Hubbard, (b), a isolant de transfert de charge (c) un isolant de transfert de charge-effectif.

Les nickelates de terres rares de structure pérovskite, RNiO$_3$ (R étant un élément de terre rare) sont un exemple type d'oxyde de métaux de transition dont l'origine des transitions de phase a longtemps été débattu. Cette famille d'oxydes possède en effet différentes transitions structurales, magnétiques et métal-isolante, comme on peut le voir dans le diagramme de phase sous forme massive montré en **Fig. 2(a)**[3,4]. Il est vu dans ce diagramme de phase que le choix du terre-rare peut modifier l'angle Ni-O-Ni, qui lui, influence les températures de transitions jusqu'à les faire disparaitre comme pour le cas du lanthane. Cette famille d'oxyde a notamment été étudié pour leur nette transition métal-isolante comme montrée dans la **Fig. 2(b)** où la modification de son intensité, sa température voire sa disparition totale, a été démontrée par le choix du terre-rare[3] ou par dopage en électrons ou trous[5].

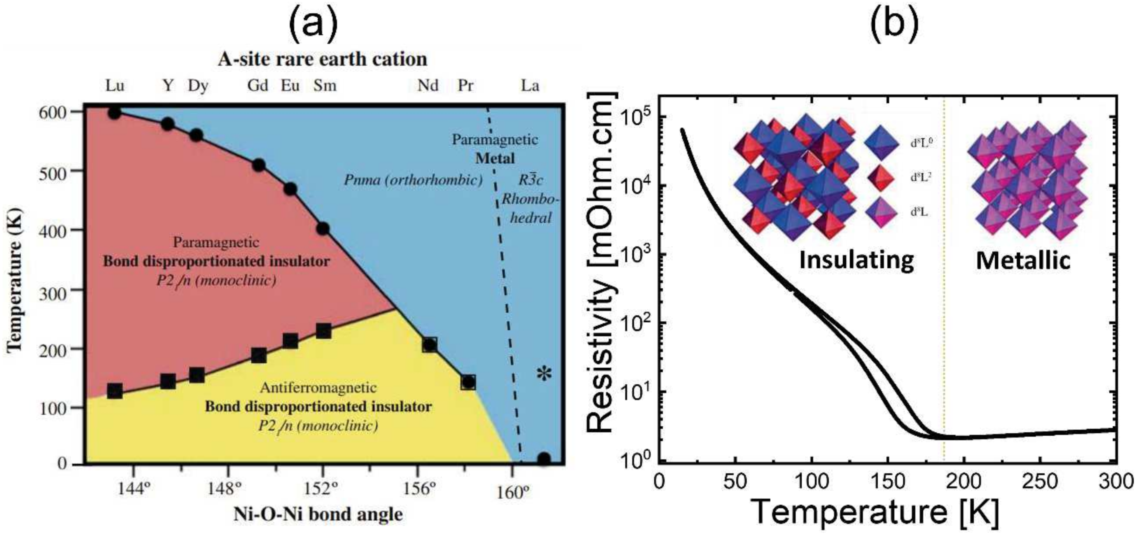

Figure 2 (a) Diagramme de phase des pérovskites de nickelates sous forme massive (b) Résistivité en fonction de la température d'une couche mince de NNO de 10 nm, montrant la distorsion de la structure entre l'état métallique et isolant.

Sous forme de couches minces, le nombre de leviers pour modifier et contrôler ces transitions sont encore plus nombreux. En effet, la contrainte ajoutée par le substrat lors de la croissance épitaxiale du matériau apporte un degré de liberté supplémentaire pour modifier les propriétés du matériau. C'est ainsi que depuis une vingtaine d'années, l'ingénierie orbitalaire et structurales des couches minces de nickelates est un sujet de recherche actif, notamment dans l'espoir de reproduire les propriétés supraconductrices des cuprates[6,7]. En effet, Rice et al. ont montré la possible existence de nickelates analogues aux cuprates, avec des plans carrés NiO_2 isostructuraux aux plans carrés CuO_2, et un cation Ni^{1+} de structure électronique $3d^9$[8]. De nombreux travaux d'ingénierie orbitalaire via l'utilisation de différents substrats et/ou de transfert de charge via des hétérostructures ont alors été entrepris et ont montré la possibilité de modifier la structure électronique du cation Ni, sans avoir, jusqu'à présent, permis l'obtention d'un état supraconducteur.

Cependant, un mois avant le début de ma thèse, Li et al. réussissent à mettre en évidence de la supraconductivité avec une température critique T_C = 15 K à Standford en aout 2019[9]. C'est dans des nickelates dits en couches infinies, $Nd_{0.8}Sr_{0.2}NiO_2$, obtenus par réduction topotactique de couches minces de nickelates pérovskites comme montré sur la **Fig. 3(a)**. Depuis cette découverte, de nombreuses équipes se sont engagées dans l'étude de ce matériau afin d'en étudier le dôme de supraconductivité, et d'établir l'influence du choix de l'élément de terre rare ou du substrat sur la T_C comme montré dans la **Fig. 3(b)**[10–14]. Cependant, il est important de noter que peu d'équipes à ce jour ont réussi à reproduire la synthèse de ce matériau supraconducteur. Cela peut s'expliquer par plusieurs raisons :

- L'obtention d'un état supraconducteur nécessite un dopage en trou, dans un premier temps avec du Sr mais le Ca a aussi démontré son efficacité, ce qui fait varier le degré d'oxydation du cation de Ni. Ce-dernier possède un degré d'oxydation +II comme état ionique le plus stable, obtenir donc un Ni^{3+} est un premier challenge lors de la synthèse de la couche mince de pérovskite. De plus, dopé en trou va encore augmenter le degré d'oxydation du Ni pour équilibrer les charges, donc pour un dopage de 20%, il faudra un $Ni^{3.2+}$, augmentant encore le défi de la synthèse d'un tel composé.
- En plus de cela, le substrat initialement utilisé pour obtenir un état supraconducteur a été le $SrTiO_3$, avec qui le $NdNiO_3$ possède une contrainte extensible de 2.5%, ce qui est considéré comme une contrainte importante lors d'une croissance épitaxiale en couche mince.
- Après le défi de la synthèse de la phase pérovskite, sur substrat de STO et dopée en Sr, il faut réduire cette couche mince par une réaction de chimie douce, la réaction nommée topotactique. Le mécanisme de cette-dernière n'est pas encore parfaitement compris par la communauté, et cela se témoigne par l'importante diversité des conditions de réductions des couches minces. En effet, ces-dernières varient selon les équipes, mais aussi selon le choix du terre-rare, le choix du substrat, la concentration de Sr, etc.

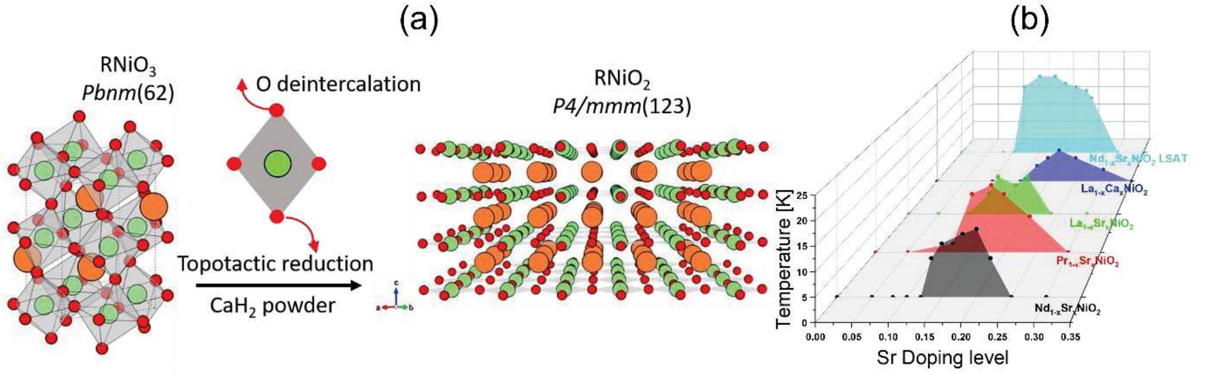

Figure 3 (a) Schéma de la réaction topotactique pour réduire la phase pérovskite en phase de couche infinies (b) Dômes de supraconductivité en fonction du choix de terre-rare et/ou du substrat.

Nous venons ici de présenter les différents défis relevant de la synthèse des couches infinies de nickelates en couches minces, et il est important de préciser sa forme puisqu'à ce jour, aucunes couches infinies de nickelate sous forme massive[15] ou de monocristal n'a montré un état supraconducteur. En effet, le rôle du substrat est pour l'instant primordial, mais il faut cependant noter que les monocristaux synthétisés n'ont toujours pas atteint le dopage en Sr requis sous forme de couches minces pour entrer dans le dôme de supraconductivité. En effet, la synthèse des monocristaux représente un défi encore plus grand, et un dopage en Sr d'uniquement 8% a été obtenu pour des monocristaux suffisamment gros pour être étudiés[16]. En plus de la forme $RNiO_2$, il a été montré qu'un état supraconducteur dans une quintuple-couche de plan carré de couches infinies de la forme $Nd_6Ni_5O_{12}$[17]. Cela a été expliqué par le remplissage électronique des couches d du Ni qui, dans ce matériau, est de $d^{8.8}$, équivalent donc à un dopage à 20% de Sr du matériau sous la forme $RNiO_2$. La difficulté de la synthèse de ce matériau n'a en rien diminué les efforts entrepris par la communauté scientifique afin de découvrir les spécificités de ce nouveau matériau supraconducteur, et notamment les similitudes et différences avec les cuprates.

Ces dernières ont été étudiées théoriquement, via des modèles obtenus par DFT ou DMFT, et aussi expérimentalement via différentes mesures de spectroscopies afin d'étudier les transitions énergétiques régissant la physique du matériau. Parmi ces méthodes expérimentales, les méthodes permettant une sensibilité spécifique à un élément sont très utilisées, tel que la spectroscopie de perte d'énergie d'électrons (EELS) ou les techniques de spectroscopie d'absorption des rayons X. Parmi ces techniques, la spectroscopie par résonance inélastique des rayons X a permis d'observer des excitations de faibles énergies au sein des nickelates de couches infinies qui ont déjà été reportées dans les cuprates, tel que des magnons[18] ou des ondes de densité de charge[19]. Ces caractéristiques ont été étudiés au sein des cuprates à cause de leur corrélation avec la supraconductivité présente dans ces matériaux. En effet, le rôle des ondes de densité de charge est toujours questionné quant à leur supposé compétition avec l'état supraconducteur des matériaux[20], alors que les magnons, signature d'un ordre magnétique à faible portée, est une des hypothèse les plus pertinentes pour être à la glue permettant la création de la paire de charge amenant l'état supraconducteur dans le matériau[21,22].

Comme dit précédemment, de nombreuses études théoriques ont été menées sur les nickelates de couches infinies afin de déterminer les leviers de l'état supraconducteur dans ce matériau. Il s'agit notamment de modeler des diagrammes de bandes afin de déterminer quels sont les orbitales jouant un rôle déterminant dans la physique de l'échantillon, et si un modèle de monobande ou multibande devait être utiliser pour refléter au mieux les propriétés physiques de ces matériaux. La valeur de transfert de charge entre l'oxygène et le nickel a d'ailleurs été calculé comme étant plus importante que dans les cuprates, avec une valeur de 4 eV contre seulement 2 eV dans ces-derniers[23]. Ces calculs ont montré que l'importance de l'hybridation entre le Ni et l'oxygène sera moins important que dans les cuprates, et d'autres études ont aussi montré que le couplage J de superexchange est bien moins important dans les nickelates de couches infinies[18,24]. D'autres leviers pouvant être corrélé à la supraconductivité du matériau ont été étudiés tel que le rôle des orbitales 4f des métaux rares[25], la présence d'un effet de Kondo dans le matériau[26], la présence d'une poche de Fermi jouant le rôle d'un réservoir de charge[27,28], l'importance du couplage de Hund pouvant mener à un état de haut spin (S=1) ou bas-spin (S=0)[29].

Ce résumé décrira à présent mes efforts concernant la synthèse de couches minces de nickelates pérovskites et leur réduction topotactique en couches infinies avec et sans présence d'une couche plafond, dans un premier temps. Puis je présenterai les divers résultats obtenus sur le physique des nickelates et de leurs excitations à faible énergies obtenus grâce aux mesures synchrotrons. Et je terminerai par un chapitre portant sur l'élaboration d'heterostructures de couches minces de nickelates avec un matériau ferroélectrique, $PbZr_{0.52}Ti_{0.48}O_3$ (PZT), dont je décrirai l'ensemble des caractérisations structurales, magnétiques et électriques effectuées sur ces matériaux, ainsi que les mesures synchrotrons associées permettant de déterminer les températures de transitions magnétiques. L'objectif de mes travaux est d'apporter des éléments de compréhension sur l'influence de différentes modifications structurales et orbitalaires dans ces matériaux.

2. Synthèse et caractérisation des couches minces de nickelates

Les couches minces de pérovskite de nickelate ont été synthétisées par ablation laser pulsée (PLD) au sein de l'IPCMS. Des substrats de $SrTiO_3$ (STO) d'orientation $(001)_{pc}$ ont été utilisés qui ont été préalablement traité au HF par la méthode Kawasaki[30] afin d'obtenir une mono-terminaison TiO_2 à la surface du substrat. Différents dopages en Sr ont été utilisés afin d'obtenir des couches hors et dans le dôme de supraconductivité une fois celles-ci réduites sous la forme de couches infinies, ainsi, des cibles contenant 0%, 5% et 20% de Sr sont utilisées dans ces travaux, dont uniquement la couche non-dopée est sous forme de monophase $NdNiO_3$. Cela s'explique par la grande difficulté des conditions de synthèse de cible de pérovskite de nickelate, difficulté augmentant lorsque les cibles sont dopées en Sr. Les couches dopées sont donc formées de $Nd_{2-x}Sr_xNiO_4$ + NiO avec x=0.1 et 0.4 pour, respectivement, un dopage final de 5% et 20% au sein de la couche mince. De plus, la croissance de ces couches a été faîte avec et sans la présence d'une couche plafond de STO d'une épaisseur de 3 mailles, au-dessus des 10 nm de nickelates, qui seront nommées cappées (avec une couche de STO) et non-cappées (sans couche de STO).

La synthèse de ces couches minces par PLD fait rentrer un grand nombre de paramètres en compte tel que la température du heater sur lequel le substrat est collé par de la laque d'argent, la distance entre la cible et le substrat, la puissance du laser, la fréquence du laser, l'atmosphère au sein de la chambre ou encore la définition de la zone à ablater sur la cible. L'optimisation de ces différents paramètres a été une constante durant tout mon travail de thèse afin d'obtenir des couches minces de la meilleure qualité possible au sein de l'institut.

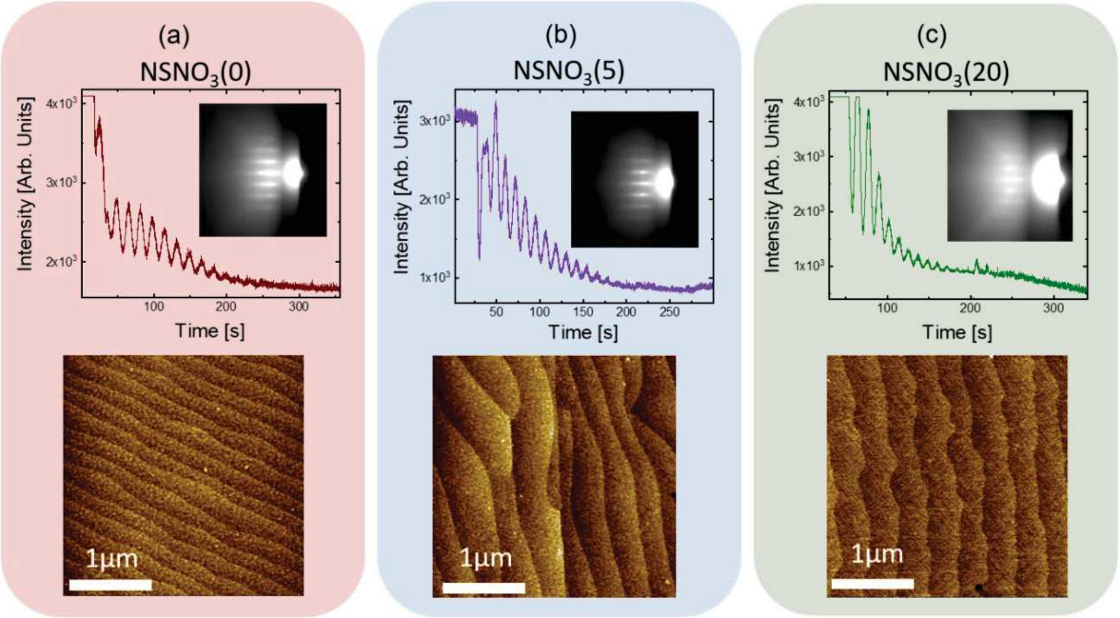

Figure 4 Oscillation et images de diffraction RHEED ainsi que les images AFM pour les 3 différents dopages

Les **Fig. 4(a)-(c)** montrent des oscillations obtenues par diffraction des électrons de haute énergie en incidence rasante (RHEED), permettant de suivre l'évolution de la croissance in-situ. En effet, chaque oscillation est la signature de la croissance d'une monocouche, permettant ainsi de suivre la vitesse de croissance en plus de l'épaisseur de l'échantillon. L'image de diffraction, composé de bandes, est due à une croissance 2D, attestant une croissance de bonne qualité jusqu'à la fin du dépôt. La grande qualité de la surface des couches est confirmée par AFM, où la topographie typique des substrats de STO traités au HF, montrant des marches, est retrouvé pour les couches minces pour les différents dopages.

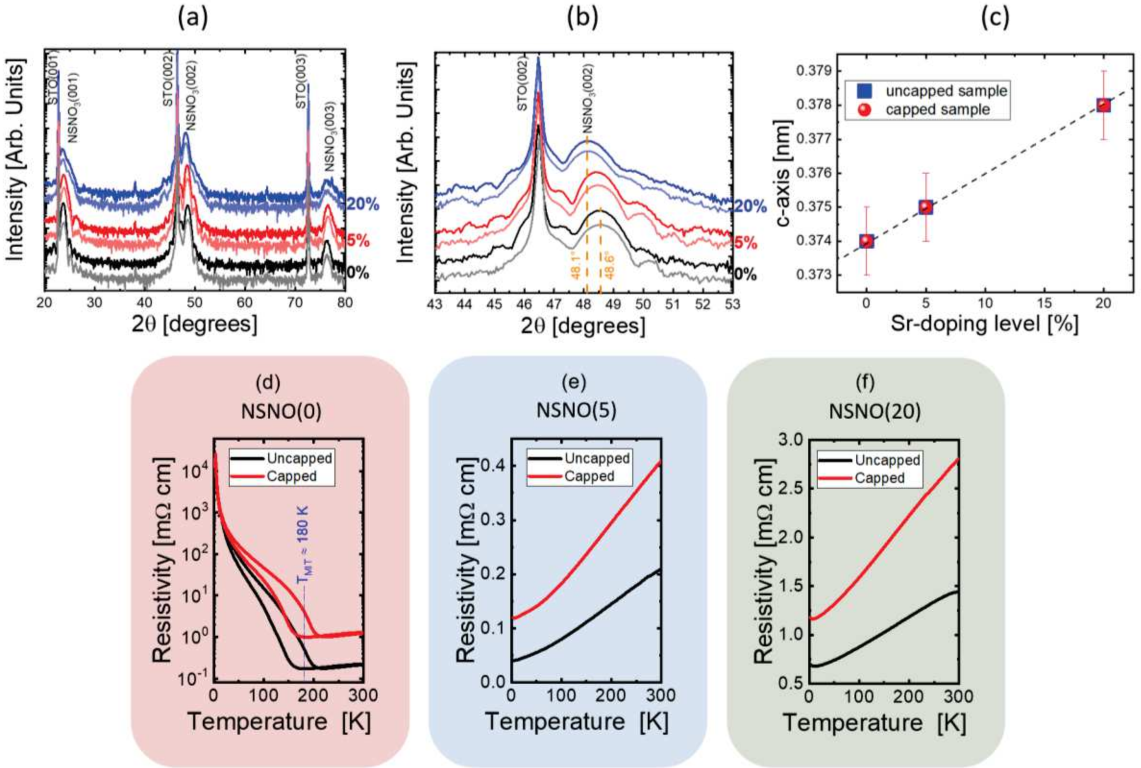

Figure 5 (a)-(c) XRD des couches minces pérovskites aux différents dopages avec et sans présence d'une couche de STO, ainsi que leur paramètre hors du plan (d)-(f) Résistivité en fonction de la température

Les **Fig. 5 (a)-(c)** montrent les diffractions des rayons X pour des couches cappées et non-cappées aux trois différents dopages de Sr. L'évolution du paramètre de maille hors du plan en fonction du dopage montre son évolution croissante, ce qui est expliqué par le plus grand rayon cationique du Sr^{2+} par rapport au Nd^{3+}. Les couches à plus faibles dopage montrent aussi un pic de Bragg (003) pour la couche de nickelate plus intense qu'à plus fort dopage, montrant la plus grande qualité des couches non-dopées ou peu-dopées, par rapport à celles contenants plus de Sr. Les mesures de résistivité dans les **Fig. 5 (d)-(f)** montrent que le dopage en Sr détruit la transition métal-isolante comme déjà montré en massif^{5}, et que la présence d'une couche de STO de modifie pas la température de transition métal-isolante pour la couche non-dopée.

Figure 6 Système utilisé pour effectuer la réaction topotactique sous vide

Après l’optimisation des couches pérovskites, la seconde étape de synthèse pour obtenir les nickelates de couche infinie est une réduction par un procédé de chimie douce, appelée réaction topotactique. Cette réaction est effectuée dans un tube en silice sous vide présentée en **Fig. 6** où sous préalablement introduit 0.5g de CaH_2 et la couche mince à réduire. Le tube est ensuite introduit dans un four où un traitement thermique, différent en fonction du dopage et de la présence d’une couche de STO ou non, permet la réduction. Le mécanisme même de cette réaction n’est pas encore pleinement compris par la communauté, ce qui se traduit par des conditions de réactions spécifiques à chacun pour chaque échantillon[11–13,31–33]. Il a donc fallu optimiser mes propres conditions de réduction, afin d’obtenir des nickelate de couche infinies.

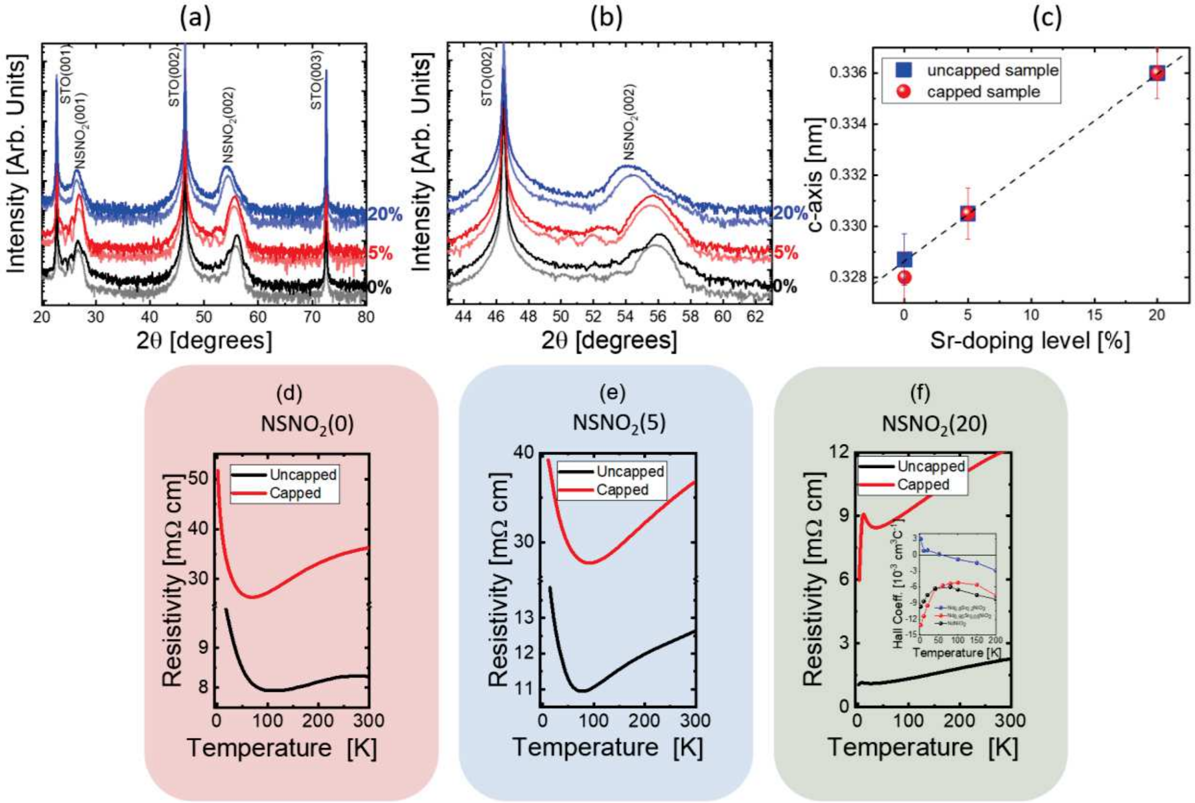

Figure 7 (a)-(c) XRD des couches minces de couche infinie aux différents dopages avec et sans présence d'une couche de STO, ainsi que leur paramètre hors du plan (d)-(f) Résistivité en fonction de la température

Les **Fig 7(a)-(c)** montrent les caractérisations par diffraction des rayons X des échantillons cappés et non cappés où le paramètre hors du plan a diminué par rapport à la phase pérovskite, passant de 0.374 nm à 0.328 nm pour un échantillon non-dopé. Cette diminution est due à la deintercalation des oxygens apicaux, passant d’un octaèdre NiO_6 à un plan NiO_2. La résistivité dans les **Fig. 7(d)-(f)** montre une transition supraconductrice à 11 K pour les échantillons dopés à 20% en Sr, mais avec une résistance qui n’atteint pas 0 Ω. Nous expliquons cela par une trop grande inhomogénéité et la présence de domaine non-supraconducteur dans notre couche mince, empêchant ainsi l’obtention d’une résistance nulle en-dessous de 10 K. Cependant, les porteurs de charge obtenus par effet de Hall dans la **Fig. 7(f)** montre un changement de nature des porteurs à 50 K, passant d’électrons à trous à plus basse température, ce qui est la signature des couches infinies de nickelates supraconductrices, soulignant la présence de domaine supraconducteur dans ces couches minces. Les échantillons moins dopés ont un comportement métallique jusqu’à 70-100 K selon le dopage, où une transition vers un comportement isolant est observée, ce qui est en accord avec la littérature.

L'optimisation des échantillons a été un travail constant lors de ma thèse, et ont de plus permis des mesures sur grands instruments, que je vais détailler dans la section suivante.

3. Étude des excitations de basse énergies dans les couches infinies de nickelates

Le but de ces mesures était d'étudier les excitations de basse énergie dans les couches minces de nickelates, afin de comparer ces-dernières aux cuprates et d'observer quels peuvent être les leviers intervenant dans l'apparition d'un état supraconducteur au sein des nickelates. Ces expériences ont été menées au sein de l'ESRF, Grenoble, France, sur la ligne ID32 montrée sur la **Fig. 8**. Ce travail n'aurait pu être réalisés sans l'expertise de Nick Brookes, scientifique de la ligne, le professeur Giacomo Ghinringhelli ainsi que son doctorant Leonardo Martinelli de l'institut polytechnique de Milan et le professeur Marco Salluzzo du CNR spin de Nâples pour leur expertise pour les mesures de résonance inélastique des rayons X (RIXS).

Figure 8 Photo de la ligne ID32

Des couches minces avec et sans couche de STO aux différents dopages de Sr ont été mesurées au RIXS. Dans un premier temps, des spectres d'absorption des rayons X (XAS) ont été réalisés sur chaque échantillon afin de déterminer l'énergie de résonance au pic L_3 du nickel. De plus, comme montré dans la **Fig. 9**, un fort dichroïsme est observé pour les échantillons, entre les orbitales dans le plan NiO_2 et perpendiculaire à ce-dernier. Cette différence d'intensité entre les deux plans souligne une plus grande quantité d'orbitales inoccupé dans le plan, soit une plus grande présence de trou dans les plans NiO_2. Cette occupation préférentielle des trous dans le plan est similaire aux cuprates et était donné comme un prérequis afin d'obtenir un état supraconducteur dans des nickelates par Rice et al[8]. Il faut aussi souligner que ce dichroïsme est plus important pour les échantillons avec une couche de STO. Cette différence n'est pas encore expliquée, et des hypothèses tel qu'une amélioration de la qualité des échantillons grâce à cette couche, ou d'un effet d'interface sont pour le moment envisagé.

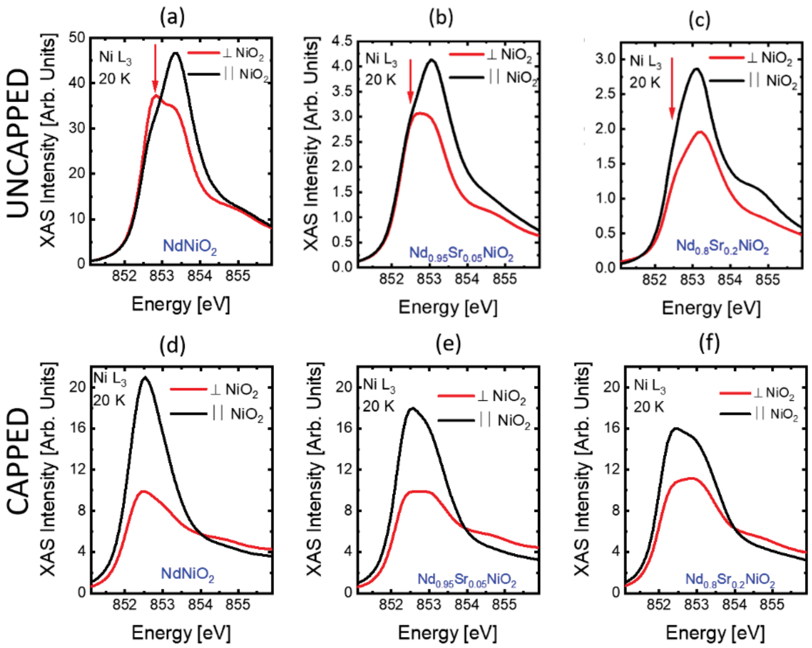

Figure 9 Spectres XAS des couches minces avec et sans couches de STO pour les trois dopages de Sr

La géométrie de l'acquisition des spectres RIXS est schématisée dans les **Fig. 10(a)-(c)** où, dans notre cas, les axes de symétrie (10) et (11) de la zone de Brillouin schématisée respectivement en rouge et en vert sur la **Fig. 10(c)** ont été mesurées lors de nos expériences. Ces mesures sont faîtes en acquérant différents spectres selon $q_{||}$ comme montré dans la **Fig. 10(d)**, résultant dans des carte RIXS comme montré en **Fig. 10(e)-(f)**. Les spectres RIXS ont été acquis à l'énergie correspondant à la résonance du Ni^{1+}, soit 852.5 eV, comme déterminer via les XAS montré dans les **Fig. 9**. Ces spectres sont ensuite traités, avec, pour la partie à faible énergie perdue (de 0 à -0.5 eV), une gaussienne pour le pic élastique à 0 eV et une lorentzienne asymétrique pour la partie à faible énergie de 0 à -0.3 eV. Le gros résultat obtenu grâce à ces mesures est la présence d'un ordre de charge et d'un magnon en fonction de la présence, ou non, d'une couche de STO comme montré sur les **Fig. 10(e)-(f)**. En effet, les cartes RIXS montrent, pour une couche mince sans couche supérieure de STO, la présence d'une modulation de l'intensité du pic élastique à une certaine valeur de $q_{||}=0.33$. Cette modulation est la signature d'un ordre de charge dans le matériau. Alors que dans une couche mince possédant une couche supérieure de STO, cette modulation d'ordre charge n'est pas présente, et le pic élastique a une intensité constante en fonction de $q_{||}$. Cependant, une excitation dispersive en énergie est observée pour ces couches minces, signature d'un ordre magnétique à faible portée, un magnon. La disparition de l'ordre de charge via l'ajout d'une couche supérieure de STO dans les couches minces infinies de nickelate a été très surprenant, puisque, comme montré précédemment, les caractérisations structurales ainsi que la résistivité des couches minces n'étaient pas altérées en fonction de la présence d'une couche supérieure de STO. Le rôle de cette couche supérieur de STO n'est toujours pas pleinement établi, mais il semblerait bien que son rôle aille au-delà de celui de modèle épitaxiale comme proposé par le groupe de Stanford[31]. De plus, nous avons observé que cet ordre de charge s'affaiblit lorsque le dopage en Sr augmente, jusqu'à disparaître complètement lorsque la couche mince est supraconductrice. Dans ce cas, nous observons bien une compétition entre l'ordre de charge et l'état supraconducteur au sein du matériau.

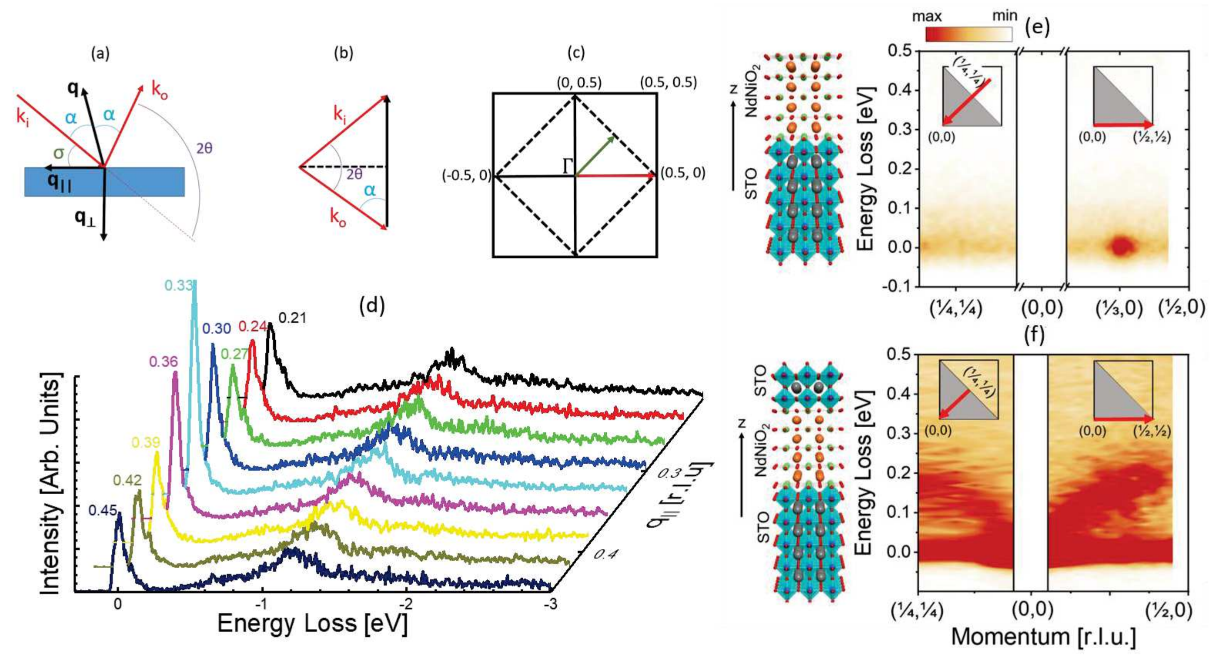

Figure 10 (a)-(c) Description de la géométrie de l'obtention d'un spectre RIXS (d) Différents spectre RIXS d'un échantillon non-dopé et sans STO en fonction de q (e)-(f) carte RIXS selon le moment q pour une couche sans STO (au-dessus) et avec STO (en-dessous)

Après s'être concentre sur l'ordre de charge dans les couches minces de nickelates de phase infinies, nous avons voulu nous concentrer sur l'évolution du magnon en fonction du dopage de Sr. Pour cela, un polarimètre a été utilisé afin d'étudier la polarisation du photon analysé. En effet, les photons incidents peuvent être polarisés verticalement ou horizontalement comme déjà vu dans les spectres XAS des **Fig. 9**. Les photons sortants seront donc aussi polarisés, mais cette polarisation peut être inversé si le photon sortant est d'origine magnétique. Cela est dû au moment angulaire non-nul d'une excitation magnétique, menant à l'inversion de la polarisation des photons. Comme montré dans la **Fig. 11(a)**, le polarimètre est composé d'une multicouche de W/B_4C, et est situé avant le détecteur. Ce-dernier permet donc de vérifier si la polarisation des photons est conservée ou, au contraire, inversée. Cela a permis de voir, comme montré en **Fig. 11(b)**, que ce qui avait été considéré comme un magnon dans les échantillons non dopés avec une couche supérieure de STO est bien une excitation d'ordre magnétique, puisque le spectre rouge, qui est l'intensité d'un photon ayant eu une inversion de sa polarisation, montre une forte intensité à -0.2 eV. De plus, les spectres RIXS obtenus pour des échantillons dopés à 20% en Sr montrent que le magnon ne disparaît pas totalement pour les échantillons supraconducteurs, mais que ces-derniers sont moins intenses et se manifestent à plus faible énergie perdue. Cette différence entre couche mince dopé et non-dopé est soulignée dans la **Fig. 11(c)** où l'intensité des photons ayant eu leur polarisation inversée est tracée, mettant en avant le magnon plus intense et à une énergie plus élevée lorsqu'il n'y a pas de Sr dans la couche mince. En plus d'observer l'influence du dopage sur l'excitation magnétique des couches minces, nous avons voulu observer si un échantillon sans couche supérieure de STO possédait aussi un magnon qui aurait été caché en partie par la grande intensité du pi élastique. En effet, une excitation magnétique est bien présente pour un échantillon sans couche supérieure de STO, et seulement un faible affaiblissement de son intensité est observé, bien moindre que pour un dopage de 20%m en Sr.

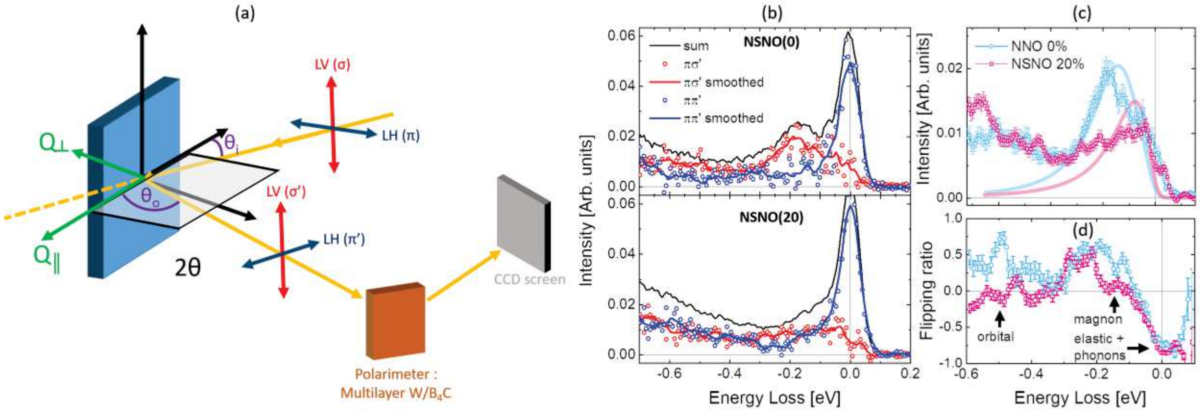

Figure 11 (a) Schéma d'une mesure RIXS avec un polarimètre (b) Spectres RIXS avec polarimètre, permettant d'observer les changements de polarisation des photons (c) Intensité du spectre RIXS pour les photons montrant une inversion de la polarisation (d) Taux de photons ayant leur polarisation inversés par rapport à ceux qui la conservent.

Ces mesures RIXS ont permis d'étudier l'influence du dopage en Sr sur les transitions énergétiques au sein des couches minces de nickelate à phase infinie, et notamment de mettre en avant le rôle de la couche supérieure de STO, même si ce-dernier n'est pas encore parfaitement compris. Divers similitudes et différences avec les cuprates ont été relevés, et aussi un grand nombre de questions soulevées, qui justifient l'attrait toujours important de ce sujet de recherche.

4. Heterostructures NNO/PZT avec différentes épaisseurs de ferroélectrique

Observer l'influence d'un matériau ferroélectrique sur les transitions de phases d'une couche de pérovskite de nickelate a été le second axe de recherche de ma thèse. Le but de ce travail était d'observer si un effet de champ ferroélectrique pouvait modifier les températures de transitions de phase d'une couche de $NdNiO_3$ et s'il était possible de quantifier la distorsion polaire induite par le ferroélectrique sur le nickelate, ainsi qu'une occupation orbitalaires préférentielle, comme cela a déjà pu être observé dans les manganites[34]. Des multicouches de NNO/PZT ont été synthétisées avec différentes épaisseurs de PZT de 6, 13 et 30 nm. Les **Fig. 12(a)-(b)** montrent un paramètre hors du plan de la couche de nickelate qui est plus grand, lorsque l'épaisseur de PZT est plus fine. Hors, une monocouche de nickelate possède un paramètre hors du plan plus proche de l'échantillon avec la plus épaisse couche de PZT au-dessus du NNO. C'est donc lorsque la couche de PZT est la plus épaisse que le NNO est le plus similaire à une monocouche de NNO, ce qui fut, dans un premier temps, un résultat contre-intuitif. D'autant plus que toutes les couches de NNO sont bien épitaxiées au substrat qu'importe l'épaisseur de PZT comme on peut le voir dans les **Fig. 12(c)-(e)**. Alors que la couche de PZT montre une relaxation par rapport à la contrainte du substrat en fonction de son épaisseur. Cette relaxation du PZT est aussi ce qui amène à une croissance monodomain des domaines ferroélectriques de la couche. En effet, si la couche de PZT est contrainte au substrat, alors la polarisation des domaines sera aléatoire, sans polarisation préférentielle. Alors que si le PZT est plus épais, et donc relaxé, ce-dernier aura une polarisation plus homogène, jusqu'à une polarisation monodomaine pour les échantillons complètement relaxé comme le PZT de 30 nm.

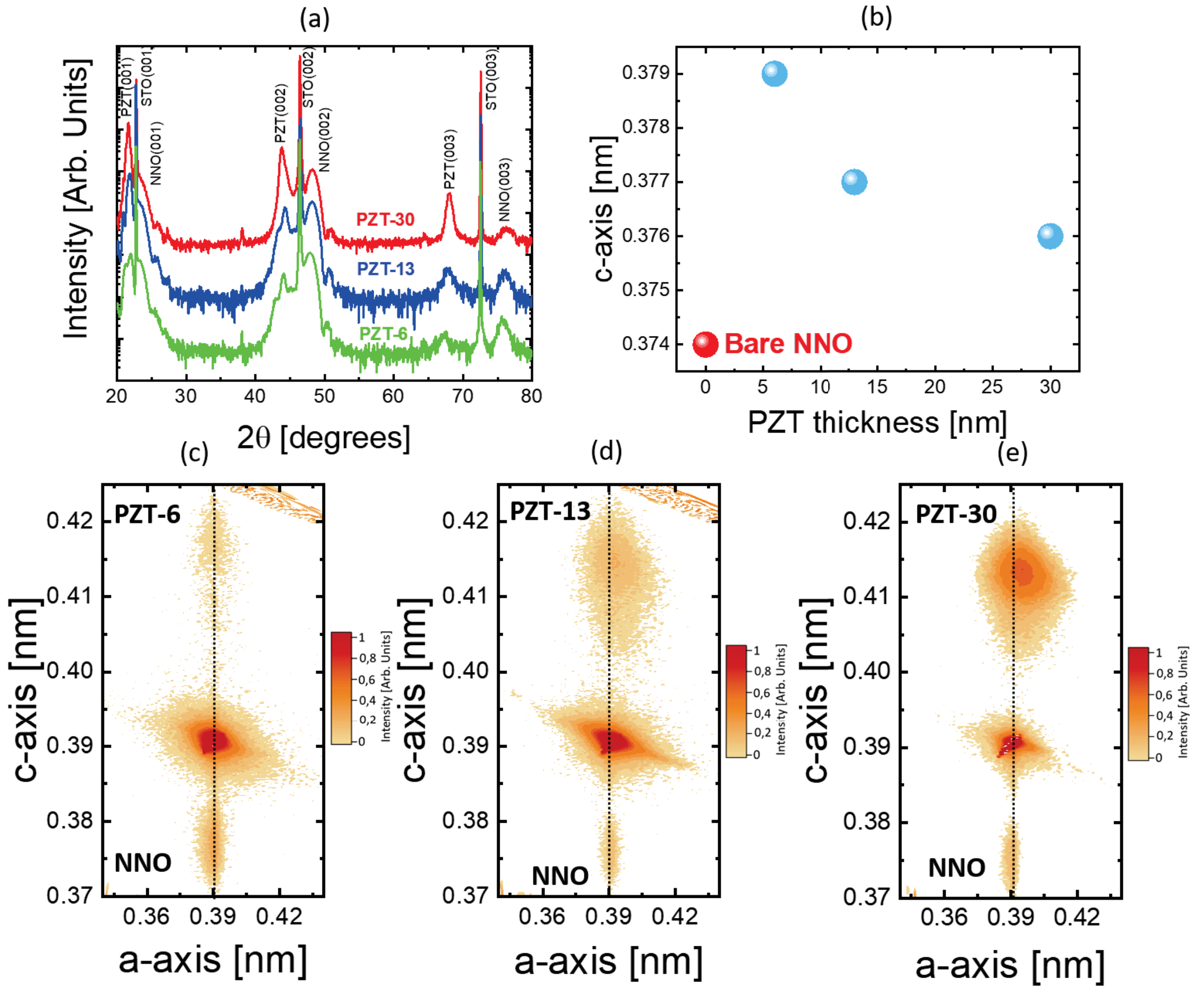

Figure 12 (a) XRD des multicouches pour les trois épaisseurs de PZT (b) paramètre hors du plan des multicouches (c)-(e) cartographie du réseau réciproque pour ces trois couches

Afin de déterminer la température d'ordre antiferromagnétique de la couche de nickelate, des mesures de spectroscopies de résonance élastique des rayons X (REXS) ont été effectué au synchrotron Diamond, sur la ligne I10. Ces mesures permettent de déterminer l'intensité de l'ordre magnétique de mes couches minces de NNO, et donc de déterminer la $T_{Néel}$ du matériau. Le résultat de ces mesures est présenté dans la **Fig. 13(a)** où il peut être observé qu'une couche de PZT plus épaisse amène à une $T_{Néel}$ plus faible. Cette tendance se retrouve dans les mesures de résistivités, où la T_{MIT} du NNO est plus faible pour la couche de PZT la plus épaisse, comme montré dans la **Fig. 13(b)**. L'inséré de la **Fig. 13(b)** met en lumière cette tendance à diminuer les températures de transitions en fonction de l'épaisseur de la couche de PZT. Cela permet de mettre en lumière que pour l'épaisseur la plus épaisse, la $T_{Néel}$ et la T_{MIT} sont quais-concomitantes, ce qui est une caractéristique du NNO massif, donc la preuve d'une couche de bonne qualité. De plus, on peut observer que la T_{MIT} d'une couche de NNO sans PZT, est elle-aussi quasi-équivalente à la T_{MIT} de la couche de NNO avec 30nm de PZT au-dessus. Ce résultat, comme déjà mentionné précédemment avec les caractérisations structurales, nous a paru contre-intuitif dans un premier temps puisque nous pensions obtenir un comportement quasi-massif pour l'échantillon avec la plus faible épaisseur de PZT, alors que c'est le comportement opposé qui est observé.

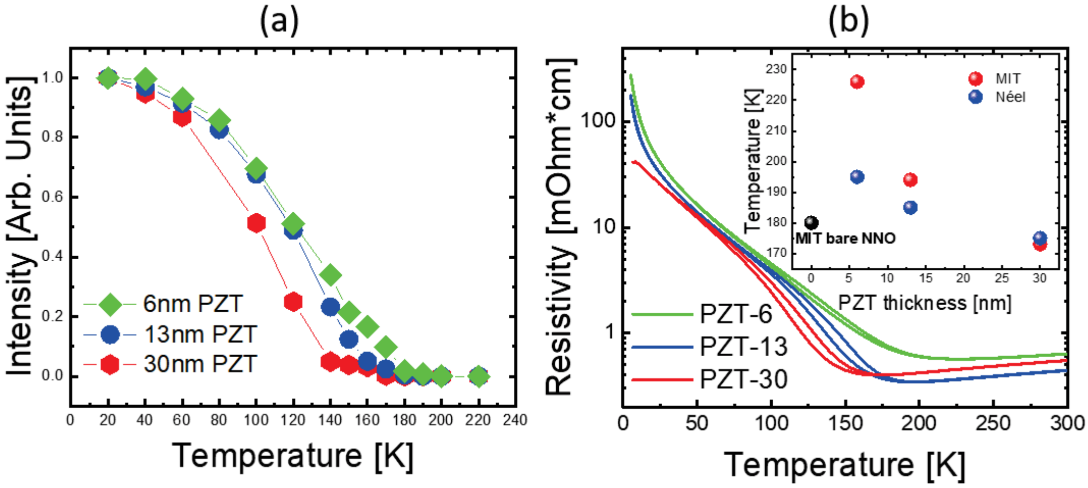

Figure 13 (a) Évolution de l'intensité du pic de Bragg magnétique obtenu par résonance élastique des rayons X (b) Résistivité en fonction de la température, et l'évolution de T_{MIT} et $T_{Néel}$ en fonction de l'épaisseur de PZT.

Afin d'expliquer ce comportement, nous voulions revenir sur l'importance de l'effet ferroélectrique du PZT due à l'évolution de sa polarisation de croissance en fonction de son épaisseur. En effet, les domaines ferroélectriques sont inhomogènes pour une faible épaisseur, et monodomaine avec une polarisation DOWN pour l'épaisseur la plus épaisse. Au vue des températures de transitions et caractérisations structurales, la couche de NNO avec la faible épaisseur de PZT au-dessus est celle possédant la structure la plus déformée comparé aux épaisseurs plus épaisse. Nous supposons que cette déformation est due à une modification de l'angle Ni-O-Ni dans la structure, induit par les différents domaines ferroélectriques via une distorsion polaire, comme schématisé dans la **Fig. 14.** La présence de différents domaines ferroélectrique induirait différents angles Ni-O-Ni, selon que leur polarisation soit UP ou DOWN, ce qui augmenterait le taux de déformation au sein de la structure pérovskite de la couche. Au contraire, une polarisation monodomaine induirait certes une distorsion polaire sur l'angle Ni-O-Ni, mais cette-dernière serait homogène au sein de la couche, amenant donc une déformation plus faible que pour une plus fine couche de PZT.

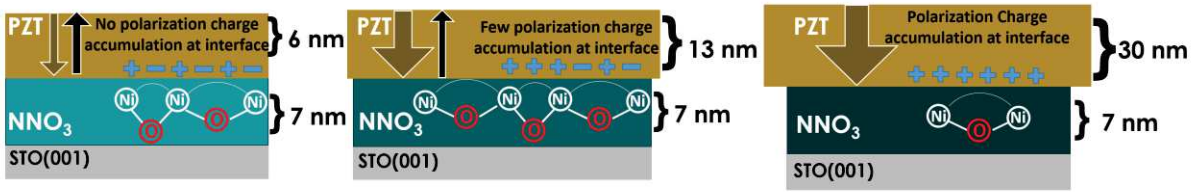

Figure 14 représentation schématique de l'évolution de la polarisation de croissance, de l'angle Ni-O-Ni en fonction de l'épaisseur de PZT

5. Conclusion

Ce travail de thèse portant sur des couches minces de nickelates, sous forme pérovskite et sous forme de phase infinies, m'a permis de développer un grand nombre de compétences via un large panel de technique de caractérisations. Tout d'abord, la croissance de ces couches au sein de l'IPCMS, ainsi que leurs caractérisations structurales et leurs propriétés de transport a été un travail qui n'a cessé d'être améliorer tout au long de mon doctorat. Par la suite, de nombreuses mesures sur grands instruments m'ont permis d'obtenir des informations sur la physique de ces matériaux, notamment avec l'aide de nos nombreux collaborateurs. L'étude fondamentale des nickelates continuera encore dans les années à venir, puisque les leviers pour modifier leurs propriétés, ou les interactions énergétiques gouvernant leur physique sont toujours en plein développement. De plus, la découverte de la supraconductivité dans les couches infinies de nickelates n'a qu'amplifier une recherche déjà importante sur le sujet, et des progrès, notamment dans la qualité des couches minces, et dans leur synthèse sous d'autres formes comme els monocristaux, continuera d'apporter des questions et des réponses dans ce champ de recherche très actif.

Références:

1. Mott, N. F. Metal-Insulator Transitions. *Pure Appl. Chem.* **52**, 65–72 (1980).
2. Zaanen, J., Sawatzky, G. A. & Allen, J. W. Band Gaps and Electronic Structure of Transition-Metal Compounds. *Phys. Rev. Lett.* **55**, 418–421 (1985).
3. Medarde, M. L. Structural, magnetic and electronic properties of perovskites (R = rare earth). *J. Phys. Condens. Matter* **9**, 1679–1707 (1997).
4. Fowlie, J. Electronic and Structural Properties of LaNiO3-Based Heterostructures. (University of Geneva, Geneva, Switzerland, 2018). doi:10.1007/BF00702719.
5. García-Muñoz, J. L., Suaaidi, M., Martínez-Lope, M. J. & Alonso, J. A. Influence of carrier injection on the metal-insulator transition in electron- and hole-doped R1-xAxNiO3 perovskites. *Phys. Rev. B* **52**, 13563–13569 (1995).
6. Disa, A. S. *et al.* Orbital engineering in symmetry-breaking polar heterostructures. *Phys. Rev. Lett.* **114**, 1–6 (2015).
7. Chakhalian, J. *et al.* Asymmetric orbital-lattice interactions in ultrathin correlated oxide films. *Phys. Rev. Lett.* **107**, 116805(4) (2011).
8. Rice, T. M., M., A. V. & D., B. Electronic structure of possible nickelate analogs to the cuprates. *Phys. Rev. B - Condens. Matter Mater. Phys.* **59**, 7901–7906 (1999).
9. Li, D. *et al.* Superconductivity in an infinite-layer nickelate. *Nature* **572**, 624–627 (2019).
10. Osada, M. *et al.* Nickelate Superconductivity without Rare-Earth Magnetism: (La,Sr)NiO2. *Adv. Mater.* **33**, (2021).
11. Zeng, S. *et al.* Phase Diagram and Superconducting Dome of Infinite-Layer Nd1-xSrxNiO2 Thin Films. *Phys. Rev. Lett.* **125**, (2020).
12. Zeng, S. *et al.* Superconductivity in infinite-layer nickelate La1-xCaxNiO2 thin films. *Sci. Adv.* **8**, 9927 (2022).
13. Li, D. *et al.* Superconducting Dome in Nd1-xSrxNiO2 Infinite Layer Films. *Phys. Rev. Lett.* **125**, 27001 (2020).
14. Osada, M., Wang, B. Y., Lee, K., Li, D. & Hwang, H. Y. Phase diagram of infinite layer praseodymium nickelate Pr1-xSrxNiO2 thin films. *Phys. Rev. Mater.* **4**, (2020).
15. Li, Q. *et al.* Absence of superconductivity in bulk Nd1−xSrxNiO2. *Commun. Mater.* **1**, (2020).
16. Puphal, P. *et al.* Topotactic transformation of single crystals: From perovskite to infinite-layer nickelates. *Sci. Adv.* **7**, 8091 (2021).

17. Pan, G. A. *et al.* Superconductivity in a quintuple-layer square-planar nickelate. *Nat. Mater.* **21**, 160–164 (2022).

18. Lu, H. *et al.* Magnetic excitations in infinite-layer nickelates. *Science (80-.).* **373**, 213–216 (2021).

19. Tam, C. C. *et al.* Charge density waves in infinite-layer NdNiO2 nickelates. (2021).

20. Chen, C. W., Choe, J. & Morosan, E. Charge density waves in strongly correlated electron systems. *Reports Prog. Phys.* **79**, 084505 (2016).

21. Chen, G. & Goddard, W. A. The magnon pairing mechanism of superconductivity in cuprate ceramics. *Science (80-.).* **239**, 899–902 (1988).

22. O'Mahony, S. M. *et al.* On the electron pairing mechanism of copper-oxide high temperature superconductivity. *Proc. Natl. Acad. Sci. U. S. A.* **119**, 1–8 (2022).

23. Botana, A. S. & Norman, M. R. Similarities and Differences between LaNiO2 and CaCuO2 and Implications for Superconductivity. *Phys. Rev. X* **10**, (2020).

24. Lin, J. Q. *et al.* Strong Superexchange in a d9-δ Nickelate Revealed by Resonant Inelastic X-Ray Scattering. *Phys. Rev. Lett.* **126**, (2021).

25. Choi, M. Y., Lee, K. W. & Pickett, W. E. Role of 4f states in infinite-layer NdNiO2. *Phys. Rev. B* **101**, 20503 (2020).

26. Been, E. *et al.* Electronic Structure Trends across the Rare-Earth Series in Superconducting Infinite-Layer Nickelates. *Phys. Rev. X* **11**, (2021).

27. Wu, X. *et al.* Surface s-wave superconductivity for oxide-terminated infinite-layer nickelates. **1**, 1–10 (2020).

28. Hirayama, M., Tadano, T., Nomura, Y. & Arita, R. Materials design of dynamically stable d9 layered nickelates. *Phys. Rev. B* **101**, 1–18 (2020).

29. Yang Wang, B. *et al.* *Isotropic Pauli-Limited Superconductivity in the Infinite-Layer Nickelate Nd0.775Sr0.225NiO2*.

30. Kawasaki, M. *et al.* Atomic control of the SrTiO3 crystal surface. *Science (80-.).* **266**, 1540–1542 (1994).

31. Lee, K. *et al.* Aspects of the synthesis of thin film superconducting infinite-layer nickelates. *APL Mater.* **8**, 41107 (2020).

32. Xiang, Y. *et al.* Physical Properties Revealed by Transport Measurements for Superconducting Nd0.8Sr0.2NiO2Thin Films. *Chinese Phys. Lett.* **38**, 047401 (2021).

33. Gao, Q., Zhao, Y., Zhou, X. J. & Zhu, Z. Preparation of Superconducting Thin Films of Infinite-Layer Nickelate Nd0.8Sr0.2NiO2. *Chinese Phys. Lett.* **38**, (2021).

34. Preziosi, D., Alexe, M., Hesse, D. & Salluzzo, M. Electric-Field Control of the Orbital Occupancy and Magnetic Moment of a Transition-Metal Oxide. *Phys. Rev. Lett.* **115**, 157401 (2015).

Acknowledgments

I would like to first thanks the jury members who accept to judge my work. So thanks to the eminent scientists Prof. Marta Gibert, Prof. Agnès Barthélémy, Prof. Jens Kreisel and Prof. Silviu Colis.

Lots of people gave their contribution in order to obtain the results presented in this thesis, and among them, my supervisor is by far the greatest contributor (maybe just after me). Thank you Daniele Preziosi for those nearly four years where you constantly made me want to learn more about oxide physics. We really work at “four hands” on this thesis, and even if lots of frustration came out from the different challenges and results that we had, I think that we still came up with amazing results and ideas and managed to learn constantly on this new interesting subject. And alongside Daniele, I wish also to give all my sincere thank you to Prof. Nathalie Viart who was always there to supervise my work (and Daniele). So thank you Nathalie for giving me the opportunity to do my thesis in this amazing environment inside the thin film team in the DCMI. In the department, special thanks are dedicated to Gilles Versini and Laurent Schlur who always help us to keep the PLD in optimal use, which allow us to grow our thin films continuously through this work. Also, I would like to thanks Marc Lenertz for its constant support on the (stubborn?) Rigaku, and Jerome Robert for its help in the introduction of the Dynacool system in the lab. Moreover, thanks to both of my co-worker in the thin film team, Laurianne Wendling and Antonio Pena-Corredor with who we always help other for our respective experiments. It was a great pleasure to work in the DCMI thanks to all the amazing persons in the group with notably the “old-PhD” Pier, Barbara, Fredéric, Alexandre, Lisa and Joëlle with who I particularly enjoy my times here, as the less old ones with Lamiae, Yihuei, Joanna, Théo, Varun, Juan, Angie, Pacôme, Arnaud and Steve. I would also thank all the other member of the department and institute who help me in this thesis, scientifically or administratively, so thanks Corinne Bouillet, Céline Kieffer, Cédric Leuvrey and Isabelle Kitzinger.

More specifically, a huge thanks is dedicated to Leonardo Martinelli, Francesco Rosa, Prof. Giacomo Ghiringhelli, Marco Salluzzo and Nick Brookes for their huge help in running the RIXS experiments in the ESRF presented in chapter V as well as their understanding. I was able to learn a lot about soft x-ray spectroscopy measurements thanks to you all, and also learn a lot on my own samples thanks to the measurements we performed together. By staying in the synchrotron environment, I want to thank Raymond Fan and Paul Steadman for the help in running the experiment on their beamline in Diamond as well as their expertise on the subject. And also Fadi Choueikani from Soleil for the help in introducing me to the XMCD measurements.

Aravind Raji, Chia-Ping Su and Alexandre Gloter, thanks a lot for the microscopy images on my thin films which provide us useful insight on their quality and stability. David Sanchez, Vincent Humbert and Javier Villegas, thank you for the experiments carried on my thin films and your incredible knowledge on the subject.

I will now switch to French for the more personal acknowledgments that I want to provide.

Les premiers que je souhaite remercier sont notamment mes parents qui m’ont toujours soutenu et supporté dans mes longues études. Merci à eux pour leur patiente, humour et amour. Merci aussi à mes grands-parents qui ont été derrière moi depuis mon enfance. Et bien sûr, merci à ma sœur et mon frère pour l’enfance qu’on a eu ensemble et les liens qu’on continue d’avoir, vous êtes géniaux les

petits, ne changez pas ! Merci aussi à Gabriel, Solange et ma cousine Laura pour être venu me soutenir lors de la défense ainsi que Nathalie et Thierry.

Après la famille, il est temps de remercier les amis, et ne sachant par où commencer je vais le faire chronologiquement. Commençons donc par les (très ?) vieilles connaissances : Rémy, ça fait maintenant presque 25 ans qu'on se suit, et le magnifique personnage que tu es ne cessera jamais de m'émerveiller, merci vieux frère. Et merci aussi à tous les conscrits, vous revoir me rend nostalgique et heureux à chaque fois. Faisons un bon dans le temps, et venons-en aux rencontres du lycée en commençant par les 94. Olivier, j'étais ton témoin de mariage mais tu as réussi à oublier le jour de ma soutenance, cela reste dans la lignée de tes actions et c'est probablement ce naturel maladroit et abruti qui me plait tant chez toi, je te rejoins aux Pays-Bas dans peu de temps. Igor, ton grand sourire et ta bonne humeur communicatrice font de toi le bourreau des cœurs de toutes les mamans et le gendre idéal, mais surtout une des plus belles personnes que j'ai pu rencontrer. Lubin, 198cm pour un bon quintal, ça fait une belle quantité d'amour à proposer, et malgré ça, je suis toujours épaté par ta capacité à en donner encore plus autour de toi chaque fois qu'on se revoit. Théo et Pauline, duo inséparable qui nous borde et nous soutient depuis plus de 10 ans, vous êtes magnifiques séparément et vous brillez ensemble. Aline, ton sens de l'humour raffiné (si si je te jure) n'a d'égal que tes valeurs toujours plus juste et engagées. Romane, ta lucidité et ton humour cinglant (si si je te jure) font de toi une personne extraordinaire. Dr. Blaghonette, ton énergie et tes idées disons… surprenantes font de toi une personne à part et exceptionnelle. Marie, ta douceur ta sensibilité et ta connaissance du répertoire de Diam's m'ont toujours touché puce. Merci à vous d'avoir toujours été là, je n'espère ne jamais vous perdre. En respectant l'ordre croissant, il y a donc les 95 après les 94. Ludo, Flo, Guérin, Gaëthan, Emma, Julia, Alexandra, Laura et Aliénor merci à vous pour toutes ces journées, weekends, vacances et tout simplement années passés ensemble. Cela fait aussi plus de 10 ans que l'on ne se perd pas de vue et j'espère que ça continuera encore longtemps, vous êtes des personnes en or. Pour les nombreuses rencontre faîtes à la faculté de chimie, lors des cours ou lors de ces nombreuses heures passées dans cette cher kfet ou ailleurs. Crunch mon binôme des années fac, Thibault, Sajan, Erika, Benji, Aurélien, Gaël, Morgane, Bryan, Élodie, Coco, Toto, Yannick, Vonesh, Franck, William, Baptiste, Swann, Lohona, Marie, Alexandra, Brice, Pauline, Axel, Émeline, Steuh, Ian, Tim, Yaya, Maxime, Chloé, Cédric, Tom Pouce, Valou, la Hallebarde, Bubul, Balthi, Noureddine et le chariot.

Pour finir, merci à celle qui me soutient en permanence. Maïwenn, tu fais de moi une meilleure personne chaque jour qu'on passe ensemble, je t'aime.